Satellite Radar Interferometry

THEORY AND PRACTICE

David T. Sandwell, Xiaohua Xu, Jingyi Chen, Robert J. Mellors, Meng Wei, Xiaopeng Tong, John B. DeSanto and Qi Ou

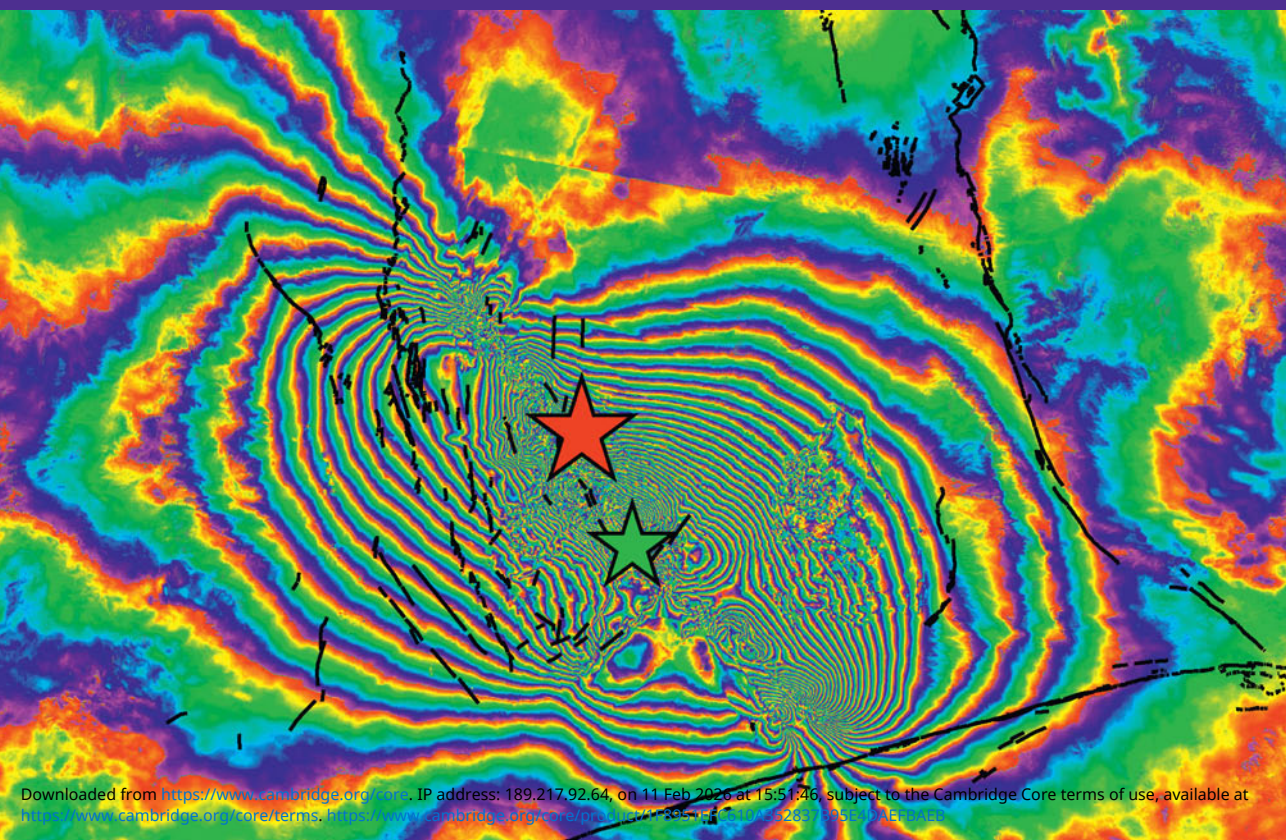

Downloaded from https://www.cambridge.org/core. IP address: 189.217.92.64, on 11 Feb 2026 at 15:51:46, subject to the Cambridge Core terms of use, available at https://www.cambridge.org/core/terms. https://www.cambridge.org/core/product/[illegible]

Downloaded from https://www.cambridge.org/core. IP address: 189.217.92.64, on 11 Feb 2026 at 15:51:46, subject to the Cambridge Core terms of use, available at https://www.cambridge.org/core/terms. https://www.cambridge.org/core/product/1F8951EFC610A352837B95E4DAEFBAEB

SATELLITE RADAR INTERFEROMETRY

Interferometric synthetic aperture radar (InSAR) is an active remote sensing method that uses repeated radar scans of the Earth's solid surface to measure relative deformation at centimeter precision over a wide swath. It has revolutionized our understanding of the earthquake cycle, volcanic eruptions, landslides, glacier flow, ice grounding lines, ground fluid injection/withdrawal, underground nuclear tests, and other applications requiring high spatial resolution measurements of ground deformation. This book examines the theory behind and the applications of InSAR for measuring surface deformation. The most recent generation of InSAR satellites has transformed the method from investigating 10s to 100s of synthetic aperture radar images to processing 1 000s and 10 000s of images using a wide range of computer facilities. This book is intended for students and researchers in the physical sciences, particularly for those working in geophysics, natural hazards, space geodesy, and remote sensing. This title is also available as Open Access on Cambridge Core.

DAVID T. SANDWELL is a professor of geophysics at Scripps Institution of Oceanography at the University of California, San Diego. His research is focused on marine tectonics, geodynamics, and the earthquake cycle using InSAR and Global Navigation Satellite System (GNSS). He is the author of more than 200 research papers and the book *Advanced Geodynamics: The Fourier Transform Method* (2022, Cambridge University Press). He is a member of the US National Academy of Sciences.

XIAOHUA XU is a professor of geophysics at the University of Science and Technology of China. His research is focused on earthquakes, faulting, crustal deformation, and tectonic geodesy.

JINGYI CHEN is an associate professor of aerospace engineering at the University of Texas at Austin. Her research is focused on the development of InSAR techniques for studying natural and induced seismicity, groundwater resources, natural disasters, and permafrost hydrology. She is a senior member of the Institute of Electrical and Electronics Engineers and a member of the American Geophysical Union.

ROBERT J. MELLORS is a researcher at Scripps Institution of Oceanography at the University of California, San Diego. His research is focused on enhancing geophysical sensing, including InSAR, global seismic instrumentation, muons, and photonic seismology. He is currently an advisor to the US Department of Energy (Advanced Research Projects Agency – Energy) on advanced energy technologies.

MENG WEI is an associate professor of oceanography in the Graduate School of Oceanography at the University of Rhode Island. His research is focused on tectonic geodesy,

Downloaded from https://www.cambridge.org/core. IP address: 189.217.92.64, on 11 Feb 2026 at 15:51:46, subject to the Cambridge Core terms of use, available at https://www.cambridge.org/core/terms. https://www.cambridge.org/core/product/1F8951EFC610A352837B95E4DAEFBAEB

fault mechanics, coastal subsidence, and natural hazards. He has published more than 30 research papers and is a recipient of the Faculty Early Career Development Program award from the National Science Foundation.

XIAOPENG TONG is an associate researcher in the Institute of Geophysics, China Earthquake Administration, Beijing. He is a PhD from the Scripps Institution of Oceanography, University of California, San Diego. His research interests include InSAR, space geodesy, and crustal deformation.

JOHN B. DESANTO is a research scientist at the University of Washington. His primary interests lie in the fields of marine tectonics and subduction zone processes. He studies these regions directly by adapting geodetic techniques such as GNSS to the offshore environment.

QI OU is a lecturer at the University of Edinburgh. She applies big Earth observation data to understand multi-hazards induced by active tectonics, climate change, and anthropogenic activities. She is the author of several highly cited papers, a convener and speaker at the Seismological Society of America and American Geophysical Society conferences, and a recipient of a Discipline Hopping Award from UK Research and Innovation.

Downloaded from https://www.cambridge.org/core. IP address: 189.217.92.64, on 11 Feb 2026 at 15:51:46, subject to the Cambridge Core terms of use, available at https://www.cambridge.org/core/terms. https://www.cambridge.org/core/product/1F8951EFC610A352837B95E4DAEFBAEB

SATELLITE RADAR INTERFEROMETRY

Theory and Practice

DAVID T. SANDWELL
University of California, San Diego

XIAOHUA XU
University of Science and Technology of China

JINGYI CHEN
The University of Texas at Austin

ROBERT J. MELLORS
University of California, San Diego

MENG WEI
University of Rhode Island

XIAOPENG TONG
China Earthquake Administration

JOHN B. DESANTO
University of Washington

QI OU
University of Edinburgh

CAMBRIDGE
UNIVERSITY PRESS

Downloaded from https://www.cambridge.org/core. IP address: 189.217.92.64, on 11 Feb 2026 at 15:51:46, subject to the Cambridge Core terms of use, available at https://www.cambridge.org/core/terms. https://www.cambridge.org/core/product/1F8951EFC610A352837B95E4DAEFBAEB

CAMBRIDGE UNIVERSITY PRESS

Shaftesbury Road, Cambridge CB2 8EA, United Kingdom

One Liberty Plaza, 20th Floor, New York, NY 10006, USA

477 Williamstown Road, Port Melbourne, VIC 3207, Australia

314–321, 3rd Floor, Plot 3, Splendor Forum, Jasola District Centre,
New Delhi – 110025, India

103 Penang Road, #05–06/07, Visioncrest Commercial, Singapore 238467

Cambridge University Press is part of Cambridge University Press & Assessment,
a department of the University of Cambridge.

We share the University's mission to contribute to society through the pursuit of
education, learning and research at the highest international levels of excellence.

www.cambridge.org
Information on this title: www.cambridge.org/9781009606233

DOI: 10.1017/9781009606226

© David T. Sandwell, Xiaohua Xu, Jingyi Chen, Robert J. Mellors, Meng Wei, Xiaopeng Tong,
John B. DeSanto, and Qi Ou 2025

This publication is in copyright. Subject to statutory exception and to the provisions of relevant collective licensing agreements, with the exception of the Creative Commons version the link for which is provided below, no reproduction of any part may take place without the written permission of Cambridge University Press & Assessment.

An online version of this work is published at doi.org/10.1017/9781009606226 under a Creative Commons Open Access license CC-BY-NC-ND 4.0 which permits re-use, distribution and reproduction in any medium for non-commercial purposes providing appropriate credit to the original work is given. You may not distribute derivative works without permission. To view a copy of this license, visit https://creativecommons.org/licenses/by-nc-nd/4.0

When citing this work, please include a reference to the DOI 10.1017/9781009606226

First published 2025

A catalogue record for this publication is available from the British Library

A Cataloging-in-Publication data record for this book is available from the Library of Congress

ISBN 978-1-009-60623-3 Hardback

Additional resources for this publication at www.cambridge.org/sandwell.

Cambridge University Press & Assessment has no responsibility for the persistence or accuracy of URLs for external or third-party internet websites referred to in this publication and does not guarantee that any content on such websites is, or will remain, accurate or appropriate.

Downloaded from https://www.cambridge.org/core. IP address: 189.217.92.64, on 11 Feb 2026 at 15:51:46, subject to the Cambridge Core terms of use, available at https://www.cambridge.org/core/terms. https://www.cambridge.org/core/product/1F8951EFC610A352837B95E4DAEFBAEB

Contents

Preface and Acknowledgments *page* ix

1 Introduction 1
- 1.1 Essential Ingredients for Satellite Remote Sensing 2
- 1.2 Main Categories of Satellite Remote Sensing 4

2 Principles of Synthetic Aperture Radar 8
- 2.1 Introduction 8
- 2.2 Fraunhofer Diffraction 8
- 2.3 Two-Dimensional Aperture 13
- 2.4 Range and Azimuth Resolution 14
- 2.5 Constraints on Pulse Repetition Frequency 15
- 2.6 Problems 17

3 Satellite Orbits 19
- 3.1 Introduction 19
- 3.2 Kepler Elements 21
- 3.3 Precession of the Orbit Plane 24
- 3.4 Ground Track of Circular Orbit 25
- 3.5 Ellipsoidal Earth Model 28
- 3.6 Special Orbits 30
- 3.7 Precise Orbits for InSAR 34
- 3.8 Problems 39

4 SAR Image Formation 41
- 4.1 Overview of the Range-Doppler Algorithm 41
- 4.2 Processing Onboard the Satellite 41
- 4.3 Digital SAR Processing 42

Downloaded from https://www.cambridge.org/core. IP address: 189.217.92.64, on 11 Feb 2026 at 15:51:46, subject to the Cambridge Core terms of use, available at https://www.cambridge.org/core/terms. https://www.cambridge.org/core/product/1F8951EFC610A352837B95E4DAEFBAEB

	4.4	Range Compression	46
	4.5	Azimuth Compression	48
	4.6	Example with ALOS L-Band Orbit	56
	4.7	Problems	58
5	Interferometric Processing		60
	5.1	Interferogram Formation	60
	5.2	Contributions to Phase	61
	5.3	Phase due to Earth Curvature	62
	5.4	Look Angle and Incidence Angle for a Spherical Earth	63
	5.5	Critical Baseline	65
	5.6	Approximate Phase due to Topography	66
	5.7	Topography from Single-Pass InSAR: SRTM	67
	5.8	Exact Phase due to Earth Curvature and Topography	68
	5.9	Geocoding	69
	5.10	Geocoded SLC InSAR Processing Strategy	71
	5.11	Problems	72
6	Coherence, Filtering, and Phase Gradient		73
	6.1	Need for Filtering an Interferogram	73
	6.2	Coherence and Filtering Techniques	74
	6.3	Goldstein Frequency Domain Filter	79
	6.4	Phase Gradient	79
	6.5	Problems	82
7	Phase Unwrapping		84
	7.1	Basic Concepts	84
	7.2	Fourier Transform Algorithm	89
	7.3	Branch Cut (Goldstein) Algorithm	92
	7.4	Minimum Cost Flow (SNAPHU) Algorithm	93
	7.5	Nearest-Neighbor Algorithm and Loop Closure	95
	7.6	Summary	97
	7.7	Problems	99
8	SAR Modes		101
	8.1	Introduction	101
	8.2	Polarization	103
	8.3	Range and Azimuth Resolution	104
	8.4	ScanSAR Processing and Interferometry	105
	8.5	Terrain Observation by Progressive Scans	111

Downloaded from https://www.cambridge.org/core. IP address: 189.217.92.64, on 11 Feb 2026 at 15:51:46, subject to the Cambridge Core terms of use, available at https://www.cambridge.org/core/terms. https://www.cambridge.org/core/product/1F8951EFC610A352837B95E4DAEFBAEB

8.6 SweepSAR 119
8.7 Problems 121

9 Troposphere, Ionosphere, and Tide Corrections 122
9.1 Contributions to Phase 122
9.2 Refractive Index of the Troposphere and Ionosphere 125
9.3 Characteristics and Mitigation of the Troposphere Delay 128
9.4 Characteristics and Mitigation of the Ionosphere Advance 136
9.5 Tides and Aliasing 142
9.6 Problems 146

10 Complementary Approaches and Time Series 147
10.1 Complementary Approaches 147
10.2 Range and Azimuth Pixel Offsets 148
10.3 Multiple Aperture and Burst Overlap Interferometry 150
10.4 Stacking Approach 154
10.5 Small Baseline Subset Method 156
10.6 Persistent Scatterer Algorithms 159
10.7 Problems 165

11 Integration of InSAR and GNSS 166
11.1 Complementary Attributes of InSAR and GNSS 166
11.2 Vector Decomposition 167
11.3 Corrected GNSS LOS Displacement for Events 171
11.4 Interseismic Velocity and Strain Rate 172
11.5 InSAR/GNSS Time Series 177
11.6 Problems 181

References 184
Index 195

Downloaded from https://www.cambridge.org/core. IP address: 189.217.92.64, on 11 Feb 2026 at 15:51:46, subject to the Cambridge Core terms of use, available at https://www.cambridge.org/core/terms. https://www.cambridge.org/core/product/1F8951EFC610A352837B95E4DAEFBAEB

Downloaded from https://www.cambridge.org/core. IP address: 189.217.92.64, on 11 Feb 2026 at 15:51:46, subject to the Cambridge Core terms of use, available at https://www.cambridge.org/core/terms. https://www.cambridge.org/core/product/1F8951EFC610A352837B95E4DAEFBAEB

Preface and Acknowledgments

This textbook provides a comprehensive overview of satellite radar interferometry for mapping surface deformation from various phenomena, including earthquakes, volcanoes, landslides, glacier flow, ice grounding lines, ground fluid injection/withdrawal, and underground nuclear tests. It is designed for students and researchers in the physical sciences, who have completed courses in introductory physics, calculus, and computer science.

The book covers the physical principles, mathematical models, and algorithms used in Interferometric synthetic aperture radar (InSAR) processing from a geodetic perspective. Readers will gain insights into both the theoretical underpinnings and practical applications of InSAR, making it a valuable resource for understanding and utilizing this powerful remote sensing technology.

Chapter 1 discusses six types of remote sensing methods possible from Earth orbit and introduces radar interferometry as the optimal approach for measuring small surface deformation.

Chapter 2 explains the basic physics of radar imaging from orbital altitude, including the limits on accuracy, spatial resolution in the range and azimuth directions, and the fundamental limitation on swath width.

Chapter 3 details the kinematics of satellite orbits and their use in InSAR processing and its automation. It covers the six parameters needed to describe an orbit (Kepler elements or Cartesian state vector), transforming coordinates from an Earth-fixed frame to the satellite frame, and methods to calculate a centimeter-accuracy satellite trajectory from a sequence of state vectors.

Chapter 4 provides a comprehensive presentation of the commonly used range-Doppler algorithm for focusing complex backscatter data into a single-look complex (SLC) image.

Chapter 5 explains the process of forming an interferogram from two geometrically aligned SLC images and methods for extracting deformation and topography

Downloaded from https://www.cambridge.org/core. IP address: 189.217.92.64, on 11 Feb 2026 at 15:51:46, subject to the Cambridge Core terms of use, available at https://www.cambridge.org/core/terms. https://www.cambridge.org/core/product/1F8951EFC610A352837B95E4DAEFBAEB

from the interferometric phase. It also covers critical baseline, geocoding, and geocoded SLCs.

Chapter 6 discusses the main methods for filtering complex interferograms and computing coherence and phase gradient.

Chapter 7 introduces the basic concepts and fundamental limitations (i.e., residues) of phase unwrapping. It presents three common unwrapping methods: the global Fourier transform method, the path-following branch-cut method, and the minimum cost flow method. Additionally, it covers methods for correcting integer ambiguities using phase closure within stacks of interferograms.

Chapter 8 explores a wide range of SAR operational modes, including polarization and wide swath modes. It reviews the fundamental limitation of the standard swath-mode acquisition and discusses three methods for increasing swath width: ScanSAR, terrain observation by progressive scans (TOPS), and SweepSAR for the upcoming NASA–ISRO–SAR mission.

Chapter 9 examines the three factors that affect radar range measurement: spatial and temporal variations of the dry and wet components of the troposphere, phase advance of radar waves through the ionosphere, and the solid Earth tides. It also discusses practical corrections and mitigation approaches.

Chapter 10 presents complementary approaches to measuring surface deformation by radar, including pixel offset tracking, multiple aperture interferometry, and burst overlap interferometry. The second part of the chapter discusses methods for extracting surface velocity and time series from a large set of interferograms, as well as identifying pixels that remain stable over long periods.

Chapter 11 highlights the need for ground control, such as Global Navigation Satellite System (GNSS) survey points, to bring InSAR deformation measurements into a geodetic reference frame. It also explains the theory for projecting vector GNSS displacement into scalar line-of-sight (LOS) InSAR displacement and the computation of strain rate from InSAR.

This textbook has been developed over the past two decades from a Space Geodesy class at Scripps Institution of Oceanography, as well as GMTSAR short courses at UNAVCO and EarthScope. Each chapter includes a set of exercises and solutions to highlight the important concepts.

The algorithms described in the book are implemented in a computer software package called GMTSAR, an open-source, InSAR processing system designed for users familiar with the Generic Mapping Tools (GMT). While the book references this specific software, the content is also relevant to any modern InSAR processing system.

GMTSAR software was developed over a period of 25 years to create a geodetically accurate, open-source InSAR processing system. Many individuals contributed to its development.

Downloaded from https://www.cambridge.org/core. IP address: 189.217.92.64, on 11 Feb 2026 at 15:51:46, subject to the Cambridge Core terms of use, available at https://www.cambridge.org/core/terms. https://www.cambridge.org/core/product/1F8951EFC610A352837B95E4DAEFBAEB

Howard Zebker (Stanford) provided the original FORTRAN code for the SAR processor. Evelyn Price (a University of California, San Diego (UCSD) student) translated this code into C, simplifying it while keeping the SAR-focusing algorithm unchanged. Price and Sandwell expanded this into a complete InSAR package by adding cross-correlation and phase modules. Paul Jamason (UCSD) wrote the preprocessors for ERS (CCRS and DPAF). Remko Sharro's (Delft University) getorb routines were used to compute precise orbits for proper focus, geolocation, and baseline estimation.

The GIPS package, developed by Peter Ford (the Massachusetts Institute of Technology), led to the creation of the SIOSAR system, which remained stable for 11 years. Sean Buckley, a student at UT Austin, developed the Envisat preprocessor. In 2010, GIPS was replaced by GMT modules. Rob Mellors (San Diego State University) developed the Advanced Land Observing Satellite preprocessing code, later translated by Matt Wei (a UCSD student) into the ERS and Envisat preprocessors. Mellors also wrote new software for image cross-correlation and Goldstein/Werner interferogram filtering.

Xiaopeng Tong (a UCSD student) tested and refined the codes, removing some approximations from SIOSAR. He also developed scripts for two-pass processing, stacking, and the time series (SBAS) C-code. The statistical-cost, network-flow algorithm for phase unwrapping C-code, written by Curtis Chen and Howard Zebker (Stanford), is used without modification.

Paul Wessel (University of Hawaii) enhanced GMT to process large binary tables and modified all the code to interface with GMT routines during his sabbatical at Scripps Institute of Oceanography in 2013. He also developed code for Keyhole Markup Language output for Google Earth. GMTSAR uses the GMT routines blockmedian and surface, developed by Walter Smith and Paul Wessel (Lamont-Doherty Earth Observatory). These routines are central to GMTSAR algorithms for transforming between geographic and radar coordinates.

Most recently, Xiaohua Xu (a UCSD student) and David Sandwell developed preprocessing and alignment codes for TOPS-mode interferometry, with assistance from Pablo Gonzalez (Leeds University, UK). Recent developments include InSAR corrections, GNSS integration by Katherine Guns, and common scene stacking by Katia Tymofyeyeva. Many users provided feedback and bug reports, helping to achieve a robust and stable software set.

Funding for research algorithms and code development was provided by the NASA Earth Surface and Interior program. The National Science Foundation Cyberinfrastructure for Sustained Scientific Innovation program supported code testing, hardening, and documentation (e.g., this book). EarthScope, formerly UNAVCO, supported GMTSAR short courses where lectures and homework problems were developed. Khalid Soofi supported the project through funding from

Downloaded from https://www.cambridge.org/core. IP address: 189.217.92.64, on 11 Feb 2026 at 15:51:46, subject to the Cambridge Core terms of use, available at https://www.cambridge.org/core/terms. https://www.cambridge.org/core/product/1F8951EFC610A352837B95E4DAEFBAEB

ConocoPhillips and by testing and developing the software. The National Geodetic Survey provided support for book development and open access publication. The Scripps Institution of Oceanography/UCSD provided many years of salary support for Sandwell to develop and publish the book.

Downloaded from https://www.cambridge.org/core. IP address: 189.217.92.64, on 11 Feb 2026 at 15:51:46, subject to the Cambridge Core terms of use, available at https://www.cambridge.org/core/terms. https://www.cambridge.org/core/product/1F8951EFC610A352837B95E4DAEFBAEB

1

Introduction

Interferometric synthetic aperture radar (InSAR) is an active remote sensing method that uses repeated radar scans of the Earth's solid surface to measure relative deformation at cm precision over a wide swath. This method has revolutionized our understanding of the earthquake cycle, volcanic eruptions, landslides, glacier flow, ice grounding lines, ground fluid injection/withdrawal, underground nuclear tests, and many other applications that require high spatial resolution measurements of ground deformation (Biggs and Wright, 2020; Joughin et al., 2010; Galloway and Hoffmann, 2007; Wei, 2017). The most recent generation of InSAR satellites has transformed the method from investigating 10s to 100s of synthetic aperture radar (SAR) images to processing 1 000s and 10 000s of images using a wide range of computer facilities. This transformation was largely driven by the Sentinel-1 mission, which was designed for InSAR time series analysis. There are a number of excellent review papers on this topic ranging from InSAR overviews (e.g., Massonnet and Feigl (1998); Bürgmann et al. (2000)) to detailed mathematical descriptions of the measurement and associated errors (Rosen et al. (2000); Simons and Rosen (2007, 2015); Franceschetti and Lanari (2018)).

The focus of this book is to provide the basic physical principles of the method as well as the mathematical model and algorithms used in InSAR processing. These algorithms are implemented in a computer software package called GMTSAR – an open-source (GNU General Public License) InSAR processing system designed for users familiar with generic mapping tools (GMT – (Wessel et al., 2019)). Although the book refers to this particular software, it is also relevant to other modern InSAR processing systems (e.g., ISCE – (Rosen et al., 2012), GAMMA – (Wegnüller et al., 2016), SNAP). This book has been developed over the past 25 years from a Space Geodesy class at Scripps Institution of Oceanography as well as GMTSAR short courses at UNAVCO and EarthScope. Each chapter has a set of problems and solutions to highlight the important concepts. In addition, we will answer 16 basic questions related to InSAR, including:

Downloaded from https://www.cambridge.org/core. IP address: 189.217.92.64, on 11 Feb 2026 at 15:51:46, subject to the Cambridge Core terms of use, available at https://www.cambridge.org/core/terms. https://www.cambridge.org/core/product/1F8951EFC610A352837B95E4DAEFBAEB

1. What are the six main categories of satellite remote sensing and why is active remote sensing at microwave wavelengths (2.5 cm–25 cm) best for measuring Earth deformation? (Section 1.2)
2. Why are SAR antennas typically 10 m long in the along-track direction and 1–2 m wide in the cross-track direction? (Section 2.3)
3. What factors control the spatial resolution of a SAR image? (Sections 2.4)
4. What factors limit the width of a SAR swath? (Section 2.5)
5. What are the typical orbital characteristics (e.g., altitude, speed, repeat cycle) of an InSAR satellite and why? (Section 3.2)
6. A C-band SAR operates at a 5 GHz carrier frequency. Why can the full-resolution radar data be recorded at a much lower rate of perhaps 15 MHz? (Section 4.2)
7. How is the raw SAR data focused by a computer to obtain a high spatial resolution image of amplitude and phase? (Chapter 4)
8. What orbit accuracy is needed to achieve an optimally focused SAR image? (Sections 4.5 and 4.6)
9. How is an interferogram constructed from repeated SAR images and what are the main contributions to the phase? (Sections 5.1 and 5.2)
10. How close in space does the repeat orbit need to match the reference orbit to achieve high correlation and good phase recovery? (Section 5.5)
11. How does decorrelation depend on radar wavelength and surface properties? (Section 6.2)
12. What is the best way to detect phase unwrapping errors? (Section 7.5)
13. What are the three main methods for achieving wide swath InSAR? (Chapter 8)
14. What are the main sources of error in most interferograms? (Chapter 9)
15. How can one construct an InSAR time series using existing freely open data sets? (Chapter 10)
16. How can a scalar InSAR time series be integrated with a vector GNSS time series? (Chapter 11)

The processing details associated with the last two questions are addressed in a companion book entitled – *Satellite Radar Interferometry: Application – GMTSAR*. This book mainly covers the theoretical aspects of InSAR. We will begin with a very brief overview of satellite remote sensing to answer the first question.

1.1 Essential Ingredients for Satellite Remote Sensing

Satellite remote sensing of the surface of the Earth relies on four essential ingredients:

Downloaded from https://www.cambridge.org/core. IP address: 189.217.92.64, on 11 Feb 2026 at 15:51:46, subject to the Cambridge Core terms of use, available at https://www.cambridge.org/core/terms. https://www.cambridge.org/core/product/1F8951EFC610A352837B95E4DAEFBAEB

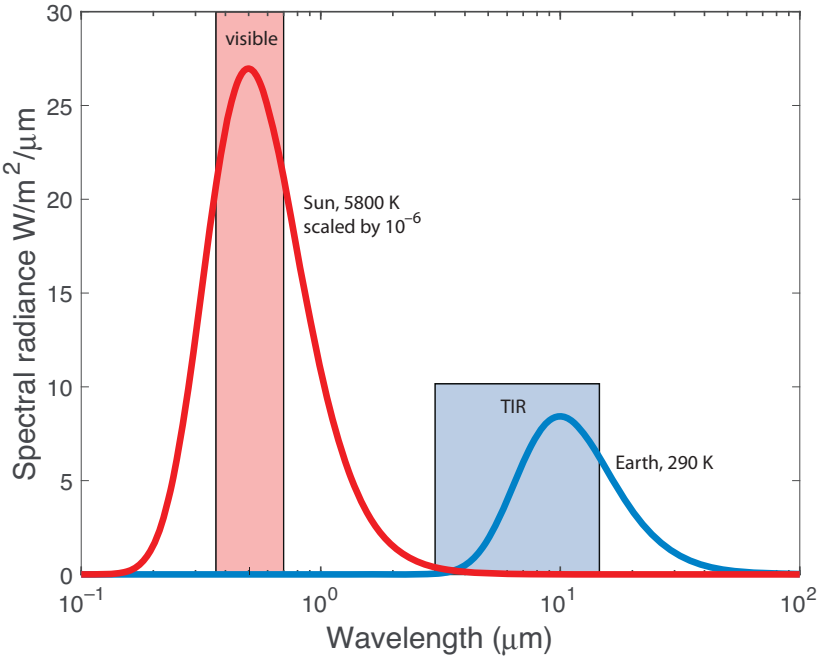

Figure 1.1 Blackbody radiation curves for a temperature of 5 800 K corresponding to the Sun and 290 K roughly corresponding to the Earth. The peak in the solar radiation (scaled by 10^{-6}) is centered on the visible part of the spectrum between 400 and 800 nanometers. The peak in the Earth's thermal radiation occurs in the thermal infrared (TIR) between 3 and 15 micrometers.

First, there must be a source of electromagnetic (EM) radiation. This could be passive radiation (Figure 1.1) from reflected sunlight, which peaks in the visible part of the spectrum (red curve), or passive radiation from the Earth's thermal emissions, which peaks in the thermal infrared (TIR) part of the spectrum (blue curve). An alternate radiation source is for the satellite to illuminate the Earth using an active sensor. While this requires significant power to generate the EM signal, the amplitude and phase of the source can be well controlled so one can measure the round-trip travel time of the pulse.

Second, the EM radiation must be able to pass through the Earth's atmosphere. As shown in Figure 1.2, there are three main windows in the visible (shaded red), thermal infrared (TIR; shaded blue), and microwave region (shaded green).

Third, there needs to be a satellite in space to collect the EM signals, digitize the signals, and transmit the data back to Earth. The satellite must be in orbit around the Earth so the inward force of gravity must be equal to the outward centrifugal force. A variety of possible orbits are discussed in Chapter 3. One can tune the orbit and platform characteristics to vary altitude, speed, revisit time, phase of the orbit

Downloaded from https://www.cambridge.org/core. IP address: 189.217.92.64, on 11 Feb 2026 at 15:51:46, subject to the Cambridge Core terms of use, available at https://www.cambridge.org/core/terms. https://www.cambridge.org/core/product/1F8951EFC610A352837B95E4DAEFBAEB

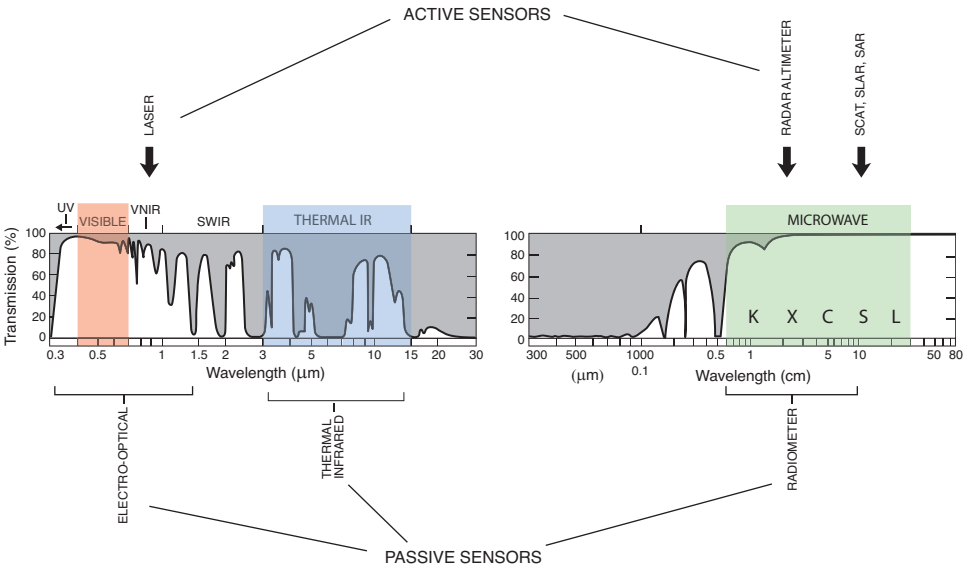

Figure 1.2 Percent transmission of EM waves through the Earth's atmosphere as a function of wavelength. There are three main windows where the atmosphere is mostly transparent. They are the visible (shaded red) centered at 0.5 micrometer, the TIR (shaded blue) centered at 8 micrometers with prominent windows at 3.5 and 10 micrometers, and the microwave (shaded green) at wavelengths between 0.6 cm and 30 cm. Note that EM waves at wavelengths greater than about 30 cm are strongly distorted and reflected by the ionosphere. The microwave region has bands noted by letters. The most common bands for radar interferometry are X, C, S, and L. The K-band is mainly used for radar altimetry and microwave radiometry.

plane with respect to solar illumination or lunar/solar tides, and platform orientation (yaw, pitch, and roll).

Fourth, there must be a computer and software (e.g., GMTSAR) to ingest the downlinked imagery/orbital information and construct maps of surface reflectance and deformation.

1.2 Main Categories of Satellite Remote Sensing

Based on these constraints, there are roughly six possible categories of Earth remote sensing instruments (i.e., three atmospheric windows and two modes – passive or active). These categories include:

The first type of passive sensor is an electro-optical instrument that operates in the visible part of the spectrum and uses cameras to construct imagery. A typical sensor is LANDSAT-7. The satellite was placed into a Sun-synchronous orbit having an inclination of 98.2 degrees and an altitude of 705 km. This seventh

Downloaded from https://www.cambridge.org/core. IP address: 189.217.92.64, on 11 Feb 2026 at 15:51:46, subject to the Cambridge Core terms of use, available at https://www.cambridge.org/core/terms. https://www.cambridge.org/core/product/1F8951EFC610A352837B95E4DAEFBAEB

LANDSAT had eight bands comprising six bands in the visible and near infrared with 30 m spatial resolution, a thermal infrared band with 60 m spatial resolution, and a panchromatic band with 15 m spatial resolution. These electro-optical sensors are usually placed into a Sun-synchronous orbit to provide relatively constant Sun illumination for each ascending (or descending) overflight. Very high spatial resolution optical sensors can measure sharp horizontal variations in surface deformation at a precision of about one tenth of a pixel size using cross-correlation methods on repeated images and these data are highly complementary to deformation measurements with InSAR (e.g., Avouac et al. (2006); Milliner et al. (2015)).

The second type of passive sensor is a TIR camera using the atmospheric window between 8 and 15 micrometers. The TIR camera measures thermal emissions from land or ocean surface, which can be used to infer surface temperature (e.g., McClain et al. (1985); Donlon et al. (2012)). These TIR cameras do not need to be in Sun-synchronous orbits and the acquisitions are designed to avoid specular reflections of solar radiation.

The third type of passive sensor is a microwave radiometer. This instrument uses the highly transparent window in the microwave part of the EM spectrum (1 cm–30 cm) to measure thermal emissions from the land (e.g., Reichle et al. (2007)) or ocean (e.g., Chelton and Wentz (2005)). Since they operate at wavelengths much longer than the ~10 micrometer peak in the blackbody radian spectrum from the Earth at 290 K, they must stare at the surface for a relatively long time (~0.1 s) to gather enough independent looks to achieve an accurate measurement of temperature. Moreover, since they operate at this relatively long wavelength λ, a large antenna diameter D is needed to achieve a useful angular resolution θ_a. In Chapter 2, we develop the Fraunhofer diffraction resolution $\sin(\theta_a) = 1.22\,\lambda/D$ to illustrate the pronounced resolution differences between short-wavelength optical systems (λ = ~0.5 micrometers) and longer wavelength microwave systems (λ = ~50 mm).

The fourth sensor is an active laser altimeter that can be used to measure the topography of a wide range of surfaces, including ocean, ice, land, vegetation, and buildings. The atmosphere is sometimes opaque over the visible part of the spectrum because of clouds. The lidar can measure distances very accurately by sending a sharp pulse of light and measuring the two-way travel time of the reflected pulse. Monitoring changes in ocean ice and continent ice thickness are two of the most important applications of this method (Markus et al. (2017)).

The fifth sensor is an active radar altimeter that is best for measuring the topography of the ocean surface and changes in sea surface height due to a wide range of oceanographic processes (Fu and Cazenave (2000)). As we will discuss in

Downloaded from https://www.cambridge.org/core. IP address: 189.217.92.64, on 11 Feb 2026 at 15:51:46, subject to the Cambridge Core terms of use, available at https://www.cambridge.org/core/terms. https://www.cambridge.org/core/product/1F8951EFC610A352837B95E4DAEFBAEB

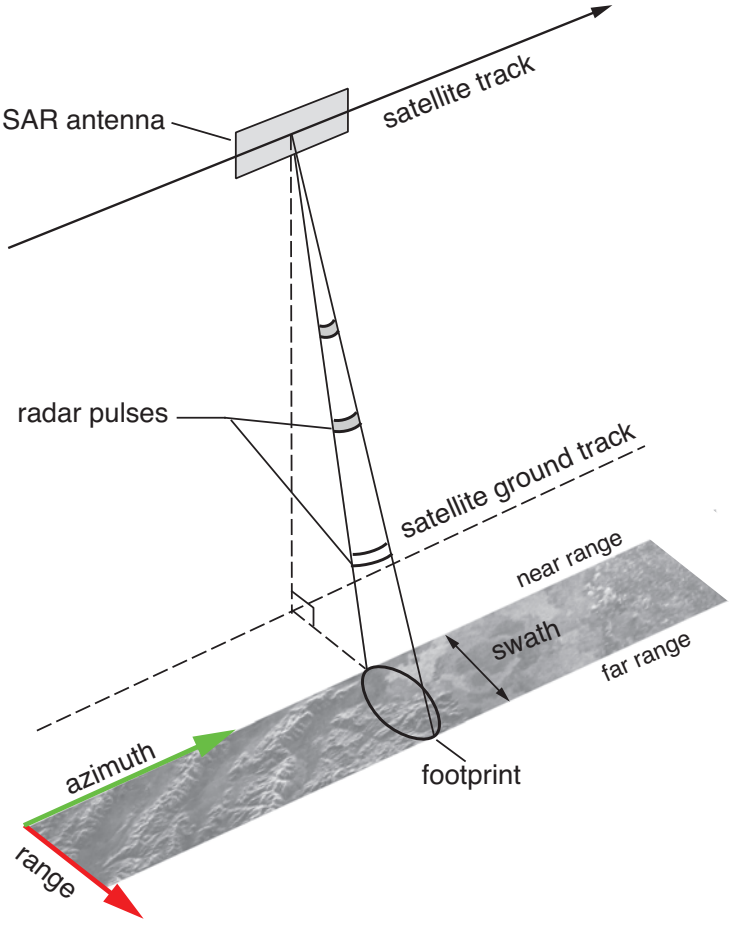

Figure 1.3 Schematic diagram of a SAR satellite in orbit. The SAR antenna has its long axis in the flight direction (also called the *azimuth* direction) and the short axis in the *range* direction. The radar sends pulses to one side of the *ground track* that illuminate the Earth over a large elliptical footprint. The reflected energy returns to the radar where it is recorded as a function of *fast time* in the range direction and *slow time* in the azimuth direction.

Chapter 2, the beam-limited footprint of a radar altimeter is 10s of km in diameter. To reduce the diameter of the footprint, the radar emits a sharp pulse having a spherical wavefront. The radar measures the two-way travel time of the leading edge of the pulse, which corresponds to the closest reflector from the satellite. Over the ocean this is also the *nadir* point as well as the zero-Doppler shift point. In practice, it is difficult to send a very sharp radar pulse so the radar emits a rather long frequency-modulated chirp that reflects from the ocean and returns to the sensor.

Downloaded from https://www.cambridge.org/core. IP address: 189.217.92.64, on 11 Feb 2026 at 15:51:46, subject to the Cambridge Core terms of use, available at https://www.cambridge.org/core/terms. https://www.cambridge.org/core/product/1F8951EFC610A352837B95E4DAEFBAEB

A sharp pulse is formed after reception by deconvolving the return chirp with a replica of the outgoing chirp.

The sixth sensor is an active radar that sends pulses of microwave energy to the side of the sub-satellite ground track (e.g., Curlander and McDonough (1991)) as shown in Figure 1.3. Like a radar altimeter, these pulses have broad spherical wavefronts that reflect off a large ellipsoidal *footprint* forming a wide *swath*. The first reflections come from the *near-range* edge of the swath. The pulse sweeps across the swath to the *far-range* edge of the swath.

The data collected by this side-looking radar have very poor spatial resolution related to the large size of the footprint. Chapters 2–4, we will describe how these data are focused first in the range direction and then in the azimuth direction using a synthetic aperture method (SAR). This is a good place to note that the raw SAR data come as a 2-D array of numbers. The rows of the file correspond to the *range* direction marked by the red arrow in Figure 1.3. The columns in the file correspond to the along-track direction of the satellite, which is also called *azimuth* marked by the green arrow in Figure 1.3. The data are equally spaced in time in both dimensions. The time spacing in the range direction is 1/*range sampling rate*. If the range cells are $\Delta\rho = 5$ meters, then the range sampling rate $\Delta t = c/(2 * \Delta\rho) = 30$ MHz, where c is the speed of light. This dimension is also called *fast time* because of the high sampling rate. The sampling rate in the azimuth direction, also called the *pulse repetition frequency* (PRF) is much lower at ~1 500 Hz; this dimension is called *slow time*. In Chapter 2, we will discuss how these sampling rates are related to the resolution of the SAR image as well as the velocity of the spacecraft and the length of the antenna.

Downloaded from https://www.cambridge.org/core. IP address: 189.217.92.64, on 11 Feb 2026 at 15:51:46, subject to the Cambridge Core terms of use, available at https://www.cambridge.org/core/terms. https://www.cambridge.org/core/product/1F8951EFC610A352837B95E4DAEFBAEB

2

Principles of Synthetic Aperture Radar

2.1 Introduction

Synthetic aperture radar (SAR) satellites collect swaths of side-looking echoes at a sufficiently high-range resolution and along-track sampling rate to form high-resolution imagery (see Figure 1.3). These notes are derived from excellent books by Curlander and McDonough (1991), Elachi and Van Zyl (2021), and Elachi (1988). As discussed in this chapter, the *range resolution* of the raw radar data is determined by the *pulse length* and the *incidence angle*. For real aperture radar, the along-track or *azimuth* resolution of the outgoing microwave pulse is diffraction limited to an angle corresponding to the wavelength of the radar (e.g., 0.05 m) divided by the length of the aperture (e.g., 10 m). When this beam pattern is projected onto the surface of the Earth at a range of say 850 km, it illuminates 8 000 m in the along-track dimension so the raw radar data are horribly out of focus in azimuth. Using the synthetic aperture method, the image can be focused on a point reflector on the ground by coherently summing thousands of consecutive echoes, thus creating a synthetic aperture perhaps 5 000-m long. Proper focus is achieved by summing the complex numbers along a constant range (Chapter 4). The focused image contains both *amplitude* (backscatter) and *phase* (range) information for each resolution cell.

2.2 Fraunhofer Diffraction

To understand why a synthetic aperture is needed for microwave imaging from orbital altitude, one must understand the concepts of diffraction and resolution. Consider the projection pattern of coherent radiation after it passes through an *aperture*. First we will consider a 1-D aperture and then go on to a 2-D rectangular aperture to simulate a rectangular SAR antenna. The 2-D case provides the shape and dimension of the footprint of the radar. Although we will develop the resolution characteristics of apertures as transmitters of radiation, the resolution

Downloaded from https://www.cambridge.org/core. IP address: 189.217.92.64, on 11 Feb 2026 at 15:51:46, subject to the Cambridge Core terms of use, available at https://www.cambridge.org/core/terms. https://www.cambridge.org/core/product/1F8951EFC610A352837B95E4DAEFBAEB

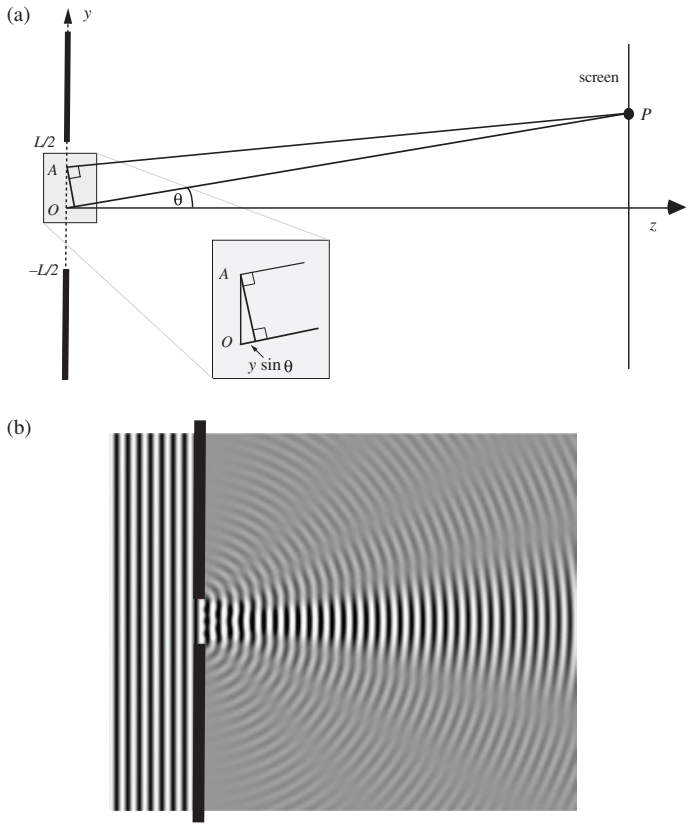

Figure 2.1 (a) Geometric diagram for the projection of coherent waves on a screen that is far from the aperture of length L. (b) Image of coherent waves passing through a slit (aperture) in a wall.

characteristics are exactly the same when the aperture is used to receive radiation. These notes were developed from Rees (2001) and Bracewell (1978).

We simulate *coherent radiation* by point sources of radiation distributed along the aperture between $-L/2$ and $L/2$ (Figure 2.1). For simplicity we will assume that all the sources have the same amplitude a, wavelength λ, and phase. Given these sources of radiation, we solve for the illumination pattern on the screen as a function of θ. We will assume that the screen is far enough from the aperture so that the rays AP and OP are parallel. Later we will determine how far away the screen needs to be in order for this approximation to hold. Under these conditions, the ray AP is slightly shorter than the ray OP by an amount $-y \sin\theta$. This corresponds to a phase shift of $\frac{-2\pi}{\lambda} y \sin\theta$. The amplitude of the illumination at point P is the integral over all of the sources along the aperture multiplied by their complex phase value

$$P(\theta) = \int_{-L/2}^{L/2} a(y) e^{-i2\pi y k \sin\theta} \, \mathrm{d}y, \tag{2.1}$$

Downloaded from https://www.cambridge.org/core. IP address: 189.217.92.64, on 11 Feb 2026 at 15:51:46, subject to the Cambridge Core terms of use, available at https://www.cambridge.org/core/terms. https://www.cambridge.org/core/product/1F8951EFC610A352837B95E4DAEFBAEB

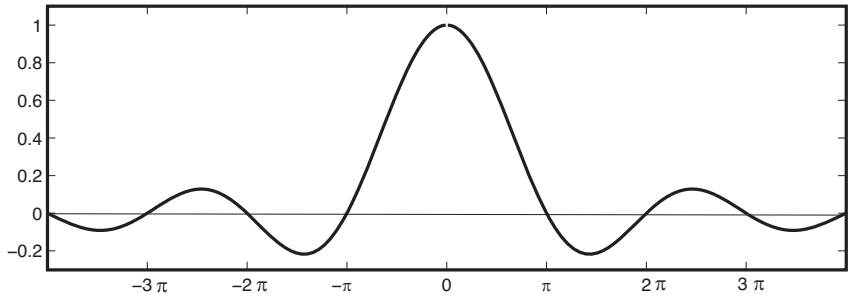

Figure 2.2 Sinc function illumination pattern for the aperture shown in Figure 2.1.

where the wavenumber $k = 1/\lambda$. This is called the Fraunhofer diffraction integral. The illumination across the aperture is uniform in both amplitude and phase, so we set $a(y) = 1$. Now, let $s = 2\pi k \sin\theta$, so the integral is easy to evaluate:

$$P(s) = \int_{-L/2}^{L/2} e^{-isy}\,\mathrm{d}y = \frac{e^{-isL/2} - e^{isL/2}}{-is} = \frac{2}{s}\sin(sL/2) = L\,\mathrm{sinc}\,(sL/2). \tag{2.2}$$

Replacing s with $2\pi \sin\theta/\lambda$, we arrive at the final result:

$$P(\theta) = L\,\mathrm{sinc}\left(\frac{L\pi \sin\theta}{\lambda}\right). \tag{2.3}$$

The illumination pattern on the screen is shown in Figure 2.2.

The first zero crossing, or *angular resolution* θ_a, of the sinc function occurs when the argument is π, so

$$\sin\theta_a = \frac{\lambda}{L}. \tag{2.4}$$

You should remember this formula. Note for small angles $\theta_a \cong \frac{\lambda}{L}$ and $\tan\theta_a \cong \sin\theta_a$. One could modify the screen illumination by changing the strength of the illumination across the aperture. For example, a theoretical Gaussian aperture would produce a Gaussian illumination function on the screen. This would eliminate the *sidelobes* associated with the sinc function, but it would also broaden the projection pattern. In addition, one could vary the phase along the aperture to shift the point of maximum illumination away from $\theta = 0$. Such a phased array aperture is used in some radar systems to continuously illuminate a feature as the satellite passed over it. This is called *spotlight mode* SAR, and it is a favorite technique for military reconnaissance.

One can perform the same type of analysis with any 2-D aperture; many analytic examples are given in Figure 12.4 from Bracewell (1978). For a circular aperture, the angular resolution is given by

$$\sin\theta_a = 1.22\frac{\lambda}{L}. \tag{2.5}$$

Downloaded from https://www.cambridge.org/core. IP address: 189.217.92.64, on 11 Feb 2026 at 15:51:46, subject to the Cambridge Core terms of use, available at https://www.cambridge.org/core/terms. https://www.cambridge.org/core/product/1F8951EFC610A352837B95E4DAEFBAEB

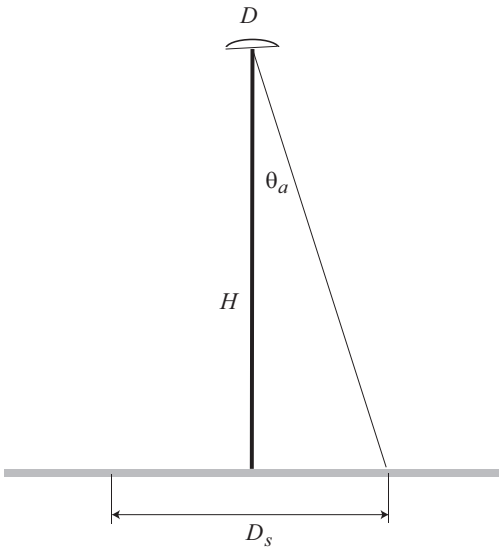

Figure 2.3 Beam-limited footprint D_s of a circular aperture (radar altimeter or optical telescope) at an altitude of H.

First consider a radar altimeter that orbits the Earth at an altitude of 800 km and illuminates the ocean surface with a 1-m diameter parabolic dish antenna operating at the Ku band (13.5 GHz, $\lambda = 0.022$ m) (Figure 2.3). The diameter of the beam-limited footprint on the ocean surface is $D_s = 2H \tan\theta_a \cong 2.44H\frac{\lambda}{D}$ or in this case 43 km.

Next consider an optical system with the same 1-m diameter aperture and at the same altitude, but operating at a wavelength of $\lambda = 5 \times 10^{-7}$ m, has a footprint diameter of 0.97 m. The Hubble space telescope reports an angular resolution of 0.5 microradian, which corresponds to an effective aperture of 1.27 m. Thus a 1-m ground resolution is possible for optical systems, while the same size aperture operating in the microwave part of the spectrum has a 44 000 times worse resolution. Achieving high angular resolution for a microwave system will require a major increase in the size of the aperture.

Before moving on to the 2-D case, we should check the assumption used in developing the Fraunhofer diffraction integral that the rays AP and OP are parallel. Suppose we examine the case when $\theta = 0$; the ray path AP is slightly longer than OP (Figure 2.4). This parallel-ray assumption breaks down when the phase of the ray path AP is more than $\pi/2$ radians longer than OP, which corresponds to a distance of $\lambda/4$. The condition that the path length difference is smaller than 1/4 wavelength is

$$\left[\frac{L^2}{4} + z^2\right]^{1/2} - z < \frac{\lambda}{4} \tag{2.6}$$

Downloaded from https://www.cambridge.org/core. IP address: 189.217.92.64, on 11 Feb 2026 at 15:51:46, subject to the Cambridge Core terms of use, available at https://www.cambridge.org/core/terms. https://www.cambridge.org/core/product/1F8951EFC610A352837B95E4DAEFBAEB

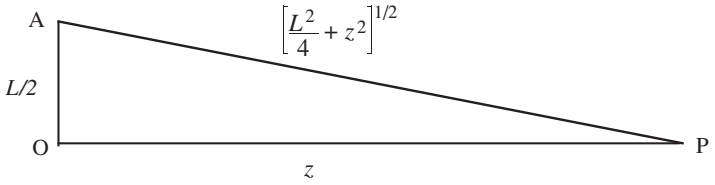

Figure 2.4 Diagram showing the increased length of path AP with respect to OP due to an offset of $L/2$.

or it can be rewritten as

$$\left[\left(\frac{L}{2z}\right)^2+1\right]^{1/2}-1<\frac{\lambda}{4z}. \tag{2.7}$$

Now assume $L \ll z$, so we can expand the term in the bracket in a binomial series

$$1+\frac{L^2}{8z^2}-1<\frac{\lambda}{4z}, \tag{2.8}$$

and we find

$$z_f>\frac{L^2}{2\lambda}, \tag{2.9}$$

where z_f is the *Fresnel distance*. So when $z < z_f$, we are in the near field and we need to use a more rigorous diffraction theory. However, when $z \gg z_f$, we are safe to use the parallel-ray approximation, and the Fraunhofer diffraction integral is appropriate. Next consider some examples:

$$\textit{Radar altimeter:} \qquad L=1\text{ m},\ \lambda=0.022\text{ m} \qquad z_f=23\text{ m}.$$

At an orbital altitude of 800 km, the parallel-ray approximation is valid. In contrast, an optical system with an orbital altitude of 800 km will require near-field optics:

$$\textit{Optical telescope:} \qquad L=1\text{ m},\ \lambda=5\times10^{-7}\text{ m} \qquad z_f=1000\text{ km}.$$

What about an SAR (discussed below) such as ERS with a 4 000-m-long synthetic aperture?

$$\textit{ERS SAR:} \qquad L=4000\text{ m},\ \lambda=0.058\text{ m} \qquad z_f=140000\text{ km}.$$

Thus near-field optics are also required to achieve full SAR resolution for ERS. This near-field correction is done in the SAR processor by performing a step called *range migration*, and it is a large factor in making SAR processing so CPU-intensive. This is discussed in Chapter 4.

Downloaded from https://www.cambridge.org/core. IP address: 189.217.92.64, on 11 Feb 2026 at 15:51:46, subject to the Cambridge Core terms of use, available at https://www.cambridge.org/core/terms. https://www.cambridge.org/core/product/1F8951EFC610A352837B95E4DAEFBAEB

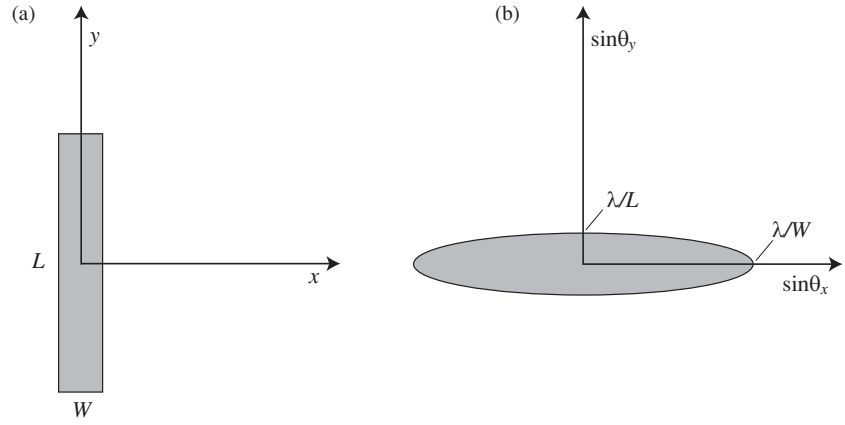

Figure 2.5 Diagram showing the projection pattern (b) for a rectangular SAR antenna (a).

2.3 Two-Dimensional Aperture

A 2-D rectangular aperture is a good approximation to a typical spaceborne strip-mode SAR. The aperture is longer in the flight direction (length L) than in the flight perpendicular direction (width W) as shown in Figure 2.5 (a). As in the 1-D case, one uses a 2-D Fraunhofer diffraction integral to calculate the projection pattern of the antenna. The integral is

$$P\left(\theta_x, \theta_y\right) = \int_{-L/2}^{L/2} \int_{-W/2}^{W/2} a(x,y) \exp\left[i\frac{2\pi}{\lambda}\left(x \sin\theta_x + y \sin\theta_y\right)\right] \mathrm{d}x\mathrm{d}y, \qquad (2.10)$$

where λ is the wavelength of the radar. As in the 1-D case, we will assume that the aperture $a(x,y)$ has uniform amplitude and phase. In this case, the projection pattern can be integrated analytically as

$$P\left(\theta_x, \theta_y\right) = LW \,\mathrm{sinc}\left(\frac{\pi W \sin\theta_x}{\lambda}\right) \,\mathrm{sinc}\left(\frac{\pi L \sin\theta_y}{\lambda}\right). \qquad (2.11)$$

The first zero crossing of this 2-D sinc function is illustrated in Figure 2.5 (b).

The ERS radar has a wavelength of 0.05 m, an antenna length (L) of 10 m, and an antenna width (W) of 1 m. For a nominal look angle of 23°, the slant range ρ is 850 km. The footprint of the radar has an along-track dimension $D_a = 2\rho\lambda/L$, which is 8.5 km. As discussed later in this chapter, this is approximately the length of the synthetic aperture used in the SAR processor. The footprint in the range direction is 10 times larger or about 85 km. This is approximately the width of an SAR swath.

Downloaded from https://www.cambridge.org/core. IP address: 189.217.92.64, on 11 Feb 2026 at 15:51:46, subject to the Cambridge Core terms of use, available at https://www.cambridge.org/core/terms. https://www.cambridge.org/core/product/1F8951EFC610A352837B95E4DAEFBAEB

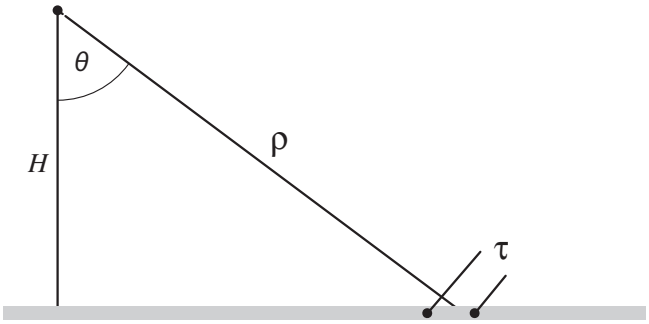

Figure 2.6 Diagram of radar flying into the page emitting a pulse of length τ. That reflects from two points on the surface of the Earth.

2.4 Range and Azimuth Resolution

The radar emits a short pulse that reflects off the surface of the Earth and returns to the antenna. The amplitude versus time of the return pulse is a recording of the reflectivity of the surface. If adjacent reflectors appear as two distinct peaks in the return waveform, then they are resolved in range. The nominal *slant-range resolution* is $\Delta\rho = c\tau/2$, where τ is the pulse length, c is the speed of light, and θ is the look angle. The factor of 2 accounts for the two-way travel time of the pulse. Figure 2.6 shows how the *ground-range resolution* is geometrically related to the slant-range resolution

$$R_r = \frac{c\tau}{2\sin\theta}. \tag{2.12}$$

Note the ground-range resolution is infinite for a vertical look angle and improves as the look angle increases. Also note that the range resolution is *independent of the height* of the spacecraft H. We will show in Section 4.4 that the range resolution is inversely proportional to the *bandwidth* of the radar after range compression. Usually, the radar bandwidth is a small fraction of the carrier frequency, so shorter-wavelength radar does not necessarily enable higher-range resolution. In many cases, the bandwidth of the radar is limited by the speed at which the data can be transmitted from the satellite to a ground station.

To understand the *azimuth resolution*, consider a single-point reflector on the ground that is illuminated as the radar passes overhead (Figure 2.7). From the Fraunhofer diffraction analysis, we know the length of the illumination (twice the angular resolution) is related to the wavelength of the radar divided by the length of the antenna. As discussed Section 2.3, the along-track dimension of the ERS

Downloaded from https://www.cambridge.org/core. IP address: 189.217.92.64, on 11 Feb 2026 at 15:51:46, subject to the Cambridge Core terms of use, available at https://www.cambridge.org/core/terms. https://www.cambridge.org/core/product/1F8951EFC610A352837B95E4DAEFBAEB

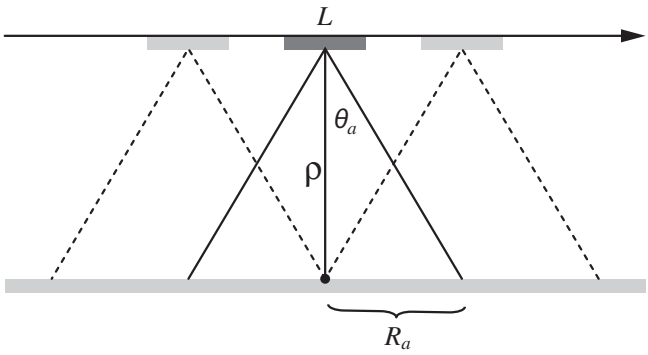

Figure 2.7 Top view of an SAR antenna imaging a point reflector. The reflector remains within the illumination pattern over the real aperture length of $2R_a$.

footprint is 8.5 km, so the nominal resolution R_a is 4.25 km, which is very poor. This is the azimuth resolution of the *real-aperture radar*

$$R_a = \rho \tan \theta_a \cong \frac{\rho\lambda}{L} = \frac{\lambda H}{L \cos \theta}, \tag{2.13}$$

where L is the length of the radar antenna, ρ is the slant range, λ is the wavelength of the radar, H is the height of the spacecraft, and θ is the look angle.

If the scatterer on the ground remains stationary as the satellite passes overhead, then one can assemble a *synthetic aperture* with a length equal to the along-track beamwidth of length, which is $2R_a$. This much longer aperture of 8.5 km results in a dramatic improvement in the azimuth resolution given by

$$R_a^{'} = \frac{\lambda\rho}{2R_a} = \frac{L}{2}, \tag{2.14}$$

which is the theoretical resolution of a *strip-mode* SAR. Note that the synthetic aperture azimuth resolution is *independent of spacecraft height* and improves as the antenna length is *reduced*. One could form a longer synthetic aperture by steering the transmitted radar beam, so it follows the target as the spacecraft (aircraft) flies by. This is called *spotlight-mode* SAR.

2.5 Constraints on Pulse Repetition Frequency

The discussion in Section 2.4 suggests that we should make the antenna length L as short as possible to improve the azimuth resolution. However, to form a complete aperture without aliasing shorter wavelengths into longer wavelengths, we must pulse the radar at an along-track distance of $L/2$ or shorter. To understand why such a rapid pulse rate is necessary, consider the maximum *Doppler shift* from a

Downloaded from https://www.cambridge.org/core. IP address: 189.217.92.64, on 11 Feb 2026 at 15:51:46, subject to the Cambridge Core terms of use, available at https://www.cambridge.org/core/terms. https://www.cambridge.org/core/product/1F8951EFC610A352837B95E4DAEFBAEB

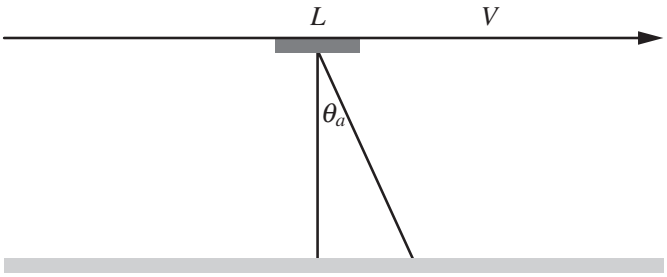

Figure 2.8 Diagram showing the angle between broadside to the antenna and the point where a reflector first enters the illumination of the antenna.

point that is illuminated at a maximum distance ahead of the radar (Figure 2.8), where the carrier frequency is $v_o = c/\lambda$ and V is the velocity of spacecraft relative to the ground.

The maximum Doppler shift occurs at a maximum angle of

$$\begin{aligned} \sin\theta_a &= \frac{\lambda}{L} \\ \Delta\nu = 2\nu_o \frac{V}{c} \sin\theta_a &= \frac{2c}{\lambda}\frac{V}{c}\frac{\lambda}{L} = \frac{2V}{L}. \end{aligned} \tag{2.15}$$

This corresponds to a maximum along-track distance between the samples of $L/2$. For ERS, this corresponds to a minimum pulse repetition frequency (PRF) of 1 400 Hz. The actual ERS PRF is 1 680 Hz.

When the PRF is too large, the return pulses from the *near range* and the *far range* can overlap in time as shown in Figure 2.9.

$$\begin{aligned} \mathrm{PRF} &< \frac{1}{t_2 - t_1} \\ t_1 &= \frac{2H}{c\cos\theta_1} \qquad t_2 = \frac{2H}{c\cos\theta_2} \\ \Delta t &= \frac{2H}{c}(\sec\theta_2 - \sec\theta_1) \\ \frac{2V}{L} < \mathrm{PRF} &< \frac{c}{2H}(\sec\theta_2 - \sec\theta_1)^{-1}. \end{aligned} \tag{2.16}$$

Take the ERS satellite as an example, the look angles to the rear range and far range are 18° and 24°, respectively. Thus the maximum PRF is 4 777 Hz. The actual PRF of 1680 is safely below this value, and the real limitation is imposed by the speed of the data link from the spacecraft to the ground. A wider swath or a higher PRF would require a faster data link than is possible using a normal X-band communication link of 105 Mbps.

Downloaded from https://www.cambridge.org/core. IP address: 189.217.92.64, on 11 Feb 2026 at 15:51:46, subject to the Cambridge Core terms of use, available at https://www.cambridge.org/core/terms. https://www.cambridge.org/core/product/1F8951EFC610A352837B95E4DAEFBAEB

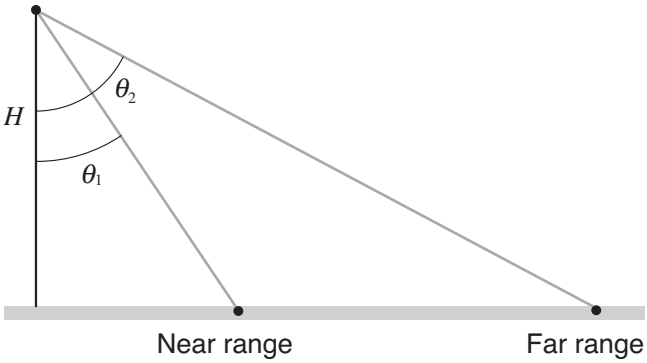

Figure 2.9 End view of the distance to the near range and the far range of the radar illumination pattern.

2.6 Problems

1. What is the illumination pattern for an aperture with a sign reversal at its center? What is $P(0)$? Is the function real or imaginary? Is the function symmetric or asymmetric?

   The aperture is

$$a(y) = \begin{cases} 0 & |y| > \frac{L}{2} \\ 1 & 0 < y \le \frac{L}{2} \\ -1 & -\frac{L}{2} \le y < 0 \end{cases} .$$

2. (a) What is the illumination pattern for the aperture in the given diagram?
   (b) What is the illumination pattern in the limit as L_1 approaches L_2?

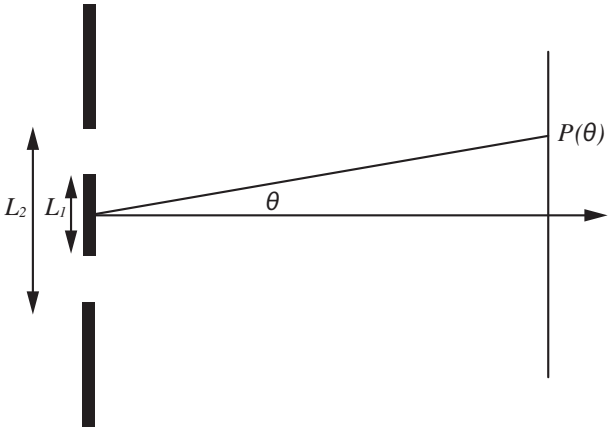

Downloaded from https://www.cambridge.org/core. IP address: 189.217.92.64, on 11 Feb 2026 at 15:51:46, subject to the Cambridge Core terms of use, available at https://www.cambridge.org/core/terms. https://www.cambridge.org/core/product/1F8951EFC610A352837B95E4DAEFBAEB

3. What is the theoretical azimuth resolution of a spotlight-mode SAR, with wavelength λ and height H, that can illuminate the target over a 10° angle as shown in the diagram below?

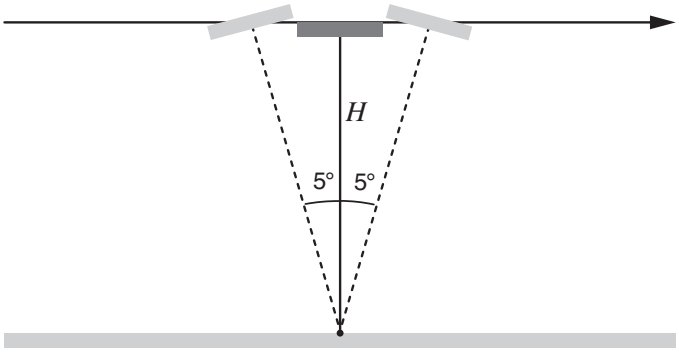

4. Derive the projection pattern for a 2-D rectangular aperture of length L and width W given in equation (2.11).
5. What is the ground-range resolution of side-looking radar with a pulse length of 6×10^{-8}s and a look angle of 45°?
6. (a) What is the period for a satellite in a circular orbit about the Moon, where the radius of the orbit is 1.9×10^6 m? (see Chapter 3, equation 3.2.) The mass of the Moon is 7.34×10^{22} kg.
   (b) You are developing an SAR mission for the Moon. The length of your SAR antenna is 10 m. What minimum pulse repetition frequency is needed to form a complete aperture? The circumference of the Moon is 1.1×10^7 m. You will need the orbital period from problem (a).
7. Derive equation (2.14).
8. An SAR with a 10-m long antenna is orbiting the Earth with a ground speed of 7 000 ms^{-1}. What is the maximum possible swath width. Use a look angle to the near range of 45° and assume the Earth is flat.
9. CryoSat is a nadir-looking altimeter (Ku-band, $\lambda = 2.2$ cm) that orbits the Earth at an altitude of 700 km, resulting in a ground-track velocity of 7 000 m/s. The radar uses a burst-mode synthetic aperture to reduce the length of the radar footprint in the along-track direction. Each burst has 64 echoes and a pulse repetition frequency of 18 kHz. What is the along-track resolution of the footprint? What is the Fresnel distance for this configuration?

Downloaded from https://www.cambridge.org/core. IP address: 189.217.92.64, on 11 Feb 2026 at 15:51:46, subject to the Cambridge Core terms of use, available at https://www.cambridge.org/core/terms. https://www.cambridge.org/core/product/1F8951EFC610A352837B95E4DAEFBAEB

3

Satellite Orbits

3.1 Introduction

As discussed in Chapters 1 and 5, Interferometric synthetic aperture radar (InSAR) can measure surface deformation to a fraction of the radar wavelength of 10–20 mm. This involves two basic measurements that are equally important and should ideally have similar accuracy. The first is the range between the satellite and a reflector on the surface of the Earth, which is measured from the two-way travel time of the radar waves. The second is the position of the satellite with respect to an Earth-fixed coordinate system. The precise trajectory of the satellite is computed using GNSS and laser tracking systems combined with satellite orbit dynamic calculations (e.g., Teunissen and Montenbruck (2017)). This precise orbit is used in four areas of the InSAR processing discussed later in this chapter: proper focus of the SAR image; projection of the reference topography from geographic to radar coordinates (i.e., *back projection*); alignment of the reference and repeat SAR images; and flattening of the interferogram. These are the four main steps of traditional InSAR processing. A newer approach uses the orbit to directly focus the SAR image onto a reference Earth topography, which is known as *geocoded single look complex* (SLC) processing as discussed in Section 5.10. These approaches rely on precise orbits having accuracies of a few centimeters. This orbital information is provided with the SAR data as a *state vector*, which consists of the Cartesian position $\mathbf{x}$ and velocity $\mathbf{v}$ of the satellite as a function of time. The six-element state vectors are provided at regular intervals at sub-mm precision (Table 3.1). Later in this chapter we describe how the discrete state vectors are interpolated in time using a Hermite polynomial interpolator. This interpolation is at the core of any InSAR processing system.

Before diving into the largely opaque numerical orbit calculations, it is worth reviewing some basic orbit geometry and dynamics. As shown in Figure 3.1, there are two basic types of satellite orbits called *near polar* and *geostationary*.

Downloaded from https://www.cambridge.org/core. IP address: 189.217.92.64, on 11 Feb 2026 at 15:51:46, subject to the Cambridge Core terms of use, available at https://www.cambridge.org/core/terms. https://www.cambridge.org/core/product/1F8951EFC610A352837B95E4DAEFBAEB

Table 3.1 *Example state vectors for the Sentinel-1 satellite (***.LED** *in GMTSAR).*

year	day	seconds	X (m)	Y (m)	Z(m)	Vx(m/s)	Vy(m/s)	Vz(m/s)
2015	145	6334.00	-3254984.5766	-5923132.6241	2088724.6473	-350.947452	2705.794737	7091.076582
2015	145	6344.00	-3258291.5669	-5895740.5804	2159516.0837	-310.428195	2772.553006	7067.077378
2015	145	6354.00	-3261192.7003	-5867682.7971	2230063.5333	-269.776909	2838.941373	7042.279672
2015	145	6364.00	-3263686.6821	-5838963.0117	2300359.0251	-228.998736	2904.952133	7016.686286
2015	145	6374.00	-3265772.2692	-5809585.0386	2370394.6167	-188.098844	2970.577632	6990.300137
2015	145	6384.00	-3267448.2704	-5779552.7686	2440162.3955	-147.082425	3035.810270	6963.124233
2015	145	6394.00	-3268713.5465	-5748870.1679	2509654.4793	-105.954694	3100.642499	6935.161670
2015	145	6404.00	-3269567.0106	-5717541.2783	2578863.0174	-64.720890	3165.066825	6906.415639
2015	145	6414.00	-3270007.6282	-5685570.2159	2647780.1916	-23.386274	3229.075810	6876.889419
2015	145	6424.00	-3270034.4175	-5652961.1712	2716398.2166	18.043873	3292.662073	6846.586380
2015	145	6434.00	-3269646.4498	-5619718.4079	2784709.3415	59.564247	3355.818288	6815.509981
2015	145	6444.00	-3268842.8494	-5585846.2631	2852705.8503	101.169526	3418.537188	6783.663770

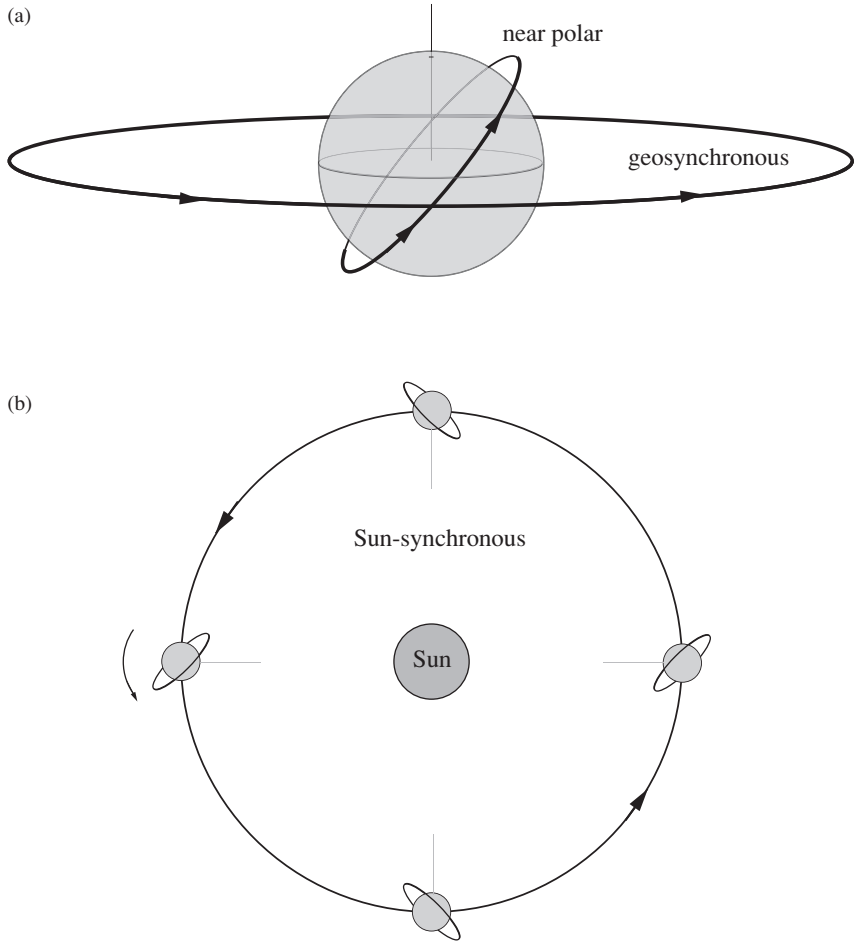

Figure 3.1 (a) The two most common types of orbits used for satellite remote sensing (near polar) and communications (geosynchronous). (b) A Sun-synchronous orbit has a precession rate of 1 year to maintain constant Sun illumination for optical sensors.

Downloaded from https://www.cambridge.org/core. IP address: 189.217.92.64, on 11 Feb 2026 at 15:51:46, subject to the Cambridge Core terms of use, available at https://www.cambridge.org/core/terms. https://www.cambridge.org/core/product/1F8951EFC610A352837B95E4DAEFBAEB

Near-polar orbits are commonly used for remote sensing applications. They have altitudes of between 400 and 1 500 km above the surface of the Earth. The orbit plane is inclined with respect to the equatorial plane of the Earth to achieve near-polar coverage. As discussed in the simple force balance calculation later, these satellites complete one orbit in about 6 000 seconds so their ground-track speed is about 6.7 km/s. The equatorial bulge of the Earth causes the orbit plane to precess like a top. The rate of precession can be adjusted to achieve a particular orbit repeat cycle or maintain a constant Sun illumination. The *Sun-synchronous orbit* (discussed later) is used by optical remote sensing satellites to maintain a constant Sun illumination direction. Satellites in geosynchronous orbit have an orbital period of one *sidereal day* (86 164 s), which requires a much larger orbital radius of 42 000 km. These satellites remain fixed at a particular longitude above the Earth's equator and are used mainly for communications as well as to track large-scale weather patterns. InSAR satellites are usually placed at low altitudes of ~700 km and have high inclinations for near full Earth coverage.

3.2 Kepler Elements

As discussed earlier, the trajectory of a satellite can be most accurately described by a time series of state vectors having three position elements and three velocity elements. A second way of describing the satellite orbit is through six Kepler elements (Kaula, 1966). The geometry of a satellite in an elliptical orbit around the Earth is shown in Figure 3.2.

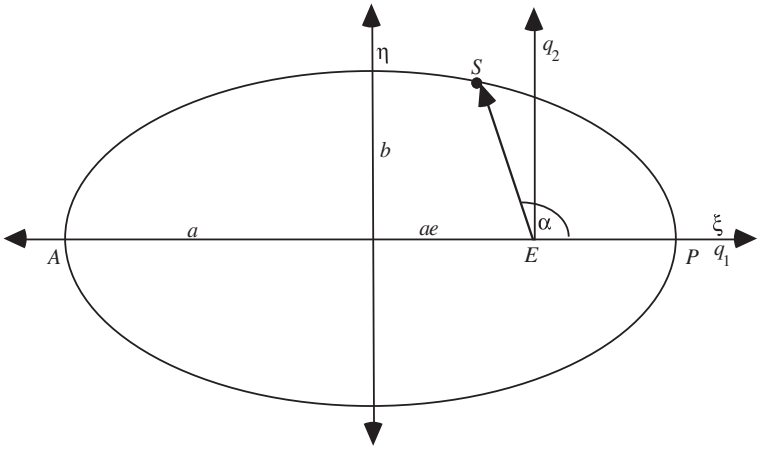

Figure 3.2 Diagram of a satellite *S* in an elliptical orbit around the Earth *E*.

Downloaded from https://www.cambridge.org/core. IP address: 189.217.92.64, on 11 Feb 2026 at 15:51:46, subject to the Cambridge Core terms of use, available at https://www.cambridge.org/core/terms. https://www.cambridge.org/core/product/1F8951EFC610A352837B95E4DAEFBAEB

The important parameters of the elliptical orbit are:

S – satellite
E – Earth
A – apogee
P – perigee
α – true anomaly (instantaneous angle from satellite to perigee)
a – semimajor axis
b – semiminor axis
e – eccentricity

where $e^2 = \frac{a^2 - b^2}{a^2}$.

Note they are not all independent, so, for example, the semiminor axis can be replaced by the eccentricity parameter. Three of these parameters, α, a, and e, are Kepler elements describing the size and shape of the orbit.

Kaula (1966) solves the general force balance for a particle of negligible mass in orbit about a large point mass M. He shows that the orbit follows an ellipse where the angular momentum $r^2 \frac{d\alpha}{dt}$ remains constant. This is Kepler's second law. The shape of the ellipse and the orbital radius versus the true anomaly are

$$\frac{\xi^2}{a^2} + \frac{\eta^2}{b^2} = 1 \Rightarrow r(\alpha) = \frac{a\left(1 - e^2\right)}{1 + e\cos\alpha}. \tag{3.1}$$

For an elliptical orbit about a point mass, the orbit frequency is given by

$$\omega_s = \left(\frac{GM}{a^3}\right)^{1/2}, \tag{3.2}$$

and the period of the orbit is $T_s = \frac{2\pi}{\omega_s}$ where $GM\left(3.98... \times 10^{14} \mathrm{m^3 s^{-2}}\right)$, the gravitational constant times the mass of the Earth, is one of the most accurately determined constants in Earth science. We can check this result for the simple case of a circular orbit. Consider a force balance on a small mass m orbiting the Earth (Figure 3.3).

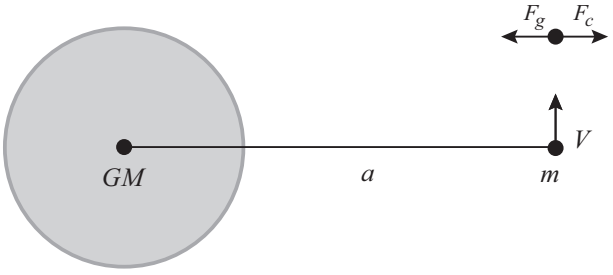

Figure 3.3 Force balance diagram of a small satellite of mass m in orbit about the Earth with a much larger mass M.

Downloaded from https://www.cambridge.org/core. IP address: 189.217.92.64, on 11 Feb 2026 at 15:51:46, subject to the Cambridge Core terms of use, available at https://www.cambridge.org/core/terms. https://www.cambridge.org/core/product/1F8951EFC610A352837B95E4DAEFBAEB

The inward-directed force of gravity is $F_g = m\frac{GM}{a^2}$, while the outward-directed centrifugal force is $F_c = m\frac{V^2}{a} = ma\omega_s^2$ where V is the velocity of the satellite.

Equating these forces, we find $\omega_s = \left(\frac{GM}{a^3}\right)^{1/2}$. Note that the orbital frequency decreases with increasing orbit radius a. A typical polar-orbiting satellite has an altitude of 700 km so an orbital radius of 7 071 km and an orbit period of 5 921 s. The circumference of the Earth is about 40 000 km so the ground track speed of this satellite is 6.75 km/s. A satellite in a higher orbit of 1 500 km has a ground track speed of 5.8 km/s. As discussed in Chapter 2, this nominal velocity of ~6 km/s places a lower bound on the pulse repetition frequency of $2V/L$ or 1 200 Hz for a 10 m long antenna.

A geosynchronous satellite orbits the Earth in one sidereal day (86 164 s – the rotation period in an inertial frame) so must have an orbital radius of 42 000 km.

Figure 3.4 shows the elliptical satellite orbit placed in an Earth-centered, quasi-inertial coordinate system where the z-axis points toward the north pole, the x-axis points toward the Sun, and the y-axis is 90° east along the equatorial plane of the Earth. The orientation of the elliptical orbit plane in this system is defined by three angles, which are three additional Kepler elements. They are the inclination of the orbit plane with respect to the equatorial plane of the Earth (i – inclination), the longitude of the point where the ascending orbit crosses the equatorial plane of the Earth (Ω – longitude of node), and the angle between the ascending crossing point (node) and perigee (ω – argument of perigee). In summary, a complete description of an ideal elliptical orbit is described by six Kepler elements:

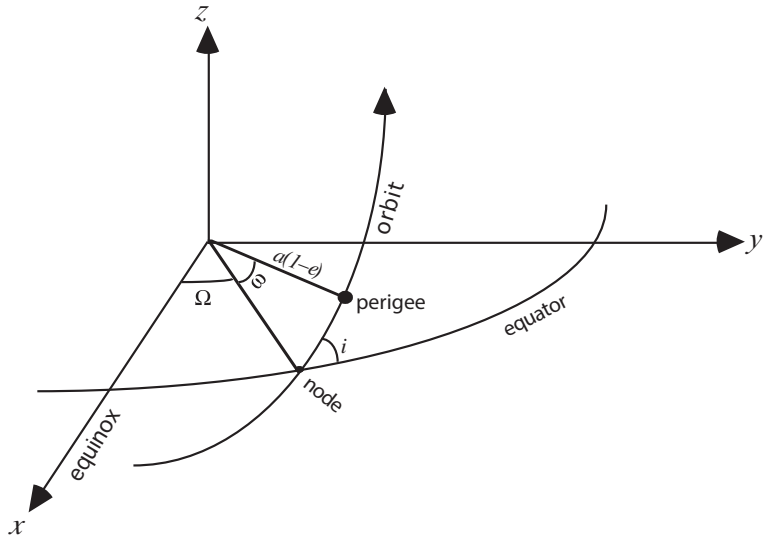

Figure 3.4 Diagram of the elliptical orbit in a quazi-inertial coordinate system.

Downloaded from https://www.cambridge.org/core. IP address: 189.217.92.64, on 11 Feb 2026 at 15:51:46, subject to the Cambridge Core terms of use, available at https://www.cambridge.org/core/terms. https://www.cambridge.org/core/product/1F8951EFC610A352837B95E4DAEFBAEB

α – true anomaly (instaneous angle from satellite to perigee)
ω – argument of perigee
Ω – longitude of node
a – semimajor axis
e – eccentricity
i – inclination.

3.3 Precession of the Orbit Plane

Because the Earth rotates, it is not spherical and is better described by an oblate ellipse (spheroid). A more precise description of the Earth's gravity potential field is

$$V(r,\theta) = \frac{-GM}{r}\left[1 - J_2\frac{a_e^2}{2r^2}\left(3\sin^2\theta - 1\right)\right], \tag{3.3}$$

where:
θ – latitude
a_e – equatorial radius
J_2 – dynamic form factor = 1.08×10^{-3}.

The dynamic form factor reflects the extra mass on the equatorial bulge of the Earth. The gravitational attraction of an oblate spheroid has two effects on the orbit. First, it decreases the orbit frequency (increases the period). Second, it causes the orbit plane to precess with respect to the inertial frame. The precession occurs because the equatorial bulge of the gravity field exerts a torque on the angular momentum vector of the orbit plane (Figure 3.5).

For a circular orbit, the precession frequency is given by

$$\frac{\omega_n}{\omega_s} = -\frac{3J_2}{2}\left(\frac{a_e}{a}\right)^2 \cos i = \frac{T_s}{T_n}, \tag{3.4}$$

where:
$\omega_n = \frac{2\pi}{T_n}$ – precession frequency and period T_n
$\omega_s = \frac{2\pi}{T_s}$ – satellite orbit frequency and orbit period
a_e – equatorial radius
a – orbital radius
J_2 – dynamic form factor = 1.08×10^{-3}
i – inclination of satellite orbital plane.

Note the precession is retrograde for $0 < i < 90^\circ$ and prograde for $i > 90^\circ$. Later we discuss how the orbit inclination and orbit radius can be adjusted so the precession is prograde and has a period of exactly 1 year.

Downloaded from https://www.cambridge.org/core. IP address: 189.217.92.64, on 11 Feb 2026 at 15:51:46, subject to the Cambridge Core terms of use, available at https://www.cambridge.org/core/terms. https://www.cambridge.org/core/product/1F8951EFC610A352837B95E4DAEFBAEB

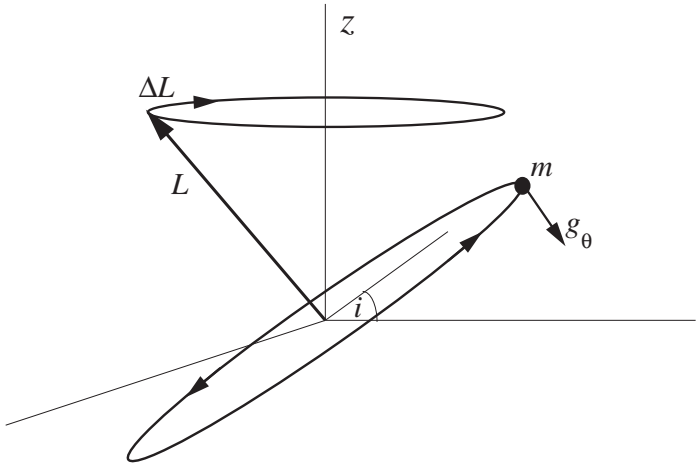

Figure 3.5 Satellite of mass m orbiting the Earth at an inclination i. The orbit has an angular momentum vector L perpendicular to the orbital plane. The θ component of the gravity vector applies a torque to the orbit, causing a retrograde precession of the angular momentum vector and thus a precession of the orbital plane.

3.4 Ground Track of Circular Orbit

(These Sections 3.4 through 3.6.6 are optional reading.) In many remote sensing applications, we would like to predict the path traced by the subsatellite point along the surface of the Earth (Figure 3.6). This could be accomplished by running an orbit simulation program. However, in many cases one only needs to know the approximate location or velocity of the satellite. Two applications include:

a) Suppose you know the basic orbit parameters (Kepler elements) of a LANDSAT-type satellite and you want to know how long it will take before the satellite is over your target area.
b) You have satellite altimeter profiles and you know the longitudes of their equator crossings. Given an equator crossing, you would like to know if the track intersects a particular area; this can be used to design an efficient way to search profiles. A related application is to align altimeter profiles along tracks so they can be compared to look for ocean variability. A crude alignment can be done using Kepler elements. Here we derive simple analytic formulas for the ground track of a satellite in a circular orbit about a rotating Earth.

Many remote sensing satellites have nearly circular orbits ($e < 0.01$), so we'll assume $e = 0.0$. Since the orbit is circular, the argument of perigee ω is no longer relevant. The basic problem is to map the position (Figure 3.7) of a satellite track in a circular orbit (inertial frame) into an Earth-fixed coordinate system (Figure 3.8).

Downloaded from https://www.cambridge.org/core. IP address: 189.217.92.64, on 11 Feb 2026 at 15:51:46, subject to the Cambridge Core terms of use, available at https://www.cambridge.org/core/terms. https://www.cambridge.org/core/product/1F8951EFC610A352837B95E4DAEFBAEB

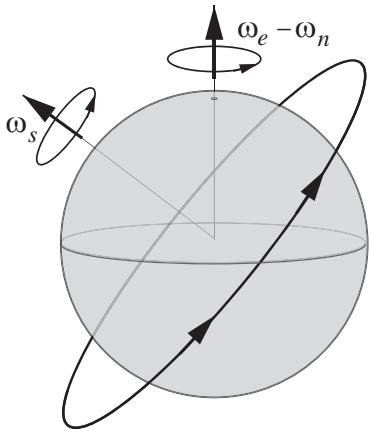

Figure 3.6 Satellite in a circular orbit around an elliptical Earth where:
ω_s – satellite orbit frequency
ω_e – Earth rotation frequency = $2\pi/86\,164$
ω_n – precession frequency.

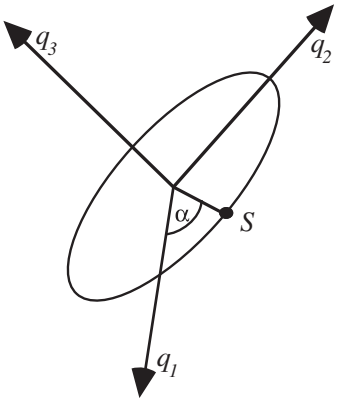

Figure 3.7 Satellite S in the coordinate system of the orbit plane where:
$q_1 = \cos\alpha = \cos\omega_s t$
$q_2 = \sin\alpha = \sin\omega_s t$
$q_3 = 0$.

Let $t = 0$ be the time when the satellite crosses the Earth's equator on an ascending orbit at a longitude of λ_o.

Two rotations are needed to align the satellite frame **q** to the Earth-fixed frame **x**. First, the **q**-frame is rotated by an angle i about the q_1 axis to account for the inclination of the orbit plane with respect to the Earth's equatorial plane. Second, the system is rotated about the x_3 axis to account for the Earth's rotation rate minus the precession rate of the orbital plane in inertial space.

Downloaded from https://www.cambridge.org/core. IP address: 189.217.92.64, on 11 Feb 2026 at 15:51:46, subject to the Cambridge Core terms of use, available at https://www.cambridge.org/core/terms. https://www.cambridge.org/core/product/1F8951EFC610A352837B95E4DAEFBAEB

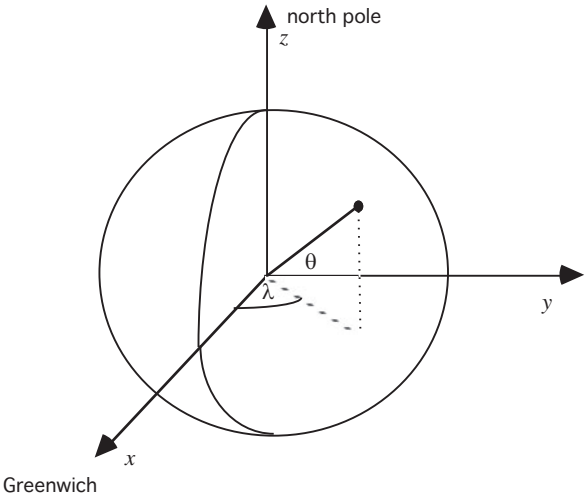

Figure 3.8 Earth-fixed coordinate system where:
$x = \cos\theta \cos\lambda$
$y = \cos\theta \sin\lambda$
$z = \sin\theta$.

Let $\Omega = (\omega_e - \omega_n)\, t = \omega'_e t$ where ω'_e is the Earth rotation rate minus the orbit precession rate. The satellite position in the **x**-frame is related to the satellite position on the **q**-frame as follows:

$$\mathbf{x} = \mathbf{R}_3\,(-\Omega)\,\mathbf{R}_1\,(i)\,\mathbf{q} \tag{3.5}$$

or

$$\begin{bmatrix} x \\ y \\ z \end{bmatrix} = \begin{bmatrix} \cos\Omega & \sin\Omega & 0 \\ -\sin\Omega & \cos\Omega & 0 \\ 0 & 0 & 1 \end{bmatrix} \begin{bmatrix} 1 & 0 & 0 \\ 0 & \cos i & -\sin i \\ 0 & \sin i & \cos i \end{bmatrix} \begin{bmatrix} \cos\alpha \\ \sin\alpha \\ 0 \end{bmatrix}. \tag{3.6}$$

By solving the rotations explicitly, one can derive analytical expressions for mapping from the satellite frame to the Earth-fixed frame and vice versa. Multiplying matrices yields

$$\begin{aligned} \cos\theta\cos\lambda &= \cos\Omega\cos\alpha + \sin\Omega\cos i\sin\alpha \\ \cos\theta\sin\lambda &= -\sin\Omega\cos\alpha + \cos\Omega\cos i\sin\alpha. \\ \sin\theta &= \sin i\sin\alpha \end{aligned} \tag{3.7}$$

The last equation relates latitude to the time since the equator crossing and vice versa.

Downloaded from https://www.cambridge.org/core. IP address: 189.217.92.64, on 11 Feb 2026 at 15:51:46, subject to the Cambridge Core terms of use, available at https://www.cambridge.org/core/terms. https://www.cambridge.org/core/product/1F8951EFC610A352837B95E4DAEFBAEB

$$\theta\,(t) = \sin^{-1}\left(\sin\omega_s t \sin i\right)$$
$$t\,(\theta) = \omega_s^{-1}\sin^{-1}\left(\frac{\sin\theta}{\sin i}\right) \tag{3.8}$$

The cosine and sine of the longitude (relative to λ_o) at some later time are given by

$$\cos\lambda = \left(\frac{\cos\omega'_e t\cos\omega_s t + \sin\omega'_e t\sin\omega_s t\cos i}{\cos\theta}\right)$$
$$\sin\lambda = \left(\frac{-\sin\omega'_e t\cos\omega_s t + \cos\omega'_e t\sin\omega_s t\cos i}{\cos\theta}\right). \tag{3.9}$$

By combining these two expressions and adding the zero-time longitude, the longitude at a later time is

$$\lambda\,(t) = \tan^{-1}\left(\frac{-\sin\omega'_e t\cos\omega_s t + \cos\omega'_e t\sin\omega_s t\cos i}{\cos\omega'_e t\cos\omega_s t + \sin\omega'_e t\sin\omega_s t\cos i}\right) + \lambda_o. \tag{3.10}$$

These equations, 3.8 and 3.10, are approximate formulas to construct the ground track of a satellite in a circular orbit around a rotating Earth and we use them later to provide simple descriptions of the main types of satellite orbits.

3.5 Ellipsoidal Earth Model

Throughout this derivation we used *geocentric latitude* θ, which is the angle between the equator and a line from the center of the Earth to the point on the surface of the Earth (Figure 3.9). However, *geographic latitude* θ_g is more commonly used for Earth location and maps. Before satellites were available for geodetic work, one would establish latitude by measuring the angle between a local plumb line and an external reference point such as Polaris. Since the local plumb line is perpendicular to the local flattened surface of the Earth (i.e., *spheroid*), it points to one of the foci of the best-fitting elliptical model for the shape of the Earth.

The conversion between geocentric and geographic latitude depends on the flattening of the Earth f as shown in Figure 3.9.

The radius of the Earth versus latitude is

$$r\,(\theta) = \left(\frac{\cos^2\theta}{a_e^2} + \frac{\sin^2\theta}{c^2}\right)^{-1/2}, \tag{3.11}$$

where:
a_e – equatorial radius = 6 378 135 m
c – polar radius = 6 356 775 m (not to be confused with the speed of light in other chapters) and the flattening of the Earth is $f = \frac{a_e - c}{a_e} \cong \frac{1}{298}$.

Downloaded from https://www.cambridge.org/core. IP address: 189.217.92.64, on 11 Feb 2026 at 15:51:46, subject to the Cambridge Core terms of use, available at https://www.cambridge.org/core/terms. https://www.cambridge.org/core/product/1F8951EFC610A352837B95E4DAEFBAEB

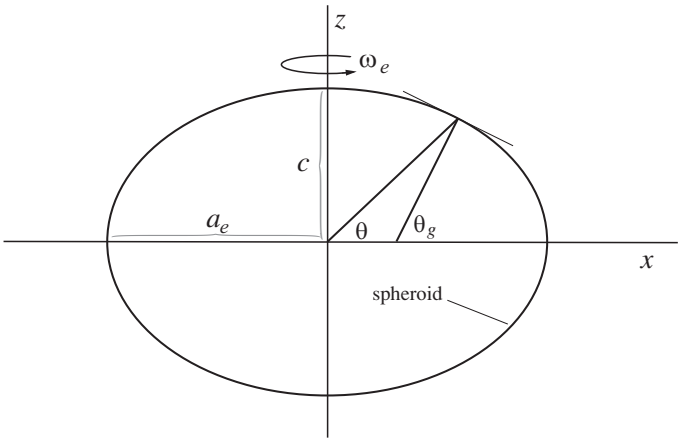

Figure 3.9 Approximate ellipsoidal shape of the Earth used to relate the geocentric and geographic latitudes.

The conversion between geocentric and geographic latitude is straightforward and is left as an exercise. The formulas are

$$\begin{aligned} \tan\theta &= \frac{c^2}{a_e^2}\tan\theta_g \\ \tan\theta &= (1-f)^2\tan\theta_g. \end{aligned} \tag{3.12}$$

To derive this equation, one starts with the equation for an ellipse $\frac{x^2}{a_e^2}+\frac{y^2}{c^2}=1$. Then take the gradient of this equation and rearrange terms.

Example: What is the geocentric latitude at a geographic latitude of 45? The answer is 44.8, which amounts to a 22 km difference in location!

Later in the book we will need to convert a point from geodetic coordinates $\left(\theta_g, \lambda, t\right)$, where λ is longitude and t is topography above the reference ellipsoid, into Earth-fixed Cartesian coordinates (x, y, z) (Figure 3.8). The conversion is

$$\begin{aligned} x &= (N+t)\cos\ \theta_g\cos\lambda \\ y &= (N+t)\cos\ \theta_g\sin\lambda \\ z &= \left(\frac{c^2}{a_e^2}N+t\right)\sin\ \theta_g \end{aligned} \tag{3.13}$$

where

$$N = \frac{a_e^2}{\left(a_e^2\cos^2\theta_g + c^2\sin^2\theta_g\right)^{1/2}}. \tag{3.14}$$

Downloaded from https://www.cambridge.org/core. IP address: 189.217.92.64, on 11 Feb 2026 at 15:51:46, subject to the Cambridge Core terms of use, available at https://www.cambridge.org/core/terms. https://www.cambridge.org/core/product/1F8951EFC610A352837B95E4DAEFBAEB

3.6 Special Orbits

This simple circular orbit calculation provided the mathematical tools to describe several commonly used orbits.

$$\theta\,(t) = \sin^{-1}\,(\sin\omega_s t \sin i)$$
$$t\,(\theta) = \omega_s^{-1}\sin^{-1}\left(\frac{\sin\theta}{\sin i}\right) \tag{3.15}$$

$$\lambda\,(t) = \tan^{-1}\left(\frac{-\sin\omega'_e t\cos\omega_s t + \cos\omega'_e t\sin\omega_s t\cos i}{\cos\omega'_e t\cos\omega_s t + \sin\omega'_e t\sin\omega_s t\cos i}\right) + \lambda_o, \tag{3.16}$$

3.6.1 Zero Inclination Orbit

In this case, $i = 0$, and the orbit precession frequency is zero.

Using formulas for the sine and cosine of sums of angles (e.g., $\sin\,(a-b) = \sin a\cos b - \cos a\sin b$), one can simplify the longitude function to the obvious result

$$\lambda\,(t) = \tan^{-1}\left[\frac{\sin\,(\omega_s-\omega_e)\,t}{\cos\,(\omega_s-\omega_e)\,t}\right] = (\omega_s-\omega_e)\,t. \tag{3.17}$$

3.6.2 Geostationary Orbit

In this case, $i = 0,\ \omega_s = \omega_e = 2\pi/86\,164$.

The satellite orbit frequency matches the Earth rotation rate. From the Equation 3.2, we have an expression for the orbit frequency versus orbital radius. Geostationary required an orbital radius of 42 170 km or about 6.6 times the Earth radius. Usually this type of orbit is used for communications or for monitoring the weather patterns from a global perspective. Coverage of this type of orbit is a small circle of radius 55° centered on the subsatellite point. About six satellites are needed to provide a complete equatorial view of the Earth and these orbits are not used for high-latitude coverage.

3.6.3 Geosynchronous Orbit

In this case, $i \neq 0,\ \omega_s = \omega_e$.

With a nonzero inclination, this orbit can cover higher latitudes, but it spends only 1/2 of its time in the correct hemisphere. Inserting these parameters into the above-ground track equations and neglecting the precession frequency of the orbit plane, one obtains

Downloaded from https://www.cambridge.org/core. IP address: 189.217.92.64, on 11 Feb 2026 at 15:51:46, subject to the Cambridge Core terms of use, available at https://www.cambridge.org/core/terms. https://www.cambridge.org/core/product/1F8951EFC610A352837B95E4DAEFBAEB

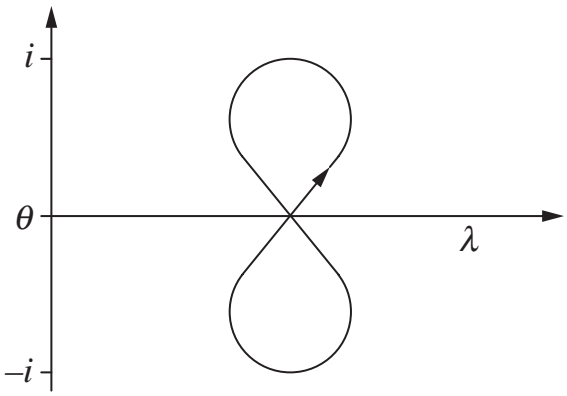

Figure 3.10 Ground track of a satellite in geosynchronous orbit traces out a figure 8.

$$\theta\,(t) = \sin^{-1}\,(\sin\omega_e t \sin i)$$
$$\lambda\,(t) = \tan^{-1}\left[\frac{\cos\omega_e t \sin\omega_e t\,(\cos i - 1)}{\cos^2\omega_e t + \cos i \sin^2\omega_e t}\right]. \tag{3.18}$$

Now consider the case of small inclination, so $\cos i \cong 1 - \frac{i^2}{2}$. The denominator is about 1 and the numerator can be simplified, so the approximate results for longitude and latitude versus time are

$$\lambda\,(t) = \tan^{-1}\left(\frac{i^2}{2}\frac{1}{2}\sin 2\omega_e t\right) \cong \frac{i^2}{4}\sin 2\omega_e t$$
$$\theta\,(t) = \sin^{-1}\,(\sin\omega_e t \sin i) \cong i \sin\omega_e t. \tag{3.19}$$

The latitude varies as a sine wave with a frequency of ω_e, while the longitude varies like a sine wave with a frequency of $2\omega_e$. At $t = 0$, both the latitude and longitude are zero. The ground track of the orbit follows a figure 8 (Figure 3.10).

3.6.4 Sun-Synchronous Orbit

For many remote sensing applications, especially optical, it is important to have the ascending node pass over the equator at the same local time so the Sun illumination angle is the same on every orbit. To create a Sun-synchronous orbit, the plane of the orbit must precess in a prograde direction with a period of exactly 1 year.

$$\omega_n = 2\pi/(365.25 \times 86\,400) = 1.991 \times 10^{-7} s^{-1}$$

Remember $\frac{\omega_n}{\omega_s} = -\frac{3J_2}{2}\left(\frac{a_e}{a}\right)^2 \cos i$ so prograde precession requires $i > 90°$. Thus the orbital inclination is dictated by the orbital altitude. For example, the

Downloaded from https://www.cambridge.org/core. IP address: 189.217.92.64, on 11 Feb 2026 at 15:51:46, subject to the Cambridge Core terms of use, available at https://www.cambridge.org/core/terms. https://www.cambridge.org/core/product/1F8951EFC610A352837B95E4DAEFBAEB

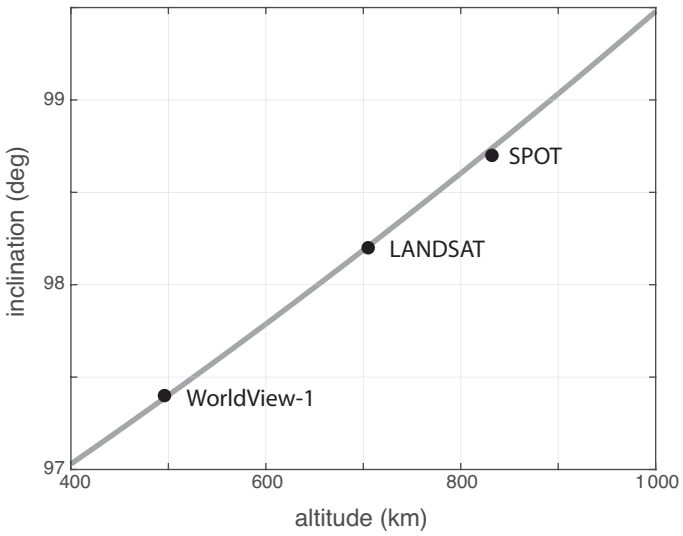

Figure 3.11 Inclination versus altitude for a Sun-synchronous orbit. Three examples of optical remote sensing satellites show excellent fits to this simplified analysis.

Sun-synchronous LANDSAT satellite has an orbital altitude of 705 km (radius $a = 6\,980$ km) so must have an inclination of 98.2° (Figure 3.11). For a typical altitude range of remote sensing satellites of 400–1 000 km, the inclination for a Sun-synchronous orbit is quite narrow (97–99.5°).

3.6.5 Orbits Tuned for Ocean Altimetry and InSAR

The following is desirable for ocean altimetry/InSAR:

(a) Ascending and descending tracks should cross at a high angle to resolve both components of sea surface slope/deformation.
(b) One should be aware of the aliasing of lunar and solar tides into the height/deformation.
(c) One should choose a repeat cycle that will optimize spatial and temporal coverage.
(d) High-latitude coverage may be desired for ice topography and deformation.

Example: The Geosat radar altimeter was launched in 1985 to measure the topography of the ocean surface in support of the Trident submarine program. The main objective of the first 1.5 years of the mission was to obtain complete marine coverage with tracks that cross at high angles for optimum gravity field recovery. An inclination of 108° provides the best compromise. However, this retrograde orbit

Downloaded from https://www.cambridge.org/core. IP address: 189.217.92.64, on 11 Feb 2026 at 15:51:46, subject to the Cambridge Core terms of use, available at https://www.cambridge.org/core/terms. https://www.cambridge.org/core/product/1F8951EFC610A352837B95E4DAEFBAEB

is nearly Sun-synchronous, which leads to aliasing of daily solar tide into a much longer period of time.

After Geosat completed its 1.5-year mapping mission, it began an extended repeat mission to observe changes in ocean topography associated with mesoscale currents. To measure changes, it was placed in an orbit having a ground track that repeats every 17.05 days. Of course, this was not optimal in terms of aliasing lunar and solar tides.

tide		period (hours)	period (days)	phase shift after 17.05 days
M2	principal lunar	12.421	0.5175	20°
K1	luni-solar	23.934	0.997	34°
S2	principal solar	12.00	0.500	36°
O1	diurnal lunar	25.819	1.076	54°

The Topex orbit was designed to minimize tidal aliasing. It was placed in a prograde orbit having an inclination of 66° and a repeat cycle of 10 days.

3.6.6 Exact Repeat Orbits

For applications measuring changes in surface deformation (i.e., InSAR) or changes in ocean topography (i.e., ocean altimetry), the orbit must retrace its ground track. To accomplish this there must be an integer relationship between the orbit frequency and the rotation rate of the Earth relative to the precessing orbit plane.

$$\frac{2\pi}{\omega_e - \omega_n} n_1 = \text{time for } n_1 \text{ rotations of the Earth relative to the orbit plane}$$

$$\frac{2\pi}{\omega_s} n_2 = \text{time it takes the satellite to complete } n_2 \text{ orbits}$$

Setting these two times to be equal provides an expression relating orbit frequencies to integer repeats.

$$\frac{2\pi}{\omega_e - \omega_n} n_1 = \frac{2\pi}{\omega_s} n_2 \Rightarrow \frac{\omega_e - \omega_n}{\omega_s} = \frac{n_1}{n_2}, \tag{3.20}$$

For example, consider the Sentinel-1 SAR, which has 175 orbit cycles in 12 days. This requires the following orbit frequencies:

$$\omega_e = 7.292 \times 10^{-5} \text{ s}^{-1}$$

$$\omega_s = 1.041 \times 10^{-3} \text{ s}^{-1}$$

$$\omega_n = \omega_e - \omega_s \frac{n_1}{n_2}.$$

Downloaded from https://www.cambridge.org/core. IP address: 189.217.92.64, on 11 Feb 2026 at 15:51:46, subject to the Cambridge Core terms of use, available at https://www.cambridge.org/core/terms. https://www.cambridge.org/core/product/1F8951EFC610A352837B95E4DAEFBAEB

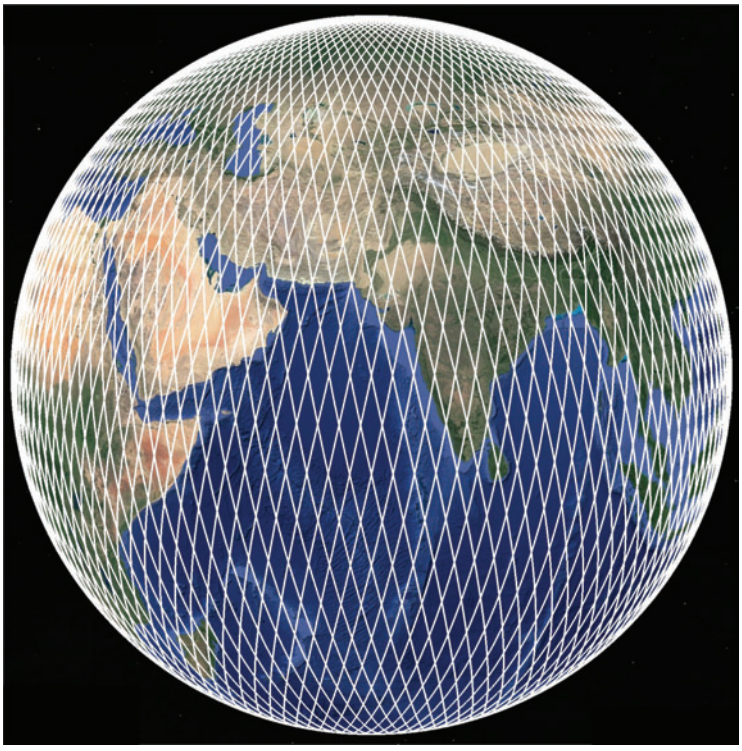

Figure 3.12 Ground track of Sentinel-1 computed using Equations 3.15 and 3.16 and an inclination of 98.2°.

An example of the Sentinel-1 ground track is shown in Figure 3.12. This is a retrograde orbit, so the ascending tracks go in a northwest direction and reach a maximum latitude of 81.8°.

3.7 Precise Orbits for InSAR

The earlier discussion on Kepler elements provides an overview of orbit kinematics and dynamics. However, these simple approaches are not sufficiently accurate for InSAR processing, which relies on orbit accuracy of 20–50 mm. In this section we describe the precise orbital information that is currently available with standard remote sensing products. The development of methods for constructing these precise orbits from a combination of precise tracking (GNSS, satellite laser ranging (SLR), and Doris) mainly comes from the radar altimeter community where they require radial orbit accuracy of better than 20 mm to achieve their objectives for monitoring global sea level (Cerri et al., 2010).

As shown in Table 3.1, the precise orbit is provided as state vectors having a time spacing of 10–60 seconds. The typical InSAR satellite travels 70 km during

Downloaded from https://www.cambridge.org/core. IP address: 189.217.92.64, on 11 Feb 2026 at 15:51:46, subject to the Cambridge Core terms of use, available at https://www.cambridge.org/core/terms. https://www.cambridge.org/core/product/1F8951EFC610A352837B95E4DAEFBAEB

the 10-second time interval, so there may be four or fewer state vectors during a typical 250 km SAR image frame. To perform the SAR processing, we will need a precise position every 1/2 antenna length or about every 5 m. Remarkably, mm-accuracy interpolation can be achieved by an algorithm called Hermite polynomial interpolation. For satellite orbits, the interpolator uses six position points and the corresponding six velocity points to construct a smooth interpolating function that exactly matches the six position and six derivative (velocity) points and provides a smooth interpolation between the central points. Note the state vectors need to extend at least three points before and after the frame for accurate interpolation. The state vectors provided with Radarsat-1 SAR data do not extend beyond the start and end of the SAR acquisition (frame), so the algorithm fails. The accuracy of the Sentinel-1 orbit is better than 30 mm in the radial and cross-track directions and 50 mm in the along-track direction. This precise orbital information is used in four aspects of the InSAR processing discussed next and is the key to robust and efficient software.

3.7.1 Proper Focus

First proper focus of the SAR image involves the coherent summation of range-aligned echoes over the length of the synthetic aperture as shown in Figure 3.13. This is discussed more completely in Chapter 4.

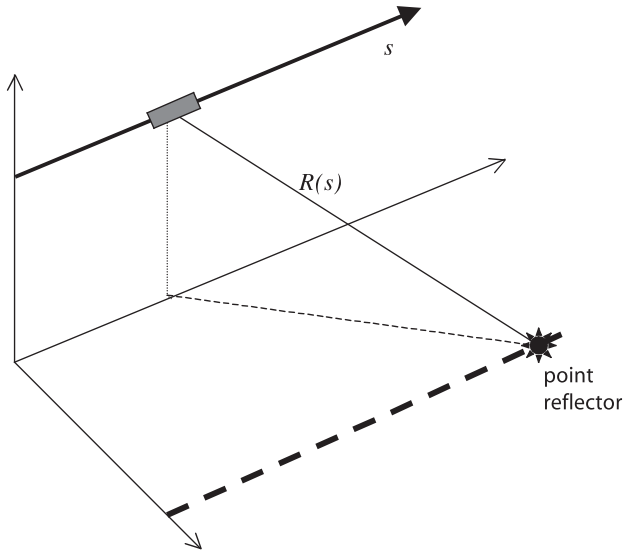

Figure 3.13 Geometry of SAR antenna flying over a point reflector on the ground. The range R varies with slow time s as measured by the precise orbit provided in an Earth-fixed coordinate system.

Downloaded from https://www.cambridge.org/core. IP address: 189.217.92.64, on 11 Feb 2026 at 15:51:46, subject to the Cambridge Core terms of use, available at https://www.cambridge.org/core/terms. https://www.cambridge.org/core/product/1F8951EFC610A352837B95E4DAEFBAEB

Therefore, we need to calculate the range as a function of slow time s (see definition of slow time in Figure 1.3.). First consider the case of a straight-line orbit passing over a fixed-point reflector. The range to the reflector would vary as a hyperbola with slow time. In the actual case, the orbital path is elliptical and the Earth is rotating so the range versus time function is a more complicated function. However, because the synthetic aperture is short (<5 km) compared with the nominal range from the satellite to the reflector (~800 km), a three-parameter parabolic approximation is commonly used to model range versus time

$$R(s) = R_o + \dot{R}(s - s_o) + \frac{\ddot{R}}{2}(s - s_o)^2 + \dots \tag{3.21}$$

where R_o is the closest approach of the spacecraft to the point reflector and s_o is the time of closest approach. These three parameters, R_o, $\dot{R}$, and $\ddot{R}$, are needed to focus an image (Chapter 4). In terms of the SAR processor, these are called the near-range R_o, the Doppler centroid f_{DC}, and the Doppler frequency rate f_R, which are related to the coefficients of this polynomial

$$f_{DC} = \frac{-2\dot{R}}{\lambda} \quad \text{and} \quad f_R = \frac{-2\ddot{R}}{\lambda}, \tag{3.22}$$

where λ is the wavelength of the radar. When a SAR image is focused at zero Doppler, the range rate at position s_o is by definition zero.

3.7.2 Transformation from Geographic to Radar Coordinates

The second use of precise orbital information is to map every point on the surface of the Earth (lon, lat, topography) into the range and azimuth coordinates of the radar. This back projecting (*SAT_llt2rat* in GMTSAR) provides a lookup table (**trans.dat** in GMTSAR) for transforming between geographic and radar coordinates. The algorithm for creating this mapping is conceptually simple but can be computationally expensive. The precise orbital information is used to determine the range from the satellite to a topography grid cell. The approximate time of the minimum range is found using a golden section search algorithm (Press et al., 2007). A second-order polynomial is fit to this range versus time function about the time of minimum range (Equation 3.21). If the SAR image is focused at zero Doppler, then the range coordinate of the mapping is simply the minimum range and the azimuth coordinate is the time of the minimum range. Of course, by definition, the range rate (Doppler) is zero at this azimuth position. If the radar image was focused at a Doppler centroid other than zero, then Equation 3.22 can be used to calculate the nonzero range-rate at this Doppler.

$$\dot{R} = -\frac{\lambda f_{DC}}{2} \tag{3.23}$$

Downloaded from https://www.cambridge.org/core. IP address: 189.217.92.64, on 11 Feb 2026 at 15:51:46, subject to the Cambridge Core terms of use, available at https://www.cambridge.org/core/terms. https://www.cambridge.org/core/product/1F8951EFC610A352837B95E4DAEFBAEB

Next, by taking the derivative of the parabolic approximation, one can determine the along-track time shift that will be produced by focusing at a nonzero Doppler. This is given by

$$\Delta s = -\frac{\lambda f_{DC}}{2\ddot{R}}. \tag{3.24}$$

The corresponding range correction is given by

$$\Delta R = \frac{\ddot{R}}{2}\Delta s^2. \tag{3.25}$$

These two corrections are needed in the transformation from geographic to radar coordinates when the image is focused at a Doppler other than zero.

3.7.3 Image Alignment

The third use of the precise orbital information is to align the secondary images to the master image to sub-pixel accuracy in order to form the interferogram. (Note that *reference* and *repeat* images refer to individual interferograms, while *master* and *secondary* images refer to a geometrically aligned stack.) There are two main approaches to this image alignment.

The traditional alignment approach is done in three steps: (1) First, the orbital information is used to make a rough (1–2 pixel accuracy) estimate of the offset of the master and secondary images. (2) Then 2-D cross-correlation of sub-patches of data (e.g., 64 by 64 pixels) is used to estimate the affine transformations needed to map the secondary image onto the master image. As described earlier, the trajectories of the master and secondary images are very smooth so their differences in both the range dr and azimuth da coordinates are well described by the following equations:

$$\begin{aligned} dr &= c_0 + c_1 r_m + c_2 a_m \\ da &= c_3 + c_4 r_m + c_5 a_m, \end{aligned} \tag{3.26}$$

where r_m and a_m are the range and azimuth coordinates of the master image and there are six unknown coefficients c_0 to c_5. The coefficients are determined by fitting planes to the range and azimuth offset data derived from the cross-correlation of the sub-patches. It seems reasonable that six parameters are sufficient to completely account for the affine transformation because the orbit is well described by a six-element state vector and the differences in the master and secondary state vectors are very small over the time span of the radar acquisition. (3) The final step is to use a 2-D sinc-function interpolator to resample the secondary image into the coordinates of the master image (*resamp* in GMTSAR). The accuracy of the alignment depends on the coherence between the master and secondary images. When coherence is high, the two images can be aligned to 0.1 pixel accuracy. When the

Downloaded from https://www.cambridge.org/core. IP address: 189.217.92.64, on 11 Feb 2026 at 15:51:46, subject to the Cambridge Core terms of use, available at https://www.cambridge.org/core/terms. https://www.cambridge.org/core/product/1F8951EFC610A352837B95E4DAEFBAEB

coherence is low, the alignment can be worse than 1.0 pixel. The method fails when the master and secondary images have poor correlation.

A second more accurate alignment approach utilizes the 50 mm accuracy of the precise orbits to perform the alignment geometrically. The advantage of this approach is that it is accurate to a small fraction of a pixel and there does not need to be any corelation between the master and secondary images. The preprocessing starts with a pixelwise estimate of range and azimuth offsets using precise orbits and a downsampled (~360 m) digital elevation model (DEM), which covers the region of the SLC satellite images. The precise orbit is used to back-project each pixel in the DEM (lon, lat, ellipsoidal height) into the range and azimuth coordinates of the master and secondary images. The algorithm first uses a golden section search method (Press et al., 2007) to quickly find the closest point at the PRF sampling between the orbital trajectory and the topography pixel. Then a polynomial refinement algorithm is used to improve the numerical accuracy to better than 10 mm in the azimuth coordinate. The range coordinate is the range between the antenna and the topography pixel evaluated at the corresponding azimuth coordinate. Note that the range rate or Doppler is zero at this closest point. A correction for alignment to a nonzero Doppler is discussed in Section 3.7.2. The differences between the range $dr\,(r,a)$ and azimuth $da\,(r,a)$ of the secondary image with respect to the master image are used to construct a dense look-up map of range and azimuth shifts, using a surfacing technique described in Smith and Wessel (1990). After these maps are generated, the coregistration is done pixelwise, which accounts for topography variation across the full image.

3.7.4 Flattening Interferogram

The fourth use of the precise orbit is for calculating the parallel and perpendicular components of the interferometric baseline that are needed for removing the interferometric phase for the range differences to every pixel in the image (*SAT_baseline* in GMTSAR). This correction depends on both the orbital trajectory and the shape of the Earth, including the ellipsoidal, geoidal, and topographic components given in Chapter 4. If this is done in a consistent way, then long swaths of data can be calculated on a frame-by-frame basis and seamlessly merged in geographic coordinates. This is only possible because the baselines, orbital heights, and topographic data are all seamless at the frame boundaries. This seamless recombination of interferograms requires that the user select a common Earth radius and near range for the entire swath in the file *configure.txt* in GMTSAR. This feature is especially useful for ScanSAR-to-ScanSAR interferometry because each of the ScanSAR subswaths can be processed independently at their original azimuth sampling rate (i.e., PRF) and then reassembled in geographic coordinates without

Downloaded from https://www.cambridge.org/core. IP address: 189.217.92.64, on 11 Feb 2026 at 15:51:46, subject to the Cambridge Core terms of use, available at https://www.cambridge.org/core/terms. https://www.cambridge.org/core/product/1F8951EFC610A352837B95E4DAEFBAEB

adjustment. Frame-by-frame processing also has an advantage because the file size of one complex SAR image and its interferometric products can be far less than the 2 Gbyte file limit on older 32-bit computers. Second, one can easily take advantage of multiple processors that are available on many computers to process multiple frames of interferometric products simultaneously, without having to rewrite any computer code.

3.8 Problems

1. Precise orbital information is used in four areas of InSAR processing. Describe the four uses.
2. A satellite orbit can be represented by six parameters. Describe two approaches to defining these six parameters. How many parameters are needed to align a secondary image to a master image for interferometry? Why not more or fewer? (Also discussed in Section 8.5.)
3. The natural coordinates of a radar image have range or time along one axis and azimuth or slow time along the other axis. Why is the term slow time used?
4. Describe an algorithm to transform a point on the surface of the Earth (longitude, latitude, elevation) into radar coordinates.
5. When a SAR image is focused at zero Doppler, the radar coordinates of a point reflector correspond to the minimum range. Why? Derive the Equations 3.24 and 3.25 for adjusting the range and azimuth coordinates when an image is focussed at a nonzero Doppler.
6. GMTSAR uses a quadratic function to approximate the changes in baseline (horizontal and vertical) along the image frame. The quadratic formula is:

$$B(s) = a + bs + cs^2$$

where s is slow time ranging from the start to the end of the frame $[0, T]$. Suppose the actual baseline is measured at three times along the frame $0, \frac{T}{2}, T$ and the values are B_1, B_2, B_3. Derive an expression for the parameters a, b, c. The forward model is

$$\begin{pmatrix} B_1 \\ B_2 \\ B_3 \end{pmatrix} = \begin{pmatrix} 1 & 0 & 0 \\ 1 & \frac{T}{2} & \frac{T^2}{4} \\ 1 & T & T^2 \end{pmatrix} \begin{pmatrix} a \\ b \\ c \end{pmatrix}.$$

7. Satellite orbital information is commonly provided as state vectors of position and velocity at regular intervals (e.g., 1 minute). Hermite polynomial interpolation is often used to interpolate the orbit to the full sampling rate of the radar (e.g., 2 000 Hz). What are the strengths and weaknesses of this approach? (This may require a literature search.)

Downloaded from https://www.cambridge.org/core. IP address: 189.217.92.64, on 11 Feb 2026 at 15:51:46, subject to the Cambridge Core terms of use, available at https://www.cambridge.org/core/terms. https://www.cambridge.org/core/product/1F8951EFC610A352837B95E4DAEFBAEB

8. Explain the terminology: master and secondary, reference and repeat.
9. Given a satellite in a circular orbit around the Earth at an orbital frequency of ω_s and an inclination of i, develop a formula for the latitude velocity $d\theta/dt$ of the satellite. (Assume a spherical Earth.) What happens when the inclination is 90°? What happens when the inclination is 0°?
10. Calculate the ground track for a satellite in a circular orbit about a spherical Earth. (Don't worry about converting from geocentric to geodetic coordinates.) Use this formula to calculate and plot the ground track of any remote sensing satellite. The following parameters will produce an exact 10-day repeat track for the Sentinel-1 satellite.

$$\omega_e = 2\pi/86\,164.1$$
$$\omega_s = 2\pi/5\,908$$
$$\omega_n = \omega_e - \omega_s \frac{12}{175}$$
$$i = 98.2\frac{\pi}{180}$$
$$\theta(t) = \sin^{-1}\left[\sin\omega_s t \sin i\right]$$
$$t(\theta) = \omega_s^{-1}\sin^{-1}\left[\frac{\sin\theta}{\sin i}\right]$$
$$\lambda(t) = \tan^{-1}\left[\frac{-\sin\omega_e' t\cos\omega_s t + \cos\omega_e' t\sin\omega_s t\cos i}{\cos\omega_e' t\cos\omega_s t + \sin\omega_e' t\sin\omega_s t\cos i}\right] + \lambda_0$$

Downloaded from https://www.cambridge.org/core. IP address: 189.217.92.64, on 11 Feb 2026 at 15:51:46, subject to the Cambridge Core terms of use, available at https://www.cambridge.org/core/terms. https://www.cambridge.org/core/product/1F8951EFC610A352837B95E4DAEFBAEB

4

SAR Image Formation

4.1 Overview of the Range-Doppler Algorithm

The *range-Doppler algorithm* is a computationally efficient method of focusing raw SAR data into a single look complex (SLC) image (Curlander and McDonough, 1991). The basic SAR theory is conceptually simple (Chapter 2), yet when one looks into the inner workings of the SAR processor, it appears quite complicated. The most difficult part of the problem is related to the coupling between the azimuthal compression and the orbital parameters. In the old days, when the satellite orbits were not known very accurately, one would use techniques such as *clutterlock* and *autofocus* to derive the orbital parameters from the data. This is no longer necessary with the high-accuracy orbits available today. A standard processing sequence follows where the first two steps are done on board the satellite while the remaining four steps are done by the user with a digital SAR processor. The discussion provided here is for the ERS-1 satellite, although the concepts translate to any modern strip-mode SAR satellite. Most of the newer satellite missions (e.g., Sentinel-1, ALOS-2, NISAR) provide SLC images as a basic product, so this focusing step is not needed. Nevertheless, the presentation is helpful for understanding how SLCs are generated.

4.2 Processing Onboard the Satellite

Demodulate The electromagnetic wave consists of a chirp of bandwidth B (~15 MHz) superimposed on carrier frequency ω_o (~5 GHz). To record the return signal, one could simply digitize the amplitude of the electric field $E(t)$ at a sampling rate of 10 GHz using 1-byte encoding. However, this would generate 10 Gbytes of data every second! We are really only interested in how the chirp has been delayed and distorted by the reflection off the Earth's surface. The trick here is to use the shift property of the Fourier transform (Bracewell, 1978, p. 108) to

Downloaded from https://www.cambridge.org/core. IP address: 189.217.92.64, on 11 Feb 2026 at 15:51:46, subject to the Cambridge Core terms of use, available at https://www.cambridge.org/core/terms. https://www.cambridge.org/core/product/1F8951EFC610A352837B95E4DAEFBAEB

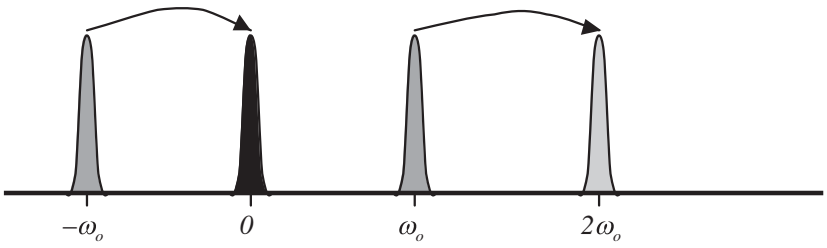

Figure 4.1 Diagram showing the power spectrum of the radar signal before and after shifting by the carrier frequency.

isolate the 15 MHz part of the spectrum containing the chirp. Suppose we multiply the signal $E(t)$ by $e^{i2\pi\omega_o t}$ where ω_o is the carrier frequency. This will shift the Fourier transform of the signal as shown in Figure 4.1.

The function $E(t)$ is a real-valued function, so we know that its Fourier transform has Hermitian symmetry about the origin, that is, $E(-\omega) = E^*(\omega)$. Because of this symmetry, all of the information in the time series is contained within the bandwidth of a single spectral peak. Next, we low-pass filter the signal to isolate the spectral peak centered at the zero frequency. The original signal $E(t)$ was a real-valued function, but after this shift/filter operation, the output is complex. No information is lost in this process and now the output can be digitized at the much lower rate of twice the bandwidth of the chirp (~30 MHz). In the engineering literature, this process is called *heterodyne* and the real and imaginary components are called *in-phase* (I) and *quadrature* (Q).

Digitize The complex signal is digitized at 5 bits per pixel so the numbers range from 0 to 31; the mean value is 15.5. Digitizing the data at 8 bits per pixel would seem more convenient, but transmitting these extra 3 bits to the ground receiving station increases the bandwidth of the telemetry so every effort is made to compress the data before transmission. Once the data are on the ground, they are expanded to 8 bits (one byte) for programming convenience. The raw signal files (e.g., ERS) contain rows of 11 644 bytes that represent a single radar echo (Figure 4.2). The first 412 bytes are timing and other information, while the remaining 11 232 bytes contain the 5 616 complex numbers of raw signal data.

4.3 Digital SAR Processing

The digital SAR processor is a computer program (*esarp* in GMTSAR) that converts the raw signal data (***.raw**) into a SLC image (***.SLC**). An overview is provided in Figure 4.3, followed by a detailed description of each step. The parameter file (***.PRM**, Table 4.1) contains all the parameters needed to focus the image.

Downloaded from https://www.cambridge.org/core. IP address: 189.217.92.64, on 11 Feb 2026 at 15:51:46, subject to the Cambridge Core terms of use, available at https://www.cambridge.org/core/terms. https://www.cambridge.org/core/product/1F8951EFC610A352837B95E4DAEFBAEB

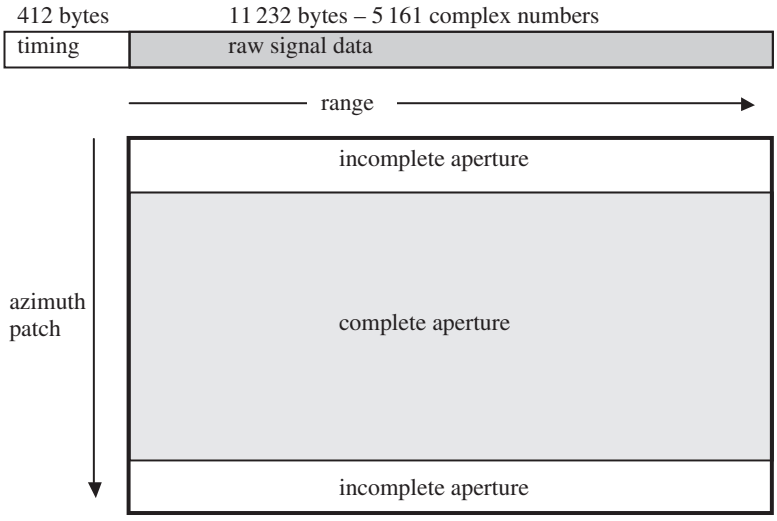

Figure 4.2 Raw signal data.

1. *Range compression* A sharp radar pulse is recovered by deconvolution of the chirp. This is done with fast Fourier transform (FFT). There are 5 616 points in the ERS-1 signal data and the chirp is 703 points long. Both are zero-padded to a length of 8 192 prior to deconvolution to take advantage of the speed of the radix-2 FFT algorithms. Later, we keep 6 144 points, which enables one to extract the phase beyond the edges of the original swath. Since the chirp really did interact with the ground outside the digitized swath, this is not magic. The number 6 144 has small prime factors that may be optimal for later 2-D FFT phase unwrapping algorithms.
2. *Patch processing* The next step is to focus the image in the along-track or azimuth direction. This is also done by FFT, but now we need to process columns rather than rows. For the ERS radar, the synthetic aperture is 1 296 points long so we need to read at least that many rows into the memory of the computer. Actually, 4 096 rows is a better number since it is a power of 2. A typical ERS raw data file has 28 000 rows so we will need to process many of these *patches*. One problem with this approach is that the synthetic aperture is only complete for the inner 2 800 points of the 4 096 data patch so the patches must have a 1 296-point overlap (Figure 4.2). A $4\,096 \times 5\,616$ patch requires at least 184 Mbytes of computer memory for single precision real numbers. In the old days, before this large memory space was available, each patch was transposed–*corner turning*–using high-speed disks so the data could be processed on a column-by-column basis. The L-band data from ALOS have

Downloaded from https://www.cambridge.org/core. IP address: 189.217.92.64, on 11 Feb 2026 at 15:51:46, subject to the Cambridge Core terms of use, available at https://www.cambridge.org/core/terms. https://www.cambridge.org/core/product/1F8951EFC610A352837B95E4DAEFBAEB

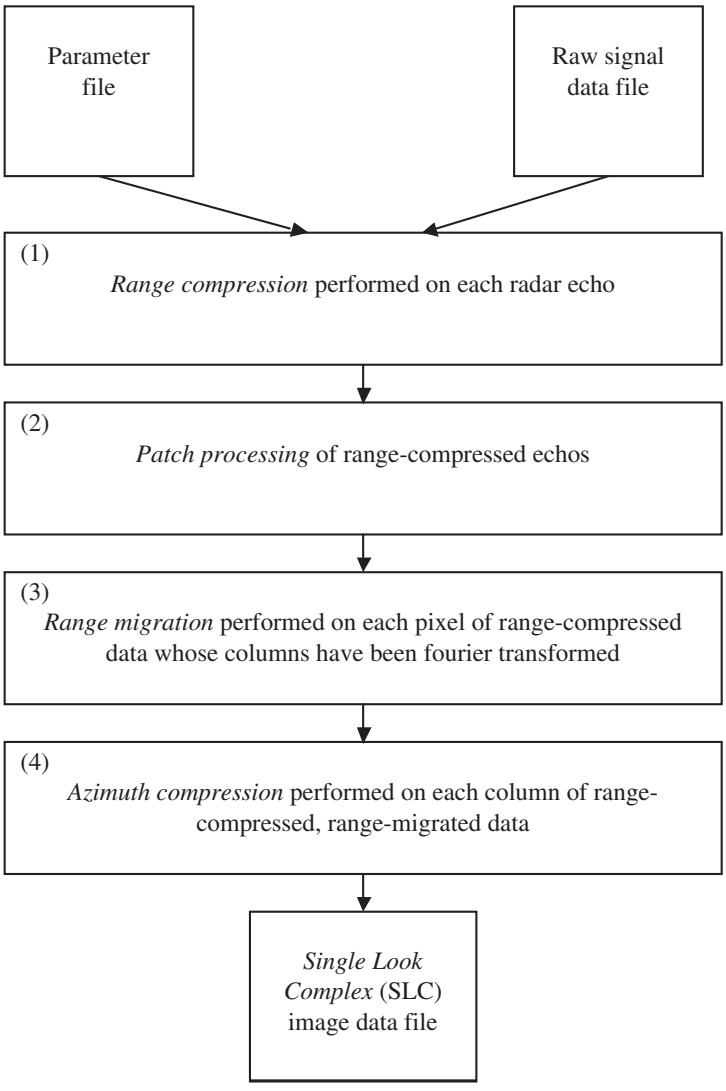
Parameter file
Raw signal data file
(1)
Range compression performed on each radar echo
(2)
Patch processing of range-compressed echos
(3)
Range migration performed on each pixel of range-compressed data whose columns have been fourier transformed
(4)
Azimuth compression performed on each column of range-compressed, range-migrated data
Single Look Complex (SLC) image data file

Figure 4.3 Digital SAR processing overview.

a much longer synthetic aperture and patch size. Efficient processing of these data requires a minimum of 2 Gbytes of computer memory.

3. *Range migration* As we will see later, a point target will appear as a hyperbolic-shaped reflection as it moves through the synthetic aperture. In addition, there could be a pronounced linear drift due to an elliptical orbit and Earth's rotation. In other words, the target will migrate in the range cell as a linear trend plus a hyperbola. The shape of this migration path is calculated from the precise orbital information and is approximated by a parabola. Prior to focusing the

Downloaded from https://www.cambridge.org/core. IP address: 189.217.92.64, on 11 Feb 2026 at 15:51:46, subject to the Cambridge Core terms of use, available at https://www.cambridge.org/core/terms. https://www.cambridge.org/core/product/1F8951EFC610A352837B95E4DAEFBAEB

Table 4.1 *Example parameter (PRM) file (e2_10001_2925.PRM).*

File information/format			
input_file	e2_10001_2925.raw	name of raw data file	
SC_identity	2	(1) – ERS-1 or (2) – ERS-2	
bytes_per_line	11 644	number of bytes in row of raw data	
first_sample	206	412 bytes of timing information to skip over	
fd1	248.115	Doppler centroid estimated from data	f_{Dc}
I_mean	15.5	mean value of real numbers	
Q_mean	15.5	mean value of imaginary numbers	
icu_start	2576039268.848	spacecraft clock for first sample	
SC_clock_start	1997078.767881851	UTC for first sample YYYDDD.DDDDDDDD	
SC_clock_stop	1997078.768074699	UTC for last sample YYYDDD.DDDDDDDD	
Radar characteristics			
PRF	1679.902394	pulse repitition frequency	PRF
rng_samp_rate	1.89625e+07	range sampling rate	f_s
chirp_slope	4.17788e+11	chirp slope	k
pulse_dur	3.712e-05	pulse duration	τ_p
radar_wavelength	0.056666	radar wavelength	λ
Orbital information			
near_range	829924.365777	distance to first range bin	R_{near}
earth_radius	6371746.4379	earth radius 1/2 way into image	R_e
SC_height	787955.52	spacecraft height above the earth_radius	H
SC_vel	7125.0330	effective speed	V_e
Processing information			
num_valid_az	2 800	size of patch to process	
num_patches	10	number of patches to process	
first_line	1		
deskew	n	deskew (yes or no)	
st_rng_bin	1	start processing at row number	
num_rng_bins	6 144	number of range bins in output file	
chirp_ext	614	extend the chirp to process outside swath	
Flip_iq	n	exchange real and imaginary numbers (yes or no)	
nlooks	1	number of azimuth echoes to average	
Image alignment			
rshift	15.1	range shift to align image to master	
ashift	483.2	azimuth shift to align image to master	
stretch_r	0.0014569	range stretch versus range	
stretch_a	−0.0019436	azimuth stretch versus range	
a_stretch_r	0	range stretch versus azimuth	
a_stretch_a	0	azimuth stretch versus azimuth	

Downloaded from https://www.cambridge.org/core. IP address: 189.217.92.64, on 11 Feb 2026 at 15:51:46, subject to the Cambridge Core terms of use, available at https://www.cambridge.org/core/terms. https://www.cambridge.org/core/product/1F8951EFC610A352837B95E4DAEFBAEB

image along a single column, these signals must be migrated back to a constant range cell. This is called *range migration* and the fastest way to do this is by Fourier transforming the columns first. Each Fourier component corresponds to a unique Doppler shift and also a unique value of range migration; for an ideal radar, the first component will have zero Doppler and will correspond to the point on the Earth that is perpendicular to the spacecraft velocity vector. The second component will have a small positive Doppler shift and a small migration of the range cells will be needed – and so on all the way through the positive and negative Doppler spectrum.

4. *Azimuth compression* The final step in the processing is to focus the data in azimuth by accounting for the phase shift of the target as it moves through the aperture. In Chapter 2, we calculated the illumination pattern on a screen due to the propagation of a coherent wave from the aperture to the screen. The azimuth compression relies on the same theory, although we do the opposite calculation–given the illumination pattern, calculate the shape of the aperture (reflectivity of the target). This is done by generating a second frequency-modulated chirp where the chirp parameters depend on the velocity of the spacecraft, the pulse repetition frequency (PRF), and the absolute range. The chirp is Fourier transformed into Doppler space and multiplied by each column of range-migrated data. The product is inverse Fourier transformed to provide the focused image.

   Single-Look Complex image As described earlier, only the inner 2 800 rows use the complete synthetic aperture so these are written to an output file (Figure 4.2). The file-reading pointer is moved back 1 296 rows to start the processing of the next patch. Because complete apertures are used for each patch, they will abut seamlessly.

4.4 Range Compression

To reduce the peak power of the radar transmitter associated with a short pulse, a long FM chirp is emitted by the radar. This chirp propagates to the ground where it reflects from a swath typically 85 km wide. When it returns to the radar, the raw signal data consists of the complex reflectivity of the surface convolved with the chirp. Our objective is to recover the complex reflectivity by deconvolution of the chirp. As discussed earlier, this is the first step in the digital SAR processor. For the ERS radar, the frequency-modulated chirp is

$$S(t) = e^{i\pi kt^2} \qquad |t| < \tau_p/2. \tag{4.1}$$

where

k chirp slope ($4.17788 \times 10^{11} s^{-2}$)

Downloaded from https://www.cambridge.org/core. IP address: 189.217.92.64, on 11 Feb 2026 at 15:51:46, subject to the Cambridge Core terms of use, available at https://www.cambridge.org/core/terms. https://www.cambridge.org/core/product/1F8951EFC610A352837B95E4DAEFBAEB

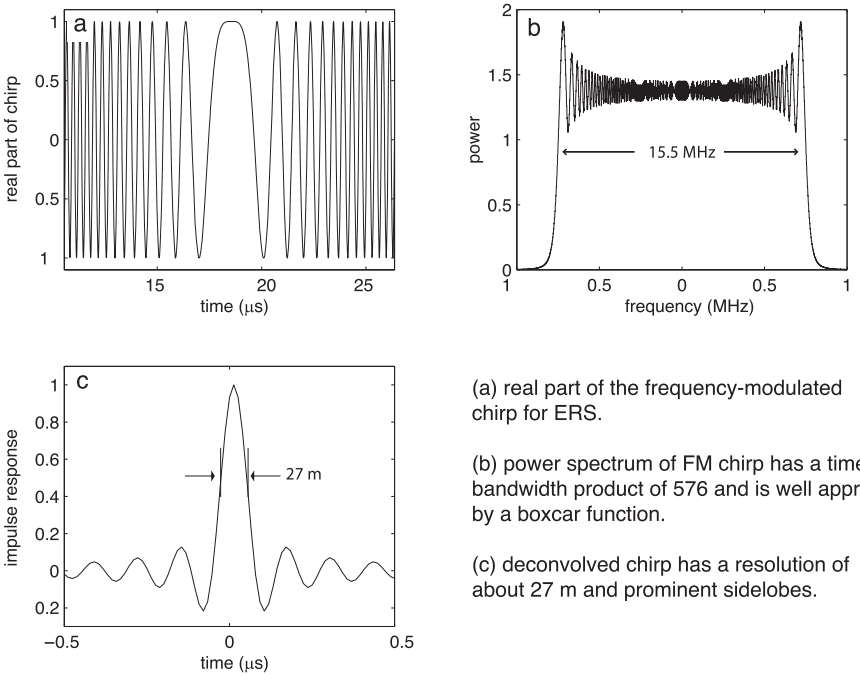

(a) real part of the frequency-modulated chirp for ERS.

(b) power spectrum of FM chirp has a time-bandwidth product of 576 and is well approximated by a boxcar function.

(c) deconvolved chirp has a resolution of about 27 m and prominent sidelobes.

Figure 4.4 Chirp for ERS-1.

τ_p pulse duration ($3.712 \times 10^{-5} s$ or ~11 km long)
f_s range sampling rate ($1.89625 \times 10^7 s^{-1}$).

An example of a portion of the chirp for the ERS radar as well as its power spectrum and impulse response is shown in Figure 4.4.

The bandwidth of the chirp, $B = k\tau_p$, has a value of 15.5 MHz for the ERS radar. A matched filter is used to deconvolve the chirp from the data. In this case, the matched filter is simply the complex conjugate of the chirp or $S^*(t) = e^{-i\pi kt^2}$. The convolution of $S^*(t)$ and $S(t)$ is shown in Figure 4.4 (c). The effective range resolution of the radar is about 27 m.

Using computer code and the radar parameters provided in the PRM file, one can deconvolve the ERS chirp. Figure 4.5 is a small patch of ERS-2 data for an area around Piñon Flat, California (track 127, frame 2 925, orbit 10 001). This area contains two radar reflectors (Figure 4.5 and Table 4.2) spaced about 600 m apart that were installed in late 1996. The amplitude of the raw signal data appears as noise with a single horizontal streak due to missing data (Figure 4.5 (a)). The range-compressed data (right image) shows two vertical streaks due to the high reflectivity of the reflectors (red circles) as they migrate through the synthetic aperture.

Downloaded from https://www.cambridge.org/core. IP address: 189.217.92.64, on 11 Feb 2026 at 15:51:46, subject to the Cambridge Core terms of use, available at https://www.cambridge.org/core/terms. https://www.cambridge.org/core/product/1F8951EFC610A352837B95E4DAEFBAEB

Table 4.2 *Coordinates of Radar Reflectors.*

position			orientation	
lat.	*lon.*	*height*	*elev.*	*azi.*
33.612246	−116.456768	1258.990	39°	257.5°
33.612246	−116.457893	1257.544	39°	102.5°
33.607373	−116.451836	1254.537	39°	102.5°

Latitude and longitude in decimal degrees and height in meters relative to the WGS-84 coordinate system and ellipsoid. The survey point is the apex (lowest corner) of each reflector. There should be a correction for the offset between the phase center of the reflector and the apex.

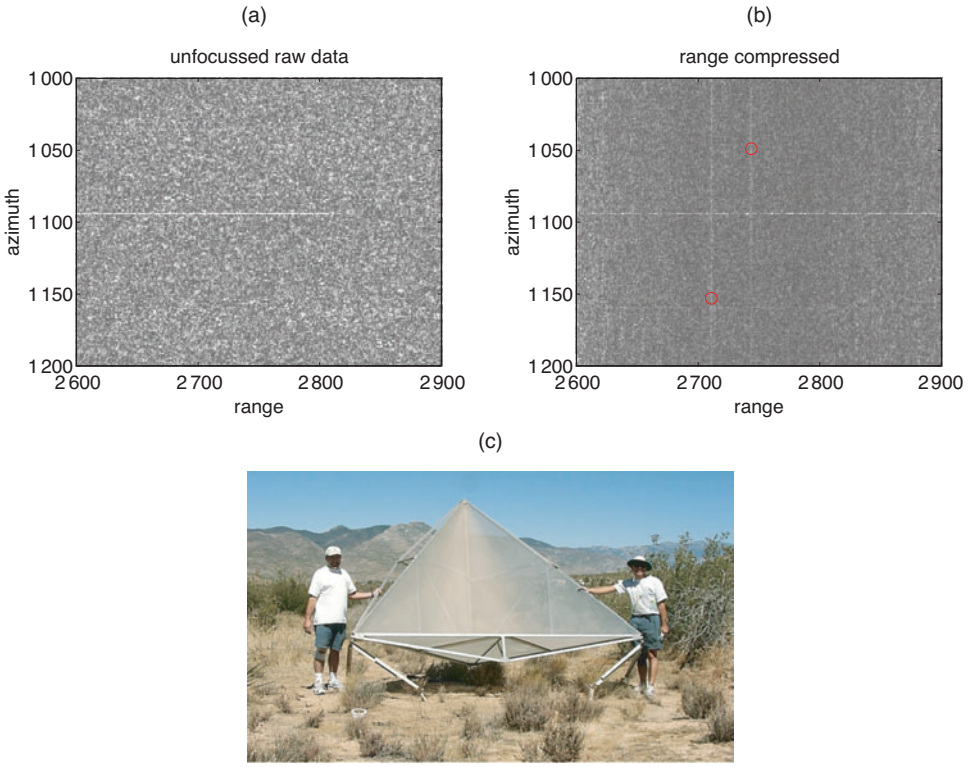

Figure 4.5 Raw ERS signal data (a) and range-compressed data (b) for data over Piñon Flat California where three radar corner reflectors are installed (c).

4.5 Azimuth Compression

Azimuth compression or azimuth focusing involves coherent summation of echos at a constant range from the point reflector. The geometry of the strip-mode

Downloaded from https://www.cambridge.org/core. IP address: 189.217.92.64, on 11 Feb 2026 at 15:51:46, subject to the Cambridge Core terms of use, available at https://www.cambridge.org/core/terms. https://www.cambridge.org/core/product/1F8951EFC610A352837B95E4DAEFBAEB

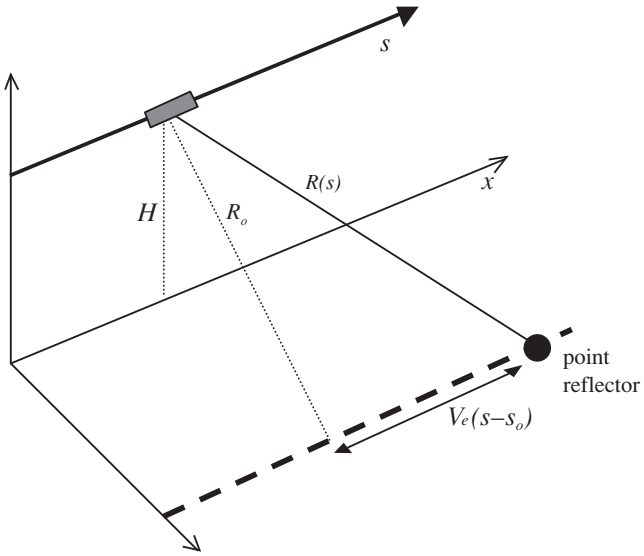

Figure 4.6 Geometry of radar passing over a point reflector where:

V_e	the effective speed as discussed later
s	slow time along the satellite track
s_o	time when the center of the radar echo passes over the point reflector
R_o	$R_{near} + n * (c/f_s)$ minimum range from the spacecraft to the target
R_{near}	near range to first data sample in the swath

acquisition is shown in Figure 4.6. The range to the point reflector evolves with time as

$$R^2(s) = R_o^2 + V_e^2(s - s_o)^2. \tag{4.2}$$

The complex phase of the return echo is

$$C(s) = \exp\left[-i\,\frac{4\pi}{\lambda}R(s)\right]. \tag{4.3}$$

The range versus slow time is approximately a hyperbola but for mathematical convenience we'll approximate this using a parabola

$$R(s) = R_o + \dot{R}(s - s_o) + \frac{\ddot{R}}{2}(s - s_o)^2 + \cdots \tag{4.4}$$

where the dot indicates derivative with respect to slow time, s. Curlander and McDonough (1991) discuss the accuracy of this polynomial approximation and it is also discussed later in terms of the ALOS SAR. The approximation is good enough for strip-mode SAR but may be inadequate for the much longer apertures associated with spotlight-mode SAR. Now we can write the phase of the return

Downloaded from https://www.cambridge.org/core. IP address: 189.217.92.64, on 11 Feb 2026 at 15:51:46, subject to the Cambridge Core terms of use, available at https://www.cambridge.org/core/terms. https://www.cambridge.org/core/product/1F8951EFC610A352837B95E4DAEFBAEB

signal as a function range, range rate, and range acceleration.

$$C(s) = \exp\left\{-i\,\frac{4\pi}{\lambda}\left[R_o + \dot{R}\,(s - s_o) + \ddot{R}(s - s_o)^2/2\right]\right\}. \tag{4.5}$$

It is more common to describe the parameters for focusing the SAR image as the Doppler centroid f_{Dc} and the Doppler frequency rate f_R. The relationships are:

$$f_{Dc} = \frac{-2\dot{R}}{\lambda} \quad \text{and} \quad f_R = \frac{-2\ddot{R}}{\lambda} \tag{4.6}$$

or

$$C(s) = \exp\left\{-i\,\frac{4\pi R_o}{\lambda}\right\}\,\exp\left\{i2\pi\left[f_{Dc}\,(s - s_o) + f_R(s - s_o)^2/2\right]\right\}. \tag{4.7}$$

Note that this function is another frequency-modulated chirp where the parameters are the Doppler centroid and the Doppler frequency rate. An example of this azimuthal chirp function for the ERS orbit/radar as well as its power spectrum and impulse response are shown in Figure 4.7.

The bandwidth of the azimuthal chirp is equal to the PRF (PRF = 1 680 Hz). In this case the matched filter is simply the complex conjugate of the azimuthal phase function (Equation 4.7) or $C^*(s)$.

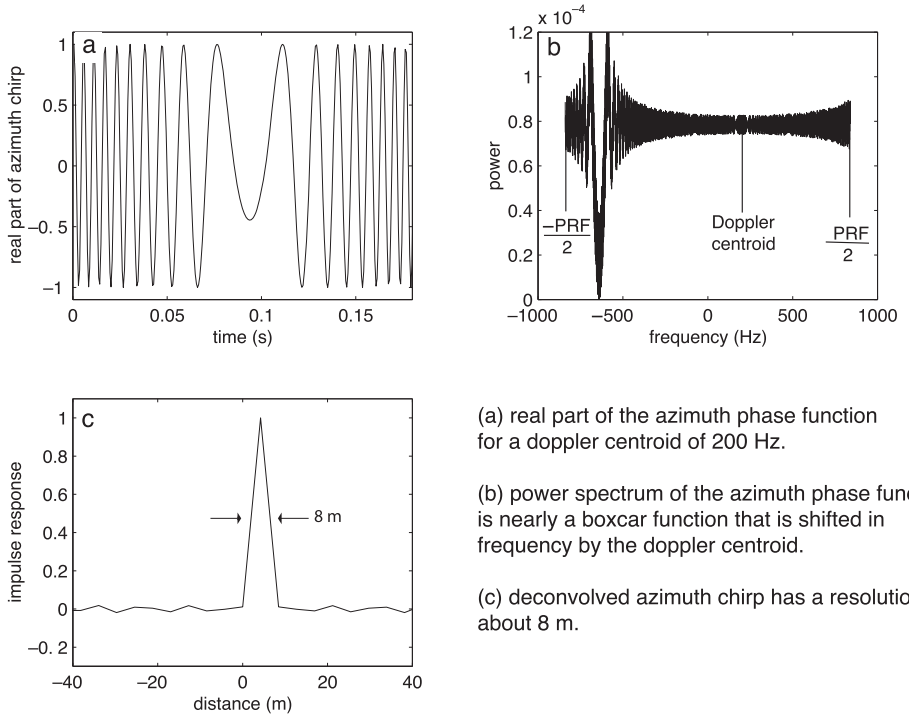

(a) real part of the azimuth phase function for a doppler centroid of 200 Hz.

(b) power spectrum of the azimuth phase function is nearly a boxcar function that is shifted in frequency by the doppler centroid.

(c) deconvolved azimuth chirp has a resolution of about 8 m.

Figure 4.7 Azimuthal phase for the ERS-1 spacecraft.

Downloaded from https://www.cambridge.org/core. IP address: 189.217.92.64, on 11 Feb 2026 at 15:51:46, subject to the Cambridge Core terms of use, available at https://www.cambridge.org/core/terms. https://www.cambridge.org/core/product/1F8951EFC610A352837B95E4DAEFBAEB

Doppler centroid, Doppler rate, and effective speed Proper focus of the image requires accurate estimates of the three parameters given in Equations 4.5 and 4.7. Actually, we only need to estimate two parameters because we will sweep through the range cells n in the raw data file and focus the image at each range $R_o = R_{near} + n^*(C/f_s)$ where C is the speed of light and f_s is the range sampling rate. Ideally, the beam of the radar would be steered so that it is centered at a point on the ground where the range is minimum so the Doppler centroid is zero or at least small. We follow the approach of Madsen (1989) and calculate the Doppler centroid directly from the raw data file by computing the average change in phase between adjacent rows of the raw data file. This assumes that the Doppler centroid does not vary with slow time, although it could vary slightly with increasing range. We use this estimated Doppler centroid to focus the image (or select a similar Doppler centroid that is closest to the mean of a stack of repeated SAR images).

Finally, as discussed later, the precise orbit (i.e., in Earth-fixed coordinates) can be used to calculate the third parameter, the range acceleration $\ddot{R}$. One approach would be to use the precise orbit to calculate range acceleration for each range, but this is unnecessary because there is a good formula for range acceleration as a function of range that involves a parameter called the effective speed V_e of the spacecraft. Indeed, the SAR processor code takes effective speed and converts this to $\ddot{R}$ to focus the image. The derivation of the effective speed parameter follows. We start by taking the first derivative of the range squared versus slow time given in Equation 4.2.

$$\frac{\partial R^2\,(s)}{\partial s} = 2R\dot{R} = 2V_e^2 s. \tag{4.8}$$

The second derivative is

$$\dot{R}\dot{R} + R\ddot{R} = V_e^2. \tag{4.9}$$

Next we assume that the radar antenna is oriented nearly perpendicular to the velocity vector of the satellite so $\dot{R} << V_e$. Note that to achieve interferometric coherence, the radar beams of the reference and repeat images must overlap spatially, which essentially requires that the Doppler centroid be less than half of the PRF. Given a typical PRF for a spaceborne SAR of 2 000 Hz and using Equation 4.6 and a wavelength of 0.05 m, the range rate must be less than 25 m/s. This is much less than the typical spacecraft velocity of 7 800 m/s so we can safely ignore the first term on the left-hand side of Equation 4.9. So the approach is to use the precise orbit to calculate the range acceleration $\ddot{R}$ at a single range R_o within the image. These two numbers are used to calculate the effective speed

Downloaded from https://www.cambridge.org/core. IP address: 189.217.92.64, on 11 Feb 2026 at 15:51:46, subject to the Cambridge Core terms of use, available at https://www.cambridge.org/core/terms. https://www.cambridge.org/core/product/1F8951EFC610A352837B95E4DAEFBAEB

$$V_e = \sqrt{R_o \ddot{R}}. \tag{4.10}$$

Finally, this parameter is used by the SAR processing code to calculate the range acceleration

$$\ddot{R} = V_e^2 / R \tag{4.11}$$

at all the other ranges in the swath.

The effective speed, which is reported as SC_vel in the PRM file, can be used to compute the ground track speed V_g of the satellite as

$$V_g = \frac{V_e}{\left(1 + \frac{H}{R_e}\right)^{1/2}}. \tag{4.12}$$

where H is the height of the spacacraft and R_e is the local Earth radius. Also note that $V_g < V_e < V_s$ where V_s is the velocity of the spacecraft at orbital altitude. Using Equation 4.12, one can show that

$$V_e = \frac{V_s}{\left(1 + \frac{H}{R_e}\right)^{1/2}}. \tag{4.13}$$

Note this is only an approximate formula for computing the effective speed from the spacecraft velocity (Curlander and McDonough (1991)). For C-band radars such as ERS and Envisat, the effective speed calculated from Equation 4.13 provides adequate focus for the SAR image. However, for L-band SARs such as ALOS, the aperture is much longer, so other factors must be considered such as the curvature and ellipticity of the orbit.

We bypass this complexity by computing the effective speed from a polynomial fit of range versus time as discussed later, but first we discuss the length of the synthetic aperture.

Length of synthetic aperture The length of the synthetic aperture L_a depends on the length of the radar ground footprint in the azimuth direction, which is approximately

$$L_a = R_o \frac{\lambda}{L} \tag{4.14}$$

where L is the physical length of the antenna, λ is the wavelength and R_o is the slant range given earlier. The length of the aperture in terms of radar echoes is given by

$$n_a = \frac{L_a \mathrm{PRF}}{V_e}. \tag{4.15}$$

This is simply the length of the synthetic aperture divided by the along-track sampling distance. Table 4.3 provides these quantities for SARs of interest for interferometry today.

Downloaded from https://www.cambridge.org/core. IP address: 189.217.92.64, on 11 Feb 2026 at 15:51:46, subject to the Cambridge Core terms of use, available at https://www.cambridge.org/core/terms. https://www.cambridge.org/core/product/1F8951EFC610A352837B95E4DAEFBAEB

Table 4.3 *Length of synthetic aperture for three satellites.*

	V_e (m/s)	λ (m)	PRF (Hz)	R_o (km)	L (m)	L_A (m)	n_a *theory*	n_a *actual*
ERS-1/2	7 125	0.057	1 679	~850	10	4 850	1 142	1 164
Envisat	7 125	0.057	2 067	~1 020	10	5 830	1 690	1 740
ALOS	7 125	0.236	2 159	~1 020	9	26 830	8 128	9 216

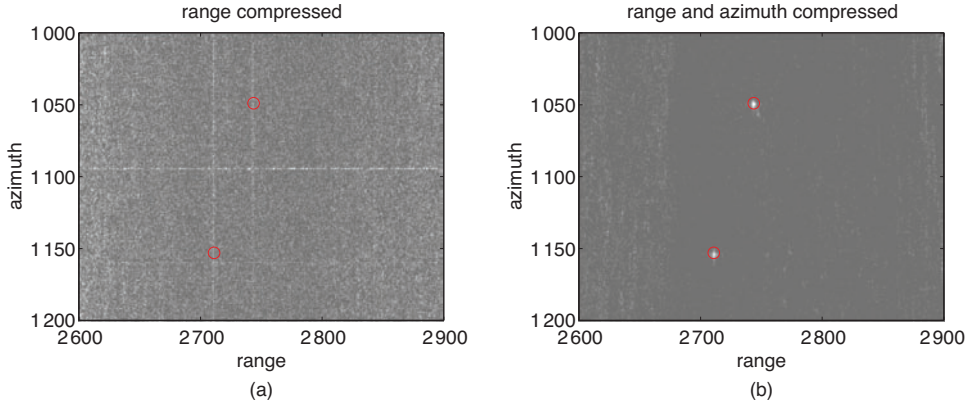

Figure 4.8 Range-compressed (a) and fully focused image (b). The two bright reflectors are 3-m corner cubes at Piñon Flat observatory. These were deployed in 1996 and therefore provide stable calibration points for ERS-1, ERS-2, Envisat, ALOS, and all future satellites.

Focused image Using the azimuth compression formulas and parameters provided earlier, one can focus the image in the azimuth direction. Figure 4.8 show the same small patch of ERS-2 data for an area of Piñon Flat, California. The range-compressed data (Figure 4.8 (a)) shows two vertical streaks due to the high reflectivity of the reflectors (red circles) as they migrate through the synthetic aperture. The fully focused image (Figure 4.8 (b)) shows the point-like reflectivity associated with the two radar reflectors.

4.5.1 Estimating $\ddot{R}$ when a Precise Orbit Is Available

(This subsection can be skipped unless the reader wants to understand the geometric details for computing $\ddot{R}$ from the precise orbit.) Estimation of the range acceleration from the orbit seems conceptually simple, although there is one complication that requires a bit of geometry. The complication is to find a point on the surface of the Earth, at a prescribed range, and convert that location to Cartesian coordinates. Consider the following three vectors that form a triangle:

Downloaded from https://www.cambridge.org/core. IP address: 189.217.92.64, on 11 Feb 2026 at 15:51:46, subject to the Cambridge Core terms of use, available at https://www.cambridge.org/core/terms. https://www.cambridge.org/core/product/1F8951EFC610A352837B95E4DAEFBAEB

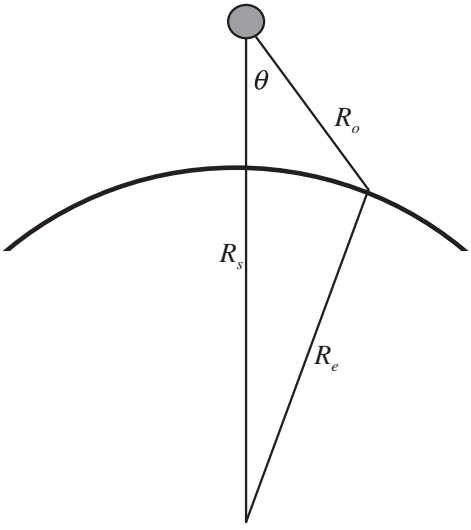

Figure 4.9 Triangle of Earth radius, satellite radius, and range to a point on the surface of the Earth used to compute look angle θ.

$\vec{R}_s$ the vector position of the satellite in the Earth-fixed coordinate system;
$\vec{R}_e$ the vector position of a point scatterer on the Earth and somewhere in the SAR scene;
$\vec{R}_o$ the line-of-sight (LOS) vector between the satellite and the point scatterer.

The three vectors form a triangle such that $\vec{R}_e = \vec{R}_s + \vec{R}_o$ (Figure 4.9). The scalar range, which is a function of slow time, is given by

$$R(s) = \left|\vec{R}_s(s) - \vec{R}_e\right| \cong R_o + \dot{R}_o(s - s_o) + \frac{\ddot{R}_o}{2}(s - s_o)^2 + \ldots \tag{4.16}$$

Measurements of scalar range versus slow time can be used to estimate the coefficients of the parabolic approximation. The algorithm is to:

1. Use the precise orbit to calculate the position vector of the satellite and compute a time series $R(s)$ over the length of the aperture.
2. Perform a least-squares parabolic fit to this time series to estimate R_o, $\dot{R}_o$, $\ddot{R}_o$.
3. Compute the effective speed as $V_e^2 = R_o\ddot{R}_o$.

The only remaining step is to calculate the position of the point target $\vec{R}_e = \vec{R}_s + \vec{R}_o$. Actually this can be any point in the image so the selection criteria is that the point lie at the proper radius of the surface of the Earth $R_e = \left|\vec{R}_e\right|$ and the $\vec{R}_o$ vector is perpendicular to the velocity vector of the satellite $\vec{V}$. If we prescribe the length of the R_o- vector, then the angle between the satellite position vector and the LOS vector is given by the law of cosines as shown in Figure 4.9.

Downloaded from https://www.cambridge.org/core. IP address: 189.217.92.64, on 11 Feb 2026 at 15:51:46, subject to the Cambridge Core terms of use, available at https://www.cambridge.org/core/terms. https://www.cambridge.org/core/product/1F8951EFC610A352837B95E4DAEFBAEB

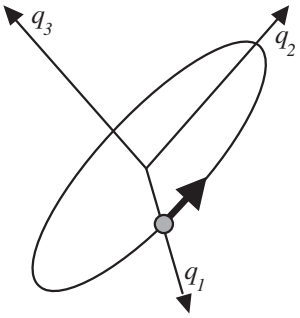

Figure 4.10 Satellite (gray) in circular inclined orbit about the Earth.

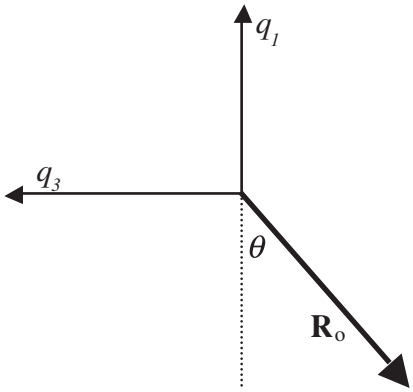

Figure 4.11 Diagram of satellite-fixed coordinate system where q_1 is the vector from the center of the Earth to the spacecraft, and q_2 is parallel to the velocity vector of the SC. The bold vector is the look vector of the radar where θ is the look angle.

This diagram has the satellite at the gray dot with the velocity vector pointing into the page. The cosine of the look angle is

$$\cos\theta = \frac{\left(R_s^2 + R_o^2 - R_e^2\right)}{2R_sR_o}. \tag{4.17}$$

Next consider a local coordinate system where the q_2 axis is aligned with the velocity vector of the satellite as shown in Figure 4.10.

In this coordinate system, the q_1 axis is parallel to $\vec{R}_s$, the q_2 axis is parallel to $\vec{V}$, and the q_3 axis is perpendicular to both and is given by their cross product

$$q_3 = \frac{\vec{R}_s}{|R_s|} \times \frac{\vec{V}}{\left|\vec{V}\right|}. \tag{4.18}$$

Downloaded from https://www.cambridge.org/core. IP address: 189.217.92.64, on 11 Feb 2026 at 15:51:46, subject to the Cambridge Core terms of use, available at https://www.cambridge.org/core/terms. https://www.cambridge.org/core/product/1F8951EFC610A352837B95E4DAEFBAEB

Figure 4.11 has the velocity vector of the satellite going into the page and aligned with the q_2 coordinate. The q_1 vector is the radial vector from the center of the Earth. The LOS right-look vector is in the q_1-q_3 plane as shown in Figure 4.11. After going through this geometry, we find the LOS vector to a point on the surface of the Earth at the prescribed range for a right-looking radar is

$$\vec{R}_o = R_o \left(-\cos\theta \hat{q}_1 \quad 0\hat{q}_2 \quad -\sin\theta \hat{q}_3 \right) \tag{4.19}$$

and for a left-looking radar is

$$\vec{R}_o = R_o \left(-\cos\theta \hat{q}_1 \quad 0\hat{q}_2 \quad \sin\theta \hat{q}_3 \right). \tag{4.20}$$

4.6 Example with ALOS L-Band Orbit

Now that we have an algorithm for finding a point on the surface of the Earth that is within the SAR scene, we can compute the time evolution of the range to that point as the satellite orbits above the rotating Earth. We consider data from a descending orbit over Koga, Japan, where three radar reflectors have been deployed. The image is a fine beam, single polarization having a nominal look angle of 34.3 degrees. A Hermite polynomial interpolation was used to calculate the $x - y - z$ position of the satellite from 28 position and velocity vectors spaced at 60-second intervals. Thus, the entire arc is 28 minutes or a quarter of an orbit. The accuracy of the Hermite interpolator was checked by omitting a central point and performing an interpolation using 6 surrounding points. The accuracy of the interpolation was found to be better than 0.2 mm suggesting that the 60-s interval provides an accurate representation of the orbital arc.

Next we compute the range to the ground point as a function of time before and after the perpendicular LOS vector $\vec{R}_o$. We used a before/after time interval of 3 seconds, which is about 1.5 times the length of the synthetic aperture for ALOS. A second-order polynomial was fit to the range versus time function and the three coefficients provide estimates of R_o, $\dot{R}_o$, and $\ddot{R}_o$. The range versus time, as well as the residual of the fit, are shown in Figure 4.12. One can learn a great deal from this exercise.

1. The first thing learned is that the parabolic approximation to a hyperbola used in the SAR processor has a maximum error of about 1 cm at a time offset of 3 seconds. This corresponds to a small fraction of the 23-cm wavelength. Note that the actual aperture length for ALOS is only ±2 seconds so this approximation is justified.
2. The range at zero offset has an error of −0.24 m. This is due to approximating the shape of the Earth as a sphere having a local radius given by the WGS84 ellipsoid formula. In other words, there is a small error in the LOS vector

Downloaded from https://www.cambridge.org/core. IP address: 189.217.92.64, on 11 Feb 2026 at 15:51:46, subject to the Cambridge Core terms of use, available at https://www.cambridge.org/core/terms. https://www.cambridge.org/core/product/1F8951EFC610A352837B95E4DAEFBAEB

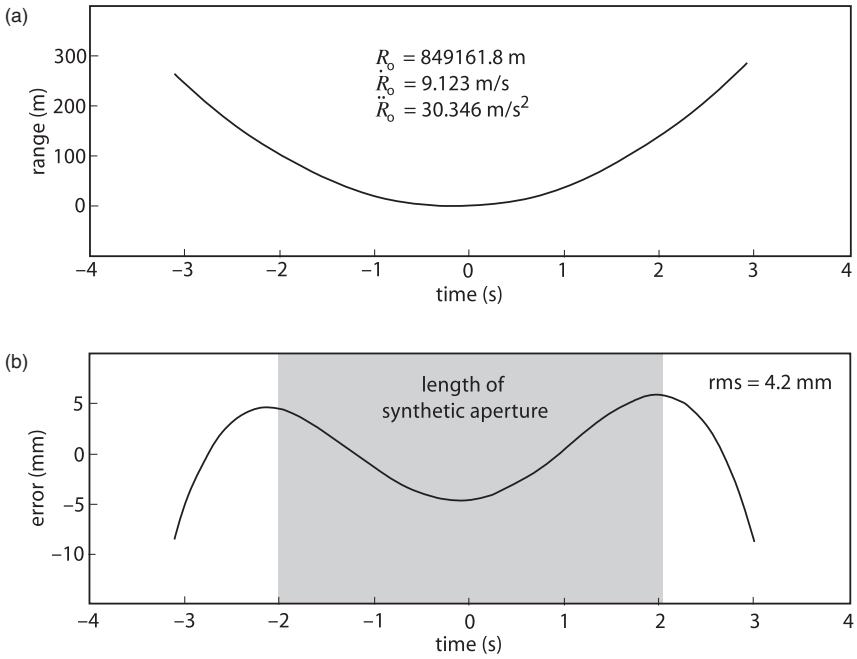

Figure 4.12 (a) range versus slow time for ALOS for a 6-second aperture. The actual aperture is 4.2 seconds (Table 4.3). (b) deviation from a parabolic fit to this range vs. time function. The shaded area is the length of the synthetic aperture.

because it intersects the surface of the Earth at a latitude that is slightly different from the spacecraft latitude so the Earth radii will differ slightly.

3. The Doppler shift when the satellite is perpendicular to the target can be calculated from the range rate coefficient using Equation 4.6.
4. Finally, the range acceleration can be used to calculate the effective speed of the satellite $V_e^2 = R_o\ddot{R}_o$. For this example we arrive at a speed of 7 174 m/s. By trial and error we found the optimal focus parameter corresponds to a speed between 7 173 and 7 183 m/s, so this new estimate is accurate. The simple spherical orbit ground speed approximation (4.13) yields an estimate of 7 208 m/s which provides poor focus.

Squint angle – Finally let's examine the quantity, $\frac{V(s-s_o)}{R_o}$. This is related to something called the squint angle, γ, as shown in Figure 4.13.

The squint angle is simply

$$\gamma = \tan^{-1}\left(\frac{V(s-s_o)}{R_o}\right). \tag{4.21}$$

For the ERS, Envisat, and ALOS satellites, the squint angle is adjusted so the zero Doppler occurs roughly in the center of the antenna beam pattern. If the satellite

Downloaded from https://www.cambridge.org/core. IP address: 189.217.92.64, on 11 Feb 2026 at 15:51:46, subject to the Cambridge Core terms of use, available at https://www.cambridge.org/core/terms. https://www.cambridge.org/core/product/1F8951EFC610A352837B95E4DAEFBAEB

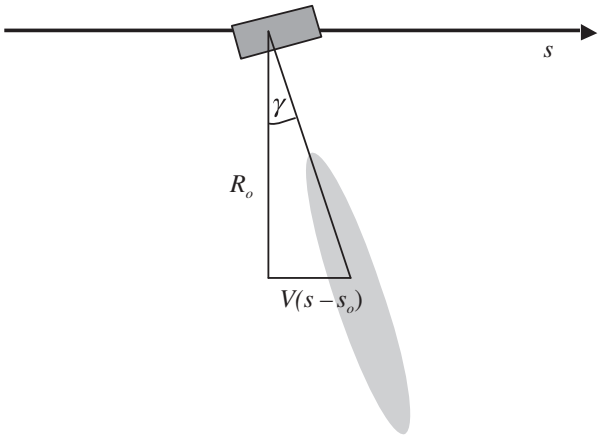

Figure 4.13 Schematic diagram of squint angle.

orbit was circular and the Earth was a nonrotating sphere, then the zero Doppler would correspond to a zero squint angle.

For interferometry it is important that the beam patterns of the reference and repeat orbits have a large overlap (>50%) at a given along-track spacecraft position. The requirement is that the Doppler centroid of the reference and repeat passes agree to about 1/2 of the PRF. In late 1999, the gyroscopes on ERS-2 failed, so it became difficult to control the squint angle of the spacecraft. Data acquired after this date may have a Doppler centroid outside of the acceptable range and thus may be useless for interferometry. The squint angle for the ALOS satellite is well controlled and the Doppler centroid is usually less than 100 Hz so we commonly focus the images at zero Doppler.

4.7 Problems

1. Explain why the raw signal data are provided as complex numbers. Why are the numbers restricted to the range 0–31?
2. Why is the SAR processing with the range-Doppler algorithm often done in patches rather than all at once? What is the minimum possible patch size?
3. Most SAR instruments emit a frequency-modulated chirp rather than a short pulse. Why? Write a Matlab program to deconvolve the FM chirp for ERS and reproduce the impulse response function shown in Figure 4.4.
4. Make a plot of the real and imaginary parts of the function given in Equation 4.5 for a time interval of −0.1 to 0.1 seconds. Use $R_o = 850$ km, $\dot{R}_o = 0$, $\ddot{R}_o = \frac{V^2}{R_o}$, where $V = 7\,125 \text{ms}^{-1}$. Use a wavelength of 56 mm.
5. Derive Equation 4.13.

Downloaded from https://www.cambridge.org/core. IP address: 189.217.92.64, on 11 Feb 2026 at 15:51:46, subject to the Cambridge Core terms of use, available at https://www.cambridge.org/core/terms. https://www.cambridge.org/core/product/1F8951EFC610A352837B95E4DAEFBAEB

6. Derive Equation 4.14. (You may need to look back at Chapter 2.)
7. Explain qualitatively how a SAR antenna should be squinted (turned) to keep the Doppler centroid of the return echoes close to zero for the following three cases: (1) an elliptical orbit about a spherical, nonrotating Earth; (2) a circular orbit about an elliptical and nonrotating Earth; (3) and a circular orbit about a rotating, spherical Earth.

Downloaded from https://www.cambridge.org/core. IP address: 189.217.92.64, on 11 Feb 2026 at 15:51:46, subject to the Cambridge Core terms of use, available at https://www.cambridge.org/core/terms. https://www.cambridge.org/core/product/1F8951EFC610A352837B95E4DAEFBAEB

5

Interferometric Processing

5.1 Interferogram Formation

Creating an interferogram from two single look complex (SLC) images involves two basic steps. The first step is to align the reference and repeat images to sub-pixel accuracy. This is done by two-dimensional cross-correlation (*xcorr* in GMTSAR) of hundreds of small sub-patches (e.g., 64×64) taken from the master and secondary images. A more modern approach is to use a topography grid and precise orbital information for alignment. Both approaches are described in Chapter 3. Then a six-parameter affine (or continuous) transformation is determined using a robust 2-D fit to the offset data (*fitoffset* in GMTSAR) or the precise orbit data as described in Chapter 3. This is used to align the secondary image to the master image. For raw data, the alignment is done in the SAR processor (*esarp* in GMTSAR). For SLC image data, the alignment is done using a sinc-interpolator (*resamp* in GMTSAR).

The second step is to multiply the two SLC images to form the complex interferogram. The complex number $C(\mathbf{x})$ in each pixel of the SLC image can be written as an amplitude $A(\mathbf{x})$ and phase $\phi(\mathbf{x})$ as

$$C(\mathbf{x}) = A(\mathbf{x})\, e^{i\phi(\mathbf{x})} \tag{5.1}$$

where $\mathbf{x} = (\rho, a)$ is the position vector consisting of range ρ and azimuth a. An interferogram is defined as

$$C_2 C_1^* = A_1 A_2 e^{i(\phi_2 - \phi_1)} = R(\mathbf{x}) + iI(\mathbf{x}) \tag{5.2}$$

The phase of the interferogram is extracted as

$$(\phi_2 - \phi_1) = \tan^{-1}\left(\frac{I}{R}\right) \tag{5.3}$$

An example of the phase of reference and repeat images and their phase difference is shown in Figure 5.1.

Downloaded from https://www.cambridge.org/core. IP address: 189.217.92.64, on 11 Feb 2026 at 15:51:46, subject to the Cambridge Core terms of use, available at https://www.cambridge.org/core/terms. https://www.cambridge.org/core/product/1F8951EFC610A352837B95E4DAEFBAEB

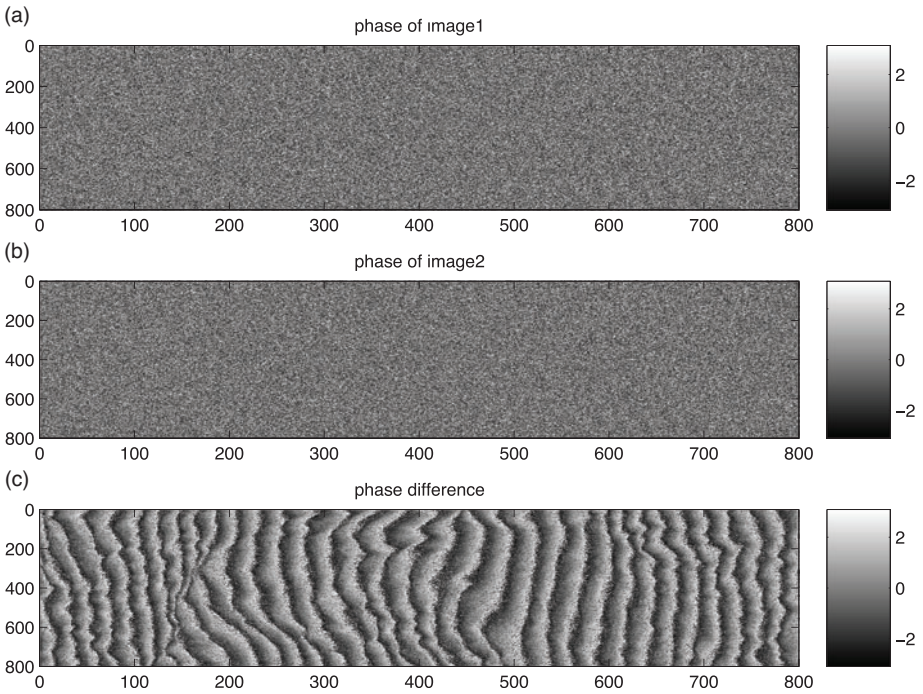

Figure 5.1 (a) The phase of a reference SLC file. (b) The phase of a repeat SLC file, and (c) the phase difference of repeat – reference SLC files calculated using Equations 5.2 and 5.3. The fringes across the interferogram are mostly due to the curvature of the Earth where the fringe rate is proportional to the perpendicular baseline between the reference and repeat images.

5.2 Contributions to Phase

The phase of an interferogram has many components as described in Equation 5.4.

$$
\begin{aligned}
\textit{phase} = {} & \textbf{Earth curvature} \text{ (almost a plane, known)} + \\
& \textbf{topographic phase} \text{ (broad spectrum)} + \\
& \textit{surface deformation} \text{ (broad spectrum, unknown)} + \\
& \textit{orbit error} \text{ (almost a plane, largely known)} + \\
& \textit{ionosphere advance} \text{ (often a plane or 20–40 km wavelength waves)} + \\
& \textit{troposphere delay} \text{ (power law, unknown)} + \\
& \textit{tides} \text{ (almost a plane, largely known)} + \\
& \textit{phase noise} \text{ (white spectrum, unknown)}
\end{aligned}
\tag{5.4}
$$

A common task in InSAR analysis is to isolate the phase associated with surface deformation from all the other contributions. The largest known contribution comes

Downloaded from https://www.cambridge.org/core. IP address: 189.217.92.64, on 11 Feb 2026 at 15:51:46, subject to the Cambridge Core terms of use, available at https://www.cambridge.org/core/terms. https://www.cambridge.org/core/product/1F8951EFC610A352837B95E4DAEFBAEB

from the irregular shape of the Earth, which can be divided into an **Earth curvature component** and a **topography component**. In the remainder of this chapter, we show derivations of the phase and phase gradient due to Earth curvature, the *critical baseline, point scatterers*, and *phase due to topography*, as presented previously in Rosen et al. (1996); Joughin et al. (1996b); Sandwell and Price (1998). These derivations are useful for exposing concepts such as *parallel* and *perpendicular baseline*. However, this standard geometric model is not adequate for achieving high-accuracy results, especially for L-band large spatial baseline interferometry cases. We next derive the exact formulas that are implemented as *phasediff* in GMTSAR. These exact formulas are also conceptually and mathematically simpler than the approximate formulas, which are preferred in InSAR processing routines.

5.3 Phase due to Earth Curvature

The geometry of repeat-pass interferometry is shown in Figure 5.2.

The key parameters are:

ρ range from reference track to reflector
B total baseline distance between reference and repeat track
θ look angle
α angle between the baseline vector and the tangent plane

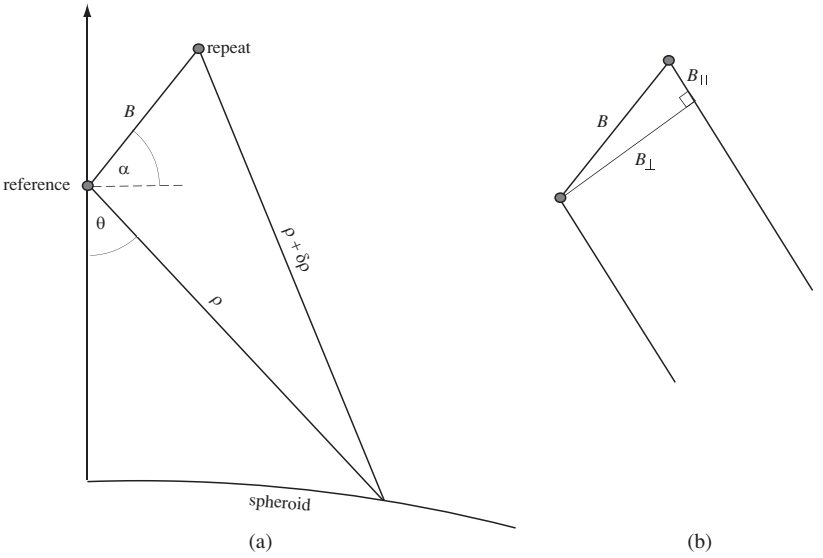

Figure 5.2 (a) Triangle for reference and repeat passes imaging the same point on the Earth. (b) The total baseline can be decomposed into parallel and perpendicular components.

Downloaded from https://www.cambridge.org/core. IP address: 189.217.92.64, on 11 Feb 2026 at 15:51:46, subject to the Cambridge Core terms of use, available at https://www.cambridge.org/core/terms. https://www.cambridge.org/core/product/1F8951EFC610A352837B95E4DAEFBAEB

The baseline B can be divided into parallel and perpendicular components given by

$$\begin{aligned} B_{\parallel} &= B \sin(\theta - \alpha) \\ B_{\perp} &= B \cos(\theta - \alpha) \end{aligned} \tag{5.5}$$

Because the look angle θ changes across the swath, the notion of a single perpendicular baseline for an interferometric combination is only an approximation. (*SAT_baseline* in GMTSAR computes the total baseline B as well as the angle α at 3 or more points along the image.) The phase difference ϕ to a point on the ground is related to the range difference $\delta\rho$.

$$\phi = \frac{4\pi}{\lambda}\delta\rho \tag{5.6}$$

where λ is the wavelength of the radar. The law of cosines provides the relationship among the repeat-pass range, the reference-pass range, the baseline length B, and the baseline orientation α as shown in Figure 5.2.

$$(\rho + \delta\rho)^2 = \rho^2 + B^2 - 2\rho B \sin(\theta - \alpha) \tag{5.7}$$

Under the assumption that $\delta\rho \ll \rho$, we have

$$\delta\rho = \frac{B^2}{2\rho} - B \sin(\theta - \alpha) \tag{5.8}$$

Furthermore, since $B \ll \rho$, the parallel ray approximation yields

$$\phi = \frac{-4\pi}{\lambda} B \sin(\theta - \alpha) \tag{5.9}$$

The phase difference depends on the parallel component of the baseline. The derivative of the phase with respect to range is

$$\frac{\partial\phi}{\partial\rho} = \frac{-4\pi}{\lambda} B \cos(\theta - \alpha) \frac{\partial\theta}{\partial\rho} \tag{5.10}$$

This phase gradient depends on two terms, the perpendicular component of the baseline $B_{\perp} = B\cos(\theta - \alpha)$ and the derivative of look angle with respect to range $\delta\theta/\delta\rho$. The perpendicular baseline varies slightly with look angle across a typical SAR image. The change in look angle usually increases with range, so $\delta\theta/\delta\rho > 0$. However, when the local terrain slope exceeds the look angle (actually the incidence angle), an increase in look angle does not produce a corresponding increase in range. This is the *layover* geometry where $\delta\theta/\delta\rho \leq 0$ (see Figure 7.2).

5.4 Look Angle and Incidence Angle for a Spherical Earth

In order to calculate the derivative of look angle with respect to range $\delta\theta/\delta\rho$, we first make the approximation that the Earth is locally spherical and then adjust the local radius of the Earth using the WGS84 ellipsoid 5.11. We note that there can

Downloaded from https://www.cambridge.org/core. IP address: 189.217.92.64, on 11 Feb 2026 at 15:51:46, subject to the Cambridge Core terms of use, available at https://www.cambridge.org/core/terms. https://www.cambridge.org/core/product/1F8951EFC610A352837B95E4DAEFBAEB

be large differences between the elliptical Earth model and the local radius for wide SAR swaths. This difference can produce topographic fringes in long-strip interferograms depending on the interferometric baseline. We address this issue later by including the ellipsoidal radius minus the local radius into a topographic correction term. The local Earth radius is given by

$$r_e(\varphi) = \left(\frac{\cos^2 \varphi}{a^2} + \frac{\sin^2 \varphi}{c^2} \right)^{-1/2} \tag{5.11}$$

where φ is latitude, and a and c are the equatorial (6 378 km) and polar (6 357 km) radii, respectively.

The radar look angle depends only on the local Earth radius r_e, the range to the sphere ρ, and the height of the spacecraft above the center of the Earth b as shown in Figure 5.3.

The law of cosines is used to calculate the look angle

$$\eta = \cos \theta = \frac{\left(b^2 + \rho^2 - r_e^2 \right)}{2\rho b} \tag{5.12}$$

On a sphere, the incidence angle is greater than the look angle by the angle ψ.

To determine the derivative of the phase (5.10), we need to determine the derivative of the look angle with respect to range from Equation 5.12. An expression for the phase gradient due to Earth curvature is

$$\frac{\partial \phi}{\partial \rho} = \frac{-4\pi B}{\lambda \rho} \frac{\cos(\theta - \alpha)}{\sin \theta} \left(\cos \theta - \frac{\rho}{b} \right) \tag{5.13}$$

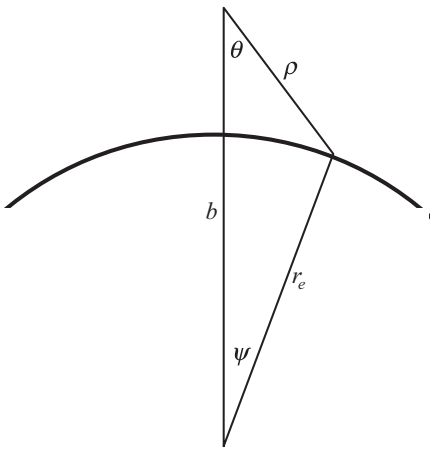

Figure 5.3 Triangle formed by the range ρ, radius of the Earth r_e, and spacecraft height b.

Downloaded from https://www.cambridge.org/core. IP address: 189.217.92.64, on 11 Feb 2026 at 15:51:46, subject to the Cambridge Core terms of use, available at https://www.cambridge.org/core/terms. https://www.cambridge.org/core/product/1F8951EFC610A352837B95E4DAEFBAEB

5.5 Critical Baseline

Consider a single range pixel of length $\Delta\rho = c\tau/2$. The phase of this pixel in the reference image is the vector sum of the phase from all scatterers in the pixel. The repeat image has the same scatterers but slightly different imaging geometry ($B > 0$). As a result, there are additional phase delays across the range cell, causing the sum of the phase from all scatterers to be different from the reference image. This is called baseline decorrelation. When the fringe rate across the interferogram exceeds 2π radians per range cell, the interferogram is completely decorrelated. This is the case of the *critical baseline*. To calculate the critical baseline, we start with Equation 5.13 and make a flat-Earth approximation $\rho/b = 0$. To avoid baseline decorrelation, change in phase with range must be less than

$$\frac{\partial\phi}{\partial\rho} = \frac{-4\pi B_\perp}{\lambda\rho}\frac{\cos\theta}{\sin\theta} < \frac{2\pi}{\Delta\rho} \tag{5.14}$$

The baseline where the fringe rate equals the critical value is

$$B_c = \frac{\lambda\rho}{c\tau}\tan\theta \tag{5.15}$$

For the parameters of the ERS satellite, the critical baseline is 1 100 m (Table 5.1). For topographic recovery, a baseline of about 1/4 critical is optimal. For change detection, a zero baseline is optimal but not usually available.

There is a second way to calculate the critical baseline. Consider a single ground range resolution pixel cell, which is related to the pulse length and the incidence angle $R_r = c\tau/(2\sin\theta)$. This cell is imaged from two positions separated by a perpendicular baseline (Figure 5.4). If the resolution cell contains only a single persistent scatterer at the center, the change in the viewing geometry does not change

Table 5.1 *Comparison of critical baseline (in km). ERS/Envisat – altitude = 790 km, wavelength = 56 mm. ALOS – altitude = 700 km, wavelength = 236 mm. Sentinel-1 – altitude = 700 km, wavelength = 55 mm, three look angles for each of the three subswaths. Shaded area is the most common mode for interferometry.*

Look angle	23°	34°	41°
ERS/Envisat 16 MHz	1.1	2.0	2.9
ALOS FBD 14 MHz	3.6	6.5	9.6
ALOS FBS 28 MHz	7.3	13.1	18.6
Sentinel-1 64 MHz	4.3	6.8	8.26

Downloaded from https://www.cambridge.org/core. IP address: 189.217.92.64, on 11 Feb 2026 at 15:51:46, subject to the Cambridge Core terms of use, available at https://www.cambridge.org/core/terms. https://www.cambridge.org/core/product/1F8951EFC610A352837B95E4DAEFBAEB

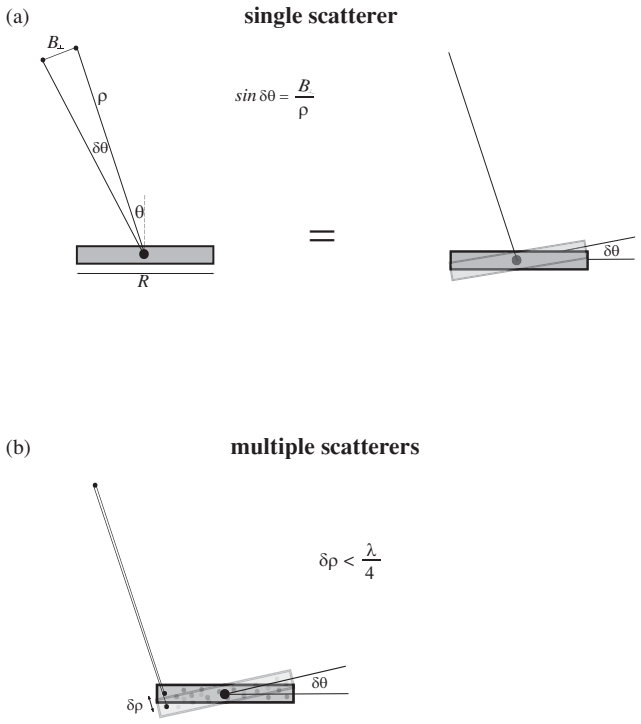

Figure 5.4 Diagrams showing the effects of changing viewing angle $\delta\theta$ for a resolution cell of length R. (a) point scatterer has no phase change with viewing angle. (b) has multiple scatterers where the vector sum of the phase will vary with viewing angle in a random way causing decorrelation.

the range to this single scatterer, and the pixel remains coherent. However, if there is a uniform distribution of persistent scatterers in the cell, the scatterers at the edges of the cell have a change in range of $\delta\rho = \frac{R_r}{2}\sin\delta\theta\cos\theta$. When $\delta\rho$ is less than a quarter of the wavelength, the phase shifts at the edge of the resolution cell do not destroy the correlation in the cell. Note that since the path delay is $2\delta\rho$, the phase delay is one half wavelength. It can be shown that the resulting critical baseline is the same as the formula found earlier

$$B_c = \frac{\lambda\rho}{2R_r\cos\theta} = \frac{\lambda\rho}{c\tau}\tan\theta \tag{5.16}$$

5.6 Approximate Phase due to Topography

We can use the approximate Equation 5.9 to calculate the topographic phase as well. The actual radius of the Earth (land), r, is usually greater than the radius of the spheroid r_e. The difference is the geometric elevation. The phase due to the actual topography can be expanded in a Taylor series about r_e

Downloaded from https://www.cambridge.org/core. IP address: 189.217.92.64, on 11 Feb 2026 at 15:51:46, subject to the Cambridge Core terms of use, available at https://www.cambridge.org/core/terms. https://www.cambridge.org/core/product/1F8951EFC610A352837B95E4DAEFBAEB

$$\phi(r) = \phi(r_e) + \left.\frac{\partial \phi}{\partial r}\right|_{r_e} (r - r_e) + \left.\frac{1\partial^2 \phi}{2\partial r^2}\right|_{r_e} (r - r_e)^2 + \cdots \tag{5.17}$$

Using Equations 5.9 and 5.12, we can calculate the first two derivatives. It turns out that the second derivative is about $(r - r_e)/r$ times the first derivative (i.e., 2.7/6 371 for our area), so we only need to keep the first two terms in the series. The first term is Equation 5.13, while the second term is

$$\frac{\partial \phi}{\partial r}(r_e) = \frac{-4\pi r_e}{\lambda \rho b} \frac{B \cos(\theta_e - \alpha)}{\sin \theta_e} \tag{5.18}$$

where θ_e is the look angle to the spheroid (5.12). The mapping of total unwrapped phase into elevation as a function of range is

$$(r - r_e) = \frac{-\lambda \rho b}{4\pi r_e} \frac{\sin \theta_e}{B \cos(\theta_e - \alpha)} (\phi - \phi_e) \tag{5.19}$$

Note that the unwrapped interferogram does not provide the complete phase difference $\phi - \phi_e$, given that there is an unknown constant of integration. While this formula is useful for demonstrating that the magnitude of the topographic phase correction is proportional to the perpendicular baseline, the formula is only an approximation. The more accurate approach used in the GMTSAR code is discussed in Section 5.8.

5.7 Topography from Single-Pass InSAR: SRTM

The Shuttle Radar Topography Mission (SRTM) used a single-pass interferometer with a fixed baseline to generate a near-global topography map of the Earth (60 N to 56 S) (Farr et al., 2007). The space shuttle was equipped with two receive antennas, one in the cargo bay and a second on a 60-m boom extending from the shuttle to form the fixed baseline. The transmit antenna was located in the shuttle bay and radar pulses were recorded by the two antennas after reflecting from the Earth's topography. The main advantage of a single-pass interferometer for topographic mapping is that the atmospheric and ionospheric phase delays cancel in the two SAR acquisitions, so the phase difference mainly reflects the topography. For a flat Earth geometry ($b/r_e = 1$), the sensitivity of the topography T to phase noise is

$$\frac{\partial T}{\partial \phi} = \frac{\lambda \rho \sin \theta_e}{2\pi B \cos(\theta_e - \alpha)}. \tag{5.20}$$

There is a factor of 2 difference from Equation 5.19 because there is only a phase difference from the reflected pulse, so this is a one-way phase difference measurement (Zebker et al., 1994). Inserting the values for the C-band radar at a nominal look angle of 45 degrees and a range to the surface of 330 km shows one fringe of phase corresponds to 108 m of topography. Since the radar was able to achieve

Downloaded from https://www.cambridge.org/core. IP address: 189.217.92.64, on 11 Feb 2026 at 15:51:46, subject to the Cambridge Core terms of use, available at https://www.cambridge.org/core/terms. https://www.cambridge.org/core/product/1F8951EFC610A352837B95E4DAEFBAEB

phase precision of 1/12 of a fringe, the nominal topography accuracy was 9 m. Note that the C-band radar does not reflect from the bare earth but from the canopy of vegetation as well as the tops of buildings. Nevertheless, this provides the optimal topography correction for C-band repeat-pass InSAR although will be suboptimal for L-band where the radar reflects deeper in the canopy or on the bare Earth.

5.8 Exact Phase due to Earth Curvature and Topography

In Sections 5.6 and 5.7, we provided approximate formulas for the phase changes from a curved Earth and local topography for a given perpendicular baseline. Here we derive the exact formulas. We start with the triangle shown in Figure 5.2. The law of cosines provides the relationship between the reference range ρ, the repeat range $\rho + \delta\rho$, the baseline length B, and the baseline orientation relative to the look angle $\theta - \alpha$. We can solve Equation 5.7 for $\delta\rho$

$$\delta\rho = \left[\rho^2 + B^2 - 2\rho B \sin(\theta - \alpha)\right]^{1/2} - \rho \tag{5.21}$$

and convert this to the phase correction $\phi = \frac{4\pi}{\lambda}\delta\rho$. The cosine of the look angle θ is given in Equation 5.12, which is valid for any Earth radius, such as the radius of a topographic reflector. In Chapter 3, we discussed an algorithm for mapping a topographic reflector from longitude, latitude, and height above the ellipsoid to range, azimuth, and topography $T(\rho, a)$ above a local spherical shape for the Earth. Using this information, we can combine the Earth curvature correction and the topographic phase correction into a single correction. The algorithm is:

1. Read a row of data from the reference and repeat SLC files, and assign every pixel in the reference image a range ρ and azimuth a.
2. Using the precise orbital information, compute the radius of the spacecraft orbit for the reference image $b(a)$, the length of the baseline $B(a)$, and the orientation of the baseline $\alpha(a)$.
3. Interpolate the topography to each range pixel and compute the look angle using the following formula from Equation 5.12.

$$\theta = \cos^{-1}\left\{\frac{\left(b^2 + \rho^2 - \left(r_e + T(\rho, a)\right)^2\right)}{2\rho b}\right\} \tag{5.22}$$

4. Using the look angle for each range pixel, calculate the phase correction to be applied to the repeat image using Equation 5.21 and the conversion from range to phase Equation 5.6.

Downloaded from https://www.cambridge.org/core. IP address: 189.217.92.64, on 11 Feb 2026 at 15:51:46, subject to the Cambridge Core terms of use, available at https://www.cambridge.org/core/terms. https://www.cambridge.org/core/product/1F8951EFC610A352837B95E4DAEFBAEB

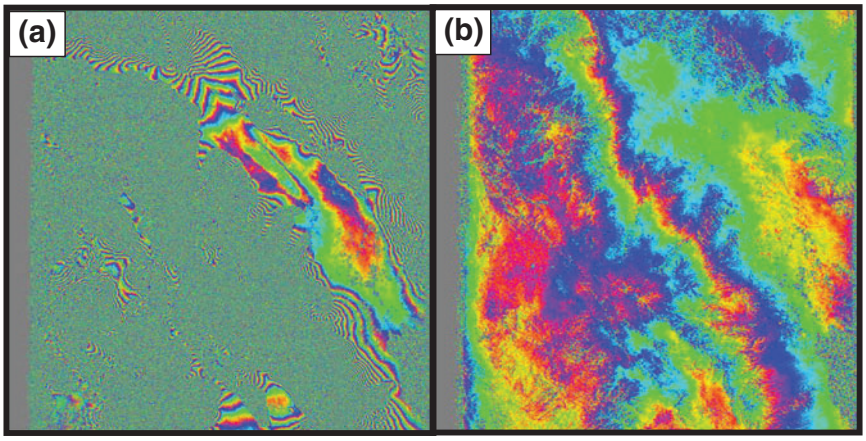

Figure 5.5 (a) A 1.95 km baseline interferogram with no topography correction has 120 fringes that need to be accurately removed. (b) Same interferogram corrected for topography phase using the exact Equations (5.21) and (5.22).

5. Multiply the repeat image by the complex phase and form the interferogram. Note this phase correction should be applied before any multilook averaging or filtering.

$$R(\mathbf{x}) + iI(\mathbf{x}) = C_2 C_1^* e^{i\phi} \tag{5.23}$$

6. Extract the interferometric phase, which is now corrected for both the Earth's curvature and the topographic phase.

$$(\phi_2 - \phi_1) = \tan^{-1}\left(\frac{I}{R}\right) \tag{5.24}$$

An example of a 1.95 km long baseline interferogram that was corrected for topographic phase is shown in Figure 5.5. There is 3 200 m of relief within this interferogram. As a result, there are 120 fringes in the full interferogram (Figure 5.5(a)) that need to be removed. The residual fringes (b) could be due to topography errors but could also be ionospheric or tropospheric delays.

5.9 Geocoding

Interferograms are naturally presented in the radar coordinates, where the x-axis corresponds to the range direction and the y-axis corresponds to the azimuth direction. It is challenging to relate the features in the radar coordinates with features seen in the latitude/longitude coordinates, because the ground features are often flipped, stretched, and rotated in the radar coordinates. Proper interpretation of interferograms requires the last step in the processing called *geocoding*, which transforms images in radar coordinates into geographic coordinates. In Section 3.7,

Downloaded from https://www.cambridge.org/core. IP address: 189.217.92.64, on 11 Feb 2026 at 15:51:46, subject to the Cambridge Core terms of use, available at https://www.cambridge.org/core/terms. https://www.cambridge.org/core/product/1F8951EFC610A352837B95E4DAEFBAEB

Table 5.2 *Lookup table for mapping from geographic to radar coordinates and vice versa.*

range	azimuth	elevation	longtitude	latitude
33484.3362	4554.8018	456.4585	-117.4900	35.7525
33462.4183	4553.8639	461.4579	-117.4891	35.7525
33438.8219	4552.9243	471.4572	-117.4883	35.7525
33415.9137	4551.9859	479.4566	-117.4875	35.7525
33395.6569	4551.0485	479.4560	-117.4866	35.7525
33376.7027	4550.1103	475.4554	-117.4858	35.7525
33356.4499	4549.1728	475.4548	-117.4850	35.7525
33335.8676	4548.2351	476.4543	-117.4841	35.7525
33315.2630	4547.2962	477.4537	-117.4833	35.7525
33294.6845	4546.3585	478.4531	-117.4825	35.7525

we discussed the use of the precise orbital information, along with a digital elevation model, to map between geographic and radar coordinates. We generated a lookup table called **trans.dat** to do the forward transformation. Now, we need to do the inverse transformation using the same table. A sample of the **trans.dat** file is provided in Table 5.2.

The first two columns of the file are the range and azimuth coordinates, column 3 is the height above the spheroid, and the last two columns are the longitude and latitude. The geocoding algorithm has the following steps:

1. Extract columns 1, 2, and 4 and use the GMT *surface* routine to make a grid of longitude versus range and azimuth. Repeat using columns 1, 2, and 5 to make a grid of latitude versus range and azimuth.
2. Extract wrapped phase observations from an interferogram.
3. Use the GMT command *grdtrack* along with the two grids of longitude versus range/azimuth, and latitude versus range/azimuth to create a table of longitude, latitude, and wrapped phase.
4. Establish the output pixel spacing in delta longitude and delta latitude to be 1/4 of the Gaussian filter wavelength to achieve full sampling. The longitude spacing is equal to the latitude spacing divided by the cosine of the latitude.
5. Use the GMT blockmedian routine to take the median value of the longitude, latitude, and wrapped phase in the previously established longitude and latitude bins.
6. Use the GMT command *xyz2grd* to populate the longitude, latitude, and wrapped phase grid. Note, some grid cells may not have entries. The empty locations will have the not-a-number flag. Also note that there is no interpolation of the regridded products. This is important for the wrapped phase, because there should be exact 2π discontinuities at the phase wrap boundaries and interpolation would blur the phase wrap.

Downloaded from https://www.cambridge.org/core. IP address: 189.217.92.64, on 11 Feb 2026 at 15:51:46, subject to the Cambridge Core terms of use, available at https://www.cambridge.org/core/terms. https://www.cambridge.org/core/product/1F8951EFC610A352837B95E4DAEFBAEB

5.10 Geocoded SLC InSAR Processing Strategy

In this chapter, we reviewed the key steps in the standard InSAR processing routines (Figure 5.6(a)): raw radar data from two satellite passes are processed into focused SAR images, and then delivered to end users. A user can use GMTSAR to coregister the radar images, and then cross-multiply the results to form an interferogram. The phase components due to Earth curvature and topography are estimated and removed based on the satellite orbit information and an existing DEM map. The geocoding step can be applied either on each individual flattened interferogram or the final surface deformation solutions derived from a stack of flattened interferograms. Zheng and Zebker (2017); Zebker (2017) proposed a geocoded SLC processing strategy (Figure 5.6(b)) that can be used to generate user-friendly radar image products for InSAR analysis:

1. Create a zero-Dopper SLC image for each scene using its orbit solutions.
2. Extract a DEM covering the region with desired postings (~SAR image resolution).

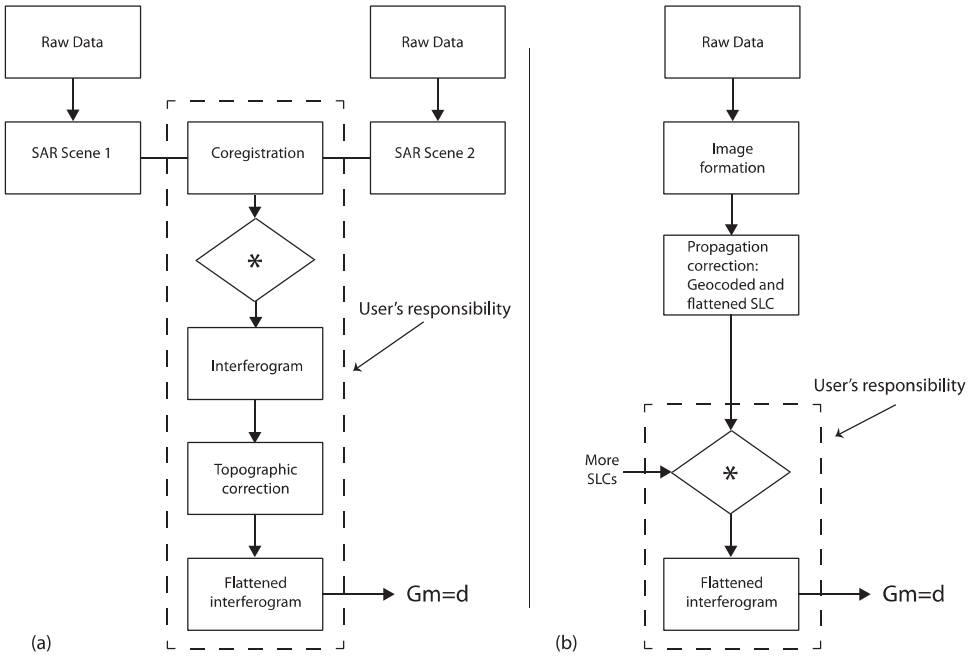

Figure 5.6 (a) Standard InSAR processing work flow that is commonly adopted by many InSAR processors. (b) Geocoded SLC InSAR processing work flow. Originally from Zebker (2017). Reprinted with permission from *IEEE Geoscience and Remote Sensing Letters*.

Downloaded from https://www.cambridge.org/core. IP address: 189.217.92.64, on 11 Feb 2026 at 15:51:46, subject to the Cambridge Core terms of use, available at https://www.cambridge.org/core/terms. https://www.cambridge.org/core/product/1F8951EFC610A352837B95E4DAEFBAEB

3. For each pixel in the DEM, find the corresponding zero-Doppler satellite observation location along the orbit.
4. Resample the SLC image to that DEM pixel, applying a phase correlation for the propagation distance from the sensor zero-Doppler point to the elevated surface point.

Compared to standard InSAR processing strategies, the topographic correction and geocoding steps are moved prior to the interferogram formation. Using this new processing architecture, interferograms can be generated with relatively low computational cost by simple cross-multiplication of pairs of these processed SLC radar images, which are automatically topography-corrected and geocoded. Depending on the desired spatial resolution, interferograms might be multi-looked to further reduce the overall storage needs and phase noise.

5.11 Problems

1. Develop a formula similar to Equation (5.12) for the incidence angle as a function of local Earth radius r_e, the range to the sphere ρ and the height of the spacecraft above the center of the Earth b.
2. Derive Equation (5.13). What happens when the change in phase with increasing range exceeds 2π radians per range resolution cell?
3. Give two reasons why the critical baseline for ALOS is more than 10 times longer than for ERS.
4. What happens to the phase of an interferogram in areas where the slope of the topography facing the radar exceeds the incidence angle of the radar?
5. Derive Equation (5.19). What is the correct zero level for the topography in this equation?

Downloaded from https://www.cambridge.org/core. IP address: 189.217.92.64, on 11 Feb 2026 at 15:51:46, subject to the Cambridge Core terms of use, available at https://www.cambridge.org/core/terms. https://www.cambridge.org/core/product/1F8951EFC610A352837B95E4DAEFBAEB

6

Coherence, Filtering, and Phase Gradient

6.1 Need for Filtering an Interferogram

In Chapter 5, we discussed how an interferogram is constructed from two geometrically aligned single look complex (SLC) images $C_1(\mathbf{x})$ and $C_2(\mathbf{x})$ where $\mathbf{x} = (r, a)$ is the position vector consisting of range and azimuth. The complex interferogram is

$$C_2 C_1^* = A_1 A_2 e^{i(\phi_2 - \phi_1)} = R(\mathbf{x}) + iI(\mathbf{x}). \tag{6.1}$$

The phase of the interferogram is

$$(\phi_2 - \phi_1) = \tan^{-1}\left(\frac{I}{R}\right). \tag{6.2}$$

This operation is performed on the full-resolution SLC images with rather large sizes. For example, a 100 km by 100 km raw interferogram with 5 m by 5 m resolution has 20 000 by 20 000 complex numbers. With 8-byte storage of each complex number, the raw interferogram size is 32 Gbytes. Additionally, each raw SLC image has a large amount of speckle noise depending on the radar characteristic, and the noise in the phase of the interferogram can be rather large as well (Curlander and McDonough, 1991). Other sources of phase noise include baseline decorrelation, volume decorrelation, temporal decorrelation, and co-registration errors between the reference and repeat images (Zebker and Villasenor, 1992; Simons and Rosen, 2007; Xu et al., 2020).

In this chapter we first discuss how the *coherence* function is calculated, and how it is used to assess phase noise. We then discuss three common *filtering* approaches for reducing the phase noise while retaining the desired small-spatial phase signal. Even with filtering, quantitative interpretation of the wrapped interferometric phase is challenging. We next review the *phase gradient*, which is constructed from the real and imaginary parts of the interferogram for deriving small-scale deformation (e.g., fractures) of the Earth's surface. In Chapter 7, we

Downloaded from https://www.cambridge.org/core. IP address: 189.217.92.64, on 11 Feb 2026 at 15:51:46, subject to the Cambridge Core terms of use, available at https://www.cambridge.org/core/terms. https://www.cambridge.org/core/product/1F8951EFC610A352837B95E4DAEFBAEB

explain the *unwrapped phase*, which can be converted to line-of-sight deformation with a factor of $\frac{-\lambda}{4\pi}$. Phase unwrapping is difficult when severe decorrelation noise is present, and the phase observations are discontinuous in space. There are dozens of approaches to phase unwrapping; we will focus on two – the branch-cut technique (Goldstein et al., 1988) and the statistical cost network flow technique (SNAPHU) (Chen and Zebker, 2000).

6.2 Coherence and Filtering Techniques

The correlation or coherence is a measure of the repeatability of the reference and repeat SLC images. As described by Zebker and Villasenor (1992), the amount of decorrelation between the two images depends on radar characteristics, geometric mis-alignment, and temporal decorrelation. Correlation is commonly measured by calculating the mean and standard deviation of the change in complex reflectivity in a small patch taken from the reference radar image $C_1(\mathbf{x})$ and the repeat radar image $C_2(\mathbf{x})$. We assume they share a common signal $C(\mathbf{x})$ and each has an uncorrelated noise $n(\mathbf{x})$

$$\begin{aligned} C_1(\mathbf{x}) &= C(\mathbf{x}) + n_1(\mathbf{x}) \\ C_2(\mathbf{x}) &= C(\mathbf{x}) + n_2(\mathbf{x}) \end{aligned} . \tag{6.3}$$

The complex correlation between the two images is given by Bendat and Piersol (2011)

$$\rho = \frac{\left\langle C_1 C_2^* \right\rangle}{\sqrt{\left\langle C_1 C_1^* \right\rangle \left\langle C_2 C_2^* \right\rangle}} \tag{6.4}$$

where $\langle\rangle$ is a filtering operator; real and imaginary parts are filtered separately. Let $f(\mathbf{x})$ be any function of $\mathbf{x} = (r, a)$. Let $g(\mathbf{x})$ be a 2-D filter. Two examples are: (1) simple boxcar average over a small patch and (2) a Gaussian-shaped filter. The filtering operator is given by the convolution integral

$$\langle f(\mathbf{x}) \rangle = \int \int f(\mathbf{x}_o)\, g(\mathbf{x} - \mathbf{x}_o)\, d^2\mathbf{x}_o \tag{6.5}$$

where g is normalized so $\int \int g(\mathbf{x})\, d^2\mathbf{x} = 1$. Since the SLC images have a discrete sampling in range and azimuth, we replace the integral with a summation over a patch. In the case of the simple averaging filter, this is called a *multilook* filter and the number of looks N_L is the number of points in the patch. In the case of the Gaussian filter (unnormalized), the number of looks is the number of points in the patch times the weight of each point. Assuming random and uncorrelated noise, these filters reduce the noise by approximately the square root of the number of looks. If the interferogram has no noise, $C_1 = C_2 = C$ and the complex correlation

Downloaded from https://www.cambridge.org/core. IP address: 189.217.92.64, on 11 Feb 2026 at 15:51:46, subject to the Cambridge Core terms of use, available at https://www.cambridge.org/core/terms. https://www.cambridge.org/core/product/1F8951EFC610A352837B95E4DAEFBAEB

is 1. For the case where the noise dominates the signal, and N_L is large, the complex correlation approaches zero. The coherence function, normally used in InSAR analysis, is the absolute value of the complex correlation $\gamma = |\rho|$.

A multilook or simple boxcar average is an appropriate type of filter when the phase of the interferogram is constant over the patch but may be ineffective in cases of high phase gradient. One of the problems with a simple boxcar multilook filter is that the filter response in the wavenumber domain has prominent sinc-function sidelobes so the short wavelength noise is not well suppressed. If the filtered interferogram is down sampled at the length of the box, then the noise in the sidelobe of the filter will be folded into the lower wavenumbers, thus increasing the noise at the longer wavelength. This issue is less of a problem with central-weighted filters. One of the simplest well-behaved filters is a 2-D Gaussian function given by

$$g(\mathbf{x}) = e^{\frac{-|\mathbf{x}|^2}{2\sigma^2}} \tag{6.6}$$

where $\mathbf{x} = (x, y)$ is the distance in meters in the ground range and azimuth directions and σ is the filter width parameter. By taking the Fourier transform of this Gaussian function, the 0.5 gain of the filter occurs at a wavelength of 5.3σ. In the case of Sentinel-1 Interferometric Wide (IW) data, a filter wavelength of about 200 m is commonly used. To avoid aliasing of the signal, the filtered output can be safely downsampled at 1/4 of this wavelength (50 m) in both dimensions. For higher resolution processing, one may reduce the filter wavelength to perhaps 60 m so the output sampling will need to be ~15 m.

The coherence depends on the product of four factors (Zebker and Villasenor, 1992)

$$\gamma = \gamma_N \gamma_B \gamma_D \gamma_T \tag{6.7}$$

where is γ_N is the combined radar noise, γ_B is the coherence due to non zero interferometric baseline, γ_D is the coherence due to less than perfect overlap between the Doppler spectra of the reference and repeat images associated with inaccurate pointing of the radar instrument in the along-track direction, and γ_T is the temporal coherence due to changes in the complex reflectivity of the surface. To quantify the radar noise, we assume that the noise and signal are uncorrelated, so coherence is

$$\gamma_N = \frac{|C|^2}{|C|^2 + |n|^2} = \frac{1}{1 + |n|^2/|C|^2} = \frac{1}{1 + SNR^{-1}} \tag{6.8}$$

where *SNR* is the signal-to-noise ratio. The baseline coherence is given by Zebker and Villasenor (1992)

$$\gamma_B = 1 - \frac{B_\perp}{B_c} \tag{6.9}$$

Downloaded from https://www.cambridge.org/core. IP address: 189.217.92.64, on 11 Feb 2026 at 15:51:46, subject to the Cambridge Core terms of use, available at https://www.cambridge.org/core/terms. https://www.cambridge.org/core/product/1F8951EFC610A352837B95E4DAEFBAEB

where the critical baseline is defined in Equation 5.15. The Doppler coherence is

$$\gamma_D = 1 - \frac{\left|f_{DC}^1 - f_{DC}^2\right|}{\text{PRF}} \tag{6.10}$$

where $f_{DC}^{1,2}$ are the Doppler centroids of the reference and repeat images and the PRF is the pulse repetition frequency; these parameters were discussed in Chapter 4. Note if the difference in the Doppler centroids exceeds the PRF, then the coherence is zero.

Finally, the temporal coherence depends on changes in the reflectivity of the surface between the reference and repeat images, and there are no simple analytic formulas to predict this type of decorrelation. Temporal decorrelation depends on environmental factors such as vegetation growth, glacial motion, freezing and thawing, and soil moisture effects. In general, moist vegetated areas decorrelate faster than dry nonvegetated areas. There is usually complete decorrelation between times when the surface temperature has gone through the freezing point between the reference and repeat radar images. In addition, temporal decorrelation is greater for shorter wavelength interferograms (e.g., X-band 31 mm) over vegetated areas, because the radar waves reflect from the leafy surfaces, which are constantly moving and growing. In contrast, temporal decorrelation is less for longer wavelength interferograms (e.g., L-band 240 mm), because the radar waves reflect from the more permanent branches, trunks, and the ground (Rosen et al., 1996).

An example of X-, C-, and L-band interferograms over the Kilauea volcano area of Hawaii is shown in Figure 6.1. This region has a range of surface types, including ocean to the south, fresh lava flows where coherence is high and a range of vegetation types to the northeast. We can observe that: (1) the X-band coherence is high on the fresh lava flows and very low over the vegetated areas; (2) the C-band coherence is high over the fresh lava flows and relatively low in the vegetated areas; (3) the L-band coherence is high over the fresh lava flows and moderate over the vegetated areas. Because each phase cycle of 2π corresponds to a LOS range difference of $\frac{\lambda}{2}$, there are more fringes in interferograms with shorter wavelengths (X-band, 31 mm; C-band, 56 mm; L-band, 236 mm).

Decorrelation increases the noise in the phase of the interferogram. Assuming uniform phase in a patch containing N_L-independent looks, the approximate uncertainty in the phase recovery is (Rodriguez and Martin, 1992).

$$\sigma_\phi^2 = \frac{1 - \gamma^2}{2N_L\gamma^2}. \tag{6.11}$$

This formula suggests that one should increase the number of looks (i.e., averaging area) indefinitely to improve the phase recovery. However, this analysis assumes

Downloaded from https://www.cambridge.org/core. IP address: 189.217.92.64, on 11 Feb 2026 at 15:51:46, subject to the Cambridge Core terms of use, available at https://www.cambridge.org/core/terms. https://www.cambridge.org/core/product/1F8951EFC610A352837B95E4DAEFBAEB

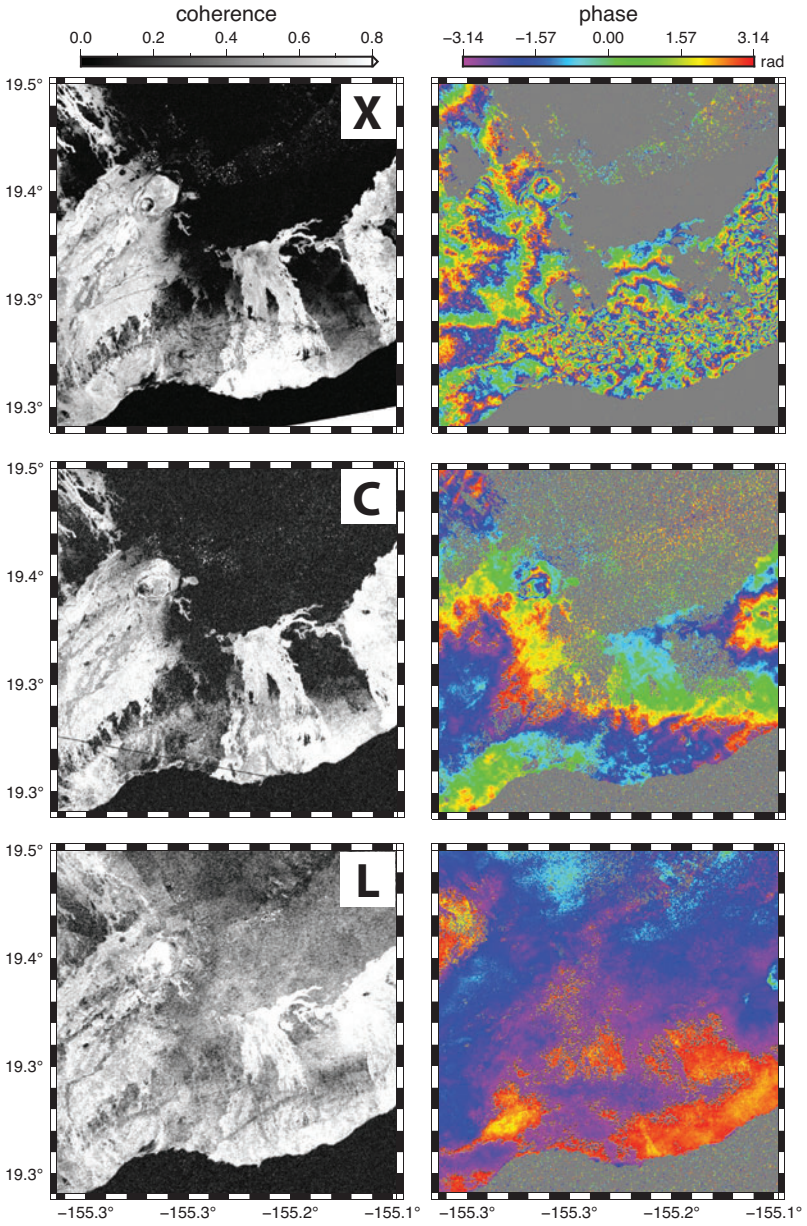

Figure 6.1 Coherence and phase for interferograms at X-, C-, and L-band over the Kilauea volcano area of Hawaii. The X-band case is from TerraSAR-X with a time interval of 44 days (2017364-2018043). The C-band case is from Sentinel-1 with a time interval of 48 days (2019005-2019053). The L-band case is from ALOS-1 with a time interval of 46 days (2009016-2009062). The phase fringes are caused by atmospheric delay with a larger number of fringes for the shorter wavelength X-band data.

Downloaded from https://www.cambridge.org/core. IP address: 189.217.92.64, on 11 Feb 2026 at 15:51:46, subject to the Cambridge Core terms of use, available at https://www.cambridge.org/core/terms. https://www.cambridge.org/core/product/1F8951EFC610A352837B95E4DAEFBAEB

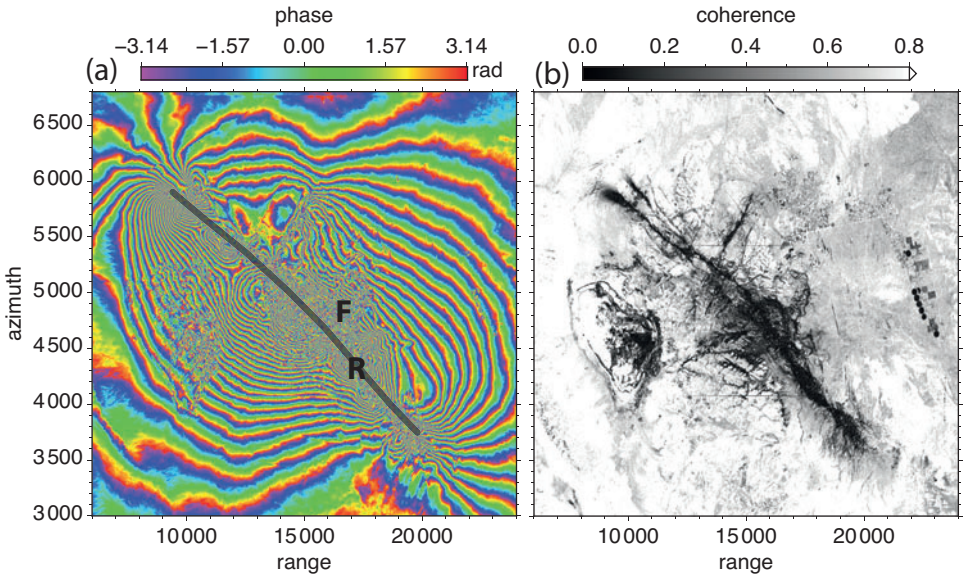

Figure 6.2 (a) Interferogram showing displacement due to the Ridgecrest earthquakes in radar coordinates. One fringe is 28 mm of ground deformation along the radar line-of-sight direction. **R** marks the main surface rupture and **F** marks the area where fringe rate exceeds 2π per pixel resulting in decorrelation. (b) Coherence for the interferogram shows mostly high coherence away from the main ruptures. The area of decorrelation to the left of the ruptures is caused by liquefaction in the Searles Lake bed. The small round decorrelation on the right side of the image is due to farms.

the phase is constant over the averaging area. Therefore, the number of independent looks available for averaging depends on the spatial variations in the phase.

An example of a C-band Sentinel-1 interferogram spanning the 2019 M6.4 and M7.2 Ridgecrest earthquakes is shown in Figure 6.2. The phase (Figure 6.2(a)) has many fringes related to the surface deformation from the earthquakes. Each color cycle represents 2π of range increase corresponding to 28 mm of surface deformation away from the radar. The coherence (Figure 6.2(b)) is relatively high over most of the image because the interferometric baseline was much shorter than the critical baseline and the time interval between the reference and repeat images is only 12 days. In addition, this area of the Mojave Desert was extremely dry during the summer months when the earthquakes occurred and is sparsely vegetated. There are a few areas of lower coherence; areas near the rupture zones suffered extreme ground shaking during the earthquake, which randomly displaced the surface scatterers causing decorrelation. There are other smaller areas of decorrelation away from the fault due to changes in vegetation from farming activities.

Downloaded from https://www.cambridge.org/core. IP address: 189.217.92.64, on 11 Feb 2026 at 15:51:46, subject to the Cambridge Core terms of use, available at https://www.cambridge.org/core/terms. https://www.cambridge.org/core/product/1F8951EFC610A352837B95E4DAEFBAEB

6.3 Goldstein Frequency Domain Filter

One of the most widely used, and highly effective, secondary filters used in the InSAR community is the Goldstein frequency domain filter initially developed by Goldstein and Werner (1998) and refined by Baran et al. (2003). We call this a secondary filter because it uses a coherence grid that is derived from the initial filtering of the full-resolution interferogram.

The basic assumption of the Goldstein filter is that the interferometric phase is locally stationary and homogeneous, and most of the power in the phase is limited to a narrow band of wavenumbers. The filter is applied in small overlapping patches of, say, 64 by 64 pixels. Consider the Fourier transform of the complex interferogram in a small patch given by $Z(k_r, k_a)$ where k_r, k_a are the wavenumbers in the range and azimuth directions, respectively. The modified Goldstein filter is (Baran et al., 2003)

$$H(k_r, k_a) = S\{|Z(k_r, k_a)|\}^{1-\bar{\gamma}} \cdot Z(k_r, k_a) \tag{6.12}$$

where $S\{\}$ is a smoothing operator, $\bar{\gamma}$ is the average of the coherence over the patch, and $H(k_r, k_a)$ is the smoothed interferogram. The filtered interferogram is recovered from the inverse Fourier transform of $H(k_r, k_a)$ then the phase is calculated using Equation 6.2. Note that when the mean coherence is 1 (i.e., $S = 1$), so there is no filtering; when the coherence approaches zero, the filtering can be extreme. An example of the Ridgecrest interferogram in the vicinity of the rupture before and after the application of the Goldstein filter is shown in Figure 6.3.

6.4 Phase Gradient

When the correlation between the reference and repeat images is high, as in this case of the Ridgecrest earthquakes, the *phase gradient* approach is an effective way to highlight fractures with surface displacements as small as a few millimeters. Instead of computing the phase gradient directly from the phase (Equation 6.2 and Figure 6.2), which may contain many 2π discontinuities, one can use the chain rule of differentiation to develop a formula for the phase gradient directly from $R(\mathbf{x})$ and $I(\mathbf{x})$ (Sandwell and Price, 1998). The result is

$$\nabla\phi(\mathbf{x}) = \frac{R\nabla I - I\nabla R}{R^2 + I^2} \tag{6.13}$$

where the gradient operator is $\nabla = \left(\frac{\partial}{\partial r}, \frac{\partial}{\partial a}\right)$. A numerical derivative filter must be designed to avoid aliasing short-wavelength noise at the Nyquist wavenumber into

Downloaded from https://www.cambridge.org/core. IP address: 189.217.92.64, on 11 Feb 2026 at 15:51:46, subject to the Cambridge Core terms of use, available at https://www.cambridge.org/core/terms. https://www.cambridge.org/core/product/1F8951EFC610A352837B95E4DAEFBAEB

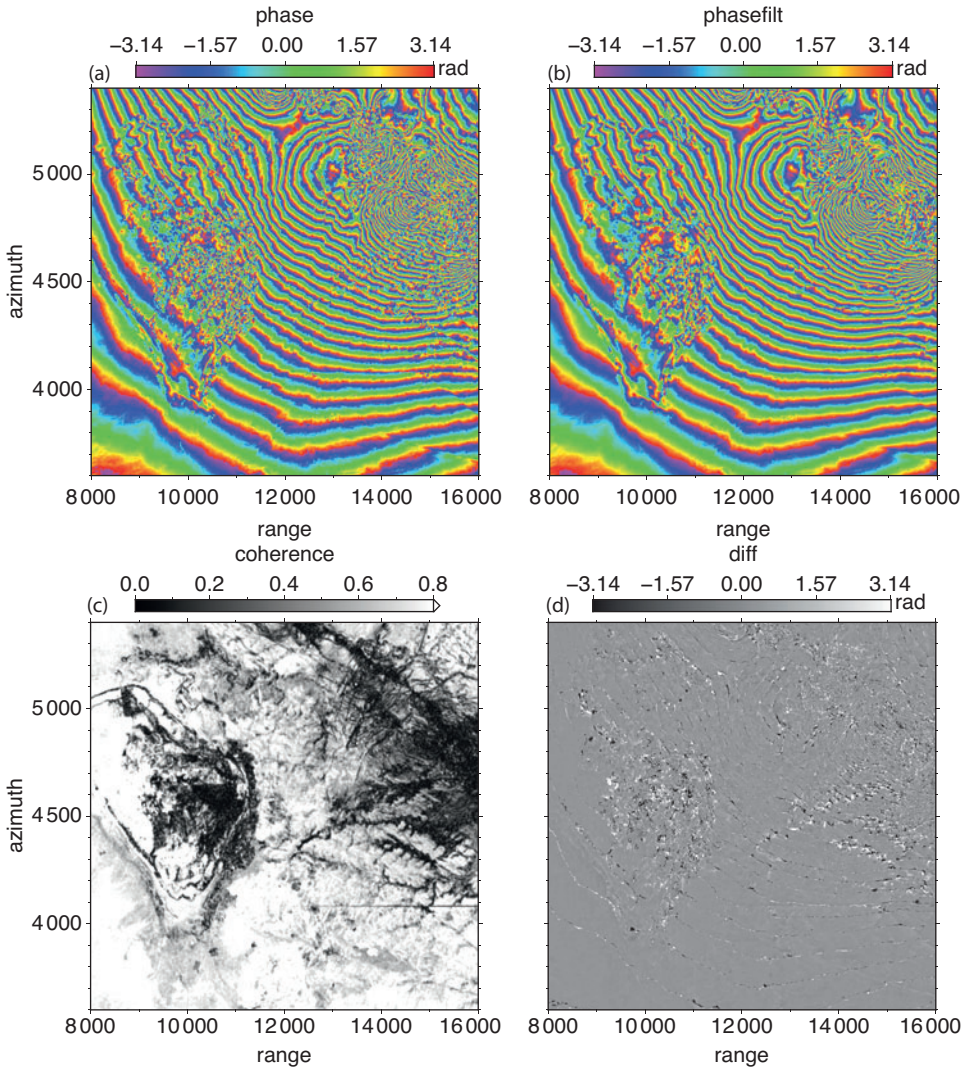

Figure 6.3 (a) Phase of original interferogram with a Gaussian filter (0.5 gain at a wavelength of 200 m). (b) Phase of interferogram after Goldstein filtering. (c) Coherence of interferogram. (d) Difference between the original phase and Goldstein-filtered phase has very small differences, where coherence is high, and large differences where coherence is low.

longer wavelengths. For the case of the Sentinel-1 images of the Ridgecrest earthquakes, a central difference filter was combined with a low-pass Gaussian filter having 0.5 gain at 30 m half-wavelength. A major advantage of the phase gradient approach is that phase gradients can be stacked to reduce noise without phase

Downloaded from https://www.cambridge.org/core. IP address: 189.217.92.64, on 11 Feb 2026 at 15:51:46, subject to the Cambridge Core terms of use, available at https://www.cambridge.org/core/terms. https://www.cambridge.org/core/product/1F8951EFC610A352837B95E4DAEFBAEB

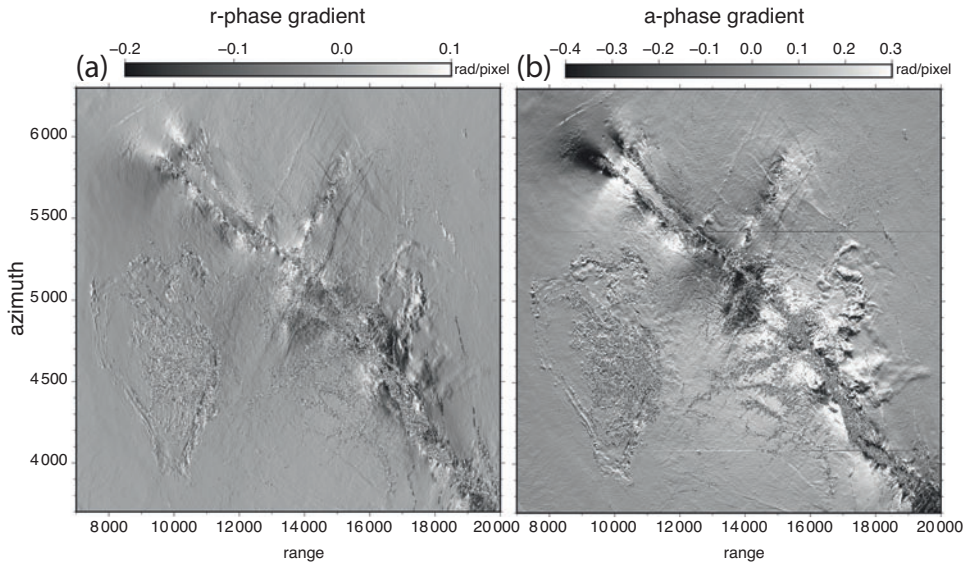

Figure 6.4 (a) Phase gradient with respect to range shows surface fractures and areas of high displacement gradient or strain. (b) Phase gradient in the azimuth direction also shows fractures and areas of high strain. (The two horizontal bands are artifacts caused by the bursts of the Sentinel-1 TOPS radar scans as discussed in Section 8.5.)

unwrapping. Images of the range and azimuth components of the phase gradient are shown in Figure 6.4.

Figure 6.5 shows the interferometric phase (Figure 6.2) and the corresponding azimuth phase gradient in geographic coordinates. It is much easier to interpret geocoded InSAR observations since it is oriented properly and features such as fault traces and the earthquake focal mechanisms can be added. The azimuthal phase gradient is computed from the real and imaginary components of the interferogram (Equation 6.13). Here the signal-to-noise ratio is higher than the phase gradient shown in radar coordinates (Figure 6.4), because four phase gradient images were averaged. Now one can see hundreds of small fractures that are not apparent in the phase map (Figure 6.2). Note that both images are still a qualitative measure of the earthquake displacement. We need to unwrap the phase and convert to line of sight (LOS) vector displacement to provide a quantitative measure of the rupture. The methods of unwrapping the phase and converting to LOS displacement are described in Chapter 7. LOS displacement can also be averaged and combined with more accurate 3-D vector displacements from GNSS, as described in Chapter 10.

Downloaded from https://www.cambridge.org/core. IP address: 189.217.92.64, on 11 Feb 2026 at 15:51:46, subject to the Cambridge Core terms of use, available at https://www.cambridge.org/core/terms. https://www.cambridge.org/core/product/1F8951EFC610A352837B95E4DAEFBAEB

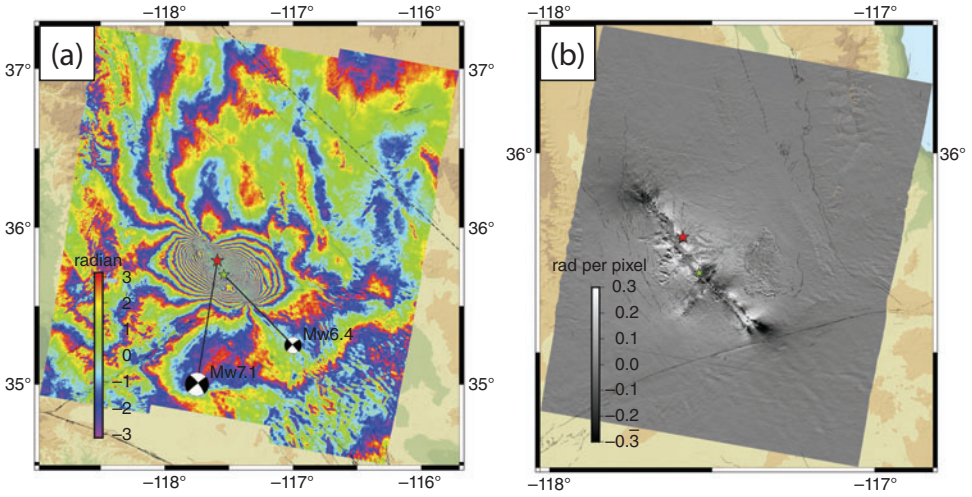

Figure 6.5 (a) An interferogram showing displacement due to the Ridgecrest earthquakes in geographic coordinates. One fringe is 28 mm of ground deformation away from the radar. (b) Azimuthal phase gradient from a stack of four interferograms, computed using Equation 6.13, reveals hundreds of small fractures nearby the main ruptures.

6.5 Problems

1. Describe the four main causes of decorrelation of an interferogram.
2. Make an interferogram from two SLC images using Matlab or Python. Online you can find two binary SAR image files, *.SLC, and 2 ascii header files, *.PRM (download at http://topex.ucsd.edu/rs/lab8). The site also contains some Matlab code for reading the data (lab8start.m). This is an ERS-1 to ERS-2 tandem pair from the Salton Sea, with a perpendicular baseline of 58 m. The *.PRM files have been included for reference only, which is not required for the rest of the problem. This lab illustrates SAR interferometry. First, look at the phase of the reference image. It looks like random noise. Then look at the phase of the repeat image. It also looks like noise. Finally examine the phase difference. This shows interferometric fringes across the image related to the curvature of the Earth.
   (a) Make the interferogram and filter it to make the best-looking phase map. Shall we apply the filter before or after interferogram formation? Shall we filter the real and imaginary components or the phases?
   (b) Estimate and remove the phase ramp across the image.
   (c) Try to unwrap the phase using Matlab or Python.

Downloaded from https://www.cambridge.org/core. IP address: 189.217.92.64, on 11 Feb 2026 at 15:51:46, subject to the Cambridge Core terms of use, available at https://www.cambridge.org/core/terms. https://www.cambridge.org/core/product/1F8951EFC610A352837B95E4DAEFBAEB

3. Suppose an interferogram of an old lava flow has a high coherence of 0.8 due to its lack of vegetation. Then lava flows over the old surface. What is the coherence between reference and repeat images that span the time of the new lava flow?
4. What is the difference between a multilook average and a Gaussian filter? How can we compute the effective number of looks for a Gaussian filter?
5. Derive the formula for computing the phase gradient from the real and imaginary images of an interferogram Equation 6.13 starting from the formula for the phase of an interferogram Equation 6.2.

Downloaded from https://www.cambridge.org/core. IP address: 189.217.92.64, on 11 Feb 2026 at 15:51:46, subject to the Cambridge Core terms of use, available at https://www.cambridge.org/core/terms. https://www.cambridge.org/core/product/1F8951EFC610A352837B95E4DAEFBAEB

7

Phase Unwrapping

7.1 Basic Concepts

In Chapters 5 and 6, we discussed the construction and filtering of a phase-wrapped interferogram derived from two geometrically aligned single look complex images. An example is shown in Figure 6.2 and repeated here as Figure 7.1. Each color cycle, or fringe, represents a phase change of 2π. This can be converted to a line of sight (LOS) distance change as

$$d_{LOS} = -\phi \frac{\lambda}{4\pi} \tag{7.1}$$

where ϕ is the phase change given in Equation 6.2 and λ is the wavelength of the radar (Table 7.1). Here, the LOS direction is defined as the direction of the ground toward the radar, so a minus sign is needed. In this case of a Sentinel-1 interferogram having a wavelength of 56 mm, one interferometric fringe represents –28 mm of LOS deformation.

The wrapped interferogram is colorful and shows the areas around the fault having the largest deformation, but we need to count, or unwrap, the fringes to determine the LOS deformation difference between any two points in the image. For example, we may want to know the surface rupture offset between two points **a** and **b** on either side of the fault shown in Figure 7.1 (a). One could manually count the number of fringes along the path shown by the black curve, but a computer can do this much faster and perhaps more accurately.

In this chapter we discuss the theory and algorithms used to unwrap the phase to produce a map of LOS deformation. It is often assumed that the unwrapped phase is a smooth function, analogous to an analytic function in calculus. In theory, converting the wrapped phase to the unwrapped phase is simple. All we need to do is add multiples of 2π to selected pixels to ensure that the differences between adjacent pixels are less than $|\pi|$. For high-quality data, this process can be automated

Downloaded from https://www.cambridge.org/core. IP address: 189.217.92.64, on 11 Feb 2026 at 15:51:46, subject to the Cambridge Core terms of use, available at https://www.cambridge.org/core/terms. https://www.cambridge.org/core/product/1F8951EFC610A352837B95E4DAEFBAEB

Table 7.1 *Radar wavelength for commonly used satellites.*

Satellite	Wavelength (λ)	Band
Sentinel-1, ERS, Envisat	56 mm	C
ALOS-1/2	236 mm	L
TerraSAR-X	31 mm	X
NISAR	93 mm and 240 mm	S and L

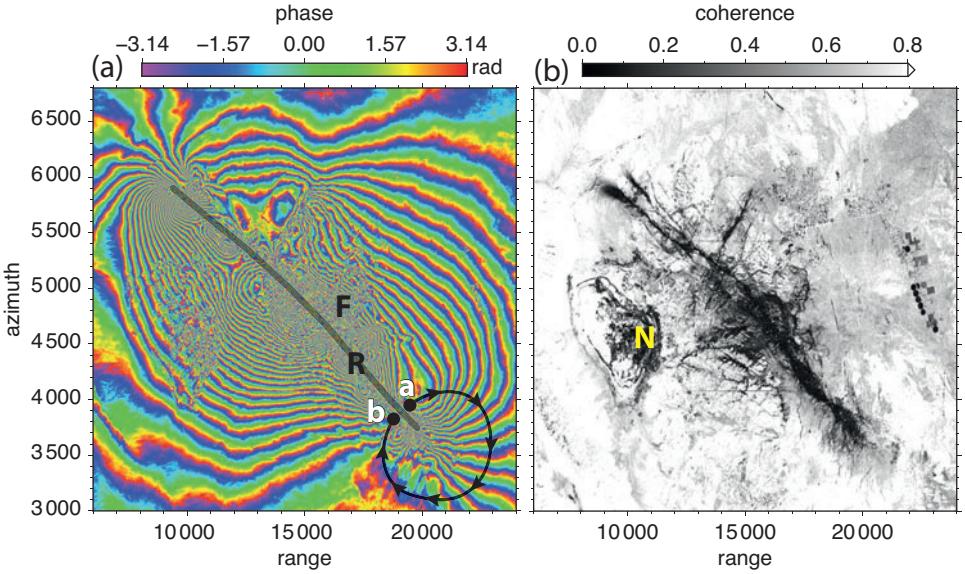

Figure 7.1 (a) Interferogram between July 4 and July 16, 2019, showing displacement due to the July 5, Ridgecrest earthquakes in radar coordinates. One fringe is 28 mm of ground deformation. Label **F** marks an area where the fringes are aliased because the rate exceeds 2π per pixel. Label **R** marks the fault rupture where the phase is discontinuous. One could count the number of fringes along the path from **a** to **b** as a measure of the offset of the surface rupture. (b) Coherence for the interferogram shows mostly high coherence away from the main ruptures. The area of low correlation along the main rupture zones and to the left of the ruptures with label **N** causes phase noise making unique unwrapping challenging.

easily (e.g., Itoh (1982)). However, for typical 2D InSAR data, this simple approach usually yields poor results because of five confounding effects:

1. phase noise due to areas of low coherence between the reference and repeat images (**N** in Figure 7.1 (b));
2. spatial aliasing in areas where the separation between fringes is smaller than the range or azimuth resolution of the filtered radar image (50 meters in this example) (**F** in Figure 7.1 (a));

Downloaded from https://www.cambridge.org/core. IP address: 189.217.92.64, on 11 Feb 2026 at 15:51:46, subject to the Cambridge Core terms of use, available at https://www.cambridge.org/core/terms. https://www.cambridge.org/core/product/1F8951EFC610A352837B95E4DAEFBAEB

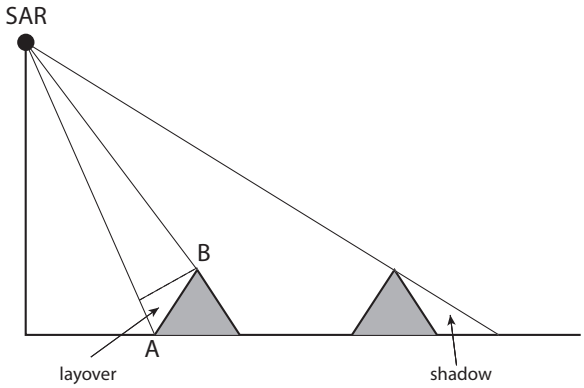

Figure 7.2 (a) Layover occurs when the range to the top of a mountain **B** is less than the range to the base of the mountain **A**; this produces discontinuous phase in an interferogram. (b) A shadow occurs when there is no radar energy reflected from the ground on the far side of the mountain; this also produces discontinuous phase in an interferogram.

3. a discontinuity in the ground displacement due to the surface rupture (**R** in Figure 7.1 (a));
4. a region of *layover* where the slope of the topography exceeds the incidence angle of the radar. In the case of Sentinel-1, the incidence angle varies from about 20° in the near range to 60° in the far range (Figure 7.2). Suppose there is a mountain having a 30° slope facing the direction of the radar in the near range of the image where the incidence angle is 20°, then the range to the top of the mountain is less than the range to the bottom of the mountain so the phase will be discontinuous;
5. similarly, if the backside of the mountain, facing away from the radar, is steeper than the incidence angle, then there will be a slope that is not illuminated by the radar (*shadow*), also resulting in discontinuous phase (Figure 7.2).

Before going into the phase unwrapping algorithms, it is instructive to review the properties of analytic functions. Let's assume we have a perfect wrapped interferogram with none of the five confounding effects discussed earlier and we want to unwrap the phase. After unwrapping the phase, it will be an analytic function of two variables x-range and y-azimuth $\mathbf{x} = (x, y)$. Consider the integration of the gradient of the phase around any closed path C containing area A. Assuming the phase is continuous, and has continuous derivatives, this closed-path integral will be zero.

$$\oint_C \nabla\phi \cdot d\mathbf{x} = 0 \tag{7.2}$$

Downloaded from https://www.cambridge.org/core. IP address: 189.217.92.64, on 11 Feb 2026 at 15:51:46, subject to the Cambridge Core terms of use, available at https://www.cambridge.org/core/terms. https://www.cambridge.org/core/product/1F8951EFC610A352837B95E4DAEFBAEB

Also, by Green's theorem, we have the following relationship relating the path integral of the phase gradient to the area integral of the curl of the phase gradient (Ghiglia and Pritt, 1998)

$$\oint_C \nabla\phi \cdot d\mathbf{x} = \int \int_A \left(\frac{\partial^2 \phi}{\partial x \partial y} - \frac{\partial^2 \phi}{\partial y \partial x} \right) dxdy. \tag{7.3}$$

We can shrink this area down to the resolution size of the interferogram and compute the integrand on the right side of Equation 7.3. In theory this should be zero. If it is significantly different from zero, then the path integral around that point is not zero. Goldstein et al. (1988) call this point a *residue* as an analogy to a residue from the integration of a function around a pole in the complex plane. The residue reflects a phase discontinuity of $N2\pi$ where N defines the integer unwrapping error.

We have performed these derivatives in Equation 7.3 using the phase gradients of the Sentinel-1 data (Figure 7.3 (a,b)) for the Ridgecrest earthquake and arrive at the residue maps shown in Figure 7.3 (c–f). Because of phase noise and other effects, the residue is never exactly zero. However, this analysis clearly reveals large residues, both positive and negative. For example, there is a concentration of residues along areas of surface fracture (Figure 7.3 (e)). Most of the phase unwrapping algorithms perform an analysis to first identify the residues and then avoid the residue areas during phase unwrapping.

A wide variety of algorithms have been developed to address these issues. The algorithms fall into two main categories: global and local (Ghiglia and Pritt, 1998). Local algorithms begin at a single pixel and expand outward along paths that cover the entire image, while global algorithms attempt to find an approximate solution that fits all pixels simultaneously (Ghiglia and Pritt, 1998). We first discuss a global algorithm that uses a Fourier transform approach for phase unwrapping. This and the other global methods, more completely discussed in Ghiglia and Pritt (1998), are mathematically elegant and sometimes computationally efficient, but they suffer from long-wavelength unwrapping errors caused by residues. The local algorithms are more accurate and have the special property that when the unwrapped phase is re-wrapped, the result matches the starting wrapped phase so they simply add $N2\pi$ to each pixel; these algorithms seek the integer phase ambiguity that minimizes some objective function, such as minimizing the phase gradient. We discuss the Goldstein et al. (1988) residue-cut algorithm and then the more widely used Statistical-Cost, Network-Flow Algorithm for Phase Unwrapping (SNAPHU) (Chen and Zebker, 2002). The notes later on the Goldstein and SNAPHU algorithms are derived from the excellent papers by Chen and Zebker (2000, 2001).

Downloaded from https://www.cambridge.org/core. IP address: 189.217.92.64, on 11 Feb 2026 at 15:51:46, subject to the Cambridge Core terms of use, available at https://www.cambridge.org/core/terms. https://www.cambridge.org/core/product/1F8951EFC610A352837B95E4DAEFBAEB

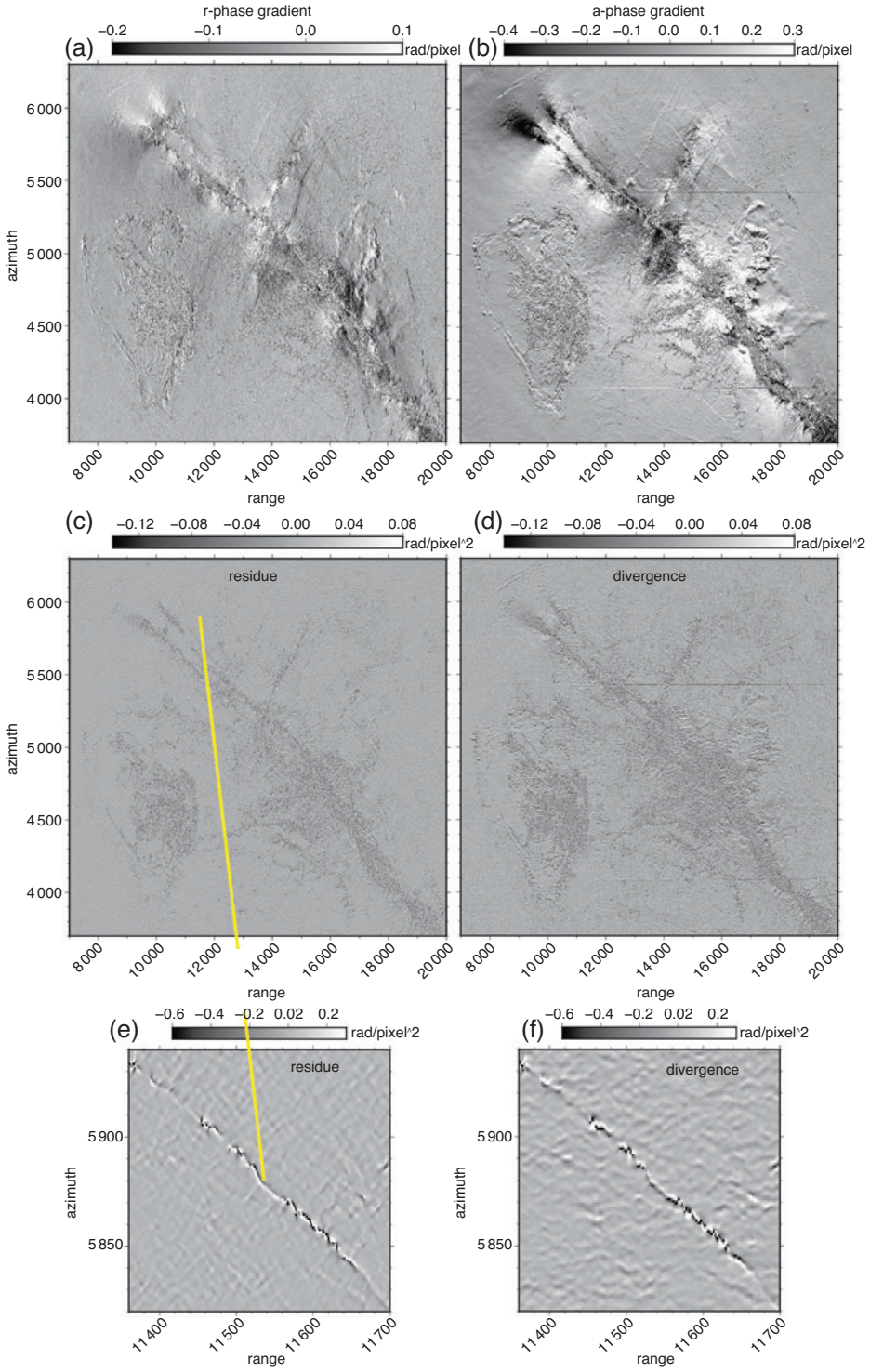

Figure 7.3 (a, b) Range and azimuth phase gradients for the Ridgecrest earthquakes. (c, e) Residue given in Equation 7.3. High residue, both positive and negative, occurs in areas of higher phase noise and surface ruptures. A zoom of a small surface rupture, having a phase offset of less than one fringe, shows a line of enhanced dipolar residue. (d, f) Divergence of the phase gradient (Equation 7.6) is used in the Fourier transform unwrapping algorithm.

Downloaded from https://www.cambridge.org/core. IP address: 189.217.92.64, on 11 Feb 2026 at 15:51:46, subject to the Cambridge Core terms of use, available at https://www.cambridge.org/core/terms. https://www.cambridge.org/core/product/1F8951EFC610A352837B95E4DAEFBAEB

7.2 Fourier Transform Algorithm

The first method considered is a global one that uses the Helmholtz identity, followed by a 2-D Fourier analysis, to perform the integration. Let the observed phase gradient be given by

$$\mathbf{u}(\mathbf{x}) = \left(\frac{\partial \phi}{\partial x}, \frac{\partial \phi}{\partial y}\right) = \frac{R\nabla I - I\nabla R}{R^2 + I^2} \tag{7.4}$$

where we use the real $R(\mathbf{x})$ and imaginary $I(\mathbf{x})$ parts of the interferogram to compute the gradient (i.e., Equation 6.13). Using the Helmholtz decomposition, the phase gradient vector field can be decomposed as the sum of an irrotational vector (curl-free) field and a solenoidal (divergence-free) vector field

$$\mathbf{u}(x) = -\nabla\phi + \nabla \times \psi \tag{7.5}$$

where ϕ is a scalar potential (i.e., unwrapped phase) and ψ is a vector potential. We assume that the phase is a conservative function so the rotational part of the vector field must be zero everywhere. As shown by Ghiglia and Pritt (1998), this corresponds to minimizing the integral of the square of the difference between the observed phase gradient and the recovered gradient. For real phase gradient data, the five factors described above introduce a rotational component that should be eliminated. This is accomplished by taking the divergence of Equation 7.5 since, by definition, $\nabla \cdot \nabla \times \psi = 0$. The phase and phase gradient are now related by Poisson's equation (Ghiglia and Pritt, 1998; Sandwell and Price, 1998).

$$\nabla^2\phi = -\nabla \cdot \mathbf{u} \tag{7.6}$$

For a finite region, the outward component of the phase gradient should be zero along the boundaries (Ghiglia and Romero, 1994); $\nabla\phi \cdot \mathbf{n} = 0$, where $\mathbf{n}$ is the outward normal. An example of the divergence of the phase gradient is shown in Figure 7.3 (d,f). The 2-D Fourier transform of Equation 7.6 is

$$4\pi^2\left(k_x^2 + k_y^2\right)\Phi(\mathbf{k}) = i2\pi\left[k_x U_x(\mathbf{k}) + k_y U_y(\mathbf{k})\right] \tag{7.7}$$

where $\mathbf{k} = \left(k_x, k_y\right)$ are the wavenumbers and the forward and inverse 2-D Fourier transforms of a function $f(x, y)$ are given as

$$\begin{aligned} F(\mathbf{k}) &= \int_{-\infty}^{\infty}\int_{-\infty}^{\infty} f(x,y)e^{-i2\pi\left(k_x x + k_y y\right)}dxdy = \mathcal{F}_2[f] \\ f(\mathbf{x}) &= \int_{-\infty}^{\infty}\int_{-\infty}^{\infty} F\left(k_x, k_y\right)e^{+i2\pi\left(k_x x + k_y y\right)}dk_x dk_y = \mathcal{F}_2^{-1}[F]. \end{aligned} \tag{7.8}$$

Downloaded from https://www.cambridge.org/core. IP address: 189.217.92.64, on 11 Feb 2026 at 15:51:46, subject to the Cambridge Core terms of use, available at https://www.cambridge.org/core/terms. https://www.cambridge.org/core/product/1F8951EFC610A352837B95E4DAEFBAEB

Solving for the total unwrapped phase, we find

$$\phi_{tot}(\mathbf{x}) = \mathcal{F}_2^{-1}\left\{\frac{i\mathbf{k}\cdot\mathcal{F}_2[\mathbf{u}]}{2\pi\left(k_x^2+k_y^2\right)}\right\}. \tag{7.9}$$

For a finite size region, the Fourier transform is replaced by a Fourier series. The zero phase-gradient boundary condition is satisfied if a 2-D cosine transform is used (Ghiglia and Romero, 1994). In practice, one takes the 2-D Fourier transform of each component of the phase gradient with a sine transform in the gradient direction and the cosine transform in the orthogonal direction. Then the result is scaled by the wavenumbers in Equation 7.9. Finally, one takes the inverse 2-D cosine transform to recover the total phase.

An example of topography derived from stacked phase gradients from ERS interferograms, combined with a 90-m Unites States Geologic Survey (USGS) reference topography, is shown in Figure 7.4 (Sandwell and Sichoix, 2000). This topography was developed so it could be removed from individual interferograms to isolate the phase caused by interseismic deformation. At that time (year 2000), the topographic phase was the largest error source in the recovery of deformation because the near-global, 30-m resolution, SRTM topography had not been collected (Farr et al., 2007).

Stacking of phase gradients increases the effective interferometric baseline, which increases the topographic signal to atmospheric noise ratio. As discussed next, the relatively low-resolution USGS reference topography is needed to minimize long-wavelength unwrapping error.

A major issue with the Fourier transform unwrapping approach is that simply removing the rotational part of the phase gradient introduces errors in areas where there are residues. In this case of topographic recovery, there is significant layover in the mountain areas, which results in long-wavelength errors in the unwrapped phase and thus errors in the recovered topography. There are three approaches to mitigating these errors. (1) One can replace the Fourier transform inversion Equation 7.6 with a weighted least-squares inversion where the weights are related to the density of the residues (Ghiglia and Pritt, 1998). The main problem with this approach is the least-squared design matrix becomes extremely large and may exceed even today's computer capabilities. Moreover, there is no guarantee that when this phase is re-wrapped, it will match the phase of the original interferogram. (2) One can use a remove–restore approach to retain the long-wavelength topography from an existing low-resolution topography model. In this case (Figure 7.4), the USGS topography was removed during the formation of each interferogram and the phase gradients were computed and stacked. After Fourier unwrapping the residual stack, the residual phase was high-pass filtered and the USGS model was

Downloaded from https://www.cambridge.org/core. IP address: 189.217.92.64, on 11 Feb 2026 at 15:51:46, subject to the Cambridge Core terms of use, available at https://www.cambridge.org/core/terms. https://www.cambridge.org/core/product/1F8951EFC610A352837B95E4DAEFBAEB

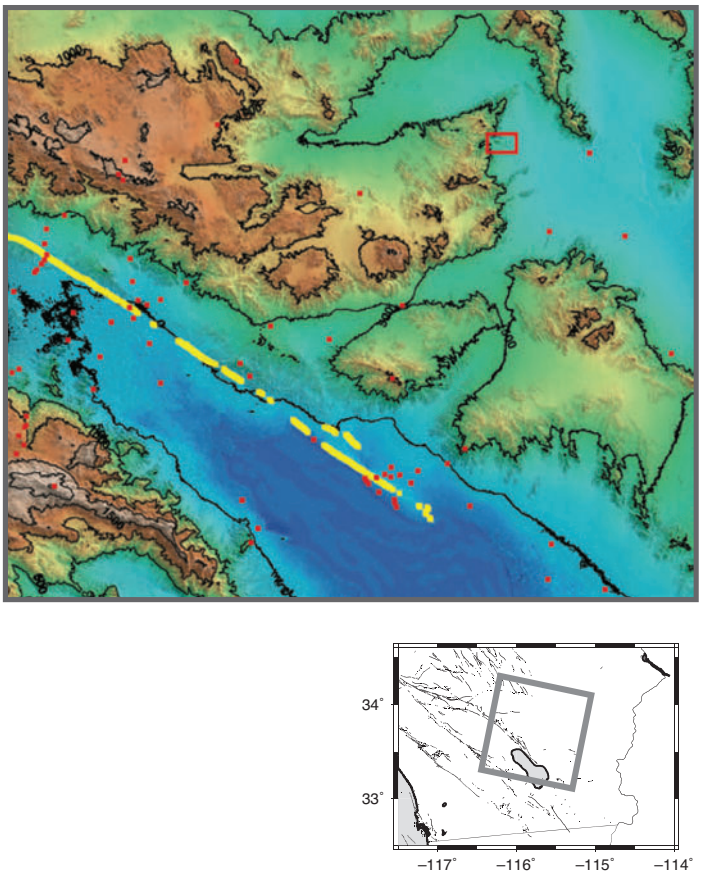

Figure 7.4 Topography (meters above WGS84 ellipsoid, 500-m contour interval, radar coordinates) of the Salton Sea area (see inset map) includes the southern segments of the San Andreas Fault (yellow) and GPS monuments (red). This image combines the long-wavelength accuracy of the USGS 90-m DEM with the short-wavelength (< 6 km) phase gradient information from a stack of 25 ERS SAR images. The combined DEM has 16-m postings and a vertical accuracy of 10 m.

restored. (3) Iterating this remove–restore approach results in a DEM having both long-wavelength accuracy and short-wavelength resolution.

The phase gradient stacking followed by Fourier unwrapping and an iterative remove–restore is a viable approach for topographic recovery. However, for measuring surface deformation, the long-wavelength errors of the Fourier transform method are not acceptable. Moreover, since the existing DEMs from the SRTM mission (Farr et al., 2007) and, more recently, the TerraSAR Tandem-X DEM (Zink et al., 2014) are available for accurate topographic phase removal, thus Fourier transform unwrapping approach is rarely used today.

Downloaded from https://www.cambridge.org/core. IP address: 189.217.92.64, on 11 Feb 2026 at 15:51:46, subject to the Cambridge Core terms of use, available at https://www.cambridge.org/core/terms. https://www.cambridge.org/core/product/1F8951EFC610A352837B95E4DAEFBAEB

7.3 Branch Cut (Goldstein) Algorithm

As discussed earlier, the main objective of 2-D phase unwrapping is to integrate the measured phase gradient to uniquely recover the total phase. If we start the integration at point a, then the phase at point b is the integral of the phase gradient along a path connecting the two points

$$\phi(x,y) = \int_a^b \nabla\phi \cdot d\mathbf{x} + \phi(x_a, y_a). \tag{7.10}$$

Of course, there is an unknown constant of integration $\phi(x_a, y_a)$. Assuming the true interferogram represents a continuous function such as topography, surface deformation, or atmospheric delay, the integration of the phase gradient, around any closed loop, should be zero. The occurrence of nonzero phase closure, or residue, is somewhat predictable. Images with low coherence typically contain high densities of residues, which can make unwrapping challenging. Topographic layover and shadows typically create lines of residues along the edge of the layover. Abrupt discontinuities due to surface faulting or glacier movement also generate residues. It is possible that entire regions of the interferogram may be isolated from other regions by residues and the associated branch cuts. In these cases, ad hoc assumptions (e.g., there are minimal phase jumps between isolated regions) may be necessary to ensure a reasonable result.

To identify the residues, consider a wrapped interferogram as a 2-D array of normalized phase values as shown in Figure 7.5. Because the phase is wrapped, all the values lie between 0 and 1. If the absolute value of the phase difference between two cells is greater than 0.5, then there is a phase wrap and one must add or subtract 1 to obtain stay within the 0.5 phase difference. Let's check some examples for phase closure. Consider the closure at node **A**. Summing the phase difference counterclockwise from the upper left corner, we have −.9+.8−.1+.2. The first two cell differences exceed 0.5, so we add 1 to the first and subtract 1 from the second so

closure at cell **A** is +.1 −.2 −.1 +.2 = 0
closure at cell **B** is +.1 −.1 −.2 +.2 = 0
closure at the **+** cell is +.2 +.3 +.2 +.3 = +1
closure the **–** cell is −.2 −.3 −.1 −.4 = −1

In this small grid, there are two residues with opposite signs. To confirm the residues cancel, we integrate around a loop containing both residues +.2+.3+.1−.3−.1−.4−.1+.3 = 0. Therefore, to achieve path independence with the phase gradient integration, the path cannot cross between the + and – residues. A

Downloaded from https://www.cambridge.org/core. IP address: 189.217.92.64, on 11 Feb 2026 at 15:51:46, subject to the Cambridge Core terms of use, available at https://www.cambridge.org/core/terms. https://www.cambridge.org/core/product/1F8951EFC610A352837B95E4DAEFBAEB

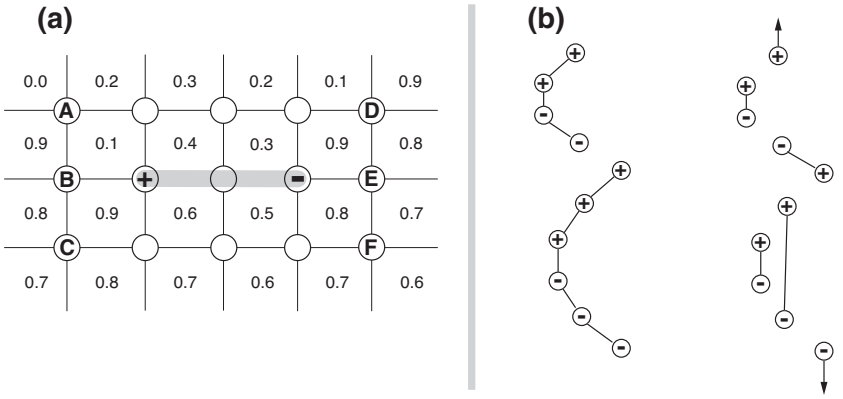

Figure 7.5 (a) The numbers represent a 2-D array of normalized wrapped phase. Summation of the wrapped phase gradient around loops should be zero unless there is a + or – residue. Any phase gradient integration that passes between these two residues will have an unwrapping error, so they are connected by a branch cut (gray line). (b) Two ways to connect residues will result in different unwrapping results. Adapted from Chen and Zebker (2000) with permission from the ©Optical Society of America.

line connecting the two residues is called a *branch cut*. If a negative residue is connected to a positive residue, the two residues are concealed, and no further branch cuts are needed. If both residues were positive, then the branch cut would need to be extended to include two negative residues or neutralized by extending to the edge of the image.

The Goldstein algorithm (Goldstein et al., 1988) first analyzes the wrapped phase to identify all the residues. Then the branch cuts are grown in a tree-like manner such that every residue is on a neutral tree where a tree is a set of connected branch cuts. A branch cut can also extend to the edge of the image where it is neutralized. The phase gradient integration path is not allowed to cross any cuts, so no path includes an unbalanced residue.

As shown in Figure 7.5, there are a variety of ways the residues can be connected. The Goldstein algorithm makes the connections by attempting to minimize the overall length of the branch cuts in an image. One deficiency in the Goldstein algorithm is that branch cuts may be connected in a way to enclose a region in the interferogram so when the path-filling integral is performed, these regions will retain their original wrapped phase.

7.4 Minimum Cost Flow (SNAPHU) Algorithm

The minimum cost flow (MCF) algorithm, as implemented in the SNAPHU program (Chen and Zebker, 2002), also begins with identifying all the residues in

Downloaded from https://www.cambridge.org/core. IP address: 189.217.92.64, on 11 Feb 2026 at 15:51:46, subject to the Cambridge Core terms of use, available at https://www.cambridge.org/core/terms. https://www.cambridge.org/core/product/1F8951EFC610A352837B95E4DAEFBAEB

the image. However, it differs in the way the residues are connected. For both algorithms, the unwrapped phase is identical to the original wrapped phase when re-wrapped. The MCF algorithm attempts to minimize the total number of phase gradient cycles added to the original image.

The MCF algorithm has two variants depending on whether the phase unwrapping is optimal for recovering topography in moderate baseline interferograms or surface deformation in small baseline interferograms. In both cases, the trees are connected in a way that tree branches never cross (i.e., minimum spanning tree), so the phase is unwrapped everywhere. Different interferogram applications may benefit from different objective functions. For example, interferograms for refining topography that are dominated by errors caused by layover differ from interferograms associated with surface ruptures.

An example of the unwrapped phase for the Ridgecrest earthquakes is shown in Figure 7.6. These data were first filtered with a 120-m wavelength Gaussian filter followed by a Goldstein filter. The phase was unwrapped using the SNAPHU algorithm with the discontinuity option set to 60 radians. Unwrapped phase was converted to LOS displacement using Equation 7.1. Figure 7.6 (a), in radar coordinates, matches the wrapped phase shown in Figure 7.1 (a). The integration path from **a** to **b** is largely free of residues, so the surface offset can be measured. Note many areas along the rupture where there are small discontinuous zones. These are mostly phase unwrapping errors. These areas should be masked using a coherence

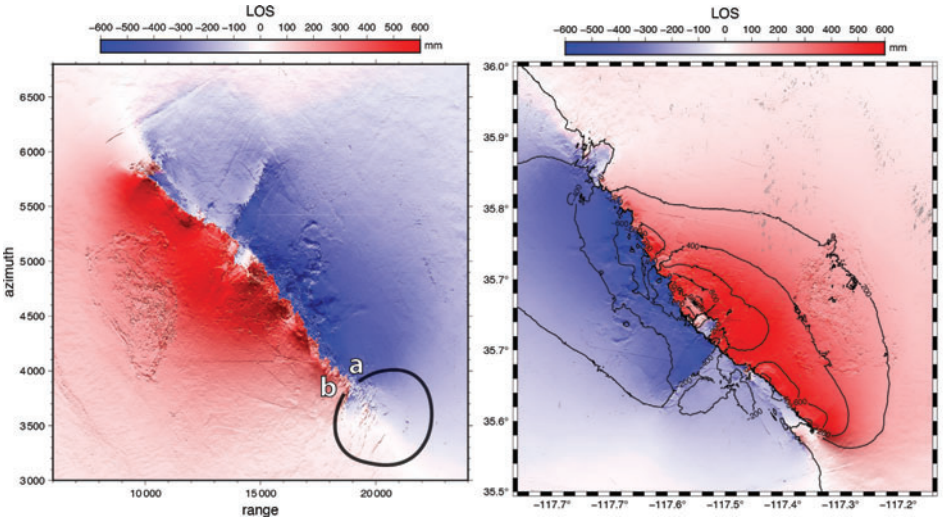

Figure 7.6 (a) LOS deformation in radar coordinates for the Ridgecrest earthquakes. There are many small unwrapping errors along the main ruptures. (b) Same LOS map in geographic coordinates with a 200-mm contour interval shows a maximum LOS offset of more than 1.6 m.

Downloaded from https://www.cambridge.org/core. IP address: 189.217.92.64, on 11 Feb 2026 at 15:51:46, subject to the Cambridge Core terms of use, available at https://www.cambridge.org/core/terms. https://www.cambridge.org/core/product/1F8951EFC610A352837B95E4DAEFBAEB

threshold (Figure 7.1 (b)) or masked manually using the fault trace mapped by geologists after the earthquakes. The right LOS image is in geographic coordinates. The red/blue regions show motion toward/away from the radar, so the NW-SE trending rupture has right-lateral motion while the smaller orthogonal rupture has left-lateral motion as expected.

7.5 Nearest-Neighbor Algorithm and Loop Closure

The SNAPHU algorithm attempts to unwrap the phase everywere including bodies of water where the phase is completely decorrelated. Unwrapping of decorrelated areas dramatically increases the computer time and also introduces phase errors. There are two approaches to minimizing unwrapping errors and computer time. First, areas of noisy phase (e.g., water and coherence < 0.1) could be set to zero, which dramatically speeds the unwrapping. However, this can produce unwrapping errors in nearby areas having high coherence. Consider an interferogram in a coastal area (Figure 7.7). To speed the unwrapping, one resets the phase over the ocean to zero. Next suppose the phase on the land has a ramp parallel to the coastline. The phase unwrapping on the land will attempt to recover this coastline-parallel ramp. However, the phase unwrapping in the ocean will attempt to recover zero phase. There will be a large discontinuity at the coastline, so the MCF algorithm may resolve the conflict by introducing a phase unwrapping error over the land and/or ocean. Of course, the unwrapping error over the land will need to be corrected.

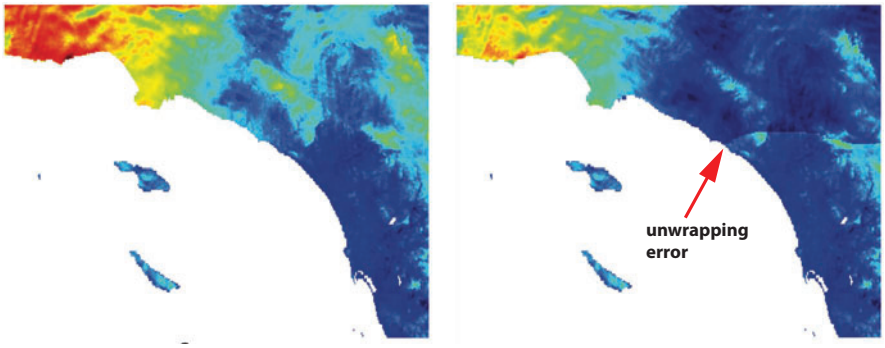

Figure 7.7 Unwrapped phase for Sentinel-1 track 071 covering Southern California in radar coordinates. The area includes Los Angeles, San Diego, and the coastal waters. (a) The phase was unwrapped after setting the water areas to zero phase. This causes an unwrapping error shown by the red arrow. (b) The phase was unwrapped after setting water areas to the phase at the nearest land area. There is no coastal unwrapping error.

Downloaded from https://www.cambridge.org/core. IP address: 189.217.92.64, on 11 Feb 2026 at 15:51:46, subject to the Cambridge Core terms of use, available at https://www.cambridge.org/core/terms. https://www.cambridge.org/core/product/1F8951EFC610A352837B95E4DAEFBAEB

The problem is that the phase over the ocean is completely wrong. Even if the ocean phase was not replaced by zero, this land unwrapping error could still occur because the random ocean phase will unwrap toward zero. To avoid this conflict, Shanker and Zebker (2009) and Lindsey et al. (2014) recommend filling the phase in the water areas with the wrapped value at the closest coastline using a *near-neighbor algorithm*. This approach corrects the phase unwrapping error over the land and dramatically speeds the unwrapping over the ocean. Of course, the unwrapped phase over the ocean will be inaccurate, so it will need to be masked.

The second approach to minimize unwrapping errors, or at least identify the errors, is to use a phase closure constraint when multiple interferograms are available. This is also called 3-D phase unwrapping since the constraint is applied over the time dimension. Consider three SAR images, A, B, and C, that are well correlated. One can construct three interferograms (i.e., phase difference maps) ϕ_{BA}, ϕ_{CB}, and ϕ_{AC}. Of course, the sum of the wrapped phase from these three interferograms should be zero. (Note there can be a small misclosure due to multilooking (Zheng et al., 2022)). After unwrapping these three interferograms, the sum of the phase will not necessarily be zero because of the unknown constant of integration. If each interferogram has no unwrapping errors, then one expects that the sum of the three unwrapped interferograms will be a constant of $N2\pi$ over the entire area. Note that the phase closure can be forced to zero by adding this constant to any of the three interferograms. Suppose further that one of the interferograms has a small area with an unwrapping error of, say, 4π. After the global correction, the sum of the interferograms will be 4π over that small area and zero everywhere else. Using this approach, one can identify the region where the unwrapping error occurred but not necessarily which interferogram has the unwrapping error.

Next consider the case where there are hundreds of interferograms (Figure 7.8). These interferograms will have $N2\pi$ integer ambiguities after the phase is unwrapped. If not properly corrected, this ambiguity term will affect every pixel in radar acquisitions and introduce a random walk-type error that will bias the time series. The use of the phase closure constraint to solve for $N2\pi$ integer ambiguities in unwrapped interferograms is common practice in InSAR time series analysis (e.g., Hussain et al. (2016)). The approach is to form all possible three-way loops in a set of interferograms so the problem can be written into the form of a minimization problem with integer unknowns (Fattahi, 2015). An example is shown in Figure 7.8 using 468 Sentinel-1 interferograms (Xu and Sandwell, 2019). Before solving for the ambiguities, there were typically 300 out of 1 207 loop misclosures in well-correlated areas. After solving for the ambiguities, there were less than 20 misclosures out of 1 207 in the well-correlated areas. Note that in the poorly correlated areas, the number of misclosures remains high 300–400 out of 1 200, so this type of analysis is also good at identifying areas with unreliable results. These areas

Downloaded from https://www.cambridge.org/core. IP address: 189.217.92.64, on 11 Feb 2026 at 15:51:46, subject to the Cambridge Core terms of use, available at https://www.cambridge.org/core/terms. https://www.cambridge.org/core/product/1F8951EFC610A352837B95E4DAEFBAEB

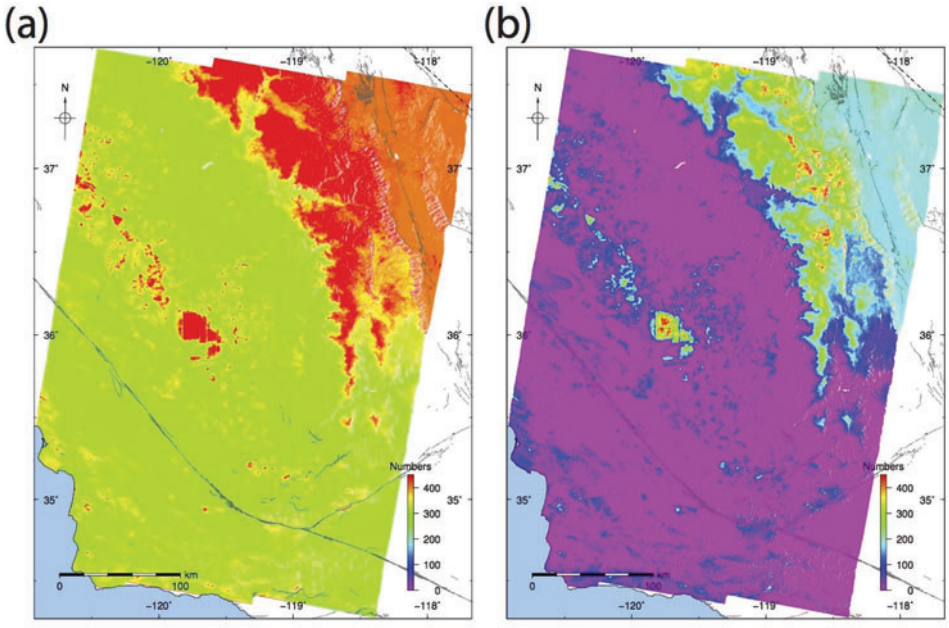

Figure 7.8 (a) Number of nonclosing loops for each pixel before applying the unwrapping ambiguity correction for 81 Sentinel-1 scenes over California (468 interferograms and 1 207 loops). (b) Number of nonclosing loops after correction. Reprinted with permission from *IEEE Transactions on Geoscience and Remote Sensing*.

of high phase misclosure should also be masked or assigned larger uncertainties in any further analysis, such as stacking or time series.

7.6 Summary

Phase unwrapping is one of the most challenging and computing-intensive aspects of radar interferometry. The concept is simple. One selects a starting point in the image and integrates the phase gradient outward to fill the scene with unwrapped phase. If the path encounters a phase jump of greater than π or less than $-\pi$, the algorithm subtracts or adds 2π to recompute the gradient. For noise-free wrapped phase data with no discontinuities, all integration paths between any two points in the image have the same phase offset. This implies that integration around any closed path will have zero phase offset. Because real interferograms are noisy and have phase discontinuities due to layover, shadowing, and surface ruptures, there are points in the interferogram (residues) where closed path integration is either 2π or -2π.

Downloaded from https://www.cambridge.org/core. IP address: 189.217.92.64, on 11 Feb 2026 at 15:51:46, subject to the Cambridge Core terms of use, available at https://www.cambridge.org/core/terms. https://www.cambridge.org/core/product/1F8951EFC610A352837B95E4DAEFBAEB

The global unwrapping approach uses a least squares algorithm to remove, or downweight, the residues and solve for the global unwrapped phase. These global algorithms usually suffer from large-scale errors. Moreover, when the total phase is re-wrapped, the results no longer match the original unwrapped phase.

Local path-following algorithms are usually more successful. The basic approach is to first identify all the residues by summing phase differences around all 2×2 cells in the wrapped phase image. Once these residues are found by thresholding, the algorithms connect them with branch cuts so the sum of the residues along the branch cut is zero. The selection of branch cuts and their assembly into trees is nonunique.

The Goldstein algorithm attempts to minimize the total length of the branch cuts. However, branch cuts can close on themselves, so large areas of the interferogram may be isolated from the path integration and remain unwrapped. One can place the starting point of integration inside this isolated area, but there is an unknown $N2\pi$ ambiguity between the unwrapped phase inside the area and outside the area. Given additional information such as GNSS measurements, one could solve for the $N2\pi$ ambiguity.

The MCF flow algorithm, as implemented in the SNAPHU computer code (Chen and Zebker, 2001), selects the branch cuts to minimize the total number of cycles added to the phase gradient. The branch cuts are connected such that when the growing tree becomes neutral, the next nearest charge is connected to the nearest branch to form a minimum spanning tree. An important property of this tree is that it never closes on itself so every point in the interferogram is connected to every other point and the path-filling integral will unwrap everywhere. Like the Goldstein approach, when this unwrapped phase is re-wrapped, it exactly matches the original unwrapped interferogram.

Just because the unwrapping is complete, it is not necessarily correct. Bodies of water, where phase recovery is impossible, takes an enormous amount of computer time and can produce phase unwrapping on land near the coastlines. To reduce these unwrapping errors, Shanker and Zebker (2009) recommend filling the phase in the water areas with the wrapped value at the closest coastline using a near-neighbor algorithm. This approach dramatically speeds up the unwrapping, including the water areas, but also allows for an accurate phase change along the coastlines.

Phase unwrapping errors can be identified when three or more SAR acquisitions are available for an area. For three SAR images, one can form three interferograms and unwrap their phase. The sum of the three interferograms should have a constant ambiguity of $N2\pi$ everywhere. If part of the summed interferogram has a different ambiguity, then at least one of the three interferograms has a phase unwrapping error. With the hundreds of SAR images available today from missions such as

Downloaded from https://www.cambridge.org/core. IP address: 189.217.92.64, on 11 Feb 2026 at 15:51:46, subject to the Cambridge Core terms of use, available at https://www.cambridge.org/core/terms. https://www.cambridge.org/core/product/1F8951EFC610A352837B95E4DAEFBAEB

Sentinel-1, one can construct and unwrap thousands of interferograms. The summation of unwrapped phase around closed loops will reveal both local and global phase ambiguities. A minimum norm algorithm can be used to approximately solve for the global ambiguities. The remaining local ambiguities reveal areas where there are significant unwrapping errors distributed throughout the interferograms. These high-ambiguity areas can be masked and not used in quantitative analyses.

Later in Chapter 11 we will discuss the use of continuous GNSS measurements to check the global ambiguities and bring the LOS deformation maps into an absolute system. Of course, these InSAR observations are still contaminated with atmospheric delays. After correcting the global ambiguities, the set of interferograms can be used to construct LOS time series. This is also discussed in Chapter 11.

7.7 Problems

1. Write a function in your favorite language/tool to create a sine wave that ranges in amplitude between -2π and 2π over one wavelength and display the image. Then create a wrapped version using atan2() or arctan2(). Then either manually or automatically, unwrap the wrapped version by adding 2π to selected intervals. Hint: Calculate the difference between adjacent pixels going from left to right. If the difference is larger than π, subtract 2π from the remaining series. If the difference is less than $-\pi$, add 2π.
2. Repeat exercise 1 but add 10% noise to the wrapped version and then try unwrapping.
3. Calculate the residue for nodes C, D, E, and F in Figure 7.5.

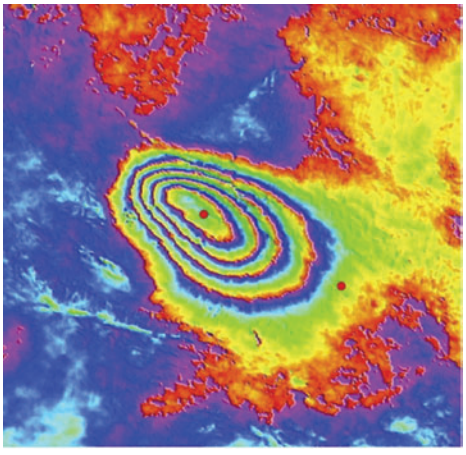

Figure 7.9 A phase change image for the 2017 Sefid Sang M 6.1 earthquake in Iran. This image is from Sentinel-1 data for a descending track.

Downloaded from https://www.cambridge.org/core. IP address: 189.217.92.64, on 11 Feb 2026 at 15:51:46, subject to the Cambridge Core terms of use, available at https://www.cambridge.org/core/terms. https://www.cambridge.org/core/product/1F8951EFC610A352837B95E4DAEFBAEB

4. Why is it 4π instead of 2π in Equation 7.1 converting phase change to displacement?
5. Figure 7.9 is an example of a wrapped phase change for the 2017 Sefid Sang M 6.1 earthquake in Iran. The data is from a descending track of Sentinel-1. How much LOS displacement has occurred between the two red points in Figure 7.9? Is the center of the pattern moving toward or away from the radar?

Downloaded from https://www.cambridge.org/core. IP address: 189.217.92.64, on 11 Feb 2026 at 15:51:46, subject to the Cambridge Core terms of use, available at https://www.cambridge.org/core/terms. https://www.cambridge.org/core/product/1F8951EFC610A352837B95E4DAEFBAEB

8

SAR Modes

8.1 Introduction

Most spaceborne synthetic aperture radars (SARs) can be operated in several imaging modes and can have up to four polarizations. Indeed, there can be 10s of possible operating configurations for some SAR missions. Interferometry requires that the reference and repeat images be in the same, or similar, modes and have the same polarization. Here we discuss the possible modes and polarizations using the ALOS-1 mission as an example. We begin this chapter by noting that the swath width of a standard strip-mode SAR is limited by the need to wait for the pulse to sweep across the Earth from the near range to the far range before sending another radar pulse (Figure 8.1). Otherwise, the return signals from the near and far ranges would overlap in time (Box 8.1).

Box 8.1

Review of Constraints on PRF and Swath Width

As discussed in Section 2.4, the single-look azimuth resolution of a SAR is equal to one half the length of the antenna, $L/2$. To achieve this resolution, the pulse repetition frequency PRF of the radar must exceed $2V/L$ where V is the ground velocity of the spacecraft. In Section 3.2 we calculated the ground velocity for a satellite in low Earth orbit. For example, a satellite at an altitude of 700 km has a ground velocity of 6.75 km/s. Increasing the altitude to 1 500 km only reduces the ground velocity to 5.8 km/s. Thus, the lower bound on the PRF is essentially determined by the length of the antenna. For a typical 10-m long antenna, the PRF must exceed 1 200 Hz.

There is also an upper bound on the PRF. Before the SAR can send a new pulse, one must wait until the prior pulse propagates from the near range to the far range (Figure 8.1). Otherwise, the return signals from the near and far ranges would overlap in time. Moreover, as discussed in Section 4.4, to reduce the peak power output of the transmit antenna, the radar sends a frequency-modulated chirp (Figure 4.4). This chirp propagates to the ground where it reflects from a swath typically 70 km wide. When it returns to the radar, the raw signal data consists of the complex reflectivity of the

Downloaded from https://www.cambridge.org/core. IP address: 189.217.92.64, on 11 Feb 2026 at 15:51:46, subject to the Cambridge Core terms of use, available at https://www.cambridge.org/core/terms. https://www.cambridge.org/core/product/1F8951EFC610A352837B95E4DAEFBAEB

surface convolved with the chirp. The chirp is deconvolved in the SAR-processor program. A typical chirp length is 10 km, so this adds roughly 30% to the required wait time. The bounds on the PRF are given by

$$\frac{2V}{L} < \text{PRF} < \frac{c}{2H}(\sec\theta_2 - \sec\theta_1)^{-1}$$

where c is the speed of light and H is the altitude of the spacecraft. The look angles to the near range θ_1 and the far range θ_2 govern the width of the swath. As discussed in Chapter 3, the sweet spot for the altitude of a remote sensing satellite is 700 km. Therefore, the only adjustable parameters on the PRF bounds are the antenna length and the swath width. One could achieve a 350 km wide swath by increasing the antenna length from 10 m to 50 m, although this would add considerable expense to the SAR mission. Also, this would reduce the PRF by a factor of 5, which would result in five times poorer azimuth resolution and thus fewer looks for averaging. Elachi and Van Zyl (2021) discuss these PRF constraints and show that the width of the swath is fundamentally limited by the area of the antenna; a longer or wider antenna is needed to make a wider swath. SweepSAR, discussed later in Section 8.6, increases the swath width by effectively increasing the width of the antenna.

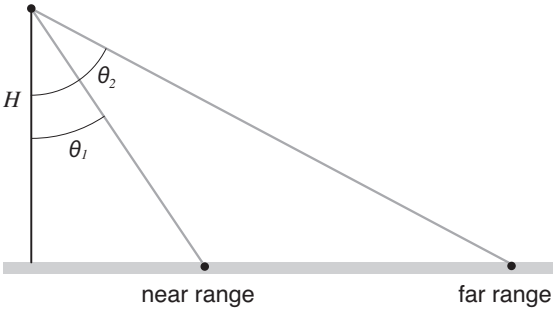

Figure 8.1 End view of the distance to the near range and far range of the radar illumination pattern. For standard strip-mode SAR, there can only be one pulse sweeping across the swath.

A diagram of two main spatial modes for the ALOS-1 PALSAR radar is shown in Figure 8.2. The standard strip mode, discussed in Chapters 2 and 4, has a swath width that is limited by the need to wait for the radar pulse to propagate from the near range to the far range before sending another pulse (Box 8.1). For the ALOS-1 PALSAR configuration, the maximum swath width is 70 km. The ScanSAR mode is used to acquire a wider swath of 350 km from a single acquisition. This ScanSAR configuration has five subswaths each 70 km wide to achieve the overall swath of 350 km (Figure 8.3). The details and limitations of the ScanSAR technique are discussed later in this chapter. As seen in Figure 8.2, there are 18 possible positions

Downloaded from https://www.cambridge.org/core. IP address: 189.217.92.64, on 11 Feb 2026 at 15:51:46, subject to the Cambridge Core terms of use, available at https://www.cambridge.org/core/terms. https://www.cambridge.org/core/product/1F8951EFC610A352837B95E4DAEFBAEB

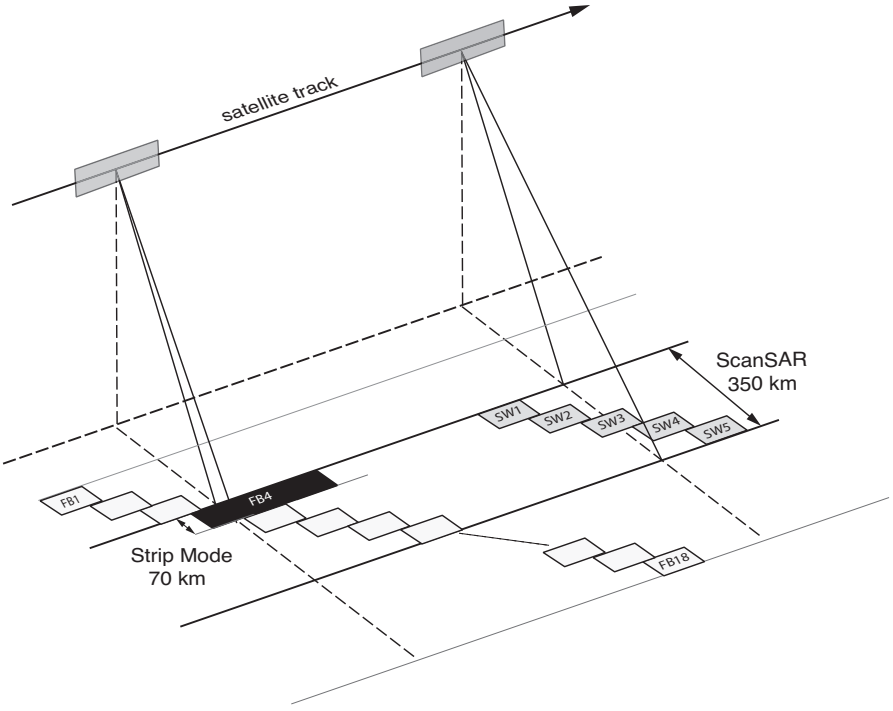

Figure 8.2 The two basic operating modes of the ALOS-1 PALSAR are strip mode and ScanSAR mode. The location of the swath in range is called the beam # and there are 18 possible beams, although only five are commonly used. The commonly used ScanSAR mode has five subswaths matching five of the beams in the swath mode data to achieve a 350 km wide swath.

for the location of the swath in range although in practice only five swath locations were commonly used.

8.2 Polarization

In addition to the cross-track position of swaths, data can be collected in four polarizations (Zebker and Van Zyl, 1991). SAR satellites generally use linearly polarized EM radiation. When the electric field vector is parallel to the ground, this is called horizontal polarization H. There is one polarization for the transmitted waves and a second for the receive waves, so four polarizations are possible:

HH — horizontal transmit, horizontal receive;
HV — horizontal transmit, vertical receive;
VV — vertical transmit, vertical receive; and
VH — vertical transmit, horizontal receive.

Downloaded from https://www.cambridge.org/core. IP address: 189.217.92.64, on 11 Feb 2026 at 15:51:46, subject to the Cambridge Core terms of use, available at https://www.cambridge.org/core/terms. https://www.cambridge.org/core/product/1F8951EFC610A352837B95E4DAEFBAEB

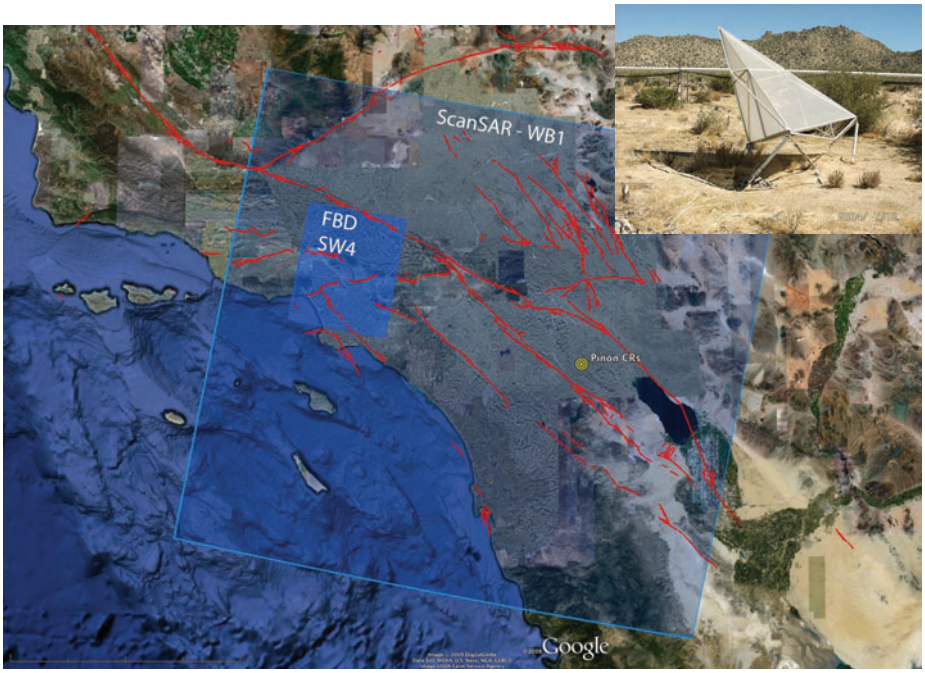

Figure 8.3 Spatial coverage of ALOS-1 strip mode and ScanSAR data. Subswath 4 (SW4) of the ScanSAR overlaps with a strip-mode fine beam dual polarization acquisition, so one can perform ScanSAR to strip-mode interferometry. A Piñon Flat corner reflector is shown in the inset.

The PALSAR was operated in three polarimetric modes (Table 8.1):

1) fine beam single polarization (FBS) (HH) or (VV);
2) fine beam dual polarization (FBD) (HH+HV) or (VV+VH); and
3) quad polarization (PLR) (HH+HV+VV+VH).

8.3 Range and Azimuth Resolution

The PALSAR was operated at two bandwidths of 14 MHz and 28 MHz. As discussed in Section 2.4, the range resolution is inversely proportional to the radar bandwidth, so the 14 MHz bandwidth has a slant range resolution of 10.8 m and the 28 MHz bandwidth has a resolution of 5.4 m. The azimuth resolution is 1/2 the length of the antenna as discussed in Section 2.4 so all the single look products have an azimuth resolution of 4.5 m, while the ScanSAR products have an azimuth resolution that is 5 times worse (22.5 m).

In the case of ALOS-1 PALSAR, there are 10s of possible configurations, but the mission planners limited the number of modes based on the science needs. Dual and quad polarimetric modes are best for studying ecosystems using temporal

Downloaded from https://www.cambridge.org/core. IP address: 189.217.92.64, on 11 Feb 2026 at 15:51:46, subject to the Cambridge Core terms of use, available at https://www.cambridge.org/core/terms. https://www.cambridge.org/core/product/1F8951EFC610A352837B95E4DAEFBAEB

Table 8.1 *PALSAR imaging characteristics in commonly used modes.*

Mode	Polarization	Band width (MHz)	Look angle (deg)	Range res. (m)	Azimuth res. (m)	B_c (km)	Swath width (km)
FBS	HH or VV	28	8–60 (34.3)	5.4	4.5	13.1	40–70
FBD	HH+HV or VV+VH	14	8–60 (34.3)	10.8	4.5	6.5	40–70
PLR	HH+HV+ VV+VH	14	8–30 (21.5)	10.8	4.5	6.5	20–65
ScanSAR	HH or VV	14 or 28	18–43 (34.3)	5.4 or 10.8	22.5	6.5	350

changes in radar backscatter; interferometry is not usually performed. Interferometry, used for coherence and phase (deformation), has several basic requirements. First, the polarizations of the reference and repeat images must match. There is not much additional information in having more than one polarization, so the fine beam single polarization (FBS) mode is preferred. Second, the reference and repeat swaths must, of course, overlap in the range direction. The radar bandwidths do not need to match, although the lower bandwidth data (14 MHz) must be resampled to match the higher bandwidth (28 Hz). Finally, for ScanSAR, the along-track positions of the bursts must have sufficient overlap to achieve phase coherence. ScanSAR interferometry is discussed in Section 8.4.

8.4 ScanSAR Processing and Interferometry

The first type of wide-swath interferometry is ScanSAR. The systematic observation strategy of ALOS-1 PALSAR provides strip-mode SAR imagery along every ascending orbital track and ScanSAR imagery (Figure 8.4) along every third descending orbital track. Therefore, to obtain a second look direction of PALSAR interferometry sometimes requires processing ScanSAR to ScanSAR mode interferograms. The ScanSAR focusing method used in GMTSAR is based on the proposal by Bamler and Eineder (1996) that, with proper preprocessing, standard strip-mode software (*esarp* in GMTSAR) can be used to construct phase-preserving SAR images and ultimately interferograms. The main advantage of using the standard strip-mode approach, instead of the traditional SPECAN approach (Sack et al., 1985), is that existing and well-tested, strip-mode InSAR processing software can be used. The main disadvantage of this approach is that the zero-padding between the bursts wastes considerable disk space and computer time. Nevertheless, the two approaches should provide equivalent results.

Downloaded from https://www.cambridge.org/core. IP address: 189.217.92.64, on 11 Feb 2026 at 15:51:46, subject to the Cambridge Core terms of use, available at https://www.cambridge.org/core/terms. https://www.cambridge.org/core/product/1F8951EFC610A352837B95E4DAEFBAEB

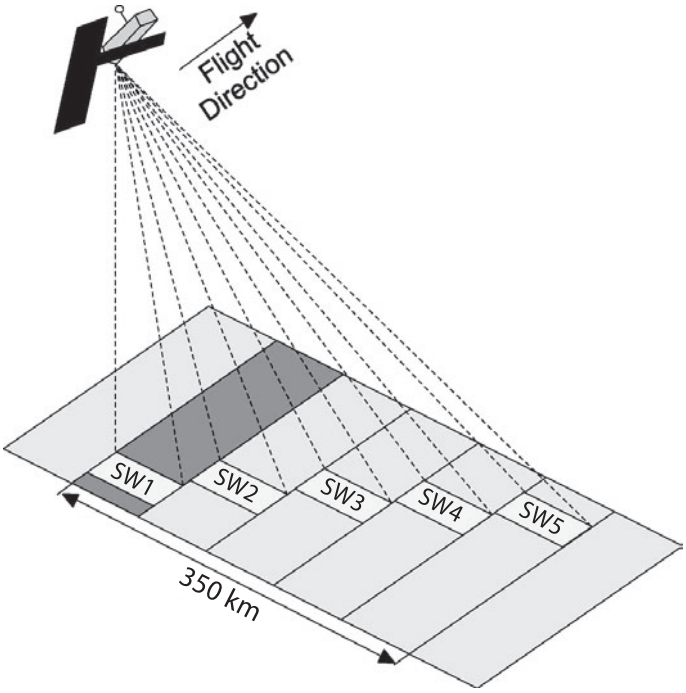

Figure 8.4 Schematic diagram of ScanSAR imaging. The radar acquires data for short bursts over each of 5 subswaths. Each subswath is illuminated over 1/5 of cycle length in the along-track direction such that 4/5 of each subswath is not illumunated. Modified from Bertran-Ortiz and Zebker (2007). Reprinted with permission from *IEEE Transactions on Geoscience and Remote Sensing*.

The GMTSAR ScanSAR mode preprocessor for ALOS was developed and tested using data along a descending orbital track (T538) over Southern California (Tong et al. (2010), Figure 8.3). This track contains two permanently installed radar corner reflectors that are used by JAXA to provide radiometric and geometric calibration for the lifetime of the mission. JAXA has collected PALSAR data over these reflectors in a variety of modes on both ascending and descending tracks. We have extended the ALOS preprocessing software to first perform ScanSAR to FBD mode interferometry and second to perform the more challenging ScanSAR to ScanSAR interferometry where a significant burst overlap is needed. Note that ALOS-2 has the ability to achieve complete burst overlap so this discussion is only relevant to ALOS-1. Indeed, both luck and accuracy are required to achieve a full swath-width ScanSAR to ScanSAR interferogram. The ScanSAR acquisition geometry and parameters for PALSAR are provided in Table 8.2. The five subswaths cover an area 350 km wide. Following Bamler and Eineder (1996), the ScanSAR data are zero-padded to construct strip-mode type data. The original wide

Downloaded from https://www.cambridge.org/core. IP address: 189.217.92.64, on 11 Feb 2026 at 15:51:46, subject to the Cambridge Core terms of use, available at https://www.cambridge.org/core/terms. https://www.cambridge.org/core/product/1F8951EFC610A352837B95E4DAEFBAEB

Table 8.2 *Nominal radar parameters for each subswath. The number of echoes in a burst, nburst, is the only fixed parameter.*

	SW1	SW2	SW3	SW4	SW5
near range (m)	730 097	770 120	806 544	848 515	878 195
PRF *(Hz)*	1 692	2 370	1 715	2 160	1 916
nburst	247	356	274	355	327
$\Delta t(s)$	0.146	0.150	0.160	0.164	0.171
nsamples	4 976	4 720	5 376	4 432	4 688
off nadir (deg)	20.1	26.1	30.6	34.1	36.5

beam (WB1) file contains the bursts of all five subswaths as consecutive rows. The preprocessor separates the data into five separate files where missing lines between the bursts are filled with zeros. Zeros are also added to the end of each echo to match the length of a standard FBD data file. Since the subswaths are processed independently and their amplitude and interferometric phase are recombined in the latitude-longitude coordinate system, an accurate geometric model, precise orbit, and consistent set of processing parameters are required to achieve a seamless recombination. The preprocessing code is rather complex because the pulse repetition frequency (PRF) of the PALSAR echoes varies in three ways. First, as shown in Table 8.2, each subswath has its own PRF optimized to reduce crosstalk. Second, the PRF can change along the satellite track on any one of the subswaths. A PRF change on any subswath changes the time interval and number of zero-pad lines needed on all the other subswaths. Finally, when considering reference and repeat images for interferometry, the PRFs on matching subswaths can be different causing the burst alignment to change along the swath as we find in the example later. In addition, each subswath has its own near range, which varies along the track, so rows must be shifted to align the near range to the common prescribed value. Any small error in the preprocessing could result in a poorly focused image and/or low interferometric coherence.

The first step in the software development was to focus the raw subswath data to form seamless amplitude imagery. We found that the best image quality (i.e., minimal scalloping) was achieved by setting the length of the synthetic aperture to be exactly six bursts. This corresponds to setting the time (~4.7 s) and along-track distance of the synthetic aperture to be exactly the same for each subswath. We also found that by processing the SAR image to zero Doppler, the position of the radar corner reflectors in the image matches the position predicted from the orbit (zero range rate) to within 1 pixel in range and 4 pixels in azimuth. This good match provided confidence that the code is geometrically accurate.

Downloaded from https://www.cambridge.org/core. IP address: 189.217.92.64, on 11 Feb 2026 at 15:51:46, subject to the Cambridge Core terms of use, available at https://www.cambridge.org/core/terms. https://www.cambridge.org/core/product/1F8951EFC610A352837B95E4DAEFBAEB

The second step in the software development was to construct ScanSAR to swath mode interferometry. This combination should always provide interference fringes because there is 100% overlap between the sparse bursts of the ScanSAR and the complete coverage of the swath (Bertran-Ortiz and Zebker, 2007). The ALOS track 538 over Los Angeles has two FBD acquisitions and three ScanSAR WB1 acquisitions. The swath of the FBD data (34.3 incidence angle) overlaps with subswath 4 of the WB1 data. We experimented with three interferometric mode combinations: FBD to FBD, FBD to ScanSAR, and ScanSAR to ScanSAR. The FBD to FBD interferogram had a 10 m baseline and a 46-day timespan, resulting in excellent overall coherence of 0.67. The FBD to ScanSAR interferogram had a somewhat longer baseline of 121 m and a 181-day timespan, resulting in a lower average coherence of 0.38.

The third step in the software development was to construct ScanSAR to ScanSAR interferometry. The major issue here is that there is only a 20% chance of having along- track alignment of the bursts between reference and repeat orbits. There is a question of how much overlap of the bursts is needed to obtain interpretable interference fringes. We were fortunate that two of the ScanSAR images along track 538 have significant burst overlap (up to 78%) and a moderate baseline of 450 m. An interesting aspect of this interferometric pair is that they have different PRFs. This produces a gradual change in burst alignment along the track from 78% at the start of the acquisition to 0% overlap after 18 bursts (Figure 8.5(a)). Phase recovery and coherence (Figure 8.5a, b) are best at the top of the swath and gradually worsen toward the bottom. A plot of row-averaged coherence versus burst overlap fraction (Figure 8.5(c)) illustrates that a maximum coherence of about 0.35 occurs where the burst overlap is greater than 50%. The coherence diminishes to below 0.2 at a burst overlap of 18%. The results show that good interferometric results can be achieved when the burst overlap is greater than about 50%.

8.4.1 M7.8 Gorkha Earthquake Imaged by ALOS-2 ScanSAR InSAR

ALOS-2 was the first L-band satellite to offer burst-aligned ScanSAR interferometry as a standard operating mode. The ScanSAR InSAR capabilities of ALOS-2 proved to be a capable tool for monitoring large continental earthquakes such as the Nepal sequence (Lindsey et al., 2015). The Himalayan region has the largest relief on the Earth, is densely vegetated, and has snow-capped peaks. The L-band radar enables adequate InSAR correlation in the vegetated areas, while tight baseline control of the spacecraft to better than 120 m in these examples (Figure 8.6) minimizes the unwanted phase due to errors in the extreme topography. Finally, the onboard navigation is now accurate enough to provide better than 70% overlap of the ScanSAR bursts between reference and repeat images. This results in

Downloaded from https://www.cambridge.org/core. IP address: 189.217.92.64, on 11 Feb 2026 at 15:51:46, subject to the Cambridge Core terms of use, available at https://www.cambridge.org/core/terms. https://www.cambridge.org/core/product/1F8951EFC610A352837B95E4DAEFBAEB

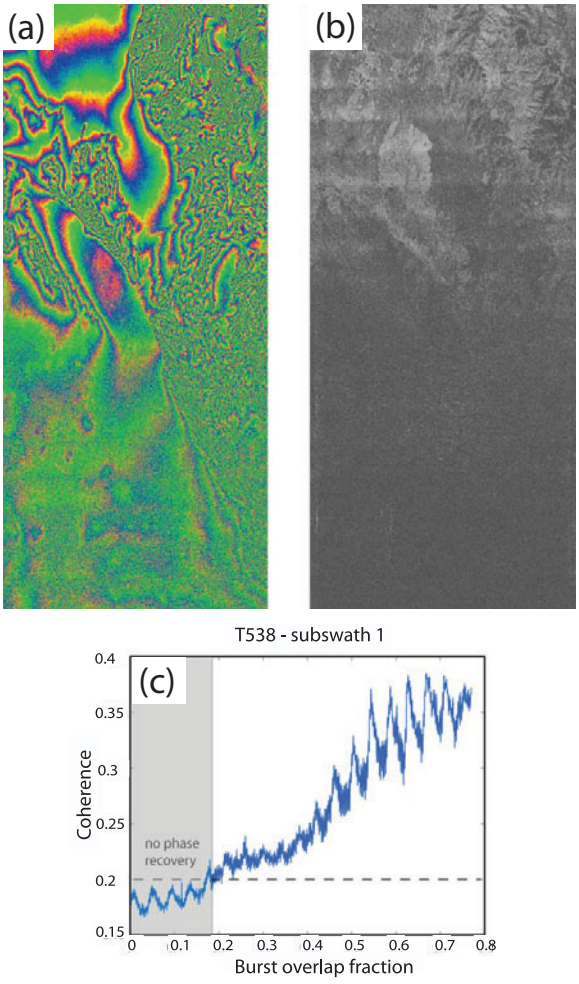

Figure 8.5 ScanSAR to ScanSAR interferogram for subswath 4 of track 538 across the Los Angeles basin. The perpendicular baseline is 450 m and the time interval is 92 days. No topographic phase has been removed. (a) Interferometric phase is high at the top of the swath where burst overlap is large and lower toward the bottom. (b) Coherence also decreases from top to bottom as burst overlap decreases. (c) Row-averaged coherence versus burst overlap.

350 km wide interferograms that can completely image the deformation resulting from these major events. This wide swath also enables a short 14-day repeat interval that enabled the collection of SAR images between the M7.8 and M7.3 events. Slip models based on the deformation spanning the M7.8 event were used to estimate the Coulomb stress that probably triggered the M7.3 event (e.g. Galetzka et al. (2015)). The slip gap observed between the two ruptures (Figure 8.6(b)) can now be monitored for coseismic slip or aseismic creep. The large vertical displacement

Downloaded from https://www.cambridge.org/core. IP address: 189.217.92.64, on 11 Feb 2026 at 15:51:46, subject to the Cambridge Core terms of use, available at https://www.cambridge.org/core/terms. https://www.cambridge.org/core/product/1F8951EFC610A352837B95E4DAEFBAEB

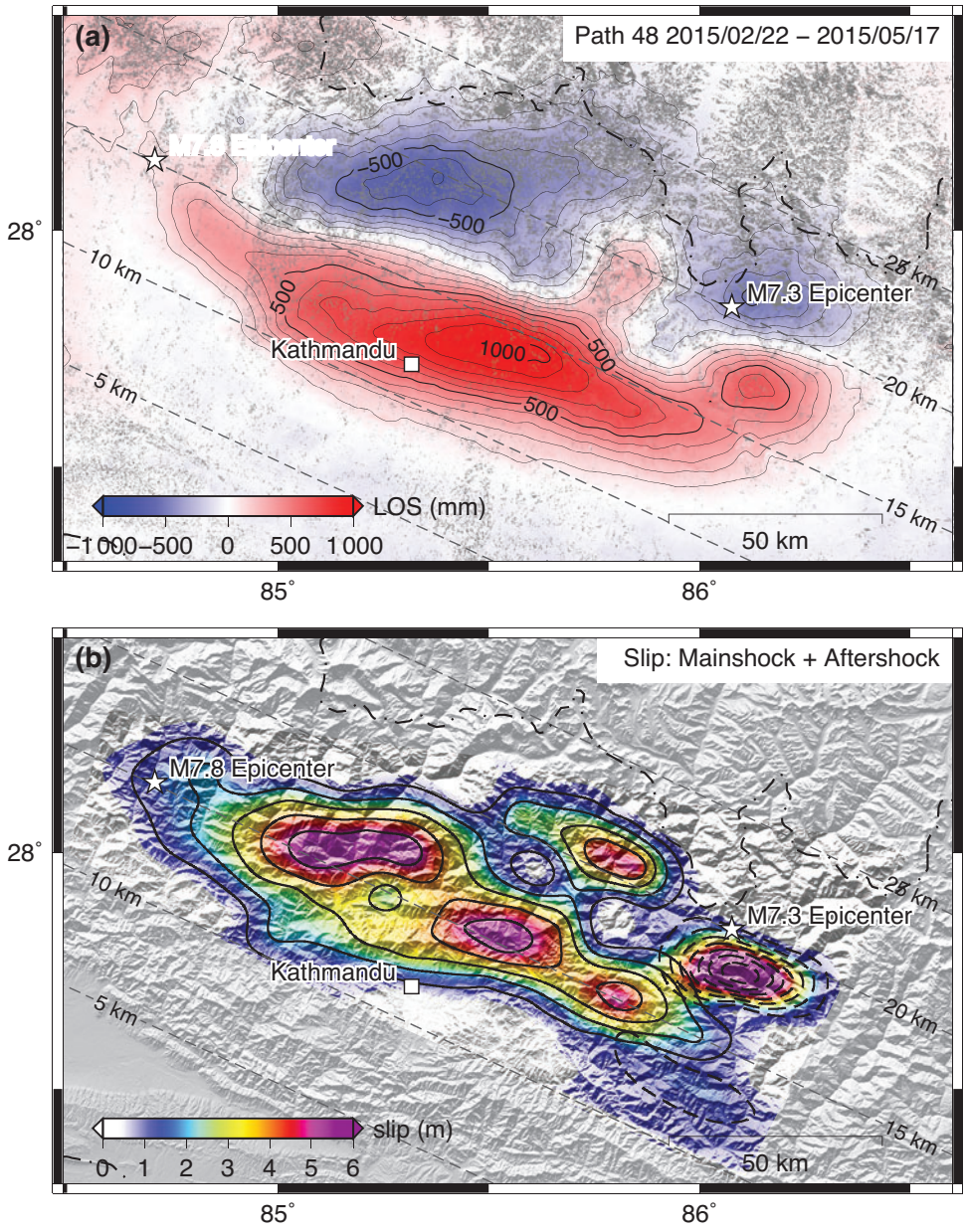

Figure 8.6 (a) Combined surface deformation caused by two major earthquakes in Nepal (M7.8 Gorkha earthquake and a M7.3 aftershock) as measured by the wide swath mode of the ALOS-2 InSAR satellite (Lindsey et al., 2015). The overall extent of the combined rupture is 170 km. This LOS map represents mainly vertical motion with a trough-to-peak amplitude of 1.6 m. (b) Slip inversion based on the modeling approach of Galetzka et al. (2015) shows a peak slip of more than 6 m at a depth of 18 km. The complete InSAR coverage shows that the shallow portion of this megathrust zone remained locked and will slip in the future.

Downloaded from https://www.cambridge.org/core. IP address: 189.217.92.64, on 11 Feb 2026 at 15:51:46, subject to the Cambridge Core terms of use, available at https://www.cambridge.org/core/terms. https://www.cambridge.org/core/product/1F8951EFC610A352837B95E4DAEFBAEB

caused by this thrust event can induce significant viscoelastic deformation over the next years to decades that we hope can be accurately imaged and modeled.

8.5 Terrain Observation by Progressive Scans

8.5.1 Introduction

The second type of wide-swath interferometry discussed in this chapter is Terrain Observation with Progressive Scans (TOPS). The TOPS observation mode is primarily associated with the Sentinel-1 satellites, which are providing regular 6-, 12-, or 24-day acquisitions over all tectonically active land areas. Unlike previous SAR missions, the data from Sentinel-1 are completely open and free through the Copernicus Dataspace Ecosystem (https://dataspace.copernicus.eu/). The short repeat cycle of the satellites was made possible by operating in a burst radar acquisition mode that covers a wide swath of ~230 km. As discussed in Chapter 2, the width of the swath is limited by the length of the antenna and the standard satellites have a maximum swath of ~80 km. One way to increase the swath width is to operate the radar in a ScanSAR mode as described in Section 8.4.1. However, the target may get scattered along azimuth and the amplitude image is subject to modulation or scalloping due to the intermittent radar bursts. A more uniform amplitude is obtained using the TOPS mode (Meta et al., 2010), that electronically steers the antenna from backward looking to forward looking each time a burst acquisition is made within a subswath (Figure 8.7). The steering angle is designed to seamlessly connect the bursts from the same subswath and across the subswaths the continuous coverage is enabled by sufficient overlap from the observations.

While this approach results in a more uniform amplitude radar image, the squint angle is constantly changing, which leads to large variations in the Doppler rate (±2 250 Hz). Traditional radar interferometry is usually performed using data close to zero Doppler or at a Doppler that is much smaller than the PRF. Indeed, to achieve phase coherence of the interferogram, the Doppler centroids of the reference and repeat image must overlap by at least 20% as described in Section 8.4.1. Data acquired in the TOPS mode sweeps over nine PRF intervals during one scan as shown in Figure 8.8(a). Thus, any resampling of the radar images requires deramping the data first. Then one can perform regular operations on the data and restore the ramping function afterward.

Another problem caused by the antenna steering is that it dramatically increased the phase sensitivity to azimuthal misregistration at burst boundaries. Typically, the small misregistrations are likely from the slight difference in the orbital velocity, or burst timing of the reference and repeat acquisitions. However, due to the large difference between the Doppler at the upper and lower edge of each burst ($f_u - f_l$), a small azimuthal misregistration will result in a significant phase difference. Indeed

Downloaded from https://www.cambridge.org/core. IP address: 189.217.92.64, on 11 Feb 2026 at 15:51:46, subject to the Cambridge Core terms of use, available at https://www.cambridge.org/core/terms. https://www.cambridge.org/core/product/1F8951EFC610A352837B95E4DAEFBAEB

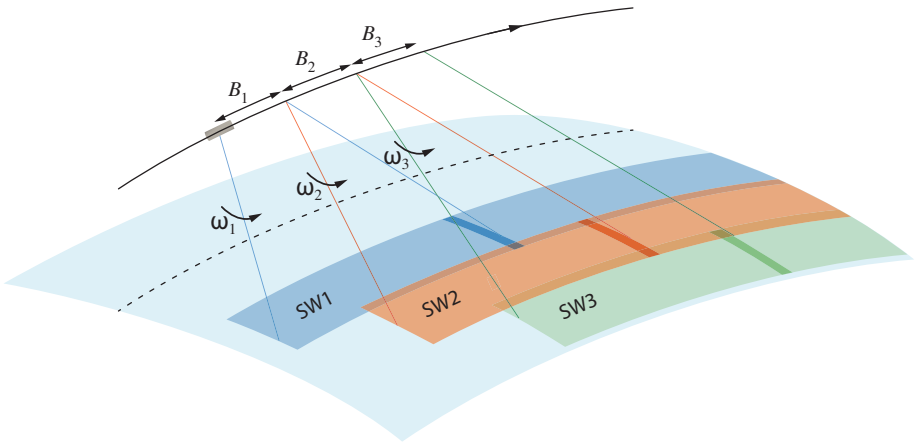

Figure 8.7 Diagram of the TOPS acquisition geometry where v is the velocity of the satellite, B is the burst duration, and ω is the steering rate. Each subswath is about 80 km wide and each burst covers a 20 km distance in the along-track direction (Mittermayer et al., 2010). There is some overlap between the subswaths and bursts to provide a seamless mosaic of amplitude and phase. The phase difference in the overlap areas can be used to refine the image alignment. This is called *enhanced spectral diversity*.

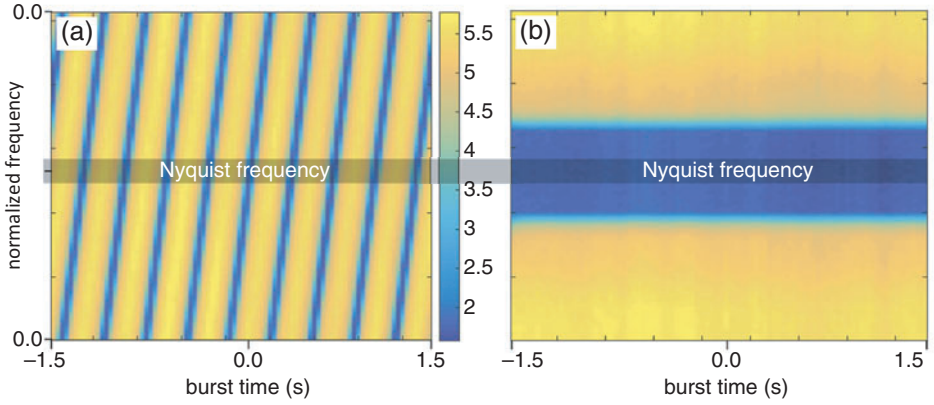

Figure 8.8 Spectrogram of one burst of TOPS-mode data plotted on a log color scale. (a) Original spectrogram of a single burst of TOPS data wraps around the Nyquist frequency nine times. (b) Spectrogram after deramping has low power close to the Nyquist, which enables accurate resampling.

one can use the phase difference ϕ in the small burst overlap areas to estimate the azimuth shift Δa needed to reduce this phase mismatch

$$\Delta a = \mathrm{PRF}\frac{\phi}{2\pi\left(f_u - f_l\right)} \tag{8.1}$$

Downloaded from https://www.cambridge.org/core. IP address: 189.217.92.64, on 11 Feb 2026 at 15:51:46, subject to the Cambridge Core terms of use, available at https://www.cambridge.org/core/terms. https://www.cambridge.org/core/product/1F8951EFC610A352837B95E4DAEFBAEB

For S1A, the top-to-bottom Doppler difference is 4 500 Hz and the effective PRF is 486 Hz. Keeping the phase mismatch below 0.54 radian (2.8 mm), for example, requires azimuth alignment to 0.01 pixel accuracy. This method is called *enhanced spectral diversity* and the implementation is discussed further in Section 8.5.4.

8.5.2 Traditional Image Alignment Fails with TOPS-Mode Data

The traditional approach to InSAR image alignment is done in three steps: (1) First, the orbital information is used to make a rough (1-2 pixel accuracy) estimate of the offset of the reference and secondary images. (2) Then 2-D cross-correlation of sub-patches of data (e.g., 64 by 64 pixels) is used to estimate the affine transformations (Equation 8.2) needed to map the secondary image onto the reference image. As described in Chapter 3, the trajectories of the reference and secondary images are very smooth so their differences in both the range dr and azimuth da coordinates are well described by the following equations

$$\begin{aligned} dr &= c_0 + c_1 r_m + c_2 a_m \\ da &= c_3 + c_4 r_m + c_5 a_m \end{aligned} \tag{8.2}$$

where r_m and a_m are the range and azimuth coordinates of the reference image and there are six unknown coefficients c_0 to c_5. The coefficients are determined by fitting planes to the range and azimuth offset data derived from the cross-correlation of the sub-patches. It seems reasonable that six parameters are sufficient to account for the orbital differences because the orbit is well described by a six-element state vector, and the differences in the reference and secondary state vectors are very small over the time span of the radar acquisition. (3) The final step is to use a 2-D sinc-function interpolator to resample the secondary image into the coordinates of the reference image (*resamp* in GMTSAR). The accuracy of the alignment depends on the coherence between the reference and repeat images. When coherence is high, the two images can be aligned to 0.1 pixel accuracy. When the coherence is low, the alignment can be worse than 1.0 pixel. The method fails when the reference and secondary images have poor correlation.

This standard approach to image alignment works well on swath-mode SAR data as well as ScanSAR data; however, it fails with the TOPS-mode data for two reasons. First, the traditional method can only achieve 0.1 pixel alignment accuracy, but as discussed earlier, the alignment must be better than 0.01 pixel to keep the phase mismatch between the burst boundaries below 2.8 mm. Second, because the azimuth spectrum of the TOPS-mode data has frequencies well above the Nyquist sampling frequency of the single look complex (SLC) data (Figure 8.8(a)), the standard sinc-function interpolation fails.

Downloaded from https://www.cambridge.org/core. IP address: 189.217.92.64, on 11 Feb 2026 at 15:51:46, subject to the Cambridge Core terms of use, available at https://www.cambridge.org/core/terms. https://www.cambridge.org/core/product/1F8951EFC610A352837B95E4DAEFBAEB

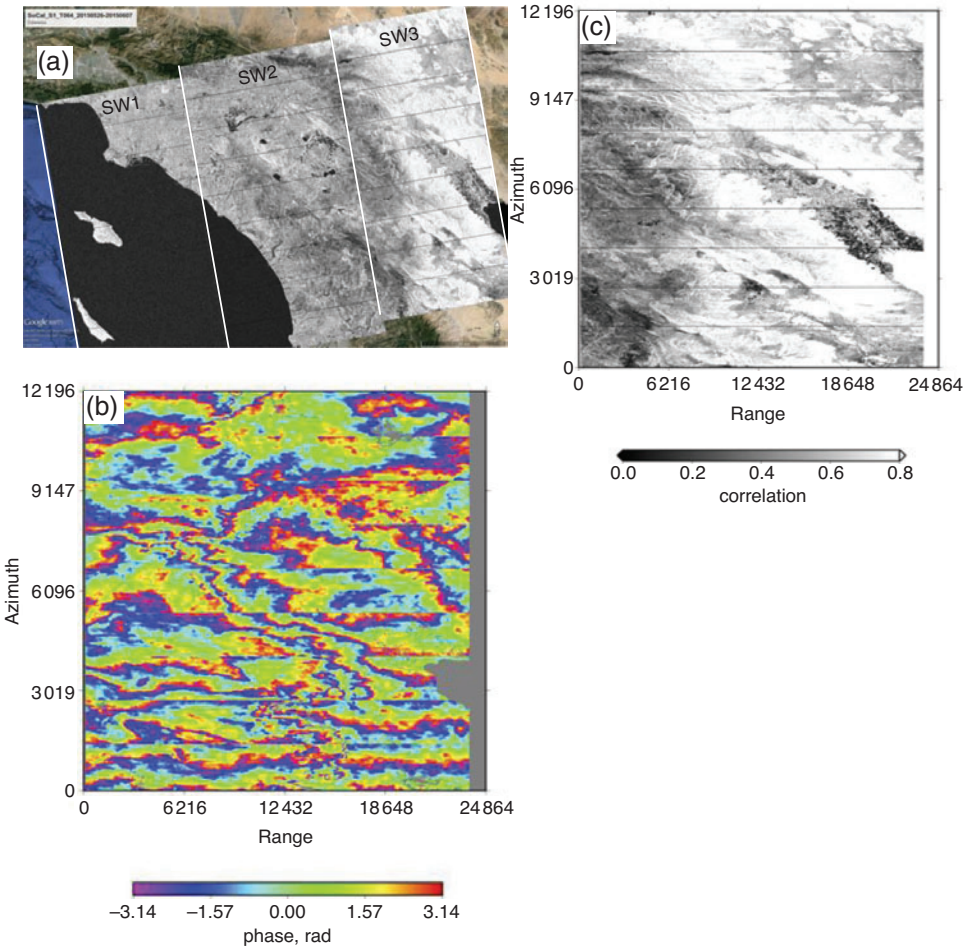

Figure 8.9 (a) Coherence image of test area for track 064 dates 20150526 and 20150607. The S1A data have three subswaths with nine bursts each. (b) InSAR phase of subswath 3 in radar coordinates shows phase mismatch at burst boundaries as well as banding within each burst. (c) InSAR coherence is generally high with eight lines of low coherence due to the phase mismatch as well as banding within each burst due to poor performance of the sinc interpolator across the Nyquist frequency.

An example interferogram of using this traditional approach to align a reference and secondary SLC image of S1A TOPS mode is shown in Figure 8.9. There are two main problems that need to be corrected. The first is that there are large phase mismatches at the eight boundaries between the nine bursts. Second, because the azimuth spectrum of the TOPS-mode data has Doppler far beyond the Nyquist frequency of the SLC data (Figure 8.8(a)), the standard sinc-function interpolation will introduce aliasing to the resampled data.

Downloaded from https://www.cambridge.org/core. IP address: 189.217.92.64, on 11 Feb 2026 at 15:51:46, subject to the Cambridge Core terms of use, available at https://www.cambridge.org/core/terms. https://www.cambridge.org/core/product/1F8951EFC610A352837B95E4DAEFBAEB

8.5.3 Geometric Alignment Approach

Overcoming these two issues requires two new approaches: geometric alignment based on a precise orbit (Sansosti et al., 2006) and deramping of the SLC data prior to interpolation. The Sentinel-1 SAR data are provided with a high-accuracy orbit (~2–3 cm radial and cross track, ~5 cm along-track (Fernandez et al., 2015) available at https://dataspace.copernicus.eu/). This high accuracy in orbital determination enables purely geometric registration to remove almost all the phase mismatch at the burst boundaries. The underlying idea is to calculate the exact radar coordinates for the same set of terrain points utilizing information from the precise reference and secondary orbits. The differences between the coordinates reflect the needed shifts to perform coregistration.

The algorithm for deramping the secondary image prior to interpolation is described in the ESA documentation (Miranda, 2015), and all the parameters are provided with the metadata that accompany the SAR imagery files. The ramps are restored to each burst after resampling, thus any possible inaccuracies in the de-ramping function will introduce no error to the radar phase. Best results are achieved if the de-ramping and re-ramping are only performed on secondary images, leaving the master image unchanged. De-ramping, interpolation, and re-ramping are performed burst by burst, after which all bursts within one subswath are stitched together to generate one SLC image. Compared to the traditional cross-correlation method, this geometric approach could essentially apply coregistration pixel by pixel instead of fitting the affine transformation parameters (Table 8.3).

The overall algorithm for coregistering the TOPS-mode Sentinel-1 data (Figure 8.10) can be summarized as follows:

1. Construct a low-resolution (~12 arc-seconds) digital elevation model covering the area of the SLC images. If no elevation data are available (e.g., Antarctica), a guess at the mean elevation can help with coregistration.

Table 8.3 *Example of precisely estimated range (r_m) and azimuth (a_m) along with range change (dr) and azimuth change (da) from master image to secondary image.*

r_m	dr	a_m	da
21612.658170	68.048382	9.502554	5.581971
21545.310230	68.050767	5.672641	5.582379
21476.796745	68.049944	1.840498	5.582791
21589.753434	68.052334	35.595495	5.582574
21522.753310	68.054712	31.765366	5.582985
21454.950368	68.057071	24.101007	5.583396
21386.133332	68.059421	16.432719	5.583806

Downloaded from https://www.cambridge.org/core. IP address: 189.217.92.64, on 11 Feb 2026 at 15:51:46, subject to the Cambridge Core terms of use, available at https://www.cambridge.org/core/terms. https://www.cambridge.org/core/product/1F8951EFC610A352837B95E4DAEFBAEB

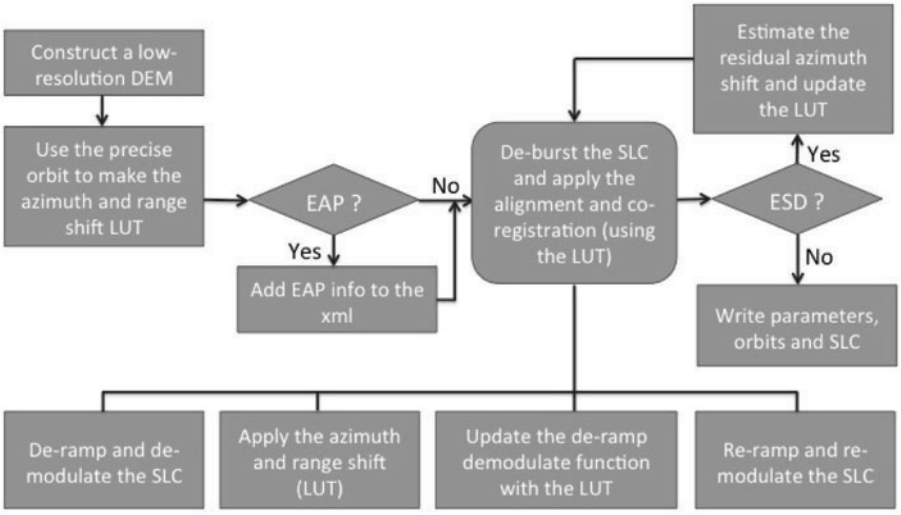
Construct a low-resolution DEM
Use the precise orbit to make the azimuth and range shift LUT
EAP ?
No
Yes
Add EAP info to the xml
De-burst the SLC and apply the alignment and co-registration (using the LUT)
Estimate the residual azimuth shift and update the LUT
Yes
ESD ?
No
Write parameters, orbits and SLC
De-ramp and de-modulate the SLC
Apply the azimuth and range shift (LUT)
Update the de-ramp demodulate function with the LUT
Re-ramp and re-modulate the SLC

Figure 8.10 Preprocessing chain for TOPS data using precise orbits and point-by-point geometric coregistration. In the flowchart, LUT denotes look-up table, EAP is short for elevation antenna pattern correction, which is only needed for SLC data processed with early Instrument Processing Facility (IPF) version. ESD is short for enhanced spectral diversity.

2. Use the precise orbital information to map each pixel of longitude, latitude, and height into the range and azimuth of the radar pixel coordinates. This is done as described in Section 3.7 where one finds the azimuth of the closest range (i.e., zero Doppler) on the orbital trajectory to each topography pixel – first using a golden section search algorithm and then performing a polynomial refinement. Step 2 is done for both the master and secondary images.
3. Construct two tables (i.e., grids) of range (azimuth) difference, secondary minus master, versus range and azimuth. An example is provided in Table 8.3. These grids provide a mapping of the secondary image onto the master image. This mapping is then used for pixel-by-pixel coregistration. An alternative approach is to estimate the six-parameter affine transformation described in Equation 8.2.
4. Deburst the master image to make a continuous SLC. This is done by calculating the boundaries between bursts using the azimuth time for each line in the burst and eliminating overlapping lines. Stitching of the bursts is done using the center of the overlapped area between bursts.
5. Read a burst of secondary SLC data, compute the deramp-demodulating function following the ESA documentation (Miranda, 2015), and apply the deramp-demodulation function to the SLC data to remove the ramp induced by the antenna steering. An example of a deramped spectrum for a burst is shown in Figure 8.8(b). This removal enables proper resampling of the secondary image.

Downloaded from https://www.cambridge.org/core. IP address: 189.217.92.64, on 11 Feb 2026 at 15:51:46, subject to the Cambridge Core terms of use, available at https://www.cambridge.org/core/terms. https://www.cambridge.org/core/product/1F8951EFC610A352837B95E4DAEFBAEB

6. Use a 2-D sinc function to interpolate the fractional part of the range and azimuth shift of the secondary SLC into the coordinates of the master image, using grids of offsets created from the look-up table developed in step 3.
7. Recompute the deramp-demodulate function applying the same range and azimuth offsets and output the coregistered burst of the secondary SLC data.
8. Repeat steps 5–7 until all bursts of the secondary SLC from the same subswath are coregistered. Deburst the secondary SLC and stitch at the center of the overlapped area between bursts.
9. If the alignment requires further coregistration using enhanced spectral diversity, steps 4–8 are replaced with outputting the overlapped area between the bursts, that is, forward-looking SLCs (SLCH) and backward-looking SLCs (SLCL). They are used to compute double-difference interferograms and estimate residual shifts needed to update the offset maps in step 3. Then perform regular coregistration as from step 4 to step 8.

   At this point, we have master and secondary SLCs that are coregistered to the accuracy of the orbit data. Note that this accuracy is far better than 0.1 pixel so the interferometric coherence between the reference and secondary should be optimal, assuming no range/azimuth shifts due to changes in the atmosphere and ionosphere between the reference and secondary imaging times. An example of the geometrically aligned interferogram for the same data as shown in Figure 8.9(b,c) is shown in Figure 8.11. Note the loss of coherence near burst boundaries is due to the sharp Doppler change. A remarkable result of this geometric alignment approach is that one can align many secondaries to a single master so after this alignment, any two of the secondary images can be used to form highly coherent interferograms. This greatly improves processing efficiency for large stacks of Sentinel-1 InSAR data.

8.5.4 Enhanced Spectral Diversity

In a few cases, the along-track orbit error (or time tag error) may result in an interferogram having an unacceptable phase mismatch at the burst boundaries. Along-track mismatch can also occur if there is motion of the surface between the reference and repeat images perhaps due to motion of the tectonic plate or ice relative to the orbit reference frame. If there is adequate coherence between the reference and repeat SAR images, the phase mismatch can be used to estimate the azimuth shift of the repeat image (Prats-Iraola et al., 2012). The phase difference ϕ in the overlap zones can be extracted from a double-difference interferogram.

$$s_{sd} = \left(s_{u,m} \cdot s_{u,s}^{*}\right) \cdot \left(s_{l,m} \cdot s_{l,s}^{*}\right)^{*} \tag{8.3}$$

$$\phi = \arg\left(s_{sd}\right) \tag{8.4}$$

Downloaded from https://www.cambridge.org/core. IP address: 189.217.92.64, on 11 Feb 2026 at 15:51:46, subject to the Cambridge Core terms of use, available at https://www.cambridge.org/core/terms. https://www.cambridge.org/core/product/1F8951EFC610A352837B95E4DAEFBAEB

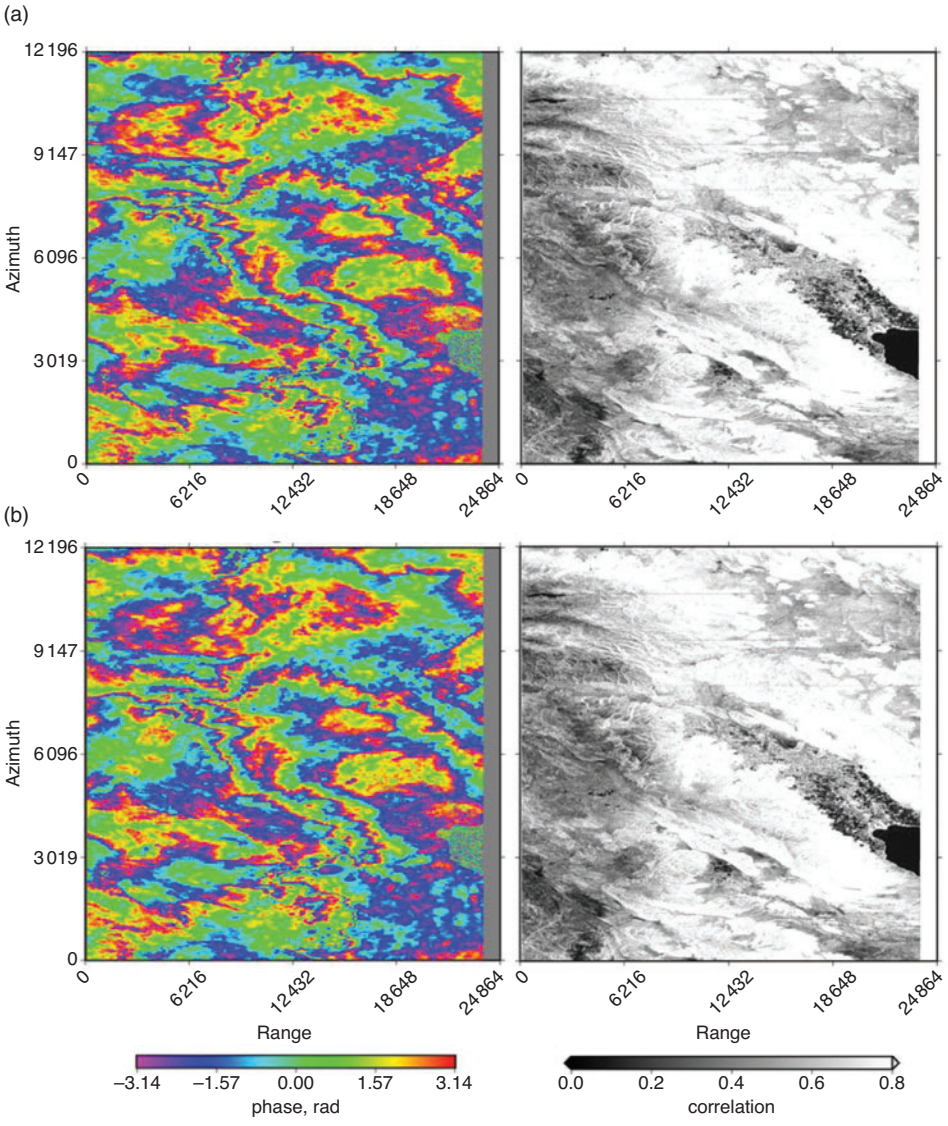

Figure 8.11 Interferogram and coherence of SW3 of the Southern California pair (20150526-20150607) processed with alignment/registration by six-parameter affine transformation (a) and point-by-point (b). The phase mismatch at burst boundaries is no longer visible. There is a slightly lower correlation at the burst boundaries reflecting a subtle phase offset. The differences between the six-par method and the PBP method are very small except in cases of long InSAR baseline and high-amplitude topography.

Downloaded from https://www.cambridge.org/core. IP address: 189.217.92.64, on 11 Feb 2026 at 15:51:46, subject to the Cambridge Core terms of use, available at https://www.cambridge.org/core/terms. https://www.cambridge.org/core/product/1F8951EFC610A352837B95E4DAEFBAEB

where, for example, $s_{u,m}$ is the SLC of the upper portion of the overlap zone for the master. In practice, one computes and filters double-difference interferograms for all the pixels in multiple overlap zones. Then the median phase from all the pixels is used in Equation 8.1 to calculate a single residual azimuth shift to update the azimuth shift *da* in Table 8.3. In some extreme cases, there is a bivariate residual azimuthal shift, likely due to strong perturbation from the ionosphere; one could use an additional range-dependent, azimuth shift parameter to account for the spatial variation (Wang et al., 2017). The major problem with ESD is that it requires adequate coherence between every secondary image and the master image, though one can improve the ESD accuracy by forming a network of estimates, thus mitigating the effect from loss of coherence (Fattahi et al., 2017). Another problem with enhanced spectral diversity (ESD) is that it absorbs all components that cause phase discontinuities and treats them as misregistration. In reality, actual ground deformation in the azimuthal direction could cause discontinuities between bursts, either from earthquakes (Grandin et al., 2016) or tectonic motion (Yague-Martinez and Prats-Iraola, 2022). In such a scenario, they should not be treated as misregistration errors, but as useful signals. We will discuss this approach of burst overlap interferometry (BOI) in Chapter 10.

8.6 SweepSAR

The third type of wide-swath interferometry discussed in this chapter is SweepSAR (Freeman et al., 2009). The ScanSAR and TOPS-mode radars achieve a wider swath by subsampling the along-track illumination of the Earth. For example, the ScanSAR-mode of the ALOS-1/2 radars achieves a 350 km wide swath using five subswaths and samples these subswaths only 1/5 of the time (Figure 8.4). Similarly, the TOPS mode has three subswaths and the radar under-samples the Doppler spectrum by a factor of 3 in the along-track direction to achieve a 250 km wide swath (Figure 8.7). These approaches have fewer looks per surface area than the strip-mode approach, so the data are noisier in both amplitude and phase.

An alternate approach that achieves a 240 km wide swath and also has the full resolution of a strip-mode SAR has been proposed by Freeman et al. (2009) and will be implemented in the upcoming (expected launch in 2025) NISAR mission (Rosen et al., 2017). This is called SweepSAR and it uses a large reflector antenna (12 m in diameter) combined with a phased array, scan-on-receive, to enable a 240 km wide swath at full resolution (Figure 8.12). On transmit, the radar illuminates the full 240 km-wide swath. To achieve full along-track resolution, the inter-pulse interval 1/PRF is shorter than the time it takes for the pulse to sweep from the near-range to the farrange. To avoid overlap of the pulses in time, the receive array can focus narrowly in the cross-track direction. A very simplified schematic of how

Downloaded from https://www.cambridge.org/core. IP address: 189.217.92.64, on 11 Feb 2026 at 15:51:46, subject to the Cambridge Core terms of use, available at https://www.cambridge.org/core/terms. https://www.cambridge.org/core/product/1F8951EFC610A352837B95E4DAEFBAEB

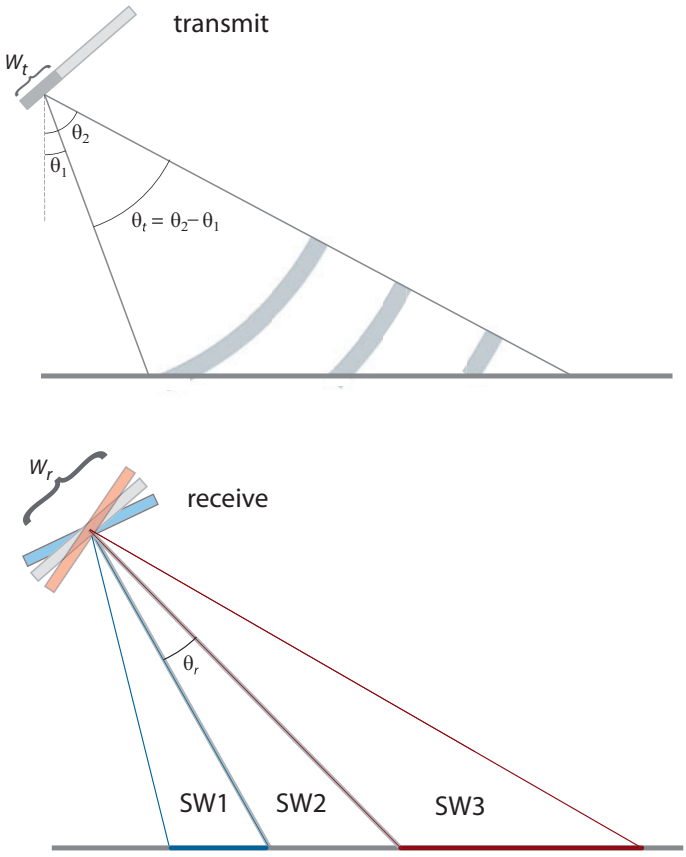

Figure 8.12 Highly schematic diagram looking along the flight direction of the spacecraft of the SweepSAR method. The full width of the antenna (or reflector in the case of NISAR) is W_r. On transmit, a fraction of that width W_t is used to create a relatively wide beam angle θ_t thus illuminating a wide swath. On receive, the full antenna width is used W_r to create a relatively narrow beam angle θ_r that records only the reflections over a narrow subswath (SW1, 2, or 3). The antenna is not actually turned to change the receive beam position; this is performed using a phase array. Note that a reflector is used on NISAR. When the pulse is transmitted, all the T-modules can be used for maximum power and maximum SNR. The wide transmit array creates a narrow beam on the reflector W_t, resulting in a relatively wide beam angle to illuminate the wide swath. Similarly, on receive, a fraction of the R-modules are used that have a broader angular aperture in the reflector, which results in a narrower beam on the ground.

this is achieved is shown in Figure 8.12. In this schematic modified from Freeman et al. (2009), the planar antenna has a width W_r, that is similar to the length of a normal SAR antenna L (12 m). Full swath illumination in the cross-track direction is achieved by using a fraction of the full antenna width W_t. From the analysis in

Downloaded from https://www.cambridge.org/core. IP address: 189.217.92.64, on 11 Feb 2026 at 15:51:46, subject to the Cambridge Core terms of use, available at https://www.cambridge.org/core/terms. https://www.cambridge.org/core/product/1F8951EFC610A352837B95E4DAEFBAEB

Chapter 2, $\sin\theta_t = \lambda/W_t$, so a smaller width, smaller than a normal strip-mode SAR, is needed to achieve a larger projection angle to illuminate the 240 km wide swath.

To avoid aliasing of the return pulses that are simultaneously reflected from the near, center, and far ranges, the full width of the antenna is used to divide the return energy into multiple beams (Figure 8.12). Beam 1 tracks the pulse over the subswath 1 (SW1), but the energy of this pulse will be outside beam 1 when it propagates to SW2 and SW3. Beam 2 tracks the pulse when it enters SW2 and beam 3 tracks the pulse when it enters SW3. This is a greatly simplified description of the SweepSAR method, but it illustrates some of the basic physics. NISAR has a 12 m diameter reflector that serves as the large planar antenna shown in Figure 8.12 and the transmit and receive arrays are located on the body of the spacecraft 9 meters below the reflector. The overall result of this marvel of engineering is a full-resolution strip-mode SAR that can achieve a wide swath. The 240 km wide swath can completely cover the Earth at the equator in 177 orbits, which corresponds to a 12-day repeat cycle. A standard strip-mode SAR has a repeat cycle 3–4 times longer.

8.7 Problems

1. ScanSAR is a technique to construct a very wide swath radar image by emitting a burst of ~300 radar pulses on a narrow subswath and systematically cycling the near range of each burst to illuminate five parallel subswaths ultimately forming a wide swath. Why is it not possible to simply illuminate the wide swath with continuous wide pulses? Hint: see Equation 2.16.
2. How can a standard strip-mode SAR processor be used to focus ScanSAR data? What are the advantages and disadvantages of this approach?
3. Phase coherence for regular swath-mode interferometry is only possible when the baseline between the reference and repeat images is less than the critical baseline and there is significant overlap in the Doppler spectra of the reference and repeat images. What additional attribute is needed to achieve phase coherence for ScanSAR interferometry?
4. How many different interferometric combinations are possible for 10 SAR images? For 100 SAR images? For n SAR images?
5. Derive Equation (8.1).
6. Give two reasons why the standard cross-correlation imaging matching approach is not adequate for TOPS-mode data?
7. Why must the bursts be deramped prior to sinc interpolation?
8. Why does a six-parameter affine transformation model work well when the interferometric baseline is small and the topography has low relief?

Downloaded from https://www.cambridge.org/core. IP address: 189.217.92.64, on 11 Feb 2026 at 15:51:46, subject to the Cambridge Core terms of use, available at https://www.cambridge.org/core/terms. https://www.cambridge.org/core/product/1F8951EFC610A352837B95E4DAEFBAEB

9

Troposphere, Ionosphere, and Tide Corrections

9.1 Contributions to Phase

Most scientists who construct interferograms are trying to measure surface deformation associated with the solid Earth or cryosphere. However, as discussed in Chapter 5, there are many contributions to the phase of an interferogram that may dominate the deformation signal. As a review, the contributions to the phase are:

$$\begin{aligned} \textit{phase} = {} & \textit{earth curvature} \text{ (almost a plane, known)} + \\ & \textit{topographic phase} \text{ (broad spectrum, known)} + \\ & \textit{surface deformation} \text{ (broad spectrum, unknown)} + \\ & \textit{orbit error} \text{ (almost a plane, largely known)} + \\ & \textbf{troposphere delay} \text{ (power law, unknown)} + \\ & \textbf{ionosphere advance} \text{ (often a plane or 20–40 km wavelength waves, unknown)} + \\ & \textbf{tides} \text{ (almost a plane, largely known)} + \\ & \textit{phase noise} \text{ (white spectrum, unknown)} \end{aligned} \tag{9.1}$$

In Chapter 5 we developed the geometry and methods to remove the contributions from the *curvature of the Earth* and *topography* using a precise orbit and a digital elevation model. These topographic phase contributions increase as the interferometric baseline increases. Modern synthetic aperture radar (SAR) missions have well-controlled interferometric baselines so given the accurate, near-global topography available today, these phase contributions can be accurately removed. The last contribution on the list, *phase noise*, is largely random in space. In Chapter 6 we discussed filtering and stacking approaches to reduce the phase noise. This chapter is focused on the three remaining contributions to the phase, including **tropospheric delay**, **ionospheric advance**, and **tides**.

Downloaded from https://www.cambridge.org/core. IP address: 189.217.92.64, on 11 Feb 2026 at 15:51:46, subject to the Cambridge Core terms of use, available at https://www.cambridge.org/core/terms. https://www.cambridge.org/core/product/1F8951EFC610A352837B95E4DAEFBAEB

9.1.1 Quiz – Where Is the Tectonic Signal?

Before moving into the details of what causes these unwanted phase contributions and how they can be removed or mitigated, we start with a quiz with 5 Sentinel-1 C-band interferograms crossing the San Andreas Fault and the Los Angeles basin (Figure 9.1). They all show interesting phase patterns. The question is, which interferogram shows the tectonic signal? At C-band, one fringe of phase corresponds to 28 mm delay or surface deformation away from the radar. We know from global navigation satellite system (GNSS) studies that the total deformation rate across this fault system is ~30 mm/yr so in 1 year we would expect to see ~10 mm of motion when projected into the line of sight (LOS) of the radar. This corresponds to about one third of one fringe per year. Since each of these interferograms has multiple fringes, the answer to the quiz is that none of the interferograms show any significant tectonic signal.

We can speculate on what causes the phase in each interferogram:

(a) This case has the smallest number of fringes amounting to a phase ramp of about –60 mm from the southwest to the northeast (i.e., the range is decreasing toward the northeast). We could attribute this to orbit error since it is almost a plane, but Sentinel-1 has orbit accuracy usually less than 30 mm so this could be a phase delay due to atmospheric pressure changes in the dry part of the troposphere or the ionosphere.
(b) This case has many wave-like signals with amplitudes of 10–20 mm. These are most likely due to gravity waves in the troposphere.
(c) This case has many fringes that correlate with the topography (4–5 fringes or up to 140 mm). These signals are probably due to a change in the water vapor in the atmosphere at levels less than the highest topography. This layered water vapor effect is discussed later.
(d) This case has a very flat phase except in the mountain areas inside the red box. The phase associated with the highest topography is decorrelated. This could be due to snow or ground freezing at the highest elevation. In addition, this case shows a lower phase (~28 mm) in the Los Angeles basin that could be due to differences in the layered water vapor.
(e) The final case has multiple fringes that are not correlated with topography and have mainly large spatial scales. This could be due to changes in the total electron content (TEC) in the ionosphere, which affect the speed of the radar waves. The satellite orbiting at 700 km is just above the maximum electron density in the ionosphere so small spatial scales in TEC will be smoothed during the construction of the synthetic aperture (~5 km).

Downloaded from https://www.cambridge.org/core. IP address: 189.217.92.64, on 11 Feb 2026 at 15:51:46, subject to the Cambridge Core terms of use, available at https://www.cambridge.org/core/terms. https://www.cambridge.org/core/product/1F8951EFC610A352837B95E4DAEFBAEB

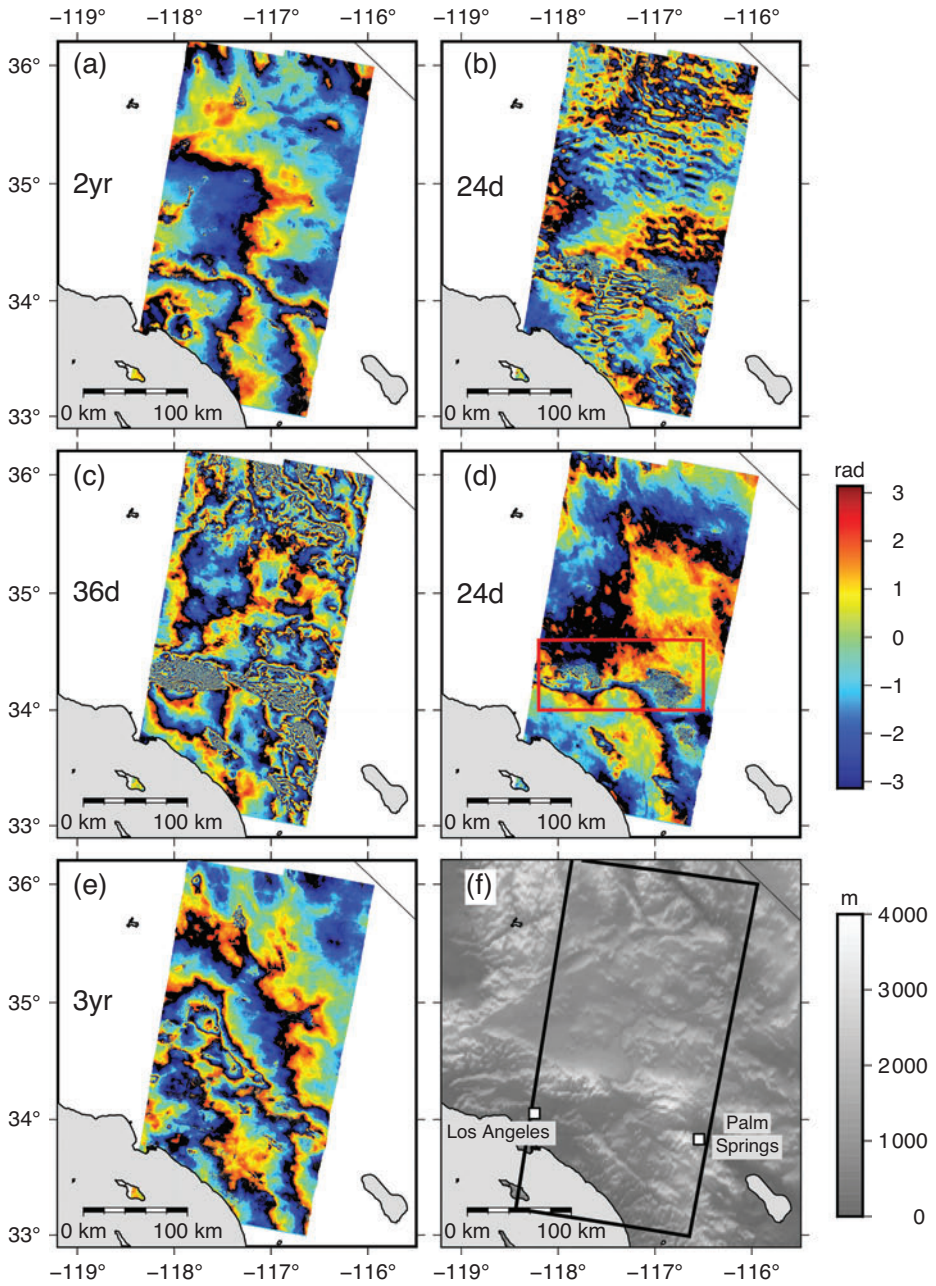

Figure 9.1 Example interferograms from Sentinel-1 wide-swath data across the Mojave Desert to the northeast and the Los Angeles basin to the southwest. The San Andreas Fault system crosses this track in a northwest direction passing through Palm Springs. Red box marks the location of the high mountains of Southern California.

Downloaded from https://www.cambridge.org/core. IP address: 189.217.92.64, on 11 Feb 2026 at 15:51:46, subject to the Cambridge Core terms of use, available at https://www.cambridge.org/core/terms. https://www.cambridge.org/core/product/1F8951EFC610A352837B95E4DAEFBAEB

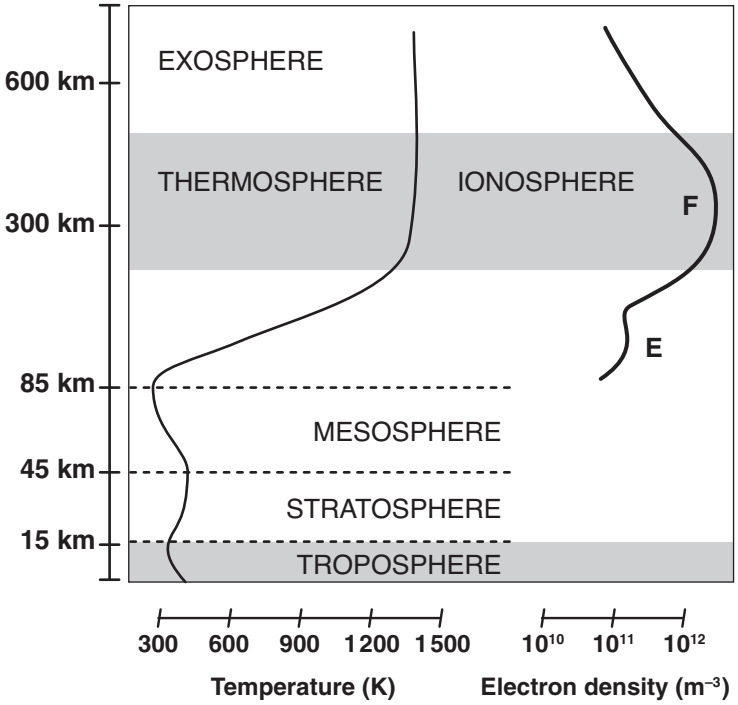

Figure 9.2 Layers of the atmosphere and ionosphere. The main layers affecting the propagation of microwaves (gray boxes) are the troposphere and the F-layer of the ionosphere. Adapted from Liang et al., 2019. Reprinted with permission from *IEEE Transactions on Geoscience and Remote Sensing*.

In the remainder of this chapter we will discuss the basic physics and properties of the troposphere and ionosphere (Figure 9.2) as well as large-scale surface deformation due to solid Earth tides. In addition, we discuss ways to correct for, or at least mitigate, the unwanted noise sources.

9.2 Refractive Index of the Troposphere and Ionosphere

So far, we have assumed that the electromagnetic waves travel at the speed of light c as they propagate from the antenna to the ground and back. However, the speed varies because of the variations in pressure, temperature, and water vapor in the troposphere as well as the free electrons in the ionosphere as shown in Figure 9.3. The relevant parameter is the refractive index n, which is the ratio of the speed of light to the phase velocity.

$$v_p = \frac{c}{n}. \tag{9.2}$$

Downloaded from https://www.cambridge.org/core. IP address: 189.217.92.64, on 11 Feb 2026 at 15:51:46, subject to the Cambridge Core terms of use, available at https://www.cambridge.org/core/terms. https://www.cambridge.org/core/product/1F8951EFC610A352837B95E4DAEFBAEB

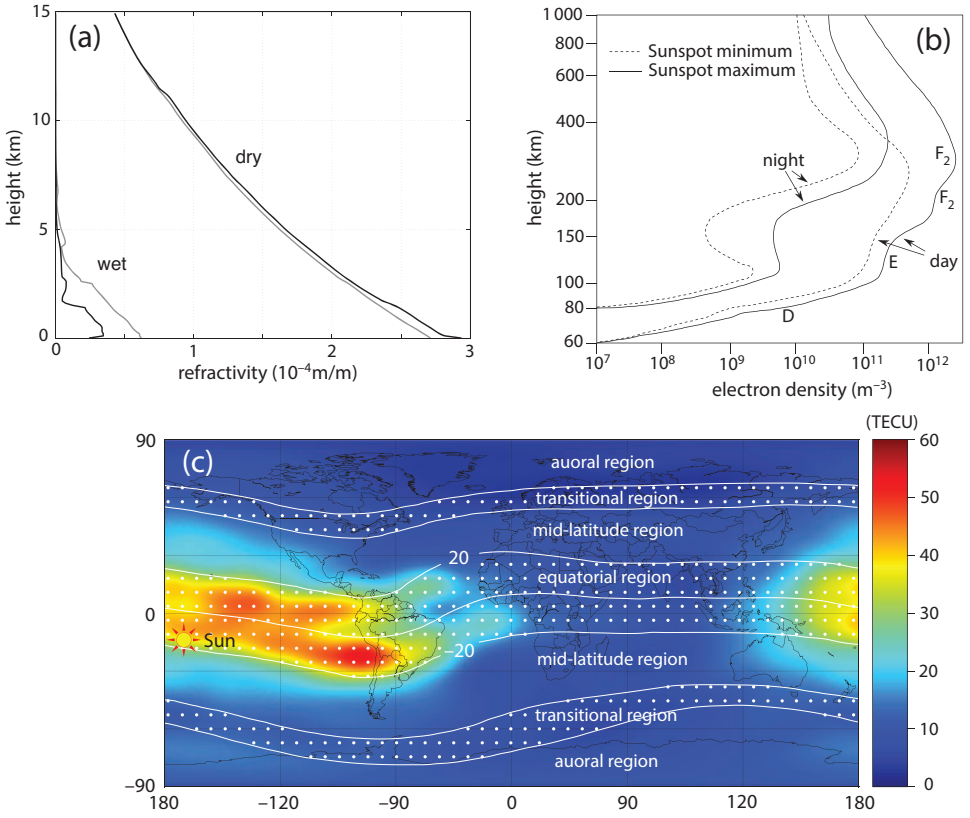

Figure 9.3 (a) The troposphere of the Earth extends from the surface to an elevation of about 15 km. Dry and wet refractivity versus height for two scenarios illustrates temporal variations (Pany, 2003). (b) Typical number density of free electrons in the D, E, and F layers of the ionosphere versus height for day and night, as well as solar maximum and minimum (from Liang et al., 2019) (c) Data from over 100 continuously operating GPS receivers in a global network are being used to produce global maps of the ionosphere's TEC (https://iono.jpl.nasa.gov/) (from Liang et al., 2019). One TEC Unit (TECU) is 10^{16} electrons m^{-2}. These global ionosphere maps (GIM) provide instantaneous "snapshots" of the global TEC distribution that can be used for a first-order correction for the largest spatial scale variations in the ionosphere. Reprinted with permission from *IEEE Transactions on Geoscience and Remote Sensing*.

The refractive index in a vacuum is 1. We are interested in the delay of the radar wave along a one-way vertical path between the surface of the Earth z_o and the radar at an altitude of H. The travel time increase is

$$\Delta t = \int_{z_o}^{H} \frac{1}{v_p\,(z)} dz - \int_{z_o}^{H} \frac{1}{c} dz = \frac{1}{c} \int_{z_o}^{H} [n\,(z) - 1]\, dz. \tag{9.3}$$

Downloaded from https://www.cambridge.org/core. IP address: 189.217.92.64, on 11 Feb 2026 at 15:51:46, subject to the Cambridge Core terms of use, available at https://www.cambridge.org/core/terms. https://www.cambridge.org/core/product/1F8951EFC610A352837B95E4DAEFBAEB

This corresponds to an excess path increase L of

$$L = \int_{z_o}^{H} [n(z) - 1]\, dz. \tag{9.4}$$

Given this excess path in the vertical, and assuming the lateral variation in the refractivity is smooth, one can compute the excess phase in the interferogram as a two-way phase increase of

$$\Delta\phi = L\frac{4\pi}{\lambda \cos\theta} \tag{9.5}$$

where θ is the local incidence angle of the radar. Incidence angle is used rather than look angle (see Section 5.4) because most of the troposphere is close to the ground rather than the satellite. We will use look angle for the ionosphere correction because the F-layer of the ionosphere is closer to the satellite.

Since the refractive index is usually slightly greater than 1, it is customary to introduce the refractivity as $N = 10^6 (n - 1)$. The refractivity of the troposphere and ionosphere is given by the following equation with four terms (Bevis et al., 1994; Doin et al., 2009)

$$N = k_1\frac{P_d}{T} + k_2\frac{P_v}{T} + k_3\frac{P_v}{T^2} - \alpha\frac{N_e}{f^2} \tag{9.6}$$

where
P_d – partial pressure of dry air (Pa)
P_v – partial pressure of water vapor (Pa)
T – absolute temperature (K)
N_e – number density of free electrons (m^{-3})
f – radar frequency (Hz)
$k_1 = 0.776$ (K Pa^{-1})
$k_2 = 0.716$ (K Pa^{-1})
$k_3 = 3.75 \times 10^3$ (K^2 Pa^{-1})
$\alpha = 40.28$ (Hz^2 m^{-3}).

The first term corresponds to the slowing of the waves due to the dry component of the troposphere and the combined second and third terms represent the slowing of the wave due to the water vapor (wet) component of the troposphere. The last term represents the increase in the phase velocity of the wave as it travels through the ionosphere containing free electrons as discussed in Section 9.4.1. Figure 9.3 (a) shows examples of the relative contributions of the wet and dry terms to the refractivity (Pany, 2003).

Our objective is to correct the two-way travel time (i.e., phase) along the non-vertical LOS path of the radar for the effects of pressure, temperature, and water

Downloaded from https://www.cambridge.org/core. IP address: 189.217.92.64, on 11 Feb 2026 at 15:51:46, subject to the Cambridge Core terms of use, available at https://www.cambridge.org/core/terms. https://www.cambridge.org/core/product/1F8951EFC610A352837B95E4DAEFBAEB

vapor in the neutral troposphere as well as the electron density in the ionosphere. For interferometry, we seek the change in the phase between the reference and repeat SAR images and how it varies spatially over the area of the interferogram.

The path-integrated tropospheric delays require a 3-D, time-dependent model of the troposphere. In Section 9.3 we discuss corrections using numerical weather models and/or GNSS measurements of the troposphere. These models/measurements are generally sparse and inaccurate, so in Section 9.3.1, we discuss a variety of approximate methods to correct for the tropospheric phase delay, including GNSS time series at known locations and common scene stacking, assuming the temporal variations in the surface deformation are slower than the cadence of the SAR acquisitions.

The ionospheric effects and correction methods are discussed in Section 9.4. The phase and group velocity of radar waves depend on the integrated electron density along the path in the ionosphere; this is called the total electron content (TEC) (Figure 9.3(c)). As seen in Equation 9.6, and derived in Section 9.4.1, the velocity perturbation is proportional to the inverse of the radar frequency squared. Therefore, the path delays are large for a low-frequency L-band radar, moderate for an intermediate frequency C-band radar, and small for a higher frequency X-band radar. Moreover, because the ionosphere is dispersive, the path delay can be accurately corrected if the radar has two widely separated frequencies. GNSS satellites broadcast timing signals at two frequencies. The receiver on the ground measures the travel-time difference between the two signals to estimate the TEC along the ray path and uses that to correct the travel time of the higher frequency signal to achieve a subcentimeter correction accuracy. The split-spectrum approach can be used to correct SAR interferograms for the ionospheric distortions, although current systems do not have sufficient frequency bandwidth to provide accurate corrections (Meyer et al. (2006); Liang et al. (2019)). The dual-frequency approach will be more accurate with the next generation of dual-frequency radars such as NISAR and ALOS-4.

9.3 Characteristics and Mitigation of the Troposphere Delay

Here we consider the zenith excess path L due to just the neutral atmosphere (mostly troposphere). The satellite altitude is well above the top of the atmosphere so the integral Equation 9.4 can extend to infinity. The zenith path delay is given by Doin et al. (2009)

$$L = 10^{-6} \int_{z_0}^{\infty} [k_1 \frac{(P_d + P_v)}{T} + (k_2 - k_1) \frac{P_v}{T} + k_3 \frac{P_v}{T^2}] dz \tag{9.7}$$

Downloaded from https://www.cambridge.org/core. IP address: 189.217.92.64, on 11 Feb 2026 at 15:51:46, subject to the Cambridge Core terms of use, available at https://www.cambridge.org/core/terms. https://www.cambridge.org/core/product/1F8951EFC610A352837B95E4DAEFBAEB

where the total pressure $P = (P_d + P_v)$ has been combined in the first term assuming hydrostatic equilibrium. This first term can be integrated analytically using $dP = -\rho g dz$ where g is the acceleration of gravity averaged over the troposphere (see Problem 9.1). The density is found using the ideal gas law such that

$$\rho = \frac{P_d}{R_d T} + \frac{P_v}{R_v T} = \frac{P}{R_d T} + \left(\frac{1}{R_d} - \frac{1}{R_v}\right)\frac{P_v}{T} \tag{9.8}$$

where R_d (287.05 J kg^{-1}K^{-1}) and R_v (461.495 J kg^{-1}K^{-1}) are the specific gas constants for dry air and water vapor, respectively.

After integration, one finds

$$10^6 L = \frac{k_1 R_d}{g} P(z_o) + \int_{z_0}^{\infty} \left[\left(k_2 - \frac{R_d}{R_v} k_1\right)\frac{P_v}{T} + k_3 \frac{P_v}{T^2}\right] dz \tag{9.9}$$

where $P(z_o)$ is the surface pressure. This equation has two important terms. The first term on the right is called the *zenith hydrostatic delay* (ZHD). Note it only depends on the measurement of the pressure at the surface at an elevation of z_o. The second term on the right is called the *zenith wet delay* (ZWD) and it depends on the integration of water vapor over the height of the troposphere. Measuring the ZWD is much more challenging because it requires a 3-D model of the pressure of the water vapor. Moreover, for InSAR, the integral should be performed along the nonvertical ray path of the radar, which could be different from the ZWD mapped using the cosine of the look angle (Equation 9.5) if there are significant horizontal variations in water vapor with lengths scales less than about 5 km.

At this point it is important to remember that an interferogram measures the phase or path difference between two acquisition times. Therefore, we only care about the difference in the ZHD and ZWD between the two times. For example, consider the first term, ZHD, in Equation 9.9. The long-term mean absolute pressure at a given position/elevation on the surface of the Earth cancels in the difference. The GNSS community places atmospheric pressure sensors at the sites so the temporal variations can be measured. However, for InSAR, spatially dense surface pressure data are not available everywhere so one needs a weather model, or surface interpolation among the GNSS sites, to estimate ZHD over the entire SAR image. Similarly, there are no spatially dense sensors to measure the vertically integrated water vapor, although this can be done at GNSS sites since the path delays to multiple GPS satellites, having many incidence angles, can be analyzed simultaneously. The conclusion is that a 3-D model of pressure, temperature, and water vapor is needed to correct the interferogram. This can be obtained from high-resolution weather models combined with sparse GPS measurements, although there are significant errors in these models (Yu et al., 2018).

Downloaded from https://www.cambridge.org/core. IP address: 189.217.92.64, on 11 Feb 2026 at 15:51:46, subject to the Cambridge Core terms of use, available at https://www.cambridge.org/core/terms. https://www.cambridge.org/core/product/1F8951EFC610A352837B95E4DAEFBAEB

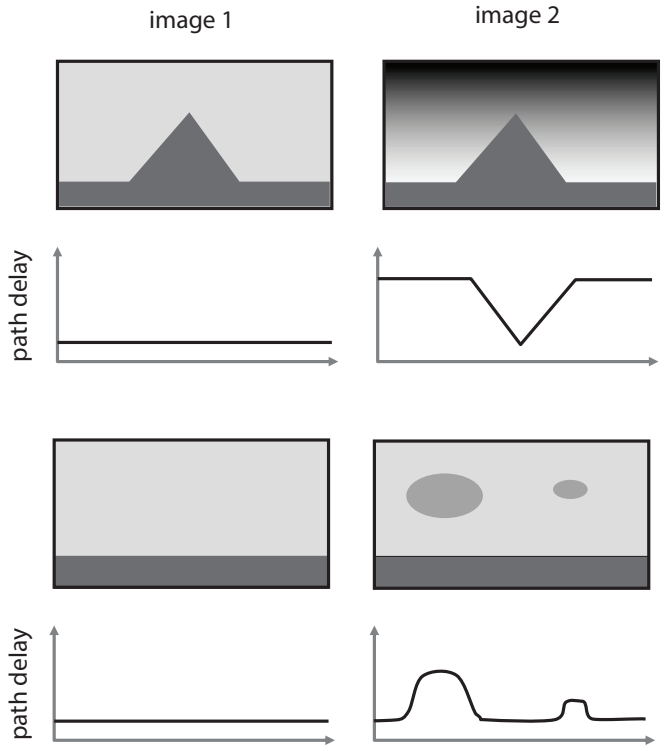

Figure 9.4 The top row illustrates the change in the atmospheric delay of image 2 with respect to image 1 for a stratified troposphere. The second row illustrates the corresponding path delay seen in the interferogram. The delay is proportional to the local topography and is commonly assumed to be linear with topography. The third row illustrates the change in atmospheric delay due to random variations (turbulence and waves) in mostly water vapor. The fourth row illustrates the path delay seen in the interferogram.

The practical approach to correcting interferograms for tropospheric delay is to first decompose the delays (refractivity) into changes caused by stratification and changes caused by turbulence (Hanssen, 2001).

$$N(\mathbf{x}, z) = \bar{N}(z) + \delta N(\mathbf{x}, z) \tag{9.10}$$

where $\bar{N}(z)$ is the vertical stratification assumed uniform across the image and $\delta N(\mathbf{x}, z)$ is the 3-D deviation from the average stratification. Figure 9.4 provides a schematic of these two terms.

The most straightforward method of correcting for both types of delays is to use a 3-D atmospheric weather model that provides the surface pressure $P[z_o(\mathbf{x})]$ needed for the ZHD as well as the partial pressure of water vapor $P_v(\mathbf{x}, z)$ needed

Downloaded from https://www.cambridge.org/core. IP address: 189.217.92.64, on 11 Feb 2026 at 15:51:46, subject to the Cambridge Core terms of use, available at https://www.cambridge.org/core/terms. https://www.cambridge.org/core/product/1F8951EFC610A352837B95E4DAEFBAEB

for the ZWD. These models must have adequate spatial and temporal resolution to perform the correction.

There are numerous studies on the spatial and temporal characteristics of the troposphere and the effects on InSAR phase (e.g., Hanssen (2001); Emardson et al. (2003); Doin et al. (2009); Bekaert et al. (2015); Yu et al. (2018)). This is an active area of research, and a full discussion is beyond the scope of this book. However, there are several important observations that inform the analysis of InSAR time series as well as the mitigation schemes. In particular, Emardson et al. (2003) examined the spatial and temporal characteristics of the atmospheric delay using continuous GNSS data to provide an overview of the issues. Their study was based on 126 GNSS stations in Southern California spanning the period January 1998 to March 2000. Over a time span of 106 seconds (12 days) or shorter, the surface deformation from tectonic or hydrological processes is assumed to be zero. The relative locations of the GNSS stations in this array are known to millimeter accuracy. The ionospheric delays are corrected using the dual-frequency approach discussed in Section 9.4 and tidal deformation is corrected using accurate models. Therefore, the position differences between any two stations primarily reflect variations in the delay of the EM waves as they traverse the neutral atmosphere (mostly troposphere). The delays include both ZHD and ZWD.

The characteristics of the atmospheric delay for each panel in Figure 9.5 are:

(a) This panel shows the variation in the atmospheric delay as a function of time offset for two spatial baselines of 20 km and 244 km (thin line). There are two important conclusions from this analysis. (1) The structure function (variance) flattens for time increments greater than one day. Most repeat-pass InSAR systems have a cadence of greater than 6 days so one can assume that the atmospheric effects of all the interferograms in a large analysis are temporally uncorrelated. (2) If one plans to use a 3-D weather model for correcting individual interferograms, ideally the model output should occur at the same times as the SAR acquisitions. However, weather models such as ECMWF provide outputs only every 6 hours. A typical mismatch in the sampling times will lead to large sampling errors. A sampling rate of 5 minutes would essentially eliminate the error due to non-coincidence sampling. In some regions, the GACOS model correction scheme uses available continuous GNSS data to perform a temporal interpolation of the poorly sampled weather models.

(b) This panel illustrates the issues related to the spatial characteristics of the tropospheric delay. There are three important conclusions. (1) The atmospheric variance, as measured by pairs of GNSS receivers, increases roughly as the square root of the distance between the receivers. For example, two points separated by 1 km will have a relative atmospheric error of less than 8 mm. (2) In

Downloaded from https://www.cambridge.org/core. IP address: 189.217.92.64, on 11 Feb 2026 at 15:51:46, subject to the Cambridge Core terms of use, available at https://www.cambridge.org/core/terms. https://www.cambridge.org/core/product/1F8951EFC610A352837B95E4DAEFBAEB

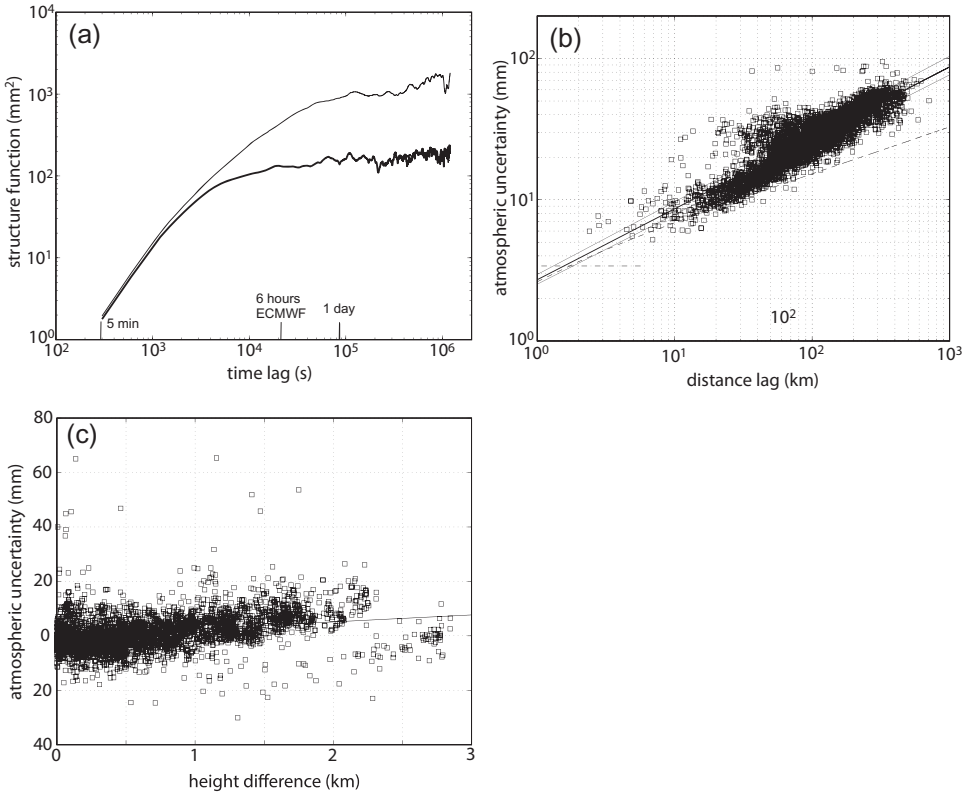

Figure 9.5 Temporal and spatial characteristics of the atmospheric delay from (Emardson et al., 2003). The details of each panel are discussed in the text.

contrast, at length scales of 100 km, the variance due to the atmospheric error is commonly 30–50 mm. Thus, to achieve say 10 mm accuracy over length scales greater than 100 km could require averaging interferograms from many SAR images (perhaps 16). (3) In a region that has a high density of continuously operating GNSS stations, one can dramatically improve the accuracy of InSAR time series by correcting each interferogram using the large-scale atmospheric estimated from the GNSS array (e.g., Neely et al., 2019). For example, the typical GNSS spacing is 20 km in Western North America so point-wide GNSS delays should be used to optimize the high spatial resolution provided by the InSAR time series.

(c) This panel illustrates the effects of the stratified tropospheric delay ZHD on the relative accuracy of two GPS measurements at differing altitudes. This effect is highly dependent on the dates of the measurements, so there is significant scatter in the uncertainty versus height difference, yet we will see next that this effect can dominate the tropospheric error and should be corrected if possible.

Downloaded from https://www.cambridge.org/core. IP address: 189.217.92.64, on 11 Feb 2026 at 15:51:46, subject to the Cambridge Core terms of use, available at https://www.cambridge.org/core/terms. https://www.cambridge.org/core/product/1F8951EFC610A352837B95E4DAEFBAEB

9.3.1 Mitigation of the Tropospheric Delay

There are three basic approaches to mitigation of the tropospheric delay.

(1) Stacking – The first approach is to assume that the deformation of the surface is steady with time and so one averages images to reduce the atmospheric noise. As shown in Figure 9.5(a), the atmospheric delay decorrelates after a time interval greater than about one day. Most InSAR systems have repeat intervals of 6 days or longer so simply averaging (stacking) many interferograms, each scaled by their temporal baseline, will reduce the error by the square root of the number of independent SAR images in the stack. This approach works well under the steady deformation rate assumption. However, many GNSS and InSAR time series display seasonal deformation signals due to annual variations in hydrology – either elastic deformation from water loading or compaction and swelling of unconfined aquifers. In the cases where the seasonal signals are large, the temporal averaging should be confined to a single season, or a multiyear average of interferograms from SAR images within the same season, assuming the seasonal amplitude is uniform.

(2) Atmospheric modeling – The second approach is to obtain the best possible atmospheric delay model using a combination of global or local atmospheric weather models along with zenith tropospheric delay measurements at GNSS sites. For example, the generic atmospheric correction online service (GACOS) correction facility (Yu et al., 2018) "integrates operational high-resolution European Centre for Medium-Range Weather Forecasts (ECMWF) data (0.125° grid, 137 vertical levels, 6-hour interval) and continuous GNSS tropospheric delay estimates (every 5 min in some regions) using an iterative tropospheric decomposition model." Their approach uses an exponential function to model the stratified delays, and then the turbulent part of the delay is constructed from interpolation of the residual path difference between the sparse GNSS sites and the ECMWF model. An example of the correction applied to a 12-day Sentinel-1 interferogram from the UK is shown in Figure 9.6. The raw interferogram (d) has strong atmospheric delay errors with a standard deviation of 27.5 mm. The correction has a component from the change in the stratified troposphere (a) and a larger scale, mostly trend from the water vapor and pressure across the scene (b). These two corrections (c) reduce the rms to 6.9 mm. The approach works best when there is a high density of GNSS stations to provide the high temporal sampling (5 minutes) as well as adequate spatial sampling. In areas of lower GNSS density or large-amplitude atmospheric perturbations, the atmospheric correction is often less effective.

(3) Parametric Modeling – The third approach is to use the InSAR data along with a digital elevation model to first estimate and remove the tropospheric signal

Downloaded from https://www.cambridge.org/core. IP address: 189.217.92.64, on 11 Feb 2026 at 15:51:46, subject to the Cambridge Core terms of use, available at https://www.cambridge.org/core/terms. https://www.cambridge.org/core/product/1F8951EFC610A352837B95E4DAEFBAEB

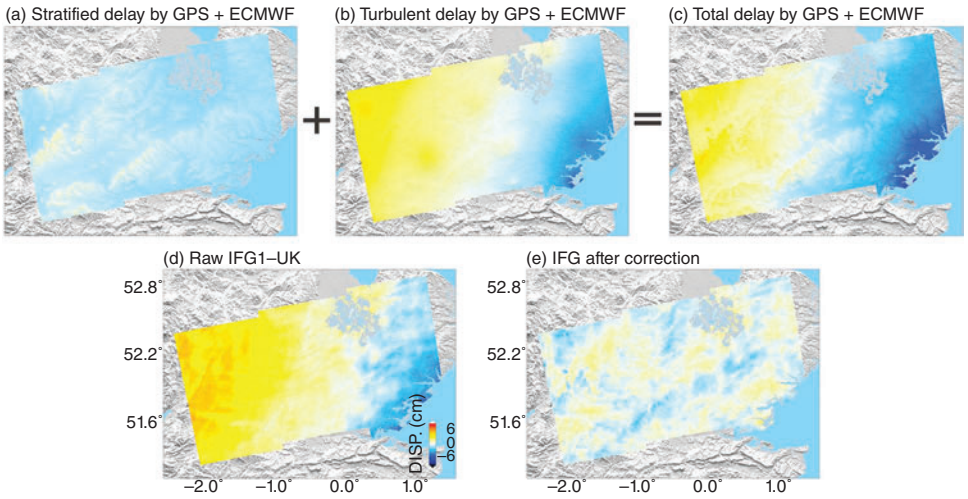

Figure 9.6 Sentinel-1, 12-day interferogram of a region in the UK has large atmospheric noise modeled by the GACOS method (from Yu et al. (2018)). (a) Model of the LOS displacement due to changes in the stratified component of the delay are correlated with topography. (b) Model of LOS displacement due to the turbulent component of the delay has a prominent linear trend with an amplitude of 40 mm. (c) Total delay is applied to the original interferogram (d) to form the corrected interferogram (e).

due to changes in atmospheric stratification and then use a method such as common scene stacking to "filter" the atmospheric signals over a prescribed timescale where the surface deformations are presumed to be steady.

An example of the effects of the changes in atmospheric stratification on an interferogram for the Southern California area is shown in Figure 9.7. This stratification error often dominates the tropospheric signal and should be modeled and removed from all the interferograms used in a stack or time series. Prior to estimating the linear regression between residual phase and elevation, one should remove the overall trend in the residual phase since this may be related to residual orbit error or other larger-scale errors such as ionosphere delay or a planar pressure variation. This linear fit with height is often very effective but can fail when the deformation signals are correlated with topography or the relationship between phase and height is not constant throughout the interferogram. After correcting for the delay from the changes in the stratified component, a second estimation method must be used to remove the turbulent component. One can use a common scene stacking/time series approach to remove the remaining small-scale residual noise as discussed in Chapter 10.

Downloaded from https://www.cambridge.org/core. IP address: 189.217.92.64, on 11 Feb 2026 at 15:51:46, subject to the Cambridge Core terms of use, available at https://www.cambridge.org/core/terms. https://www.cambridge.org/core/product/1F8951EFC610A352837B95E4DAEFBAEB

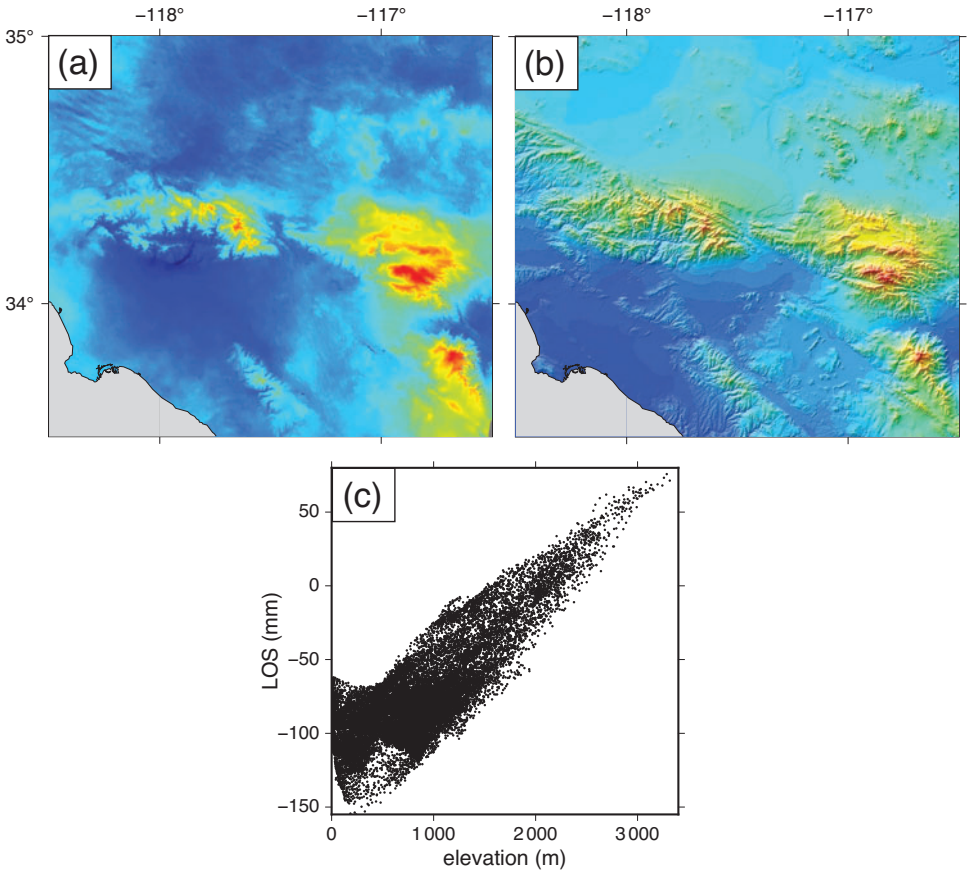

Figure 9.7 Example of correlation between interferometric phase (a) and elevation (SRTM DEM) (b) due to temporal changes in atmospheric stratification. This is the same 36-day Sentinel-1 TOPS mode interferogram shown in Figure 9.1(c). A plot of LOS versus elevation shows a high correlation with 140 mm of phase delay due to the stratified troposphere draped on the topography of 3 000 m.

In summary, atmospheric delay is a dominant source of error in the InSAR technique. Typical errors are 20 – 50 mm and can be as large as 100 mm in extreme cases of atmospheric fronts. The GNSS community removes most of this error because the stations are fixed in space, they have a high temporal sampling rate, and they observe the LOS atmospheric distortions from a multitude of satellite overpasses, and thus can develop a highly accurate map of the atmospheric water vapor for the ZWD. In addition, pressure sensors at each site provide accurate measurement of the ZHD. InSAR has much poorer temporal sampling and only one LOS look through the troposphere, so separating the ZHD from a small surface deformation signal (10 mm or less) is problematic. Moreover, since the surface pressure

Downloaded from https://www.cambridge.org/core. IP address: 189.217.92.64, on 11 Feb 2026 at 15:51:46, subject to the Cambridge Core terms of use, available at https://www.cambridge.org/core/terms. https://www.cambridge.org/core/product/1F8951EFC610A352837B95E4DAEFBAEB

is only known at a few widely spaced GNSS sites, changes in the stratified component of the lower troposphere can dominate the deformation signal, especially in areas of high topographic relief. This topographically correlated delay is especially problematic in areas where the volcanic or fault deformation is correlated with topography.

9.4 Characteristics and Mitigation of the Ionosphere Advance

The ionosphere is a region of the Earth's upper atmosphere, extending from approximately 50–1 000 km in altitude (Figure 9.3(b)). Ultraviolet radiation from the sun ionizes atoms and molecules of oxygen and nitrogen, resulting in a plasma of free electrons. The ionosphere is characterized by its dynamic nature, exhibiting variations with altitude, latitude, time of day, and phase of the 11-year solar cycle. Understanding and mapping these complex variations is essential for assessing and mitigating its impact on microwave geodetic systems, including GNSS and InSAR.

Altitude is a primary factor in ionosphere structure (Figure 9.3(b)). The ionosphere is conventionally divided into several layers, including the D, E, and F layers (Figure 9.3(b)). The D region, closest to the Earth's surface, is most prominent during the daytime and absorbs/reflects lower-frequency radio waves. The E region is prominent during daylight hours and reflects medium-frequency radio waves. The F region, with sublayers F1 and F2, has the highest electron density between 200 and 500 km altitude and delays and distorts the propagation of microwaves. SAR satellites have typical orbital altitudes of 500–800 km and thus travel within the upper part of the F-region. In Section 9.4.1, we develop the theory for the phase velocity of an EM wave as it propagates through a plasma. The most important parameter for microwave signal propagation is the integral of the density of free electrons along the ray path from the satellite to the ground; this is called the total electron content and has units of electrons per area. Therefore, the radial variations in ionospheric properties are not as important as the temporal and spatial variations in TEC.

Time of day significantly affects the ionosphere's behavior (Figure 9.3(c)). During the day, solar radiation increases ionization and thus TEC, while at local sunset the electrons recombine with their associated atom/molecule, and there is a dramatic and sometimes turbulent decrease in density that affects microwave signals. The TEC is minimum just before sunrise.

Latitudinal variations (geomagnetic latitude) introduce additional complexity to the ionosphere's behavior (Figure 9.2(c)). At low latitudes (0°–20°), ionization is highest due to maximum solar illumination. There are local maxima on both sides of the geomagnetic equator between 10° and 15°. The ionosphere is quietest at mid-latitudes (20°–60°), with low spatial variations except for occasional geomagnetic

Downloaded from https://www.cambridge.org/core. IP address: 189.217.92.64, on 11 Feb 2026 at 15:51:46, subject to the Cambridge Core terms of use, available at https://www.cambridge.org/core/terms. https://www.cambridge.org/core/product/1F8951EFC610A352837B95E4DAEFBAEB

storms. At high latitudes (>60°), the ionosphere is strongly affected by the converging lines of the geomagnetic field and charged particles from the solar wind entering the ionosphere. There are many dynamic processes that delay and distort the GNSS and InSAR signals at high latitudes so mitigating these effects is important even at C-band (Liang et al., 2019). Ionospheric disturbances often occur as wave-like perturbations in the electron density and thus TEC within the area of an interferogram.

The 11-year solar cycle, characterized by fluctuations in solar activity, significantly influences the ionosphere. During periods of high solar activity (Figure 9.3(b), sunspot maximum), increased ionization results in higher electron density and greater signal delays and distortions. Conversely, solar minimum has lower ionization and weaker signal delay.

9.4.1 Propagation of EM Waves through a Plasma

The theory of the propagation of electromagnetic (EM) waves in a plasma, such as the Earth's ionosphere, is well developed (e.g., Jackson (2012)). First, consider an EM wave traveling in the z-direction having a single x-component of electric field of strength E_o.

$$E_x(z,t) = E_o e^{i(\omega t - kz)} \tag{9.11}$$

where $\omega = 2\pi/T$, T – is the wave period, $k = 2\pi/\lambda$, and λ – is the wavelength. Note the frequency in radians per second is related to the frequency in Hz by $\omega = 2\pi f$.

The phase of this wave has a constant value when $\omega t = kz$, so the velocity of the wave, corresponding to constant phase, is $v_p = \frac{z}{t} = \frac{\omega}{k}$. EM waves traveling in a medium free of charges and currents obey the wave equation

$$\frac{\partial^2 E_x}{\partial z^2} - \frac{\varepsilon}{c^2}\frac{\partial^2 E_x}{\partial t^2} = 0 \tag{9.12}$$

where c is the speed of light and ε is the relative permittivity, also called the dielectric constant. Note by definition, $c = (\varepsilon_o \mu_o)^{-1/2}$ where $\varepsilon_o = 8.854 \times 10^{-12}$ F m^{-1} is the permittivity of free space and $\mu_o = 4\pi \times 10^{-7}$ H m^{-1} is the magnetic permeability of free space. Equation 9.11 is a solution to the wave Equation 9.12 so by taking the derivatives, one finds:

$$(-ik)^2 e^{i(\omega t - kz)} - \frac{\varepsilon}{c^2}(i\omega)^2 e^{i(\omega t - kz)} = 0 \quad \text{or} \quad k^2 + \frac{\varepsilon}{c^2}\omega^2 = 0 \tag{9.13}$$

Therefore, the phase velocity of the wave is $v_p = \frac{\omega}{k} = c\varepsilon^{-1/2}$. Since the phase velocity is also defined as $v_p = cn^{-1}$, we have the usual relationship between the index of refraction and the dielectric constant $n = \varepsilon^{1/2}$.

Downloaded from https://www.cambridge.org/core. IP address: 189.217.92.64, on 11 Feb 2026 at 15:51:46, subject to the Cambridge Core terms of use, available at https://www.cambridge.org/core/terms. https://www.cambridge.org/core/product/1F8951EFC610A352837B95E4DAEFBAEB

Next, consider this wave propagating through a low-density electron plasma (e.g., ionosphere). The plasma consists of free electrons of density N_e (electrons m^{-3}) having charge $e = 1.602 \times 10^{-19}$ Coulombs and mass $m = 9.109 \times 10^{-31}$ kg and an equal number of positively charged molecules of oxygen/nitrogen, and so on. The positive ions are too massive to move in response to the variations in the electric field. The x-component of the differential equation for the forces acting on the free electron is:

$$m\ddot{x} + m\omega^2 x = -eE_x\,(x,t) \tag{9.14}$$

In the high-frequency limit, the solution to this equation has a natural resonant frequency (Jackson, 2012) given by:

$$\omega_p^2 = \frac{N_e e^2}{\varepsilon_o m}. \tag{9.15}$$

For a typical electron density of the F-layer of the ionosphere of 10^{12} electrons m^{-3}, the plasma frequency is 9 MHz. The lowest frequency L-band SAR satellites operate at 1.3 GHz so the high frequency approximation $\omega \gg \omega_p$ is valid. Under this approximation, the dielectric constant and index of refraction are:

$$\varepsilon = n^2 = 1 - \frac{\omega_p^2}{\omega^2}. \tag{9.16}$$

The phase velocity of the wave is:

$$v_p = c\left(1 - \frac{\omega_p^2}{\omega^2}\right)^{-1/2}. \tag{9.17}$$

Note the phase velocity exceeds the speed of light since the denominator is always less than 1. However, this does not violate the law that no information can travel faster than c, because a single frequency wave does not carry any information. Information can only be carried by a wave group having a finite band of frequencies. The group velocity of a wave is given by $v_g = \frac{\partial \omega}{\partial k}$. It is left as an exercise (Problem 9.2) to show that the group velocity of a plasma, in this high-frequency limit, is:

$$v_g = c\left(1 - \frac{\omega_p^2}{\omega^2}\right)^{1/2}. \tag{9.18}$$

Note the product of the phase and group velocities is c^2. It is interesting to note that the ionospheric effects on both GNSS and InSAR methods involve both the phase velocity $> c$ and the group velocity $< c$. In the case of GNSS, the phase of the carrier wave between the satellite and receiver on the ground is advanced after propagating through the ionosphere with respect to propagation through a vacuum.

Downloaded from https://www.cambridge.org/core. IP address: 189.217.92.64, on 11 Feb 2026 at 15:51:46, subject to the Cambridge Core terms of use, available at https://www.cambridge.org/core/terms. https://www.cambridge.org/core/product/1F8951EFC610A352837B95E4DAEFBAEB

In contrast, the range signal that carries the timing information is delayed after propagating through the ionosphere. Similarly, for InSAR, the phase difference between a reference and repeat interferogram will be advanced by an increase in the electron density of the ionosphere between the reference and repeat times. However, the radar backscatter signal, which consists of multiple wavelengths, will be delayed by an increase in electron density between the reference and repeat times. This dispersive nature of the ionosphere leads to an elegant way to correct for both the phase advance and range delay.

Now we have almost all the tools needed to calculate these advances and delays. The last term in Equation 9.6 for the refractivity of the ionosphere depends on the electron density and inversely on the frequency squared:

$$N_{ion} = -\alpha \frac{N_e}{f^2}. \tag{9.19}$$

Note there is a constant α that is still undefined. Our equation for the index of refraction has a square root, so it does not match the form of Equation 9.19

$$n = \left(1 - \frac{\omega_p^2}{\omega^2}\right)^{1/2}. \tag{9.20}$$

However, since we are in the limit where the wave frequency is much greater than the plasma frequency, we can use the binomial expansion to rewrite Equation 9.20 as:

$$n \cong 1 - \frac{\omega_p^2}{2\omega^2} = 1 - \frac{e^2 N_e}{2\varepsilon_o m \omega^2}. \tag{9.21}$$

Therefore, the refractivity of the ionosphere in terms of frequency in Hz is

$$N_{ion} = -\frac{e^2}{8\pi^2 \varepsilon_o m} \frac{N_e}{f^2}. \tag{9.22}$$

We see that the constant α in Equation 9.6 is based on well-known physical parameters

$$\alpha = \frac{e^2}{8\pi^2 \varepsilon_o m} = 40.28 \text{ Hz}^2\text{m}^3. \tag{9.23}$$

Now using Equation 9.4, we can calculate the 1-way phase advance due to the ionosphere

$$L = \int_{z_o}^{H} [n(z) - 1]\, dz = -\frac{\alpha}{f^2} \int_{z_o}^{H} N_e(z) dz = -\frac{\alpha}{f^2} TEC. \tag{9.24}$$

Downloaded from https://www.cambridge.org/core. IP address: 189.217.92.64, on 11 Feb 2026 at 15:51:46, subject to the Cambridge Core terms of use, available at https://www.cambridge.org/core/terms. https://www.cambridge.org/core/product/1F8951EFC610A352837B95E4DAEFBAEB

Table 9.1 *Typical ionosphere phase advance.*

Frequency GHz	Wavelength (mm)	Band	Two-way phase advance (m)
1	300	P	20
1.3	230	L	12
5	60	C	0.8
10	30	X	0.2
13	23	Ku	0.1

The integral on the right side of the equation of the electron density over the path is the TEC, which has units of electrons per unit area. It is interesting to calculate the two-way phase advance for a typical TEC of 25 TECU or 2.5×10^{17} electrons m^{-2} as provided in Table 9.1.

Of course, this theory also provides the range delay of a microwave pulse as it travels through the ionosphere. The group velocity is $v_g = c^2/v_p$, so the range delay is the negative of phase advance.

9.4.2 Ionospheric Corrections for GNSS and InSAR

Precise GNSS positioning systems exploit the dispersive nature of the ionosphere to correct for the phase advance and range delay of the signals. GPS broadcasts its signals at two frequencies, f_1 (1.575 GHz) and f_2 (1.227 GHz). Consider a pseudo range measurement between the satellite and the ground receiver $P = c\Delta t$ where Δt is the time of flight of the pulse as measured by the receiver. After a bit of algebra (Problem 9.3), one can show that the range correction is given by:

$$\Delta\rho = \frac{f_2^2}{\left(f_1^2 - f_2^2\right)}(P_1 - P_2). \tag{9.25}$$

where $\Delta\rho$ is the excess range to be subtracted from pseudo range P_1. Similarly, one should add $\Delta\rho$ to correct to the advance of the phase of the carrier at frequency f_1. Since one can only count cycles of wavelengths of distance between the satellite and the receiver, the $\Delta\rho$ is used to correct for integer cycle ambiguities of the carrier phase.

Note that the pseudo range difference in Equation 9.25 is scaled by the f_2 carrier frequency squared but more importantly also scaled by the inverse of the difference of the two carrier frequencies squared. Thus an error in the pseudo range measurements will be amplified by this scale factor. In the case of GPS, the overall scale factor is 2.54, which is not large. However, this amplification of the error would be

Downloaded from https://www.cambridge.org/core. IP address: 189.217.92.64, on 11 Feb 2026 at 15:51:46, subject to the Cambridge Core terms of use, available at https://www.cambridge.org/core/terms. https://www.cambridge.org/core/product/1F8951EFC610A352837B95E4DAEFBAEB

larger if the two frequencies were closer together. Next, we will discuss the same method for correcting the phase advance of an interferogram due to the ionosphere.

To date there are no dual-frequency InSAR satellites, so the main approach to ionospheric correction is to artificially split the SAR range spectrum into two subbands (e.g., Meyer et al. (2006); Gomba et al. (2015); Liang et al. (2019)). Recall, the slant-range resolution of a SAR is equal to the inverse of the radar bandwidth as described in Chapter 4. A typical bandwidth for an L-band satellite such as ALOS-2 is 28 MHz, the typical bandwidth for a C-band satellite such as Sentinel-1 TOPS-mode is 43 MHz, and the bandwidth for an X-band satellite such as TerraSAR-X is sometimes very high 150/300 MHz.

The original SLC or raw signal data is band-pass filtered to create two SLC images having subbands with a small separation as shown in Figure 9.8. The center frequency of the lower subband is f_l and the upper subband is f_u. Then one creates two interferograms from two SAR images. The phase of the low interferogram $\Delta\phi_l$ is generated from the two low SLC images and the phase of the upper interferogram $\Delta\phi_u$ is generated from the two high SLC images using the same approach of

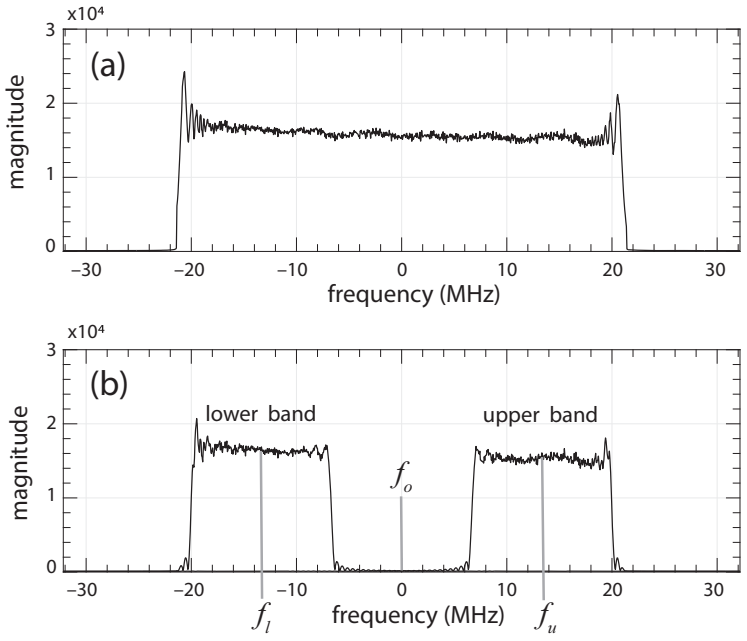

Figure 9.8 (a) Amplitude spectrum (flattened) of the radar signal of the Sentinel-1 TOPS mode has a bandwidth of 43 MHz and a center frequency of 5.405 GHz. Bandpass filtering is used to split the range signal into two subbands at frequencies of +/–14 MHz with respect to the carrier frequency. The accuracy of the split spectrum approach is best when each subband is 1/3 of the total bandwidth (Brcic et al., 2011).

Downloaded from https://www.cambridge.org/core. IP address: 189.217.92.64, on 11 Feb 2026 at 15:51:46, subject to the Cambridge Core terms of use, available at https://www.cambridge.org/core/terms. https://www.cambridge.org/core/product/1F8951EFC610A352837B95E4DAEFBAEB

complex multiplication as the standard interferogram (Equations 5.2 and 5.3). To calculate the phase advance, each interferogram must be unwrapped and filtered and the 2π phase ambiguity must be accurately estimated (Figure 9.9). The formula for the ionospheric phase correction to be applied to the original interferogram is:

$$\Delta\phi_{ion} = \frac{f_l f_u}{f_o\left(f_u^2 - f_l^2\right)}\Delta\phi_l f_u - \Delta\phi_u f_l \tag{9.26}$$

where f_o is the carrier frequency.

Similar to the calculation of the noise amplification factor for the GPS case, we find that an error in the noise of the difference interferogram in Equation 9.26 will be amplified by 96.5 times in the case of the Sentinel-1 data having the 43 MHz bandwidth (Figure 9.8). This means that any small amount of noise will dominate the correction, so the interferograms must be heavily filtered (Liang et al. (2019); Xu and Sandwell (2019)). Indeed, because the noise is amplified by nearly 100 times, the InSAR correlation must be nearly perfect, or the correction will add more noise than the ionospheric advance signal. NISAR will overcome this noise amplification issue by using a radar having a true split spectrum of 72.5 MHz. For the NISAR case at L-band, with a carrier frequency of 1 300 MHz, the noise amplification factor will be only 4.77, which is 20 times better than the split spectrum approach applied to Sentinel-1 data and only 1.9 times worse than the GPS dual-frequency approach.

The ionosphere has two additional effects on radar interferometry that are more fully discussed in other publications (e.g., Gray et al. (2000)). First, any along-track gradients in the TEC will cause an azimuth shift of the pixels between the reference and repeat images. The amount of azimuth shift can be estimated by first performing a geometric co-registration of the images using the precise orbits. Then one can perform a patch-wise cross-correlation between the images similar to the pixel tracking approach discussed in Chapter 10. Note that the satellite is orbiting within and just above the F-layer of the ionosphere so if the TEC gradients have a shorter length scale than the length of the synthetic aperture (Table 4.3), the resulting image will be defocused in the azimuth direction. The third effect is related to polarized SAR images where the polarization vector is rotated with respect to the original polarization by Faraday rotation (Gomba et al., 2015).

9.5 Tides and Aliasing

Corrections for the surface deformation due to the solid earth tide are an essential step for precise GNSS analysis because tidal amplitudes are large (~150 mm) and the tide models are extremely accurate (~1 mm) (McCarthy et al., 2004). Similarly, one should correct interferograms for the LOS displacement change between

Downloaded from https://www.cambridge.org/core. IP address: 189.217.92.64, on 11 Feb 2026 at 15:51:46, subject to the Cambridge Core terms of use, available at https://www.cambridge.org/core/terms. https://www.cambridge.org/core/product/1F8951EFC610A352837B95E4DAEFBAEB

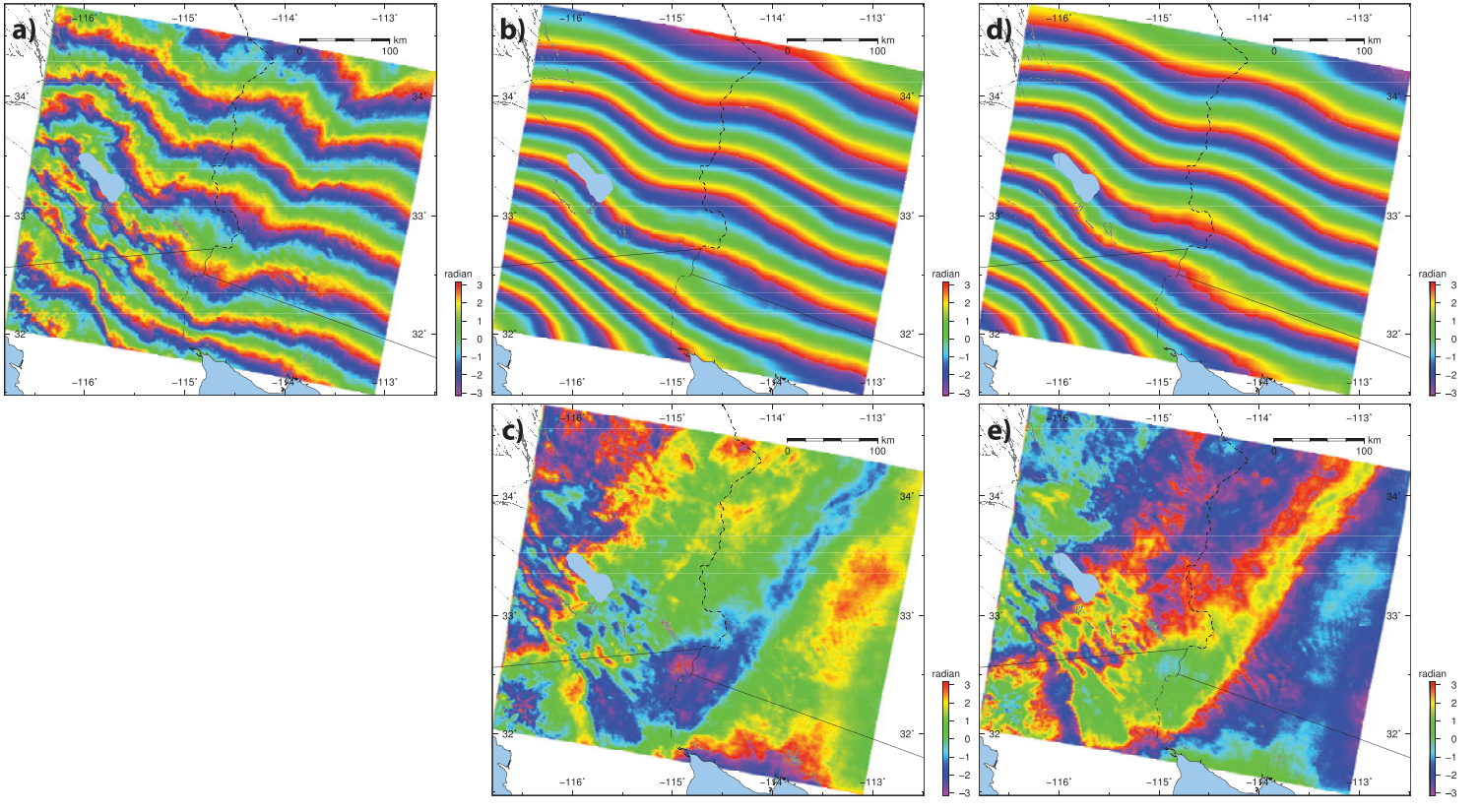

Figure 9.9 Split-spectrum ionospheric correction applied to an ALOS-2 ScanSAR interferogram (from Xu and Sandwell (2019)). (a) Original interferogram. (b) Ionospheric phase estimated using the split-spectrum method. (c) Ionospheric phase-corrected interferogram. (d) Estimated ionosphere correction if unwrapping ambiguity exists in both band-passed interferograms. (e) Applying the wrong correction from (d) to (a) results in a phase shift. Reprinted with permission from *IEEE Transactions on Geoscience and Remote Sensing*.

Downloaded from https://www.cambridge.org/core. IP address: 189.217.92.64, on 11 Feb 2026 at 15:51:46, subject to the Cambridge Core terms of use, available at https://www.cambridge.org/core/terms. https://www.cambridge.org/core/product/1F8951EFC610A352837B95E4DAEFBAEB

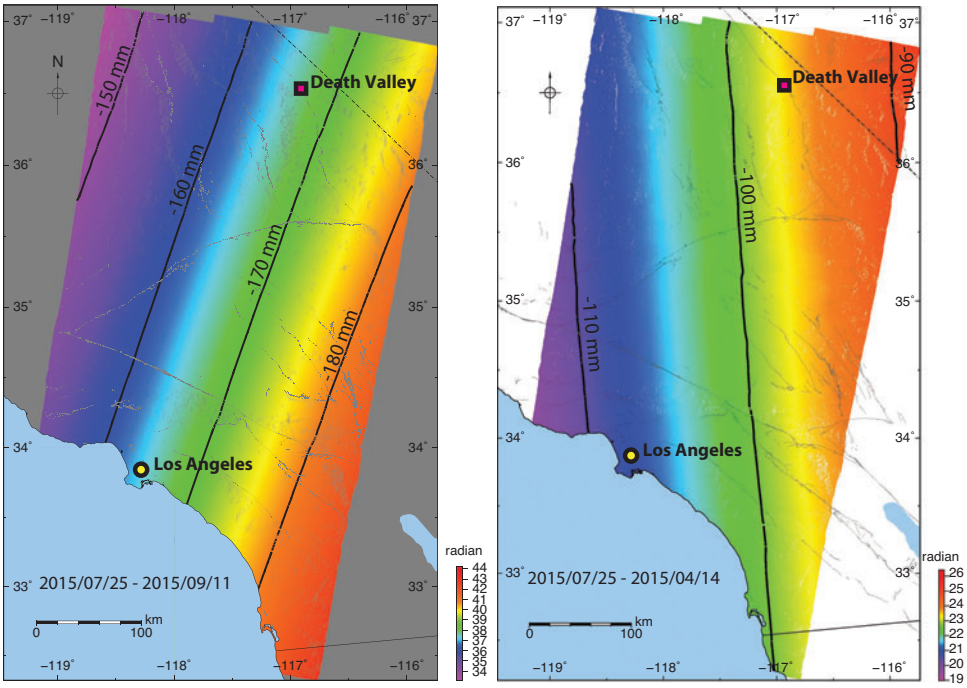

Figure 9.10 Solid earth tide phase/displacement for two Sentinel-1 TOPS interferograms (July 25, 2015–September 11, 2015 and July 25, 2015–April 14, 2015). Reprinted with permission from *IEEE Transactions on Geoscience and Remote Sensing*.

the reference and repeat images due to the solid earth tide (*solid_tide* in GMTSAR). Most InSAR studies ignore the tidal deformation signal because it is largely a constant over distances of 100 km. However, there are two important enhancements provided by the new generation of SAR satellites that make the tide correction important. First, the new satellites have greater swath widths and lengths of 250 km or greater, so the tide signal is not uniform in the swath. Second, the newer satellites have a regular acquisition cadence, so accurate time series relies on improved corrections.

Figure 9.10 illustrates how the mostly large spatial scale of the solid earth tide produces large-scale tilt signals in interferograms in both range and azimuth. The trend in the range is mostly due to the change in incidence angle across the swath. Consider Sentinel-1 TOPS-mode interferograms. For a maximum tide amplitude of 180 mm, the LOS component will be 156 mm in the near range (29°) and 124 mm in the far range (46°) resulting in a 32-mm trend across the interferogram in range. The tilt in azimuth depends on the change in latitude within a scene. As an example, the trend between Long Beach, CA, and Death Valley, CA (~300 km N-S

Downloaded from https://www.cambridge.org/core. IP address: 189.217.92.64, on 11 Feb 2026 at 15:51:46, subject to the Cambridge Core terms of use, available at https://www.cambridge.org/core/terms. https://www.cambridge.org/core/product/1F8951EFC610A352837B95E4DAEFBAEB

Table 9.2 *Aliasing of solid earth tide by InSAR satellites*

	repeat (days)	M2	S2	K1	O1	P1
amplitude (mm)		384.83	179.05	191.78	158.11	70.88
ERS/Envisat	35	94.50	–	365.23	75.06	365.23
RADARSAT	24	64.07	–	365.23	77.70	365.23
ALOS-1	46	398.63	–	365.23	190.60	365.23
ALOS-2	14	270.08	–	365.23	1036.73	365.23
Sentinel-1A/B	12	64.07	–	365.23	77.04	365.23
NISAR	12	64.07	–	365.23	77.04	365.23
Sentinel-1A&B	6	14.77	–	365.23	14.19	365.23

distance), has a peak-to-trough amplitude of ~20 mm. These trends in tide in both the range and latitude directions will go directly into the unwrapped interferogram, so they should be removed. Note the effects are identical at X, C, and L-band in terms of LOS displacement.

The more important issue is tidal aliasing. The sun-synchronous orbits of the current generation of SAR satellites cause the diurnal and semidiurnal tides to be aliased into much longer periods. For example, the semidiurnal solar tide S2 has a period of one day and an amplitude of 180 mm (Table 9.2). This tide component is aliased into zero frequency when sampled at an exact integer number of days. In general, the alias frequency f_a due to sampling a tide of frequency f_t at a frequency f_s is given by the following formula:

$$f_a = f_t - f_s \text{round}\left(\frac{f_t}{f_s}\right) \tag{9.27}$$

For example, the M2 tide, with a period of 0.517542 days, when sampled at an interval of 12 days, has an alias period of 64.07 days (Table 9.2). The next largest tidal component K1 has an alias period of 365.23 days when sampled at an integer number of days. The overall result is that the 12-day sampled tide has alias periods of 64.07, 365.23, and 77.04 days (Table 9.2). The aliases at 64 and 77 days could be filtered out with smoothness in an small baseline subset methods SBAS analysis. However, the aliases having a 1-year period could be confused with real deformation signals associated with seasonal variations in water loading. Since the solid earth tide can be computed accurately, it should be removed. Indeed, GMT now has an earthtide tool to compute deformation from the solid earth tide.

Ocean tides, which deform the crust significantly within about 100 km of a coastline (Agnew, 2010), will have similar aliasing properties. However, these tides are less predictable, and the loading models depend on the local elastic properties of the

Downloaded from https://www.cambridge.org/core. IP address: 189.217.92.64, on 11 Feb 2026 at 15:51:46, subject to the Cambridge Core terms of use, available at https://www.cambridge.org/core/terms. https://www.cambridge.org/core/product/1F8951EFC610A352837B95E4DAEFBAEB

crust and mantle, so accurate corrections are more challenging – although probably important for very accurate InSAR time series analysis in coastal areas.

9.6 Problems

1. Integrate the first term in Equation 9.7 using the hydrostatic approximation and the first term in the ideal gas law (Equation 9.8) to obtain the first term in Equation 9.9 that relates the ZHD to the surface pressure.
2. Use the definition of the group velocity of a wave and the dispersion formula for the phase velocity of a wave propagating in a plasma (Equation 9.17) to derive the formula for the group velocity of a wave propagating in a plasma (Equation 9.18). Show that the product of the phase velocity and the group velocity is the speed of light squared.
3. Use the formula for the one-way path delay of a radar pulse traveling through the ionosphere (Equation 9.24) to derive the range correction for a dual-frequency GPS measurement given the pseudorange at two frequencies (Equation 9.25).

Downloaded from https://www.cambridge.org/core. IP address: 189.217.92.64, on 11 Feb 2026 at 15:51:46, subject to the Cambridge Core terms of use, available at https://www.cambridge.org/core/terms. https://www.cambridge.org/core/product/1F8951EFC610A352837B95E4DAEFBAEB

10

Complementary Approaches and Time Series

10.1 Complementary Approaches

In Chapters 5, 6, and 7 we discussed repeat-pass radar interferometry for measuring the range component of surface deformation, which corresponds to the line of sight (LOS) vector between a point on the ground and the satellite. In Chapter 11 we discuss how deformation measurements can be combined from ascending and descending orbits to obtain two LOS components of deformation in cases where the deformation event occurs as a step function in time (e.g., earthquake). However, two components do not resolve the full vector motion, and the deformation may not occur as a step function in time. Moreover, the magnitude of the deformation gradient may exceed the capabilities of the InSAR system (i.e., greater than $\sim\pi$ radian per pixel) and/or the extreme deformation event may result in InSAR decorrelation. In these cases, methods have been developed to provide this additional information. We discuss these complementary approaches in this chapter.

We first review SAR image cross-correlation methods to recover large displacements in the range and azimuth directions. At best, these approaches can recover deformation to a precision of 1/10 of a pixel, so they are mainly used for estimating large deformations (0.5–10 m). Of course, the range measurement is in the same LOS direction as the interferogram, so this measurement is most useful to augment the interferogram in regions of large displacement gradient and/or decorrelated areas. The azimuth measurement is parallel to the ground track and perpendicular to the range measurement so provides new vector information (Fialko et al., 2001; Wright et al., 2004), but the precision is limited to about 1/10 of an azimuth pixel. The same azimuth component of deformation can be derived at a somewhat higher accuracy using multiple aperture interferometry (MAI) as discussed in Section 10.3.

The remainder of the chapter discusses methods for combining a set of interferograms derived from many SAR images to recover deformation time series with

Downloaded from https://www.cambridge.org/core. IP address: 189.217.92.64, on 11 Feb 2026 at 15:51:46, subject to the Cambridge Core terms of use, available at https://www.cambridge.org/core/terms. https://www.cambridge.org/core/product/1F8951EFC610A352837B95E4DAEFBAEB

either uniform velocity in time (stacking, Section 10.4) or with a nonuniform time history (i.e., small baseline subset methods (SBAS), Section 10.5). Section 10.6 discusses methods for reconstructing displacement time series in regions where there is significant decorrelation. This is accomplished by first identifying pixels that remain coherent over long time periods; these pixels have stable amplitude and phase, so they are called persistent scatterers (PS).

10.2 Range and Azimuth Pixel Offsets

Surface deformation between a reference and repeat image produces localized pixel displacement relative to the pixels within the larger image. This can be used to measure deformation and the approach is called *pixel offset tracking* (POT). This approach was originally developed to measure deformation in repeated optical images (e.g., Van Puymbroeck et al., 2000) and can also be used for measuring deformation from repeated SAR images. Indeed, the optical and SAR approaches are often combined to improve overall accuracy and coverage of surface deformation (He et al., 2023).

As discussed in Section 3.7.3, the reference and repeat images must first be aligned to subpixel accuracy to achieve high interferometric coherence. This can be accomplished using either geometric alignment based on precise orbits or 2-D complex cross-correlation of small patches typically 64 by 64 pixels. (Larger patches will provide a more robust offset estimate but will use more computer time.) Let $C_1\,(r,a)$ be a patch from the reference SLC image and $C_2\,(r,a)$ be a patch from the repeat image where r and a are the range and azimuth coordinates, respectively. The normalized 2-D cross-correlation function is

$$\gamma\,(\Delta \mathrm{r}, \Delta \mathrm{a}) = \frac{C_1 * * C_2^*}{\sqrt{C_1 C_1^*}\sqrt{C_2 C_2^*}}. \tag{10.1}$$

where the $**$ operation represents a 2-D convolution and $\sqrt{C_1 C_1^*}$ is the amplitude in the reference image (at zero shift). The location of the peak in the cross-correlation function provides an estimate of the displacement between the two images $(\Delta \mathrm{r}, \Delta \mathrm{a})$, while the strength of the correlation peak provides an estimate of the reliability of the offset estimate. (As a practical note, the mean is removed from each patch and the edges are zero-padded to minimize edge effects.)

Note that the convolution theorem can be used to replace the numerically slow 2-D convolution with the product of the Fourier transforms given by

$$\gamma\,(\Delta \mathrm{r}, \Delta \mathrm{a}) = \frac{\mathcal{F}_2^{-1}\left[\mathcal{F}_2\,(C_1)\,\mathcal{F}_2\left(C_2^*\right)\right]}{\sqrt{C_1 C_1^*}\sqrt{C_2 C_2^*}}. \tag{10.2}$$

Downloaded from https://www.cambridge.org/core. IP address: 189.217.92.64, on 11 Feb 2026 at 15:51:46, subject to the Cambridge Core terms of use, available at https://www.cambridge.org/core/terms. https://www.cambridge.org/core/product/1F8951EFC610A352837B95E4DAEFBAEB

The patches could be complex numbers taken from the SLCs of the reference and repeat images or SAR amplitude images. To avoid aliasing, the amplitude images should be oversampled by two times (Werner et al., 2005). These functions (Equations (10.1) and (10.2)) are available in the GMTSAR program *xcorr* and there are many options for setting the patch size, the oversampling of the amplitude data, and the oversampling factor for the cross-correlation output.

If there is a large amplitude deformation within the prealigned images, the local offset estimates are a measure of local surface deformation (Zitova and Flusser, 2003). This method is called pixel offset tracking and compared to the interferometric approach, POT is better suited for larger displacements and is more tolerant to decorrelations (Werner et al., 2005; Colesanti and Wasowski, 2006) (Figures 10.1 and 10.2). For example, in the case of a large earthquake, the InSAR phase is often decorrelated in the epicentral area of extreme ground shaking (Figure 10.1(a)). However, pixel offset tracking can provide deformation measurement even at the rupture trace (Figure 10.1(b/c)).

Theoretically, the interferometric approach can only detect deformation at a maximum deformation gradient of $\sim\pi$ radians per pixel, especially considering the noise in the data, but there is no upper limit for pixel offset tracking. For example, the very first applications using SAR images to track glacier streams were using interferometry (Goldstein et al., 1993; Massonnet and Rabaute, 1993; Joughin et al., 1996a; Rignot et al., 1997), but soon scientists determined that offset tracking performs well even on very fast-flowing ice streams (Strozzi et al., 2002), and can potentially detect seasonal velocity changes (Sundal et al., 2011).

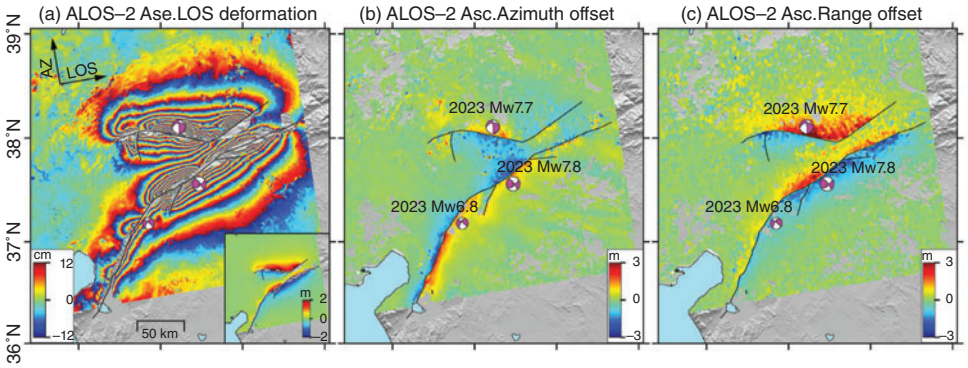

Figure 10.1 Deformation of the 2023 Turkey earthquake doublet derived by ALOS-2 ScanSAR data (He et al., 2023). (a) is the measured radar phase with the inset map being unwrapped LOS deformation. (b) is the azimuth offset with (c) being range offset.

Downloaded from https://www.cambridge.org/core. IP address: 189.217.92.64, on 11 Feb 2026 at 15:51:46, subject to the Cambridge Core terms of use, available at https://www.cambridge.org/core/terms. https://www.cambridge.org/core/product/1F8951EFC610A352837B95E4DAEFBAEB

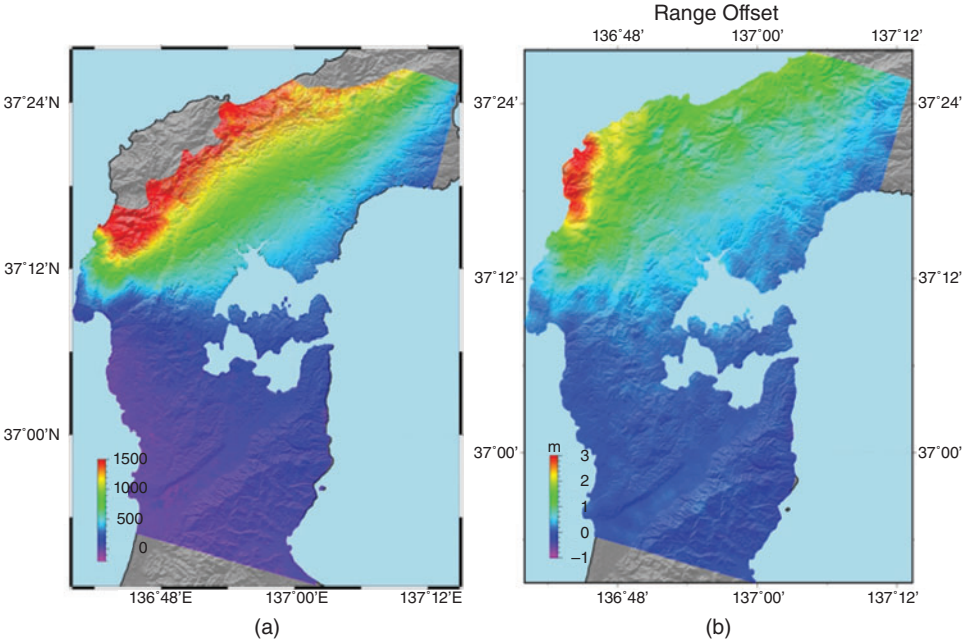

Figure 10.2 (a) unwrapped interferogram for the 2024 Noto Earthquake in Japan using ALOS-2 stripmap data, masked areas close to the shorelines are solutions with unwrapping errors due to strong shaking of the earth's surface. (b) Range offset estimate using POT can help acquire displacement estimates even at area with strong decorrelation. Adapted from Schmidt and Bürgmann (2003).

10.3 Multiple Aperture and Burst Overlap Interferometry

Azimuth offsets can be estimated using a completely different approach called *multiple aperture interferometry* (MAI) (Bechor and Zebker, 2006). Consider a localized surface displacement in the azimuth direction having a magnitude of x. Suppose the SAR is focused at a forward squint angle on the ground of θ_f and the localized deformation is imaged before and after the event. An interferogram constructed from the reference and repeat images will have a localized phase corresponding to the small component of deformation projected into the squinted LOS vector of $\phi_f = \frac{4\pi}{\lambda} x \sin\theta_f$ where λ is the radar wavelength (Bechor and Zebker, 2006). For a large magnitude of azimuth deformation (~1 m) and a nominal squint angle of a fraction of a degree, this phase change will be small, and the interferogram will be dominated by much larger phase distortions due to the troposphere and ionosphere. The MAI approach deliberately filters a single SAR image into a forward-looking image and a backward-looking image so two sub images are available. Then one constructs the forward and backward interferograms and computes their difference as

Downloaded from https://www.cambridge.org/core. IP address: 189.217.92.64, on 11 Feb 2026 at 15:51:46, subject to the Cambridge Core terms of use, available at https://www.cambridge.org/core/terms. https://www.cambridge.org/core/product/1F8951EFC610A352837B95E4DAEFBAEB

$$\phi_f - \phi_b = \frac{4\pi}{\lambda} x \left(\sin\theta_f - \sin\theta_b\right) \tag{10.3}$$

The phase changes due to the atmospheric and ionospheric effects largely cancel in the difference interferogram, while the phase change due to the along-track motion is doubled. Since the change in squint angle is related to the Doppler spectrum, a zero-Doppler SAR image, having an azimuth bandwidth of the PRF, can be decomposed into forward and backward-looking images with a band-pass filter in the azimuth direction (Scheiber and Moreira, 2000).

Thus, the computation for MAI interferograms involves three steps. The first step is to filter the full aperture SAR data into forward-looking and backward-looking subbands (along the track direction or column-wise). This is done on both reference and repeat SAR images. During this step, one should also compute the spectral separation between the forward-looking and backward-looking subbands (i.e., Δf). The second step is to compute interferograms between the forward-looking reference and forward-looking repeat and the backward-looking reference and backward-looking repeat subband datasets. Then one will be able to derive the azimuthal deformation with Equation 10.4

$$\Delta a = \frac{\mathrm{PRF}\left(\phi_f - \phi_b\right)}{2\pi\Delta f} \tag{10.4}$$

where PRF is the pulse repetition frequency. The azimuth pixel shift is converted to pixel shift in meters by multiplying by the ground-track pixel size $l_a = V_g/\mathrm{PRF}$ where V_g is the ground track velocity. Figure 10.3 shows examples of azimuthal deformation estimated using this MAI technique in comparison with pixel offset tracking; theoretically they should be equal, but there are practical issues associated with each approach.

Essentially, the MAI technique maps any azimuthal change into the double difference radar phase, and it does not differentiate whether it is caused by true ground deformation, along-track orbit error, or bias from the ionosphere. The bending of the radar beam caused by variation in the ionosphere can be assumed as a linear function related to the azimuthal gradient of the ionospheric phase as described in Liang and Fielding (2017)

$$\phi_{MAI-iono} = a\frac{\partial\phi_{iono}}{\partial a} + b \tag{10.5}$$

where a and b are coefficients of the polynomial fit to the gradient in the TEC of the ionosphere. Thus, the removal of this effect depends on the accurate estimates of

Downloaded from https://www.cambridge.org/core. IP address: 189.217.92.64, on 11 Feb 2026 at 15:51:46, subject to the Cambridge Core terms of use, available at https://www.cambridge.org/core/terms. https://www.cambridge.org/core/product/1F8951EFC610A352837B95E4DAEFBAEB

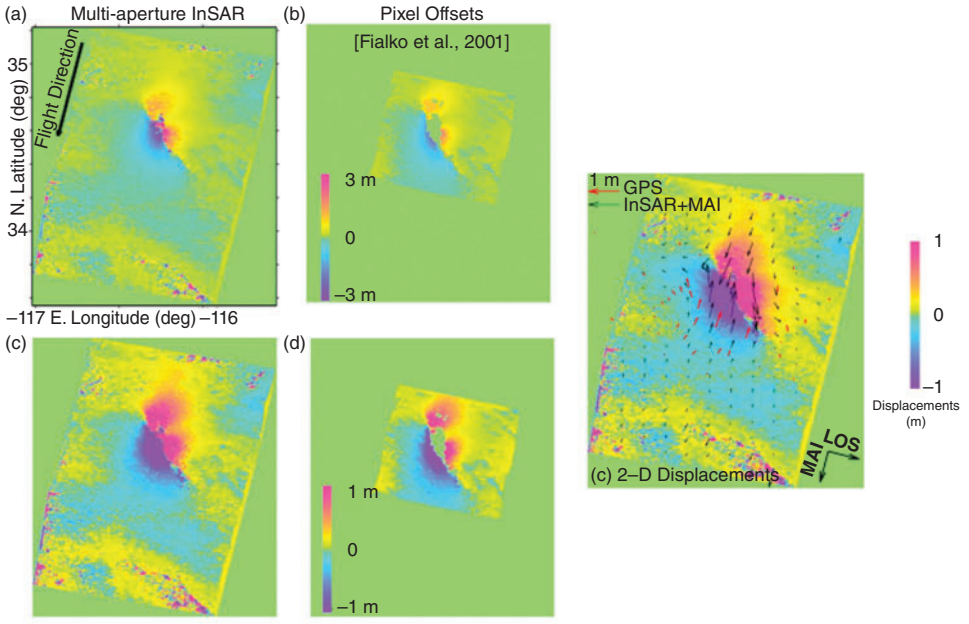

Figure 10.3 Multiple aperture interferograms (a and c) and their corresponding pixel offsets estimate (Bechor and Zebker, 2006). (b) The along track and InSAR LOS measurements with black arrows and GNSS vector measurements in red arrows. Do note the GNSS arrows are projected into radar LOS for comparison purposes.

the ionosphere (Figure 10.4). Since the quality (and coherence) of a subband interferogram is generally lower than the original full-bandwidth interferogram, and the ionospheric estimate also depends heavily on the coherence of the interferogram, thus such a method is usually considered only viable for good quality SAR data.

The underlying theory of the MAI technique takes advantage of the frequency separation between the forward-looking and backward-looking radar beams. Nonetheless, this separation can also be achieved with an intentionally steering the antenna as described in Section 8.5 on TOPSAR (Figure 8.7). Due to the designed sweeping antenna, the induced frequency separation is much larger than the PRF bandwidth of a strip-mode SAR. With such a design, this larger frequency separation makes double-difference phase more sensitive to any azimuthal motion or misregistration, but at a cost that this calculation can only be achieved at the 2-km-wide burst overlap area in the SAR image. This is referred to as *burst overlap interferometry* (BOI).

Thus, when one aims to measure azimuthal motion to form a 3-D displacement field with BOI, interpolation has to be made using the intermittent measurements. An example of such analysis is shown in Figure 10.5. Due to its high sensitivity

Downloaded from https://www.cambridge.org/core. IP address: 189.217.92.64, on 11 Feb 2026 at 15:51:46, subject to the Cambridge Core terms of use, available at https://www.cambridge.org/core/terms. https://www.cambridge.org/core/product/1F8951EFC610A352837B95E4DAEFBAEB

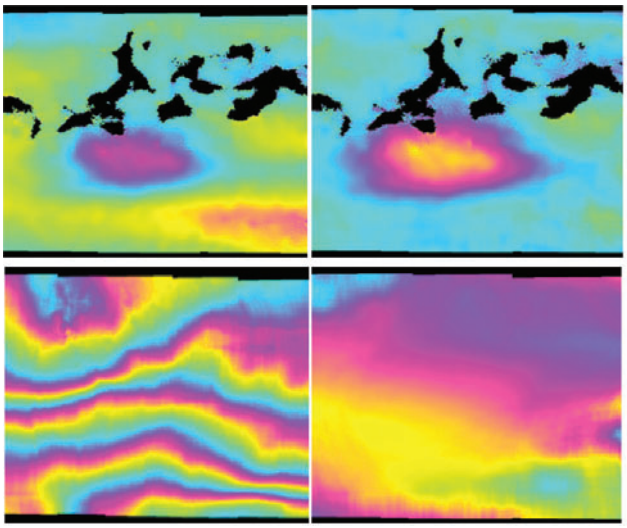

Figure 10.4 MAI interferogram estimated for the 2015 Nepal earthquake using ALOS-2 ScanSAR data (Liang and Fielding, 2017). Top left is the MAI interferogram without ionospheric phase correction using a two-burst cycle length ($2T_C$). Top right is the MAI interferogram with the ionospheric phase corrected. Bottom left is the ionospheric phase estimated using the range split-spectrum method used for correction. Bottom right is the estimated ionospheric effect in the MAI interferogram using Equation 10.5. Reprinted with permission from *IEEE Transactions on Geoscience and Remote Sensing*.

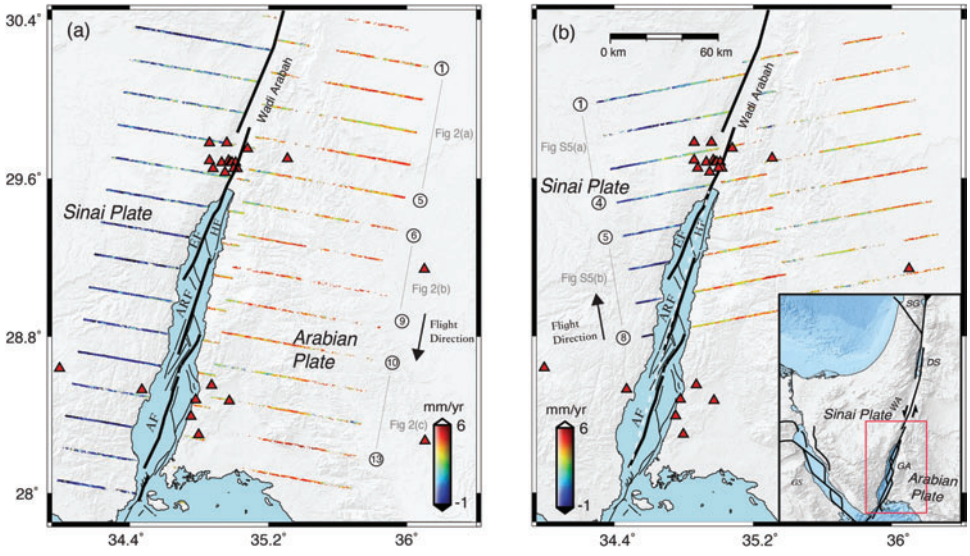

Figure 10.5 Along-track velocity derived from burst overlap interferometry (Li et al., 2021).

Downloaded from https://www.cambridge.org/core. IP address: 189.217.92.64, on 11 Feb 2026 at 15:51:46, subject to the Cambridge Core terms of use, available at https://www.cambridge.org/core/terms. https://www.cambridge.org/core/product/1F8951EFC610A352837B95E4DAEFBAEB

to azimuthal motion, such a technique is now also used to map subtle interseismic deformation as small as a few millimeters per year (Li et al., 2021) and mapping plate motion in a global framework (Lazeckỳ et al., 2023).

10.4 Stacking Approach

An interferogram measures surface deformation that occurred between the two SAR acquisition times along the radar LOS direction, and the stacking approach solves for the surface deformation rate by averaging interferograms with sufficient phase coherence that contain the common deformation signal of interest. More specially, the average LOS velocity v_{avg} of each ground pixel over a time period of interest T can be calculated as (Sandwell and Price, 1998):

$$v_{avg} = \frac{\sum_{i \in G} d_i}{\sum_{i \in G} t_i} \tag{10.6}$$

where G is a subset of coherent interferograms that were formed using two SAR scenes acquired within the time period T. The LOS measurement (in meters) and the temporal baseline of the i^{th} interferogram in G are written as d_i and t_i, respectively. To analyze how surfaces deform over time, we can solve for the average LOS velocities over multiple periods of interest using Equation 10.6. Over each period of interest T_j, we compute the cumulative LOS surface deformation over this period as the product of $v_{avg,j}$ and T_j.

Averaging interferograms that contain the common deformation signal of interest reduces the impact of random noise (e.g., tropospheric turbulence noise) by $\sim \sqrt{S}$, where S is the number of independent SAR acquisitions used in stacking. Alternatively, averaging interferograms that are formed using a particular SAR scene provides a way to characterize the InSAR noise term associated with that SAR acquisition. Under the assumption that spatially coherent tropospheric noise is the primary error source, the observed InSAR phase ϕ_{rn} at an interferogram pixel can be written as (Hanssen, 2001):

$$\phi_{rn} \approx \frac{4\pi}{\lambda}(d_{rn} + a_n - a_r) \tag{10.7}$$

where λ is the radar wavelength and d_{rn} is the LOS deformation $(d_n - d_r)$ between two SAR acquisition dates r and n. The tropospheric noise along the LOS direction on the two SAR acquisition dates is a_r and a_n, respectively.

We can generate up to $S-1$ interferograms using a common-reference SAR scene r (Tymofyeyeva and Fialko, 2015) from S SAR scenes over an area of interest. We define the common scene stacking (CSS) solution of size K as the average of a subset of K interferograms (Zebker et al., 2023):

Downloaded from https://www.cambridge.org/core. IP address: 189.217.92.64, on 11 Feb 2026 at 15:51:46, subject to the Cambridge Core terms of use, available at https://www.cambridge.org/core/terms. https://www.cambridge.org/core/product/1F8951EFC610A352837B95E4DAEFBAEB

$$\begin{aligned}\overline{\mathrm{S}}_{r,K} &= \frac{\lambda}{4\pi K}\sum_{n\in G, n\neq r}\phi_{rn} \\ &\approx \frac{1}{K}\sum_{n\in G, n\neq r} d_{rn} - a_r + \frac{1}{K}\sum_{n\in G, n\neq r} a_n\end{aligned} \tag{10.8}$$

where G is a set of SAR acquisitions that were used to form K ($K \leq S-1$) randomly selected interferograms with a common-reference SAR acquisition r.

The CSS solution $\overline{\mathrm{S}}_{r,K}$ contains three terms: the sum of LOS deformation signals of the K interferograms, the tropospheric noise a_r on the reference date r, and the average tropospheric noise of all other acquisition dates in G. Because tropospheric noise is typically not correlated beyond a few hours (Emardson et al., 2003), the term $\sum_{n\in G, n\neq r} a_n$ approaches zero when K is sufficiently large. In this scenario, $\overline{\mathrm{S}}_{r,K}$ only contains the sum of deformation signals and $-a_r$. In the case that no deformation signal is present in a dataset, the common-reference stacking solutions derived from randomly selected interferogram subsets converge to $-a_r$ as K increases.

While the deformation term d_{rn} is typically different in these K interferograms with a common-reference scene r because of different temporal baselines, the tropospheric noise term a_r remains the same. When the common-reference stacking solutions derived from randomly selected interferogram subsets do not converge, the differences between these subset stacking solutions can be used to determine the temporal characteristics of the deformation signal. For the linear deformation case, Tymofyeyeva and Fialko (2015) developed a method to separate deformation signals and noise. A common-reference stacking solution of a forward K subset as the average of K forward interferograms:

$$\overline{\mathrm{F}}_{r,K} = \frac{\lambda}{4\pi K}\sum_{n=r+1}^{r+K}\phi_{rn} \approx \frac{1}{K}\sum_{n=r+1}^{r+K} d_{rn} - a_r \tag{10.9}$$

where the reference date r is earlier in time than the nonreference date n for a forward interferogram. Similarly, a common-reference stacking solution of a backward K subset is defined as the average of K backward interferograms:

$$\overline{\mathrm{B}}_{r,K} = \frac{\lambda}{4\pi K}\sum_{n=r-K}^{r-1}\phi_{rn} \approx \frac{1}{K}\sum_{n=r-K}^{r-1} d_{rn} - a_r \tag{10.10}$$

where the reference date r is later in time than the nonreference date n for a backward interferogram.

By combining Equations 10.9 and 10.10, we eliminate a_r and estimate the average deformation rate, v_r, between SAR acquisitions $r-K$ and $r+K$ as:

Downloaded from https://www.cambridge.org/core. IP address: 189.217.92.64, on 11 Feb 2026 at 15:51:46, subject to the Cambridge Core terms of use, available at https://www.cambridge.org/core/terms. https://www.cambridge.org/core/product/1F8951EFC610A352837B95E4DAEFBAEB

$$
\begin{aligned}
v_r &\approx \frac{K}{T_{tot}}(\overline{\mathrm{F}}_{r,K} - \overline{\mathrm{B}}_{r,K}) \\
&\approx \frac{1}{T_{tot}}\left(\sum_{n=r+1}^{r+K} d_{rn} - \sum_{n=r-K}^{r-1} d_{rn}\right)
\end{aligned}
\tag{10.11}
$$

where T_{tot} is defined as the total time spanned by all interferograms as:

$$
T_{tot} = \sum_{n=r+1}^{r+K} \Delta t_{rn} + \sum_{n=r-K}^{r-1} |\Delta t_{rn}| \tag{10.12}
$$

For a backward interferogram ($n < r$), Δt_{rn} is negative. Similarly, we eliminate the deformation term and estimate the tropospheric noise term as:

$$
a_r \approx -\frac{1}{2}(\overline{\mathrm{F}}_{r,K} + \overline{\mathrm{B}}_{r,K}) \tag{10.13}
$$

The sum of deformation signals in the forward and backward K interferogram subsets equals zero when (1)$\sum_{n=r+1}^{r+K} \Delta t_{rn}$ equals $\sum_{n=r-K}^{r-1} |\Delta t_{rn}|$ and (2) the deformation signal is linear in time. The presence of nonlinear deformation signals can lead to differences in solutions derived from Equation 10.13 for different K values. These differences can be used as a measure of the uncertainty in the tropospheric noise estimates (Zebker et al., 2023).

10.5 Small Baseline Subset Method

Berardino et al. (2002) and Schmidt and Bürgmann (2003) developed the SBAS approach for reconstructing surface deformation time series from a stack of interferograms. Here we review how the SBAS algorithm works. Suppose we want to solve for the unknown LOS phase history $\phi(t)$ at a ground pixel as shown in Figure 10.6. The i^{th} interferogram formed from two SAR scenes acquired at t_m and t_n measures the unwrapped phase $\Delta\phi_i$ at this pixel. Assuming the topography-related phase has been removed, $\Delta\phi_i$ can be related to the LOS deformation d_i that occurred between two SAR acquisition times t_m and t_n as:

$$
\Delta\phi_i = \frac{4\pi}{\lambda}(d_i + n_i) \approx \frac{4\pi}{\lambda}\sum_{l=m}^{n-1} m_l \tag{10.14}
$$

where λ is the radar wavelength, n_i is the noise term of the i^{th} interferogram, and m_l is the unknown LOS deformation at the l^{the} epoch between SAR acquisition times t_l and t_{l+1}.

An interferogram can measure $\Delta\phi_i$ in Equation 10.14 with negligible topographic or spatial decorrelation error only if the spatial baseline (the distance

Downloaded from https://www.cambridge.org/core. IP address: 189.217.92.64, on 11 Feb 2026 at 15:51:46, subject to the Cambridge Core terms of use, available at https://www.cambridge.org/core/terms. https://www.cambridge.org/core/product/1F8951EFC610A352837B95E4DAEFBAEB

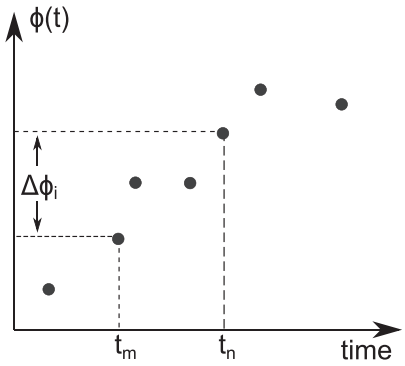

Figure 10.6 An LOS phase history we want to solve for at a given ground pixel location. The phase in a single interferogram formed from SAR data acquired at t_m and t_n measures $\Delta\phi_i$. Adapted from Tong and Schmidt (2016).

between the satellite locations at two SAR acquisition times) is small. The interferogram correlation becomes zero when the baseline component perpendicular to the LOS direction (perpendicular baseline) is larger than the critical baseline B_c, defined as:

$$B_c = \frac{\lambda \rho}{c\tau} \tan\theta \tag{10.15}$$

where ρ is the range between the radar satellite and the ground pixel, λ is the signal wavelength, θ is the radar incidence angle, c is the speed of light, and τ is the radar pulse length. In practice, an interferogram with a perpendicular baseline smaller than B_c may still suffer from severe decorrelation artifacts (e.g., due to vegetation growth). To limit phase decorrelation noise in the final time series, the SBAS method selects coherent interferograms as input data based on user-defined temporal and spatial baseline thresholds. These thresholds depend on the specific site characteristics and radar system parameters (e.g., radar wavelength), and it is recommended to include as many coherent InSAR phase measurements as possible in the SBAS inversion. This is because (1) interferograms with longer temporal baselines often contain larger secular deformation signals and (2) random phase noise tends to decrease as the number of coherent InSAR observations increases.

The formulation of the SBAS inversion is shown schematically in Figure 10.7. Given $S+1$ SAR images forming N interferograms with small baselines, we can define a matrix representation of the N-equation SBAS system as:

$$Gm = d \tag{10.16}$$

where $m = [\ m_1\ \ldots\ m_S\ ]^T$ is the vector of S unknown LOS deformation between each consecutive SAR acquisition, and $d = [\ d_1\ \ldots\ d_N\ ]^T$ is the vector of N known InSAR observations at the pixel of interest. The $N \times S$ design matrix G is also called

Downloaded from https://www.cambridge.org/core. IP address: 189.217.92.64, on 11 Feb 2026 at 15:51:46, subject to the Cambridge Core terms of use, available at https://www.cambridge.org/core/terms. https://www.cambridge.org/core/product/1F8951EFC610A352837B95E4DAEFBAEB

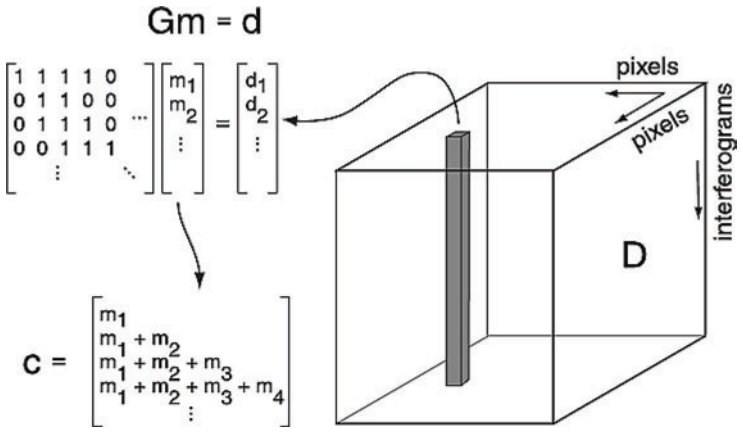

Figure 10.7 Schematic showing the relationship between InSAR phase data and model vectors in the SBAS inversion. From Schmidt and Bürgmann (2003).

the SBAS matrix. If the i^{th} interferogram measures the InSAR phase $\Delta\phi_i$ between SAR data acquisition times t_m and t_n as defined in Equation 10.14 at the pixel of interest, the i^{th} row of G has ones in the l^{th} entry for $l = m, \ldots, (n-1)$ and zeros in the remaining entries.

The vector m in Equation 10.16 can be approximately solved as:

$$m = G^{\dagger} d \tag{10.17}$$

where $G^{\dagger}$ is any generalized inverse of G. Here we choose $G^{\dagger}$ as the Moore–Penrose pseudoinverse, which can be efficiently computed using the singular value decomposition (SVD). A running sum of the incremental LOS deformation m_l yields the LOS deformation time series at the k^{th} epoch $C_k = \sum_{l=1}^{k} m_l$ at the pixel of interest.

Under the assumption that tropospheric noise can be approximated as random in time, we introduce a temporal smoothness constraint reduce tropospheric noise signatures in the LOS deformation estimates, and solve a regularized least squares problem as:

$$\begin{bmatrix} 1 & 1 & 0 & \cdots & \beta B_1 \\ 0 & 1 & 1 & \cdots & \beta B_2 \\ \vdots & \vdots & \vdots & \ddots & \vdots \\ \frac{\lambda}{\Delta t_1} & -\frac{\lambda}{\Delta t_1} & 0 & \cdots & 0 \\ 0 & \frac{\lambda}{\Delta t_2} & -\frac{\lambda}{\Delta t_2} & \cdots & 0 \\ \vdots & \vdots & \vdots & \ddots & \vdots \\ 0 & \cdots & \frac{\lambda}{\Delta t_{S-1}} & -\frac{\lambda}{\Delta t_{S-1}} & 0 \end{bmatrix} \begin{bmatrix} m_1 \\ m_2 \\ \vdots \\ m_S \\ \Delta h \end{bmatrix} = \begin{bmatrix} d_1 \\ d_2 \\ \vdots \\ d_N \\ 0 \\ \vdots \\ 0 \end{bmatrix} \tag{10.18}$$

Downloaded from https://www.cambridge.org/core. IP address: 189.217.92.64, on 11 Feb 2026 at 15:51:46, subject to the Cambridge Core terms of use, available at https://www.cambridge.org/core/terms. https://www.cambridge.org/core/product/1F8951EFC610A352837B95E4DAEFBAEB

Here λ is the temporal smoothing factor that penalizes unrealistically large temporal variations in m. To give each epoch an equal weight in the inversion, λ is scaled by the corresponding temporal interval Δt_l of the consecutive SAR observations. The choice of the smoothing factor can be optimized using independent data such as the GPS surface deformation time series. This SBAS formulation allows the estimation of the error Δh in the digital elevation model (DEM) at the pixel of interest from InSAR data (Berardino et al., 2002) because: (1) Δh can lead to an error in the i^{th} InSAR LOS deformation observation Δd_i that is linearly proportional to the InSAR perpendicular baseline B_i and (2) the constant scaling factor β can be calculated from the radar wavelength, the incidence angle of the radar wave, and the distance from the radar to the ground.

To reduce decorrelation noise, we may also solve for m using a weighted least squares scheme (Tong and Schmidt, 2016):

$$WGm = Wd \tag{10.19}$$

Here W is a diagonal weight matrix defined as:

$$W = \begin{bmatrix} \gamma_1 & 0 & 0 & 0 & \cdots & 0 \\ 0 & \gamma_2 & 0 & 0 & \cdots & 0 \\ \vdots & \vdots & \vdots & \vdots & \ddots & \vdots \\ 0 & 0 & \cdots & \gamma_N & \cdots & 0 \\ \vdots & \vdots & \vdots & \vdots & \ddots & \vdots \\ 0 & 0 & 0 & 0 & \cdots & 0 \end{bmatrix} \tag{10.20}$$

where γ_i is the spatial phase coherence of the *ith* interferograms. An example of interseismic velocity derived from coherence-based SBAS is shown in Figure 10.8.

10.6 Persistent Scatterer Algorithms

Both stacking and SBAS time series analysis methods require that InSAR phase observations are sufficiently coherent at the pixel of interest. Changes in surface scattering properties (e.g., due to vegetation growth) between consecutive radar acquisitions lead to InSAR phase decorrelation noise (Zebker and Villasenor, 1992). Because InSAR phase measurements at severely decorrelated radar pixels can be considered as random wrapped phase values between 0 and 2π, they cannot be used to reconstruct spatially coherent surface deformation patterns. *Persistent scatterer* (PS) techniques (e.g., Ferretti et al. (2000); Hooper et al. (2004); Ferretti et al. (2011)) have been developed to identify radar pixels with minimal changes in surface scattering properties (e.g., man-made structures, rocks, and barren lands).

Downloaded from https://www.cambridge.org/core. IP address: 189.217.92.64, on 11 Feb 2026 at 15:51:46, subject to the Cambridge Core terms of use, available at https://www.cambridge.org/core/terms. https://www.cambridge.org/core/product/1F8951EFC610A352837B95E4DAEFBAEB

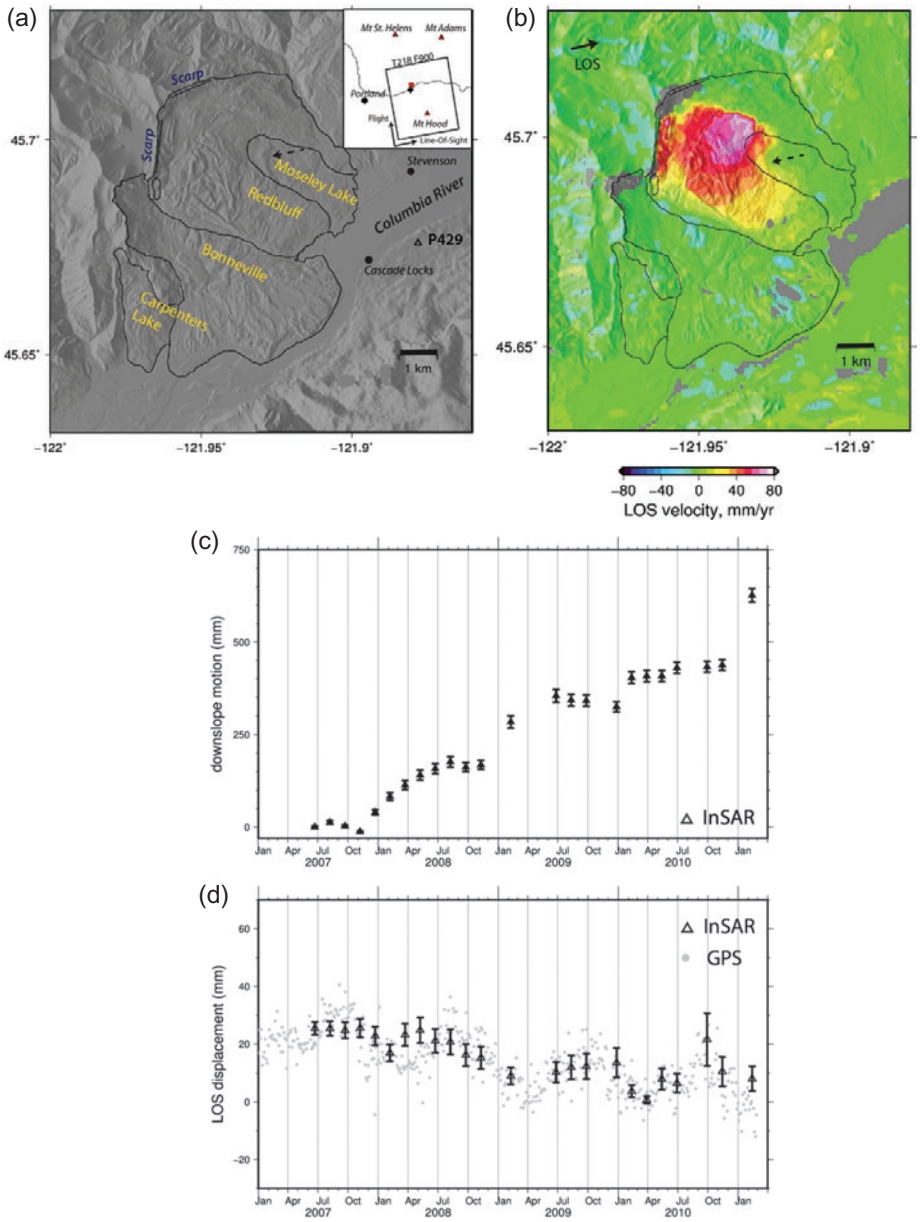

Figure 10.8 (a) Shaded relief map of the Cascade Landslide Complex and the Columbia River Gorge. The four main lobes of the landslide complex are outlined with black lines. A continuous GPS site is marked by the open triangle. The inset map shows the location of the Cascade Landslide Complex and the footprint of the ALOS-1 scene. (b) Average LOS velocity (a best-fit estimate to displacement time series) of the Cascade Landslide Complex. Warm colors indicate motion away from the satellite in the look direction (black solid arrow). (c) Cumulative downslope displacement in the deformation zone of the Red Bluff landslide from the InSAR time-series analysis. The location of the deformation time series is marked in (b). (d) Comparison of the InSAR time-series with a nearby GPS station P429. Gray dots show the daily position measured by the GPS and projected into the radar LOS direction for comparison. Negative LOS displacement corresponds to ground moving away from the satellite, that is, subsidence. The error bars of the LOS displacement are estimated from the standard deviations of the InSAR data within a 1 km window surrounding the sample location (Tong and Schmidt, 2016).

Downloaded from https://www.cambridge.org/core. IP address: 189.217.92.64, on 11 Feb 2026 at 15:51:46, subject to the Cambridge Core terms of use, available at https://www.cambridge.org/core/terms. https://www.cambridge.org/core/product/1F8951EFC610A352837B95E4DAEFBAEB

In areas with dense vegetation, only phase measurements at PS pixels have a high quality that is suitable for surface deformation time series analysis.

The first generation of PS algorithms (Ferretti et al., 2001; Lyons and Sandwell, 2003; Van Leijen, 2014) modeled radar echoes as the sum of a constant real signal and a complex circular Gaussian random noise. Based on this model, the returns from a radar pixel with a high signal-to-noise ratio (SNR) have relatively small amplitude variations. A pixel with high amplitude stability is identified as a PS pixel if its phase observations fit a given deformation model. One limitation of such approaches is that there are typically very few radar pixels with sufficient SNRs to be selected in natural terrain. To overcome this limitation, Hooper et al. (2004); Hooper and Zebker (2007); Shanker and Zebker (2007); Huang and Zebker (2019) selected PS pixels based on the statistics of InSAR phase measurements. Using a complex circular Gaussian model for both signal and noise terms, Shanker and Zebker (2007) estimated the signal-to-clutter ratio (SCR) of each radar pixel using phase measurements of interferograms that share a common reference SAR image. A PS pixel is expected to have a relatively high SCR and a narrow phase distribution. The capability of PS interferometry was further advanced by the SqueeSAR method (Ferretti et al., 2011; Goel and Adam, 2014; Lv et al., 2014). Ferretti et al. (2011) jointly analyzed nearby pixels with homogeneous amplitude distributions (referred to as statistically homogeneous pixels or SHP). The InSAR phase observations from each SHP group are averaged to improve SNR, and a covariance matrix model was employed to filter phase measurements and select PS pixels (Guarnieri and Tebaldini, 2008). The SqueeSAR-based approach is one of the very few existing methods that take into account the amplitude statistics of nearby distributed scatterers (DS). Alternatively, Costantini et al. (2008, 2014) modeled the phase difference between two adjacent radar pixels as a function of the deformation rate difference and elevation difference. For each neighboring pixel pair, an optimized deformation rate difference and elevation difference are solved to minimize the residual phase difference. The pixel pair is selected as PS if the residual phase difference is small. Because scattering signal models that take into account the phase correlation of nearby PS pixels have not been fully developed, existing PS selection algorithms are mainly based on the statistics of InSAR phase measurements at each individual radar pixel. In many cases, a deformation model (e.g., constant velocity) is employed in the selection process. However, surface deformation characteristics over the area of interest are often unknown. To overcome these limitations, a PS identification algorithm that analyzes the phase correlation of nearby radar pixels based on a similarity measure (the cosine similarity) was proposed (Wang and Chen, 2022). Here we give a review of the cosine similarity algorithm, which can be integrated with any existing PS selection algorithm to reduce the false positive and false negative PS selections at a very low computational cost.

Downloaded from https://www.cambridge.org/core. IP address: 189.217.92.64, on 11 Feb 2026 at 15:51:46, subject to the Cambridge Core terms of use, available at https://www.cambridge.org/core/terms. https://www.cambridge.org/core/product/1F8951EFC610A352837B95E4DAEFBAEB

Given K single look complex (SLC) radar images $S_1, \ldots, S_K$, $K-1$ wrapped interferograms that share a common reference SLC image can be formed. The phase values of these $K-1$ interferograms at a pixel m can be written as a phase vector $\boldsymbol{\varphi}_m = [\varphi_{m,1}, \varphi_{m,2}, \ldots, \varphi_{m,K-1}]$. We define the phase similarity between two radar pixels m and n as the cosine similarity between the phase vectors $\boldsymbol{\varphi}_m$ and $\boldsymbol{\varphi}_n$:

$$s_{mn} = \frac{1}{K-1} \sum_{k=1}^{K-1} \cos(\varphi_{m,k} - \varphi_{n,k}) \tag{10.21}$$

Here the phase similarity score s_{mn} ranges from -1 and 1. A similarity score of 1 means $\boldsymbol{\varphi}_m$ and $\boldsymbol{\varphi}_n$ are identical, 0 means $\boldsymbol{\varphi}_m$ and $\boldsymbol{\varphi}_n$ are not correlated, and -1 means $\varphi_{m,k}$ and $\varphi_{n,k}$ differ by π radians for all k's.

The cosine similarity algorithm is designed to retrieve accurate deformation signals over low-PS-density natural terrains. In this scenario, the deformation signal of interest is often caused by geophysical processes, including but not limited to coastal processes, aquifer pumping and recharge, volcanism, or fault activities. Because the Earth's crust can be modeled as a solid continuum, such surface displacements typically vary slowly in space (Segall, 2010). Because the deformation signal of interest and tropospheric noise are both spatially coherent, the phase vectors of two nearby PS pixels are expected to be similar (e.g. with phase similarity > 0.5). By contrast, the similarity score of a decorrelated pixel (a non-PS pixel) and a nearby pixel is ~0 when the total number of SAR acquisitions K is sufficiently large. This is because the phase of a decorrelated pixel can be considered as a random value between 0 and 2π (Zebker and Villasenor, 1992).

It is computationally expensive to calculate the phase similarity between all radar pixel pairs. To improve computational efficiency, a set of PS candidate pixels can be selected using an existing PS selection algorithm such as the maximum likelihood estimation (MLE) selection method (Shanker and Zebker, 2007). Following Shanker and Zebker (2007), the received echo from a radar pixel can be modeled as a coherent sum of returns from a dominant scatterer and clutter scatterers, and both components are considered as circular complex Gaussian random variables. The relative power of the dominant scatterer signal to the background clutter noise is defined as the signal-to-clutter ratio (SCR; γ). Based on this model, the probability density function (PDF) of the observed InSAR phase φ for a given SCR γ can be written as:

$$p(\varphi|\gamma) = \frac{1-\rho^2}{2\pi} \frac{1}{1-\rho^2\cos^2\varphi} \left(1 + \frac{\rho\cos\varphi \arccos(-\rho\cos\varphi)}{\sqrt{1-\rho^2\cos^2\varphi}}\right) \tag{10.22}$$

where ρ is defined as $\rho = 1/(1+\gamma^{-1})$. A PS pixel has a high SCR and a relatively narrow phase distribution, while a non-PS pixel has a low SCR and a relatively

Downloaded from https://www.cambridge.org/core. IP address: 189.217.92.64, on 11 Feb 2026 at 15:51:46, subject to the Cambridge Core terms of use, available at https://www.cambridge.org/core/terms. https://www.cambridge.org/core/product/1F8951EFC610A352837B95E4DAEFBAEB

wide phase distribution. The SCR value $\hat{\gamma}_{\mathrm{ML},m}$ at a given pixel m is estimated by comparing the observed InSAR phase vector $\boldsymbol{\varphi}_m$ to Equation 10.22 in a maximum likelihood sense:

$$\hat{\gamma}_{\mathrm{ML},m} = \arg\max_{\gamma} \prod_{k=1}^{K-1} p(\tilde{\varphi}_{m,k}|\gamma) \tag{10.23}$$

where $\tilde{\varphi}_{m,k}$ is the residual phase at pixel m in the k^{th} interferogram after removing the spatially correlated phase component through filtering. PS candidates are chosen as the pixels with $\hat{\gamma}_{\mathrm{ML},m} > 2$. This threshold value was suggested by previous SCR-based PS selection studies (Shanker and Zebker, 2007; Huang and Zebker, 2019; Adam et al., 2003; Chen et al., 2017) as a reasonable trade-off between the false positive and false negative rates. A higher $\hat{\gamma}_{\mathrm{ML},m}$ value leads to a lower false positive rate and a higher false negative rate.

During the preliminary PS candidate selection, the SCR value at each pixel is estimated independently. The spatial phase consistency between PS pixels is not taken into account, which may lead to inaccurate PS selections (Chen et al., 2017). To overcome this limitation, the false positive PS pixels in the current PS candidates pool are removed if their median cosine similarity score to their N nearest neighbor PS candidates is lower than a user-defined threshold. To further recover false negatives in the preliminary PS candidate pool, the phase similarity of every non-PS pixel m with its N nearest neighbor PS pixels is also calculated, and the pixel m is selected as a new PS if the maximum phase similarity is greater than a user-defined threshold. The search of false negative PS pixels is performed iteratively to expand the PS set, and the number of PS pixels increases monotonically through iterations. Because the number of detected PS pixels is upper-bounded by the total number of radar pixels, our algorithm is guaranteed to terminate when no more PS pixels can be identified through additional iterations. Because the phase vectors of two non-PS pixels are unlikely to be similar when the number of SAR acquisitions is sufficiently large (e.g., $K > 30$), the search for false negatives typically introduces very few false positive PS pixels. More discussion on the similarity threshold selection can be found in Wang and Chen (2022).

Once PS pixels are identified, an adaptive spatial interpolation can be employed between PS pixels (Chen et al., 2015) to reconstruct spatially coherent phase observations (including deformation signals and tropospheric noise). Given a wrapped interferogram, the phase value at pixel m is replaced by the weighted average phase value of its N nearest neighbor PS pixels as:

$$\varphi_m^{\mathrm{interp}} = \arg\left(\sum_{n \in \mathrm{NN}(m,N)} w_n e^{i\varphi_n} \right) \tag{10.24}$$

Downloaded from https://www.cambridge.org/core. IP address: 189.217.92.64, on 11 Feb 2026 at 15:51:46, subject to the Cambridge Core terms of use, available at https://www.cambridge.org/core/terms. https://www.cambridge.org/core/product/1F8951EFC610A352837B95E4DAEFBAEB

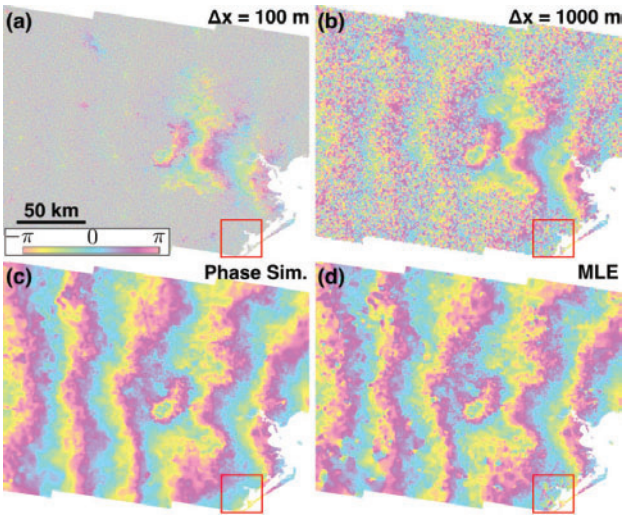

Figure 10.9 (a) 672-day Sentinel-1 interferogram (January 3, 2018–November 6, 2019) over the Greater Houston area (100-m pixel spacing). (b) Same interferogram with an additional 10 looks in both dimensions (1 000-m pixel spacing). (c) Interpolated interferogram using PS pixels identified by the phase similarity algorithm. (d) Interpolated interferogram using PS pixels identified by the MLE algorithm. From Wang and Chen (2022).

where $\arg(z)$ is the argument of the complex number z, $\mathrm{NN}(m,N)$ represents the N nearest neighbor PS pixels of pixel m, and φ_n is the wrapped phase value at pixel n. $w_n = e^{-r_n^2/2R}$, where r_n is the distance between the center pixel m and pixel n and $R = \max_n r_n$.

The PS interpolation method can not only fill the spatial gaps in high-quality InSAR phase measurementsi (Figure 10.9) but also substantially improve the accuracy and computational efficiency of phase unwrapping (Chen and Zebker, 2001). Additionally, PS interpolation can be used to evaluate the accuracy of PS selection. While accurate PS selection usually results in spatially smooth phase reconstruction, interpolation from inaccurate PS sets can cause abrupt phase changes near false positive PS pixels. Such phase artifacts can be easily identified through visual inspection or quantified by the phase unwrapping error at a radar pixel m defined as:

$$\varphi_m^{\mathrm{err}} = \sum_n |\Delta\varphi_{mn}| f_\pi(|\Delta\varphi_{mn}|) \tag{10.25}$$

where $\Delta\varphi_{mn}$ is the unwrapped phase difference between pixel m and pixel n (or $\varphi_m^{\mathrm{unwrap}} - \varphi_n^{\mathrm{unwrap}}$), f_π being an indicator function such that $f_\pi(x) = 1$ if $x > \pi$ and $f_\pi(x) = 0$ otherwise. The summation is performed on the four adjacent pixels of the center pixel m. The total phase unwrapping error of an interferogram is calculated as the sum of the phase unwrapping errors over all radar pixels.

Downloaded from https://www.cambridge.org/core. IP address: 189.217.92.64, on 11 Feb 2026 at 15:51:46, subject to the Cambridge Core terms of use, available at https://www.cambridge.org/core/terms. https://www.cambridge.org/core/product/1F8951EFC610A352837B95E4DAEFBAEB

10.7 Problems

1. An ice stream has a typical velocity of 2 m per year and was imaged by a C-band radar with a 12-day cadence. Why would the pixel offset tracking method provide better results than standard interferometry?
2. Derive Equation (10.4). Consider the relation between the squint angle and the corresponding Doppler caused by the moving platform.
3. What are the limitations of CSS? Consider a few scenarios in which such a technique fails to produce a valid estimate of atmospheric phase screens. One example is very strong atmospheric noise on two consecutive observation dates.
4. What complementary approach is best for measuring deformation in an area that is highly decorrelatead?
5. Create a synthetic deformation time series with a linear deformation signal of 1 cm/year. The first synthetic SAR scenes are acquired on day 0 and then every 12 days for a year. At each SAR acquisition, add a random Gaussian noise with a zero mean and standard deviation of 1 cm. Generate all possible InSAR pairs as your synthetic InSAR data at a pixel location. Using stacking and SBAS algorithms to solve for the deformation rate. Comment on the statistics of the estimation error based on 1 000 synthetic InSAR data vectors with different random noise samples. Now repeat the experiment with different set ups (e.g., 6-day revisit cycle or different noise levels) and comment on the results. If interferograms with a temporal baseline longer than 24 days are completely decorrelated, what is the impact on the results?

Downloaded from https://www.cambridge.org/core. IP address: 189.217.92.64, on 11 Feb 2026 at 15:51:46, subject to the Cambridge Core terms of use, available at https://www.cambridge.org/core/terms. https://www.cambridge.org/core/product/1F8951EFC610A352837B95E4DAEFBAEB

11

Integration of InSAR and GNSS

11.1 Complementary Attributes of InSAR and GNSS

Interferometric synthetic aperture radar (InSAR) and the global navigation satellite system (GNSS) can provide measurements of surface deformation at the accuracy of 10 mm or better, yet they have very different spatial and temporal resolution. Continuously operating GNSS sites provide three components of surface deformation with 5–30 mm accuracy at high temporal sampling (1–15 seconds). As discussed in Chapter 9, the two frequencies of GNSS systems enable very accurate correction of the path delays through the ionosphere. In addition, tropospheric delays can be estimated and corrected by measuring the LOS path delay to numerous satellites as they transit across the sky. These multiple paths, combined with the high sampling rate and the assumption that the site is moving slowly relative to a 10-minute satellite transit, provide the atmospheric delay data needed to make a very accurate ionospheric and tropospheric noise correction. The main limitation of GNSS is the sparse spatial sampling. In densely instrumented regions such as Japan or California, the typical spacing of GNSS sites is 20 km or closer. However, in many remote areas, the site spacing may be 200 km or more. Because InSAR measures relative deformation with respect to a reference point, GNSS surface deformation observations are often used to calibrate InSAR measurements to the absolute reference frame of the Earth (including moving plates) as defined by the International Terrestrial Reference Frame ITRF20 (Altamimi et al., 2023).

InSAR has very different attributes. First, a single interferogram provides only one component of deformation in the LOS direction. Current InSAR-capable satellites do not have sufficient bandwidth to enable reliable ionospheric correction, so the longer-wavelength SAR systems (-L- and S-band) may have meter or more errors across the swath of an interferogram, especially in high-latitude regions. In addition, there is no spatial or temporal redundancy in a single interferogram, so it is not possible to correct for the tropospheric delay directly from InSAR data, which

Downloaded from https://www.cambridge.org/core. IP address: 189.217.92.64, on 11 Feb 2026 at 15:51:46, subject to the Cambridge Core terms of use, available at https://www.cambridge.org/core/terms. https://www.cambridge.org/core/product/1F8951EFC610A352837B95E4DAEFBAEB

is typically ~50–80 mm on larger scales (>100 km) and ~8 mm on scales less than 10 km (Figure 9.5). The temporal sampling of InSAR is much worse than GNSS. For example, the Sentinel-1 satellite(s) currently have a 12-day cadence, although when both S-1a and S-1b were operating, the cadence was 6 days in some locations. The COSMO-SkyMed system can achieve a 4-day revisit cycle, but these data are not freely available. While InSAR decorrelation commonly restricts the time span of individual interferograms to be less than a few months over vegetated regions due to temporal decorrelation, it is possible to use the SBAS method discussed in Chapter 10 to create longer time series. However, this limits the number of InSAR phase observations suitable as input for the SBAS inversion and reduces the ability to mitigate random tropospheric turbulence noise. Increasing the InSAR timespan using SBAS introduces large temporal errors on long timescales due to the noise and decorrelation in the individual interferogram unless external constraints are available.

The conclusion is that InSAR and GNSS measurement systems need to be combined to achieve high accuracy (<20 mm), high spatial resolution (<1 km), vector displacements, and long-timespan accuracy at a cadence of the InSAR system. A diagram crudely showing the space-time scales at which each system excels is shown in Figure 11.1. Note there is a small overlap zone, centered at the characteristic spacing of the GNSS sites and the time over which several interferograms can be combined to reduce the ionospheric/atmospheric noise. In this overlap zone, measurements from the two systems can be combined to achieve a single geodetic system with improved space/time sampling. However, such a combination for a single InSAR look direction time series still does not provide vector displacements. In this chapter we discuss the strengths and limitations of the InSAR systems, the methods of using GNSS data to improve the InSAR accuracy and temporal resolution, and ways to use multiple InSAR look directions and ancillary products such as pixel tracking and burst overlap interferometry to reconstruct vector deformation time series. There are many ways to approach this integration, so we will move from the simplest to the most advanced.

11.2 Vector Decomposition

As discussed in Chapter 7, the unwrapped phase of a single interferogram can be converted to a line-of-sight (LOS) deformation d_{los} map by multiplying by the λ and dividing by 4π

$$d_{los} = -\phi \frac{\lambda}{4\pi}. \tag{11.1}$$

where the extra factor of 2 is needed to account for the two-way travel time of the radar pulse. The negative sign is used to convert the range increase to a decrease in

Downloaded from https://www.cambridge.org/core. IP address: 189.217.92.64, on 11 Feb 2026 at 15:51:46, subject to the Cambridge Core terms of use, available at https://www.cambridge.org/core/terms. https://www.cambridge.org/core/product/1F8951EFC610A352837B95E4DAEFBAEB

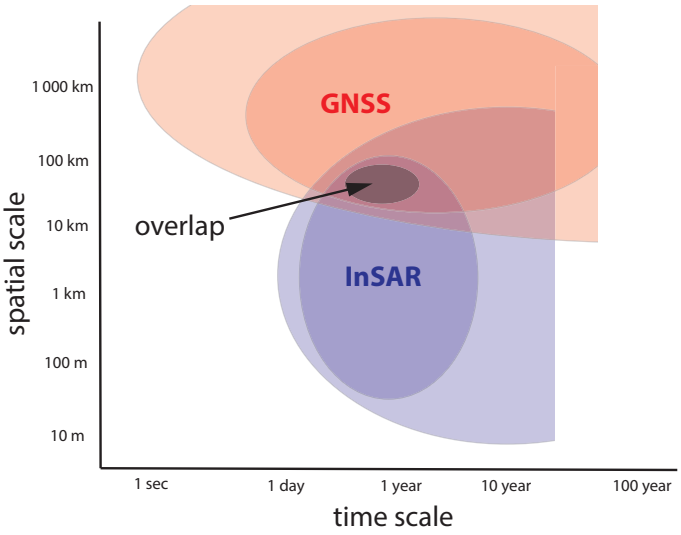

Figure 11.1 Schematic diagram showing the approximate spatial and temporal sampling of GNSS and InSAR systems; darker is better. GNSS has the highest accuracy and best range of temporal resolution from 1 second to the time span since numerous sites were installed ~30 years ago. InSAR has superior spatial resolution and broad spatial coverage, but the temporal resolution is limited by the cadence of the measurements. There is an overlap zone with a spatial scale of ~30–100 km and a time scale of one month to several years where the more accurate GNSS data can be used to bring the less accurate InSAR data into the global reference system (e.g., ITRF20, (Altamimi et al., 2023)).

the LOS distance between the ground and the spacecraft. Throughout this chapter we will use a local coordinate system of East, North, and Up (ENU) to match the coordinates commonly used by the GNSS and modeling communities.

As a first step, we use the location and elevation of a point on the ground to compute the look vector between that point and the satellite. For a particular point in the interferogram (lon, lat, elevation), we compute its Earth-centered Earth-fixed (ECEF) Cartesian coordinate (x_o, y_o, z_o) as shown in Figure 3.8 using Equation 3.13. Given the precise orbit, we can use the back project algorithm, described in Section 3.7.2, to calculate the position of the satellite at minimum range (x_s, y_s, z_s). The unit look vector $\mathbf{n}$ from the ground to the satellite is

$$\mathbf{n} = \frac{\mathbf{x}_s - \mathbf{x}_o}{|\mathbf{x}_s - \mathbf{x}_o|}. \tag{11.2}$$

Now we need to rotate this unit vector from the ECEF coordinates to the ENU coordinates. This involves two rotation matrices described at https://gssc.esa.int/navipedia/index.php/Transformations_between_ECEF_and_ENU_coordinates. First consider a simple case of the ENU axes located at 0° latitude and 0°

Downloaded from https://www.cambridge.org/core. IP address: 189.217.92.64, on 11 Feb 2026 at 15:51:46, subject to the Cambridge Core terms of use, available at https://www.cambridge.org/core/terms. https://www.cambridge.org/core/product/1F8951EFC610A352837B95E4DAEFBAEB

longitude. The E and N components are tangent to the ellipse of the Earth. The E axis is rotated 90° with respect to the Earth's x-axis and the U axis is rotated by –90° with respect to the Earth's z-axis. For proper alignment of an ENU frame at any latitude and longitude location, we need the following

$$\theta_r = \frac{\pi}{2} - \theta_g \tag{11.3}$$

$$\lambda_r = \frac{\pi}{2} + \lambda_g \tag{11.4}$$

where θ_g and λ_g are the geographic latitude (also called geodetic latitude) and longitude, respectively. Then two rotations are needed to transform a unit vector from the ECEF coordinates to the ENU coordinates

$$\mathbf{n}_{ENU} = \mathbf{R}_1\,(\theta_r)\,\mathbf{R}_3\,(\lambda_r)\,\mathbf{n} \tag{11.5}$$

where the two rotation matrices are given by

$$\mathbf{R}_1\,(\theta_r) = \begin{pmatrix} 1 & 0 & 0 \\ 0 & \cos\theta_r & \sin\theta_r \\ 0 & -\sin\theta_r & \cos\theta_r \end{pmatrix} \tag{11.6}$$

$$\mathbf{R}_3\,(\lambda_r) = \begin{pmatrix} \cos\lambda_r & \sin\lambda_r & 0 \\ -\sin\lambda_r & \cos\lambda_r & 0 \\ 0 & 0 & 1 \end{pmatrix} \tag{11.7}$$

There is a function in the GMTSAR software package called *SAT_look* that uses the precise orbit of the reference SAR image to compute a unit look vector $\mathbf{n}_{ENU}$ from the ground to the satellite at a particular geographic longitude, latitude, and elevation above the WGS84 ellipsoid.

Now we can transform a surface deformation vector, either from GNSS measurements $\mathbf{d}_{gnss}$ or a model output, to the LOS direction of an interferogram

$$d_{los} = \mathbf{d}_{gnss} \bullet \mathbf{n}_{ENU}. \tag{11.8}$$

Many studies assume this transformation is uniform over the entire frame of an interferogram. That is approximately true for the 100 km by 100 km frames of the European Remote Sensing satellite (ERS) and Envisat data. However, the incidence angle for Sentinel-1 varies from 29° in the near range to 46° in the far range, so we will consider that the unit look vector changes with position. One could compute the local incidence angle θ_i as

$$\theta_i = \tan^{-1}\frac{u}{\left(e^2 + n^2\right)^{1/2}} \tag{11.9}$$

Downloaded from https://www.cambridge.org/core. IP address: 189.217.92.64, on 11 Feb 2026 at 15:51:46, subject to the Cambridge Core terms of use, available at https://www.cambridge.org/core/terms. https://www.cambridge.org/core/product/1F8951EFC610A352837B95E4DAEFBAEB

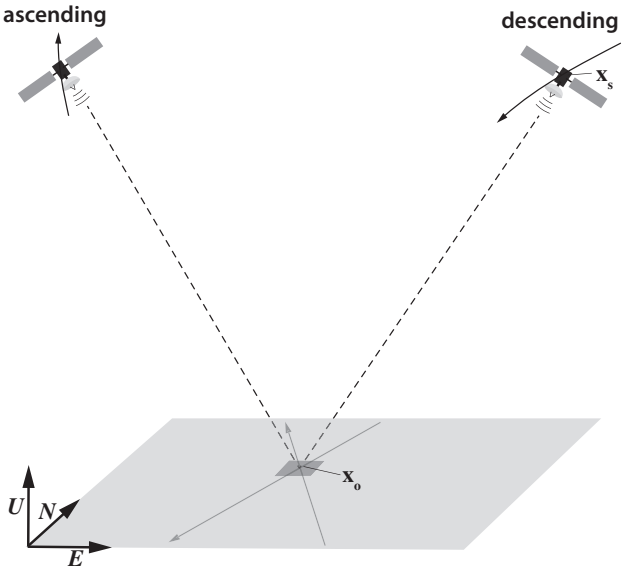

Figure 11.2 Schematic view of line of sight (LOS) measurements on ascending and descending satellite passes (after Fuhrmann and Garthwaite (2019)).

where $\mathbf{n}_{enu} = (e, n, u)$ are the components of the local ENU look vector. Similarly, the satellite azimuth is

$$\alpha = \tan^{-1} \frac{n}{e} \tag{11.10}$$

As discussed earlier, most InSAR satellites can provide surface deformation measurements along two look directions. When the deformations are large, pixel tracking methods, as discussed in Chapter 10, can provide a third component of deformation (Fialko et al., 2001).

Figure 11.2 shows the radar imaging geometry from ascending and descending look angles. First consider a pixel located exactly halfway between the two satellite tracks. In this case the look angle on the ascending and descending passes is equal. Also, the satellite azimuth of the two passes is equal but opposite in sign. For this ideal case, one can project the ENU deformation into the two LOS deformations measured by the satellite as

$$\begin{pmatrix} d_a \\ d_d \end{pmatrix} = \begin{pmatrix} e & n & u \\ -e & n & u \end{pmatrix} \begin{pmatrix} d_e \\ d_n \\ d_u \end{pmatrix}. \tag{11.11}$$

By subtracting the ascending and descending LOS deformations, one can uniquely relate the east motion to the difference between the two LOS measurements

$$d_a - d_d = 2ed_e. \tag{11.12}$$

Downloaded from https://www.cambridge.org/core. IP address: 189.217.92.64, on 11 Feb 2026 at 15:51:46, subject to the Cambridge Core terms of use, available at https://www.cambridge.org/core/terms. https://www.cambridge.org/core/product/1F8951EFC610A352837B95E4DAEFBAEB

The sum of the two LOS deformations gives

$$d_a + d_d = 2nd_n + 2ud_u. \tag{11.13}$$

Note the sum of the ascending and descending interferograms is a mixture of north and up displacement. For a typical mid-latitude ERS image, the ascending unit vector is (0.387 0.082 0.918). Here the unit vector for the north component is more than 10 times smaller than the up component and 4.7 times smaller than the east component. This is because at mid and low latitudes, the satellite track is only 13° from an N-S direction and the LOS measurement is almost perpendicular to the N-S vector. Since most InSAR satellites have high-inclination orbits, they are not sensitive to N-S deformation. Indeed, if one is studying a process that is dominated by vertical motions such as a hydrologic basin or volcanic inflation, one could ignore the N-S contribution to Equation 11.13 and relate the vertical deformation as $d_u = (d_a + d_d)/2u$. Moreover, if only the ascending or descending track is available, one may approximate the vertical deformation as $d_u = d_a/u$, although Fuhrmann and Garthwaite (2019) note that this latter approximation is not accurate for a finite size deformation feature with non-negligible east/west motions.

This simplified geometric analysis highlights the strengths and weaknesses of measuring deformation with InSAR. For example, InSAR is suitable for monitoring strike-slip deformation on an E-W-trending fault such as the North Anatolian fault in Turkey, but not suitable for monitoring strike-slip deformation on the N-S trending Dead Sea Transform. In a general case, we can compute the ENU look vectors for ascending and descending geometries at a pixel location and then perform the LOS decomposition similar to Equation 11.11.

11.3 Corrected GNSS LOS Displacement for Events

First consider a displacement event that occurs on a timescale shorter than the repeat cycles of an InSAR satellite. A good example is the 2019 Ridgecrest earthquakes. For this discussion, we consider the two earthquakes (M6.4 July 4 and M7.1 July 6) as a single event and ignore the postseismic deformation on the 12-day repeat timescale of Sentinel-1. The objective is to combine the InSAR and GNSS data to obtain the best possible surface displacement model.

A descending LOS displacement map, spanning both Ridgecrest, is shown in Figure 11.3 along with the positions of continuous GNSS sites. The large-scale errors were corrected using the GNSS sites in the area. The GMTSAR routine *SAT_look* uses the longitude, latitude, and elevation of each GNSS site, along with the orbital state vector for the SAR image, to create a different unit vector $\mathbf{n}_{ENU}$ for each GNSS site. The dot product of the unit vector and the vector displacement of the GNSS between the two times of the reference and repeat images results in

Downloaded from https://www.cambridge.org/core. IP address: 189.217.92.64, on 11 Feb 2026 at 15:51:46, subject to the Cambridge Core terms of use, available at https://www.cambridge.org/core/terms. https://www.cambridge.org/core/product/1F8951EFC610A352837B95E4DAEFBAEB

an estimate of the InSAR error at each site. These point errors are fit with a surface using a polynomial or 2-D spline that is subtracted from the interferogram to make the correction. A plot of the corrected LOS displacement and the GNSS LOS displacement is shown in Figure 11.3.

We note that there are many papers on this topic and many go far beyond this simple exercise to use ascending and descending passes from multiple satellites (e.g., Jin and Fialko (2020)) and pixel offsets from optical imagery to recover the near-fault horizontal displacements as well as GNSS time series and seismic waveforms to decompose the deformation from the M6.4 and 7.1 events (Antoine et al., 2021; Guns et al., 2022). Indeed, in most of these studies the ultimate objective is to invert for the slip at depth using all surface displacements available (e.g., Jin and Fialko (2020)).

11.4 Interseismic Velocity and Strain Rate

Unlike earthquake deformation, which typically ranges between 10s of cm and a few meters in a matter of seconds or minutes, interseismic velocities are slow and steady. Typical interseismic slip rates on active faults can range from <1 mm/yr (e.g., the Longmenshan Fault (Zhang, 2013)) to >30 mm/yr (e.g., the San Andreas Fault (Guns et al., 2022)). Such rates can be easily dwarfed by noise in a single interferogram (e.g., tens of millimeters). Therefore, long time series (Chapter 10) derived from hundreds of high-quality interferograms (with major noise terms corrected; see Chapter 9) are typically required to constrain interseismic velocity to an accuracy of 1 mm/yr. This velocity accuracy gives an equivalent strain rate accuracy of 100 nanostrain/yr over 10 kilometers, a distance comparable to typical fault locking depth, thus useful for seismic hazard assessment (Xu et al., 2021).

We can calculate the theoretical uncertainty of interseismic LOS velocity, σ_v, using

$$\sigma_v \simeq \frac{2\sqrt{3}\sigma_e}{\sqrt{NT}} \tag{11.14}$$

where σ_e is the time series uncertainty per epoch, N is the total number of epochs, and T is the total time span of the time series in years (Zhang et al., 1997). The epoch uncertainty is a function of the coherence of interferograms and the quality of atmospheric and earth tide corrections. Using $\sigma_e \approx 10$ mm as a rough estimate for C-band time series after tropospheric correction (Morishita et al., 2020), a 1 mm/yr velocity uncertainty requires at least 60 epochs over 4.5 years (Ou et al., 2022).

Downloaded from https://www.cambridge.org/core. IP address: 189.217.92.64, on 11 Feb 2026 at 15:51:46, subject to the Cambridge Core terms of use, available at https://www.cambridge.org/core/terms. https://www.cambridge.org/core/product/1F8951EFC610A352837B95E4DAEFBAEB

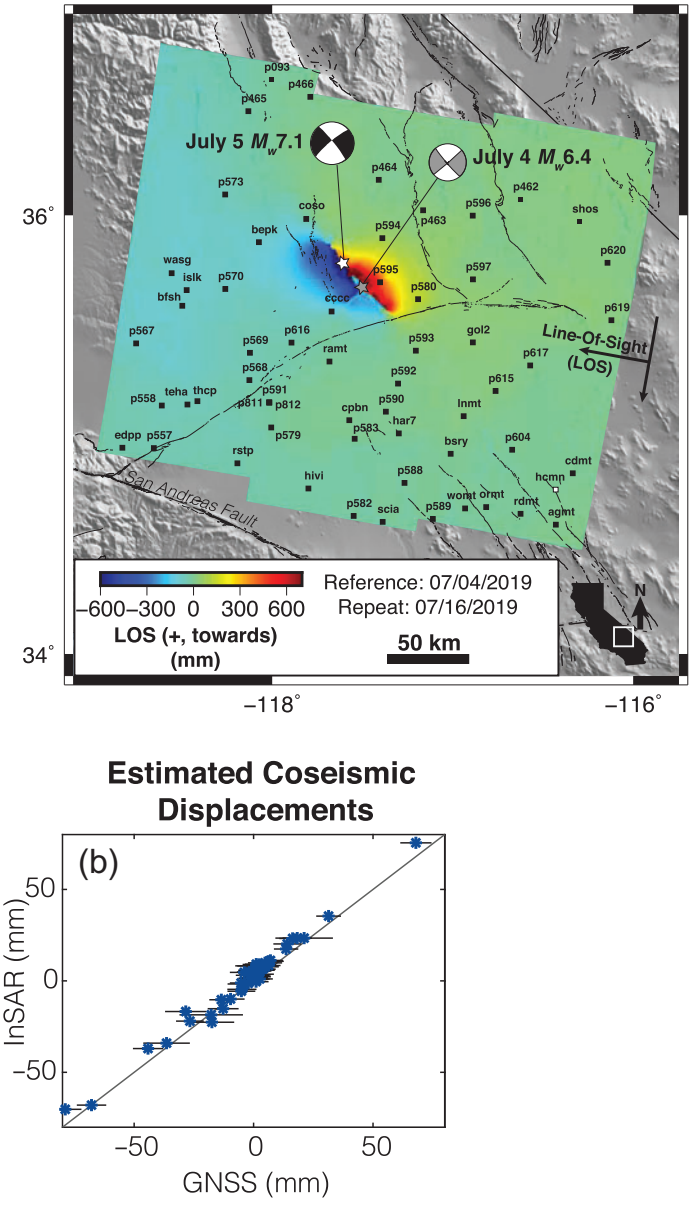

Figure 11.3 (a) Descending LOS unwrapped interferogram spanning the two Ridgecrest earthquakes. Continuously operating GNSS stations within the frame of the interferogram were used to correct long-wavelength errors due to atmospheric, ionospheric, and orbital errors. (b) After correction, the RME misfit between the GNSS and InSAR data is 13 mm (Guns et al., 2022).

Downloaded from https://www.cambridge.org/core. IP address: 189.217.92.64, on 11 Feb 2026 at 15:51:46, subject to the Cambridge Core terms of use, available at https://www.cambridge.org/core/terms. https://www.cambridge.org/core/product/1F8951EFC610A352837B95E4DAEFBAEB

The horizontal strain rate tensor, $\dot{\varepsilon}_h$, is the symmetrical part of the horizontal velocity gradient tensor (e.g., Wang and Shen, 2020):

$$\begin{aligned}
\dot{\varepsilon}_h &= \begin{bmatrix} \dot{\varepsilon}_{xx} & \dot{\varepsilon}_{xy} \\ \dot{\varepsilon}_{yx} & \dot{\varepsilon}_{yy} \end{bmatrix} = \begin{bmatrix} \frac{\partial V_E}{\partial x} & \frac{1}{2}\left(\frac{\partial V_E}{\partial y} + \frac{\partial V_N}{\partial x}\right) \\ \frac{1}{2}\left(\frac{\partial V_N}{\partial x} + \frac{\partial V_E}{\partial y}\right) & \frac{\partial V_N}{\partial y} \end{bmatrix} \\
\dot{\varepsilon}_{dil} &= \dot{\varepsilon}_{xx} + \dot{\varepsilon}_{yy} \\
\dot{\varepsilon}_{shear} &= \sqrt{\dot{\varepsilon}_{xy}^2 + (\dot{\varepsilon}_{xx} - \dot{\varepsilon}_{yy})^2/4} \\
\dot{\varepsilon}_{II_h} &= \sqrt{\dot{\varepsilon}_{xx}^2 + 2\dot{\varepsilon}_{xy}^2 + \dot{\varepsilon}_{yy}^2}
\end{aligned} \tag{11.15}$$

where V_E and V_N are the east and north velocities, and $\dot{\varepsilon}_{dil}$, $\dot{\varepsilon}_{shear}$ and $\dot{\varepsilon}_{II_h}$ are the dilatation, maximum shear, and second invariant of the horizontal strain rate tensor (Figure 11.4).

We can only obtain V_E in Equation 11.15 from InSAR by decomposing the LOS velocities from the ascending and descending tracks. For V_N, we rely on interpolating the GNSS north velocities (Figure 11.4(a)). Combining these two data sets is an art. Given the different spatial and noise characteristics of InSAR and GNSS as discussed in Section 11.1, there are several goals one might wish to achieve in this step: (1) Suppress noise while retaining the high resolution of the InSAR V_E; (2) Interpolate the irregularly spaced GNSS V_N without generating artifacts; (3) Settle on a resolution that allows InSAR to reveal tectonically interesting features without overstretching the GNSS resolution; otherwise, the V_N gradients can be significantly smoother than the V_E gradients, resulting in strain rate fields with unbalanced constituting components.

For applications where we expect the velocity field to be strictly increasing in one direction (e.g., deformation under a regional tectonic stress), median filtering the InSAR V_E is a powerful way to suppress noise, localize strain onto faults, and highlight creeping sections (Figure 11.4(b), Ou et al. (2022)). The appropriate filter window is a function of the velocity step and locking depth of the fault, as well as the noise level of the velocity field (Figure 11.5). Interpolating just the GNSS V_N can be achieved through fitting velocities using spatial basis functions such as splines (e.g., GMT surface) or employing geostatistical weighted neighborhood methods (e.g., kriging). The former requires assumptions that are not necessarily tectonic. The latter, if pushing the resolution too hard relative to the GNSS station spacing, can result in a ringing effect in the strain rate field at common radii to GNSS stations.

There are also two types of methods designed to work with both V_E and V_N, or even LOS velocities, at the same time. The first type is through inverting velocity vectors at vertices of either a fixed (*VELMAP*, Wang and Wright (2012)) or an ensemble of variable (Pagani et al., 2021) triangular mesh(es) and calculating

Downloaded from https://www.cambridge.org/core. IP address: 189.217.92.64, on 11 Feb 2026 at 15:51:46, subject to the Cambridge Core terms of use, available at https://www.cambridge.org/core/terms. https://www.cambridge.org/core/product/1F8951EFC610A352837B95E4DAEFBAEB

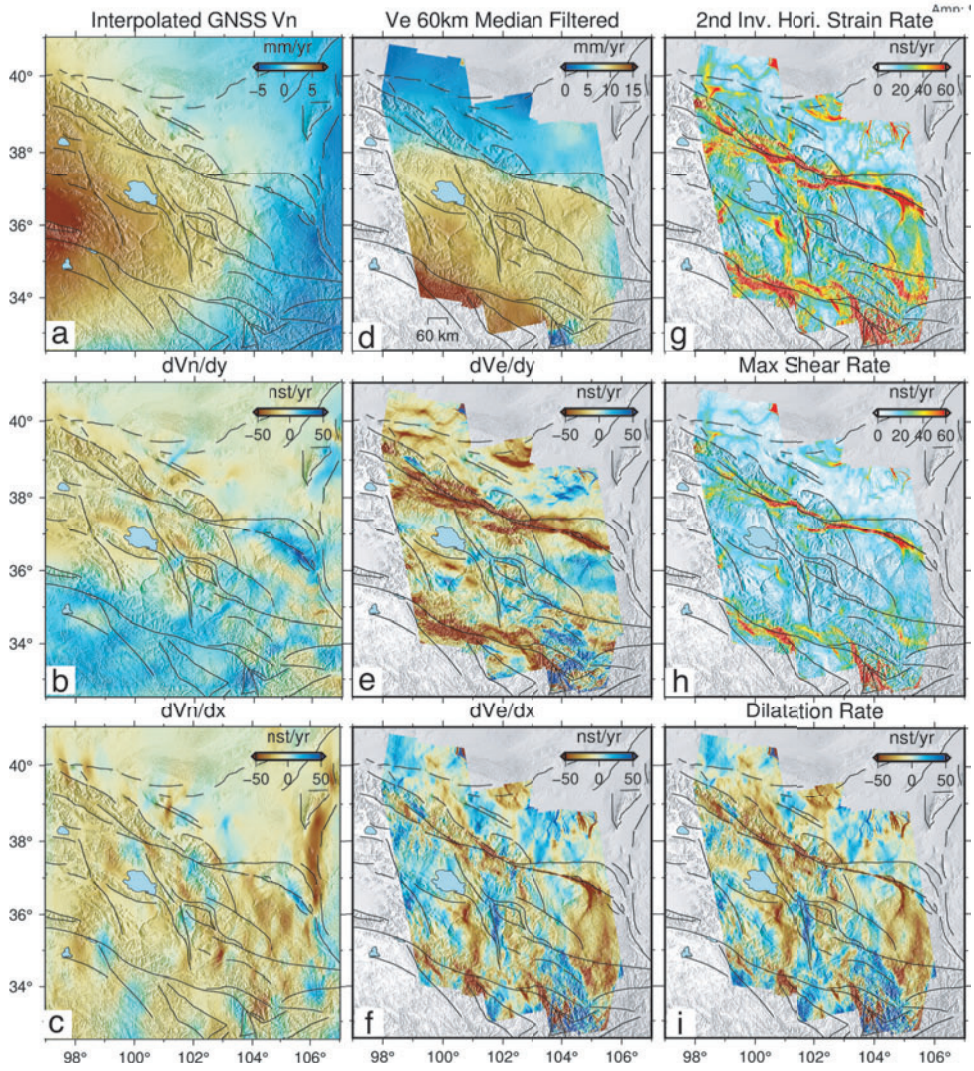

Figure 11.4 (a) Interpolated north velocities from GNSS. (b, c) Horizontal gradients of (a). (d) Median filtered InSAR east velocities. (e, f) Horizontal gradients of (d). (g) Second invariant of horizontal strain rate. (h) Maximum shear strain rate. (i) Dilatation rate (Ou et al., 2022).

strain rates within the mesh triangles. The second type is through velocity vector interpolation based on the physical assumption of elasticity (*gpsgridder*, Sandwell and Wessel (2016)) and the direct inversion of strain rates of stresses (Haines et al., 2015; Haines and Holt, 1993). For all, except the ensemble methods, the choice of the smoothing parameter has a strong influence on the resultant strain rate fields. The traditional L-curve method is a useful approach to balance model smoothness

Downloaded from https://www.cambridge.org/core. IP address: 189.217.92.64, on 11 Feb 2026 at 15:51:46, subject to the Cambridge Core terms of use, available at https://www.cambridge.org/core/terms. https://www.cambridge.org/core/product/1F8951EFC610A352837B95E4DAEFBAEB

Downloaded from https://www.cambridge.org/core. IP address: 189.217.92.64, on 11 Feb 2026 at 15:51:46, subject to the Cambridge Core terms of use, available at https://www.cambridge.org/core/terms. https://www.cambridge.org/core/product/1F8951EFC610A35283789SE4DAEFBAEB

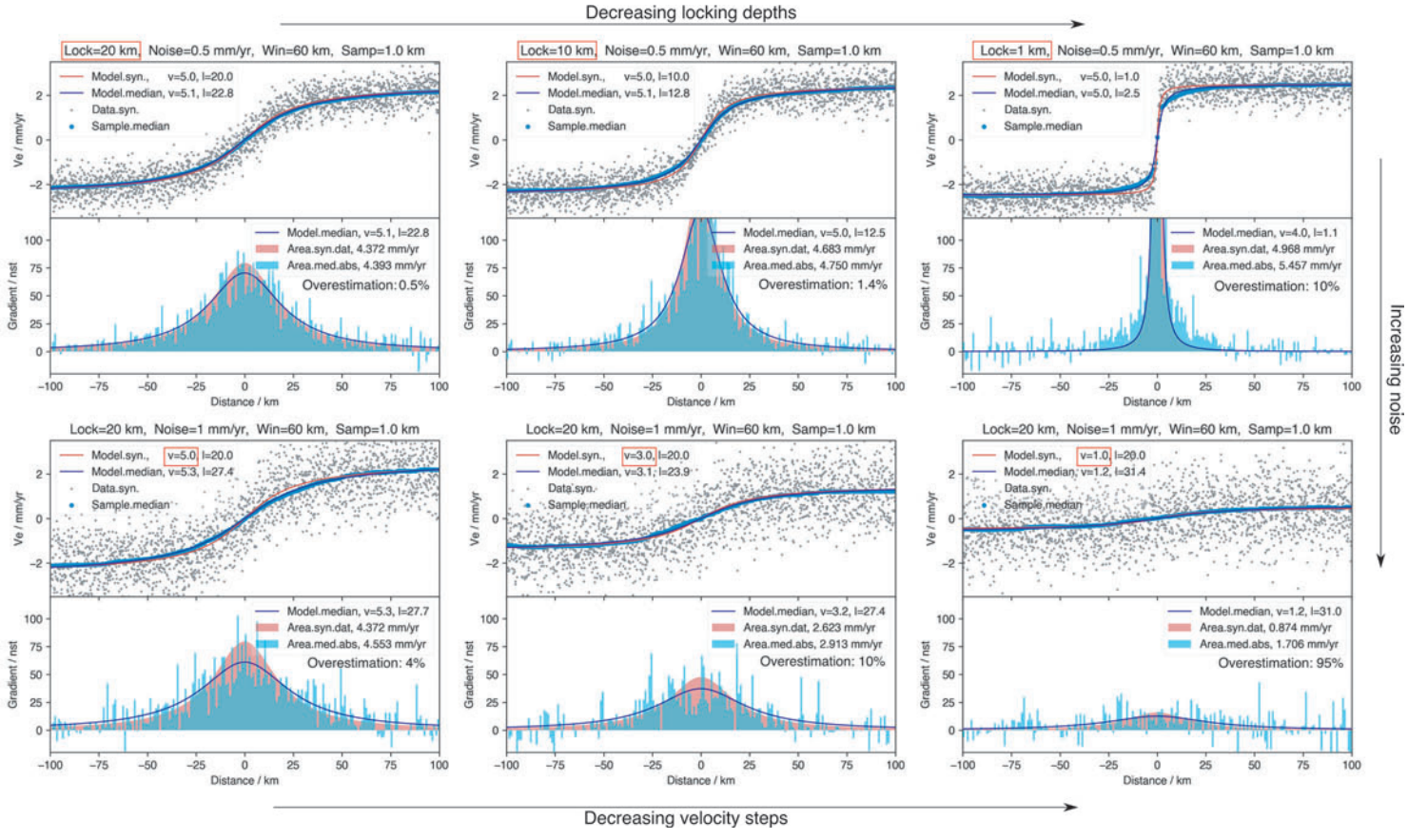

Figure 11.5 Synthetic tests of filtering a 1-D arctangent velocity profile (red line) with Gaussian noise (gray dots) with a median filter window of 60 km. A larger filter window is needed for smaller locking depths, higher noise, and smaller velocity steps across the fault (Ou et al., 2022).

and data misfit (Maurer and Materna, 2023) and is implemented in the open-source Python package, *Strain_2D* (Materna et al., 2021), which allows cross-comparison of strain rate fields from different methods.

11.5 InSAR/GNSS Time Series

InSAR and GNSS time series are useful for constraining deformation in different parts of an earthquake cycle (Liu et al., 2021; Guns et al., 2022), characterizing spatiotemporal variability of fault creep (Khoshmanesh et al., 2015; Li et al., 2023), detecting volcanic unrest (Gaddes et al., 2019; Liu et al., 2023), tracing groundwater recharge (Hu et al., 2021; Neely et al., 2021), and monitoring permafrost dynamics (Li et al., 2015; Daout et al., 2020a). The InSAR time series is generally more uncertain than the GNSS time series due to the lower temporal sampling rates (Figure 11.6). However, the spatial pattern of InSAR velocities coupled with

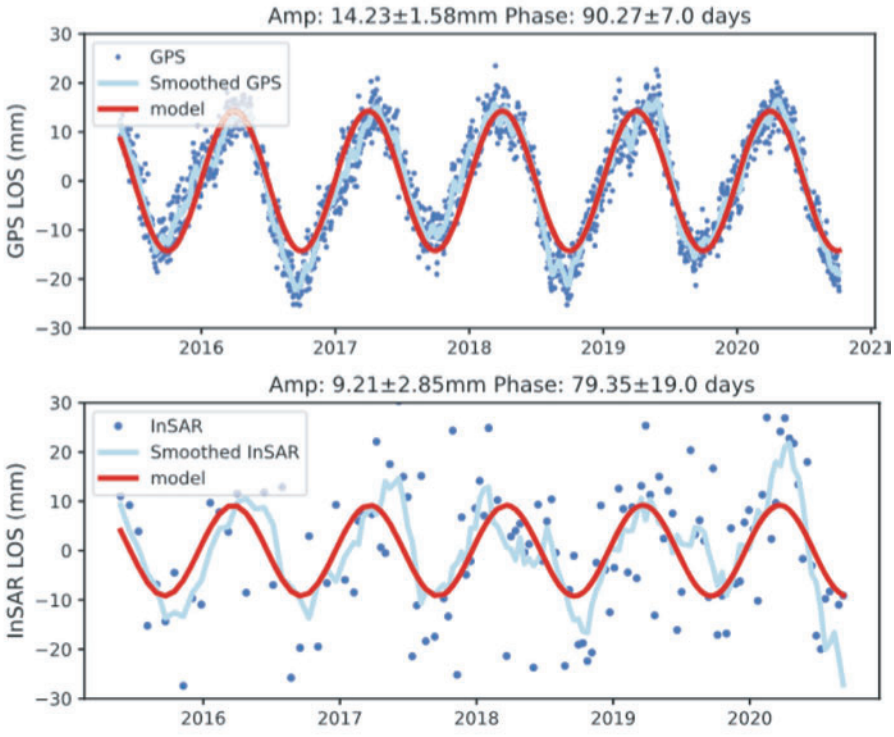

Figure 11.6 Comparison between continuous GNSS time series and InSAR time series extracted from a pixel colocated with GNSS station P242 in California (Li et al., 2023).

Downloaded from https://www.cambridge.org/core. IP address: 189.217.92.64, on 11 Feb 2026 at 15:51:46, subject to the Cambridge Core terms of use, available at https://www.cambridge.org/core/terms. https://www.cambridge.org/core/product/1F8951EFC610A352837B95E4DAEFBAEB

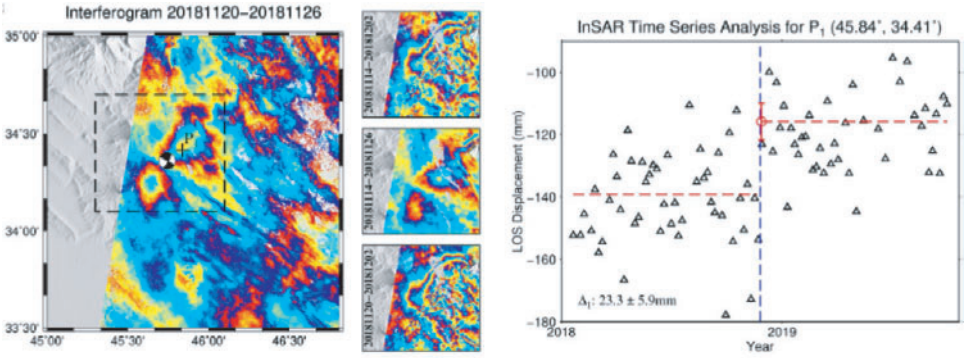

Figure 11.7 Four coseismic interferograms straddle the 2018 Nov 25 Mw 6.3 earthquake at the Iran–Iraq border. Fitting a step function to the noisy time series at pixel P_1 helps obtain a more accurate coseismic deformation field (Liu et al., 2021).

independent data sets often gives clues to the dominant deforming source in an otherwise blind mixture of latent deformation sources.

The knowledge of the temporal characteristics of the dominant deforming source is useful for deciding the linear combination of independent temporal components for parametric time series inversion. For small and deep earthquakes where surface deformation is small, fitting a Heaviside (step) function to the time series pixel by pixel can resolve a coseismic deformation field that is cleaner than the best single interferogram (Figure 11.7; Liu et al., 2021). For larger or shallower earthquakes where postseismic deformation is observable over months or years, fitting a logarithmic function following the Heaviside function helps resolve the coseismic and postseismic components of the earthquake cycle (Figure 11.8; Daout et al., 2019). Inverting cumulative creep on fault patches from InSAR time series can reveal spatial-temporal variations in creep kinematics (Figure 11.9; Khoshmanesh et al., 2015). Surface deformation induced by groundwater withdrawal and recharge often exhibits seasonal oscillations. The amplitude and phase of the sinusoidal functions are indicative of groundwater level fluctuations and flow timing and paths (Figure 11.10; Neely et al., 2021). Similar sinusoidal patterns can be observed on high mountains experiencing permafrost freeze-and-thaw cycles (Daout et al., 2020a). Net subsidence rate suggests overall decay of mountain permafrost due to climate change, and the increasing amplitude of the seasonal oscillation suggests increasing permafrost active layer thaw (Figure 11.11).

When the purpose is to detect changes such as the onset of volcanic unrest, independent component analysis is an effective tool (Ebmeier, 2016; Gaddes et al., 2018). This method is particularly useful for automatically monitoring global active volcanoes. Independent component analysis is performed on the historical time

Downloaded from https://www.cambridge.org/core. IP address: 189.217.92.64, on 11 Feb 2026 at 15:51:46, subject to the Cambridge Core terms of use, available at https://www.cambridge.org/core/terms. https://www.cambridge.org/core/product/1F8951EFC610A352837B95E4DAEFBAEB

Downloaded from https://www.cambridge.org/core. IP address: 189.217.92.64, on 11 Feb 2026 at 15:51:46, subject to the Cambridge Core terms of use, available at https://www.cambridge.org/core/terms. https://www.cambridge.org/core/product/1F8951EFC610A35283789SE4DAEFBAEB

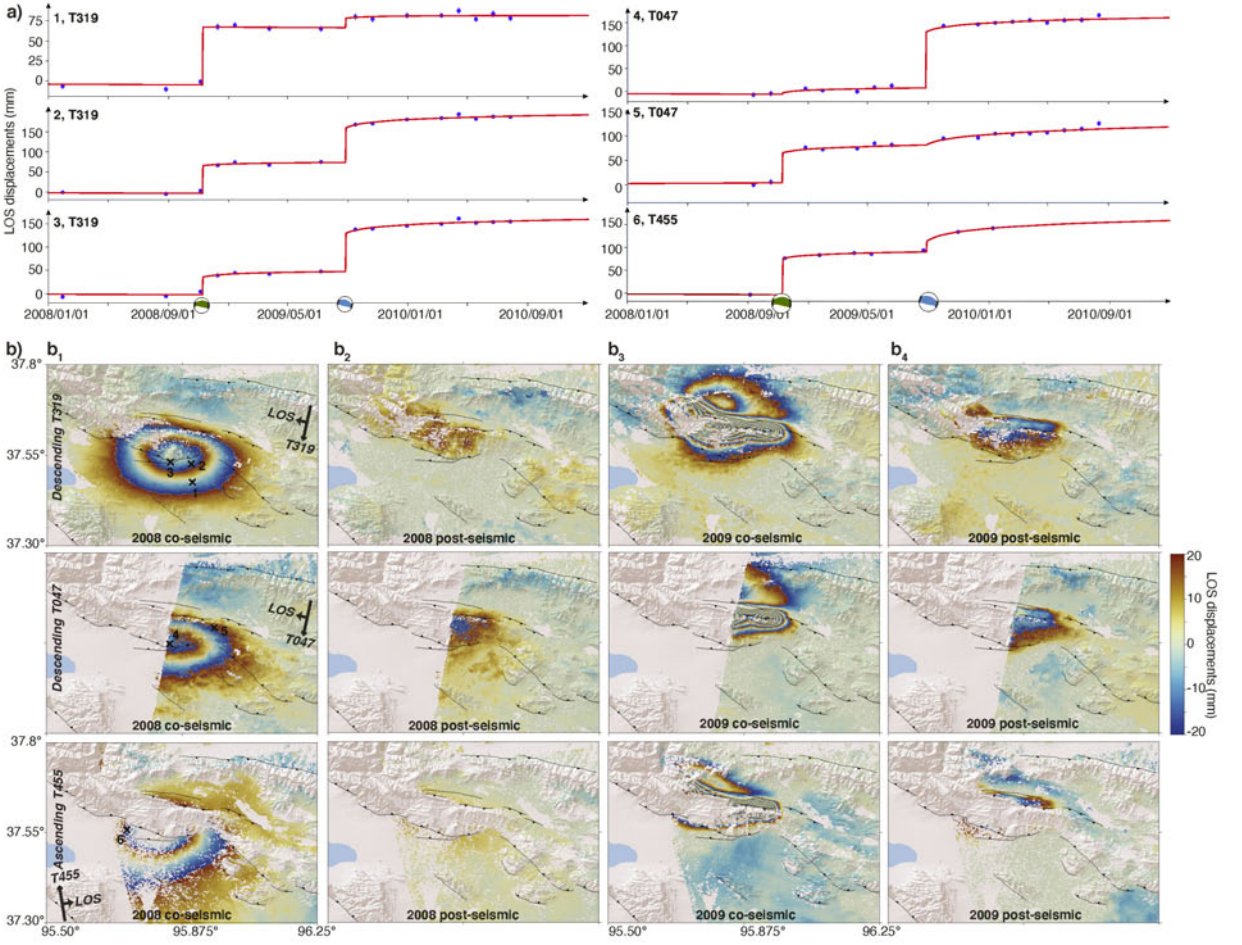

Figure 11.8 Two Heaviside functions followed by logarithmic decays fitted to time series to extract coseismic and postseismic deformations of an earthquake doublet in the Qaidam basin in 2008 and 2009 (Daout et al., 2020b).

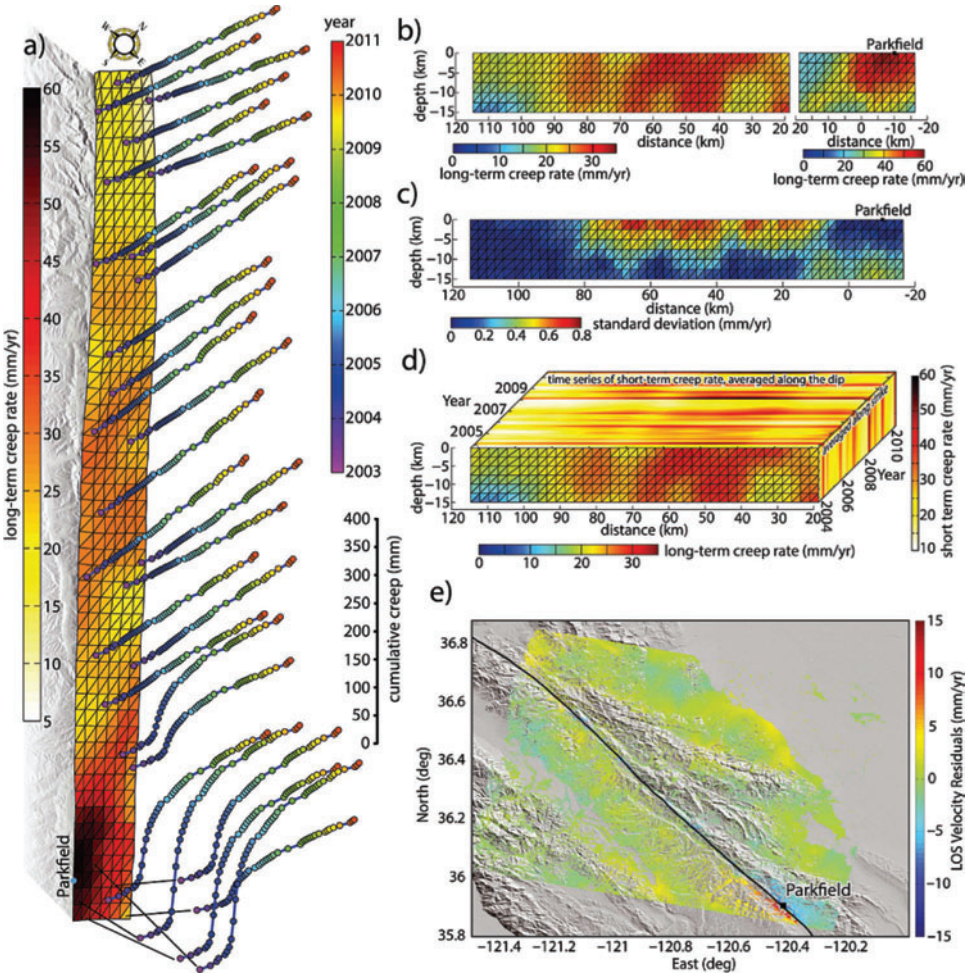

Figure 11.9 Inverted spatial-temporal variation of creep along the Central Segment on the San Andreas Fault (Khoshmanesh et al., 2015).

series to obtain a set of spatially independent sources, which are used to fit the future interferograms. An unrest is flagged when either the relative importance of the independent components changes or the misfit changes significantly (*LiCSAlert*; Figure 11.12; Gaddes et al. (2019)).

It is also possible to infer large-scale deformation sources by investigating temporal characteristics of the time series. Lemrabet et al. (2023) analyzed the time series of range and azimuth coefficients of planar ramps inverted from InSAR time series (Maubant et al., 2020) to identify dominant periodicity in the large-scale features (Figure 11.13). The fortnightly periodicity in the atmospheric delay-corrected time series represents solid earth tide.

Downloaded from https://www.cambridge.org/core. IP address: 189.217.92.64, on 11 Feb 2026 at 15:51:46, subject to the Cambridge Core terms of use, available at https://www.cambridge.org/core/terms. https://www.cambridge.org/core/product/1F8951EFC610A352837B95E4DAEFBAEB

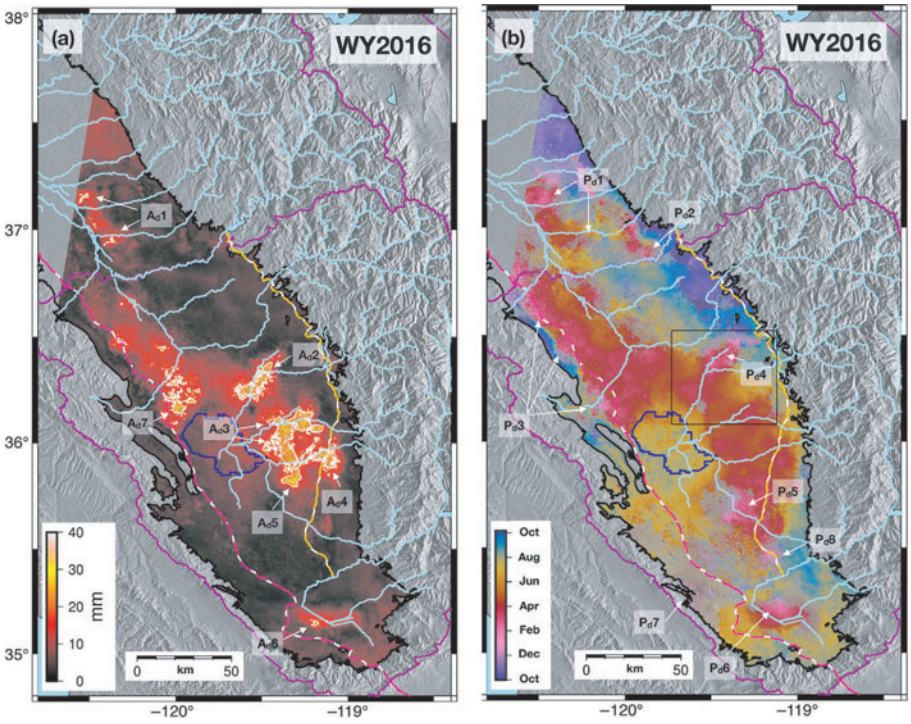

Figure 11.10 Seasonal (a) amplitude and (b) phase of LOS displacement during the water year 2016 in California's San Joaquin Valley (Neely et al., 2021).

11.6 Problems

1. How would you correct the long-wavelength errors in InSAR displacement and velocity mapping in the following cases: (1) dense GNSS stations available with continuous time series; (2) dense GNSS stations available with data available only as long-term averaged velocities and not time series; (3) sparse GNSS stations relative to SAR swath width; (4) no GNSS data available.
2. Generalize Equation 11.11 for cases where the pixel is not exactly in the center range of the ascending and descending SAR images. Derive the (e, n, u) unit look vectors from an arbitrary ground pixel $\mathbf{x}_o$ to the satellites in the ascending and descending orbits at positions $\mathbf{x}_s^a$ and $\mathbf{x}_s^d$, respectively (Figure 11.2). This equation is rank-deficient. How would you approach solving this equation?
3. Why is a larger filter window needed for median filtering the arctangent-shaped velocity profile with smaller locking depths, higher noise, and smaller velocity steps across the active fault for strain rate calculations (Figure 11.5)?
4. How would you construct the linear equations for parametric time series inversion? Consider a time series affected by an earthquake happening at time t_e

Downloaded from https://www.cambridge.org/core. IP address: 189.217.92.64, on 11 Feb 2026 at 15:51:46, subject to the Cambridge Core terms of use, available at https://www.cambridge.org/core/terms. https://www.cambridge.org/core/product/1F8951EFC610A352837B95E4DAEFBAEB

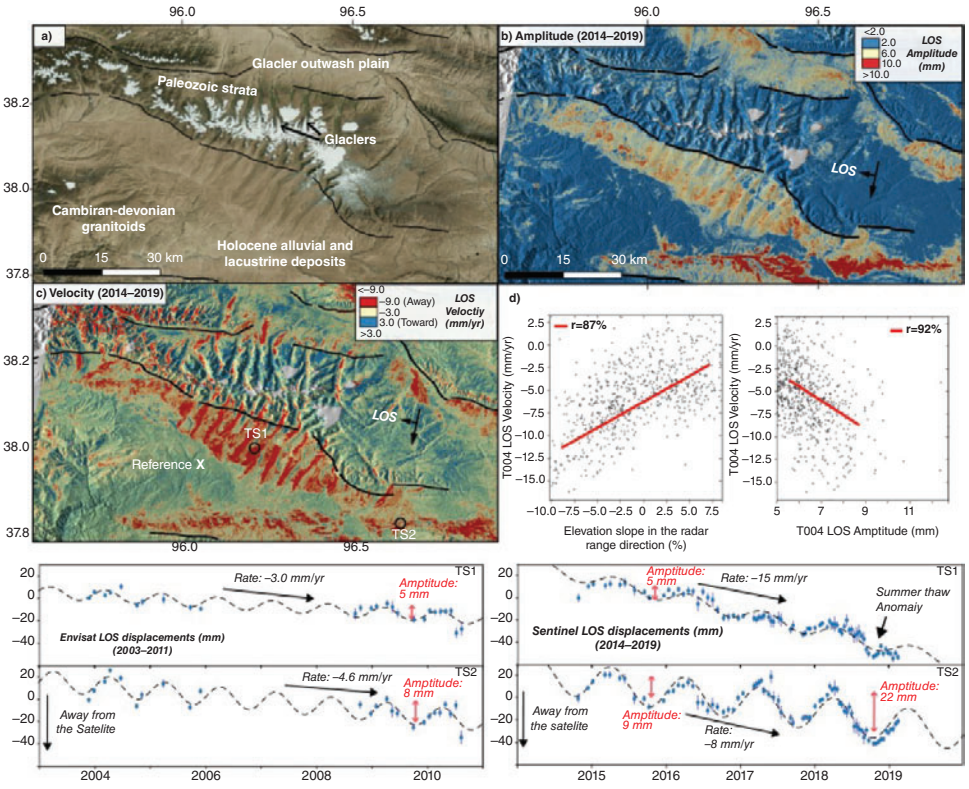

Figure 11.11 (a) Satellite imagery, (b) seasonal amplitude, and (c) LOS velocity over western Qilianshan. (d) Correlation between LOS velocity and topographic gradient. (e) Time series showing increasing amplitude of seasonal oscillations over time (Daout et al., 2020a).

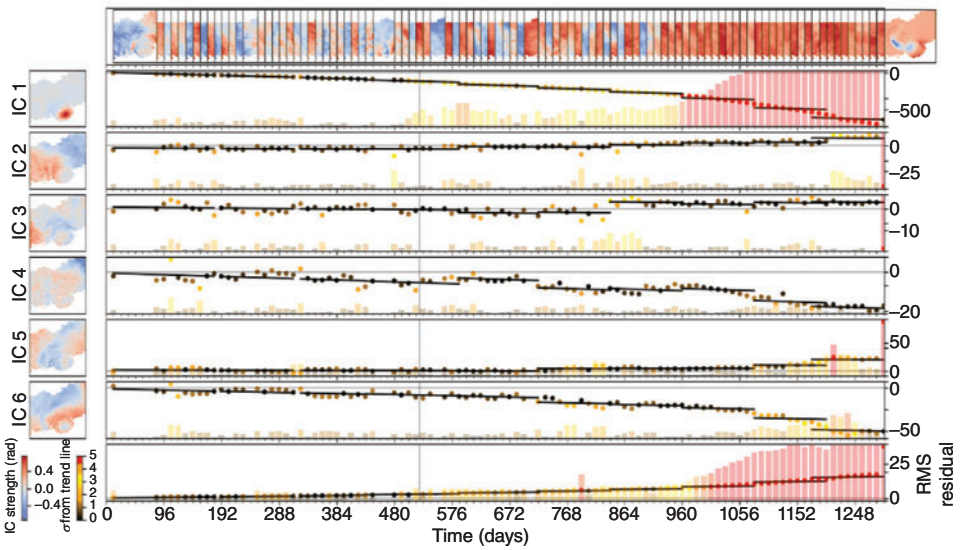

Figure 11.12 Detecting volcanic unrest using significant changes in the relative weighting of different independent components and the ability to fit the time series with independent components, implemented in *LiCSAlert* (Gaddes et al., 2019).

Downloaded from https://www.cambridge.org/core. IP address: 189.217.92.64, on 11 Feb 2026 at 15:51:46, subject to the Cambridge Core terms of use, available at https://www.cambridge.org/core/terms. https://www.cambridge.org/core/product/1F8951EFC610A352837B95E4DAEFBAEB

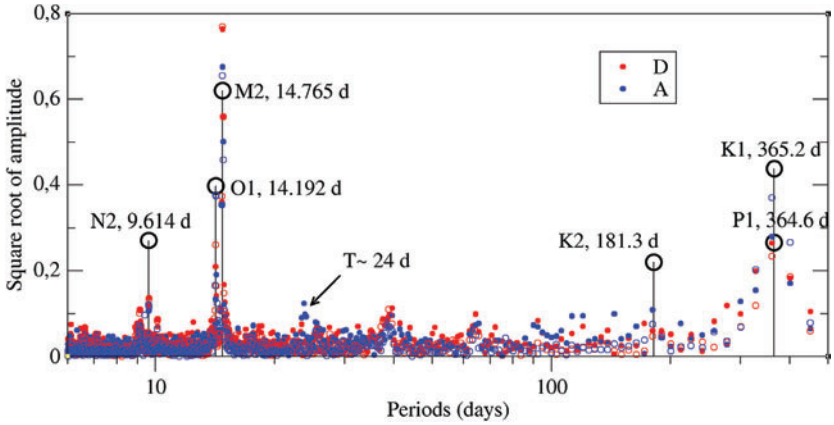

Figure 11.13 Lamb-Scargle periodogram for observed (filled circles) and modeled (open circles, alias periods for Sentinel-1, 6-day repeat, Table 9.2) solid Earth tide time series in range inverted from descending (red) and ascending (blue) tracks (Lemrabet et al., 2023).

followed by postseismic deformation with a logarithmic decay with characteristic time τ, in an area experiencing permafrost decay due to global warming with seasonal freeze-and-thaw cycles of increasing seasonal amplitude over time (Figures 11.8 and 11.11).

Downloaded from https://www.cambridge.org/core. IP address: 189.217.92.64, on 11 Feb 2026 at 15:51:46, subject to the Cambridge Core terms of use, available at https://www.cambridge.org/core/terms. https://www.cambridge.org/core/product/1F8951EFC610A352837B95E4DAEFBAEB

References

Adam, N., B. Kampes, M. Eineder, J. Worawattanamateekul, and M. Kircher, The development of a scientific permanent scatterer system, in *Proceedings of the Joint ISPRS/EARSeL Workshop "High Resolution Mapping from Space 2003,"* ISPRS, 2003.

Agnew, D., 6-Earth tides, *Treatise Geophysics*, *3*, 163–195, 2010.

Agnew, D. C., SPOTL: Some programs for ocean-tide loading, *Technical report*, Scripps Institution of Oceanography, 2012.

Altamimi, Z., P. Rebischung, X. Collilieux, L. Métivier, and K. Chanard, ITRF2020: An augmented reference frame refining the modeling of nonlinear station motions, *Journal of Geodesy*, *97*(5), 47, 2023.

Antoine, S. L., Y. Klinger, A. Delorme, K. Wang, R. Bürgmann, and R. D. Gold, Diffuse deformation and surface faulting distribution from submetric image correlation along the 2019 Ridgecrest, California, ruptures, *Bulletin of the Seismological Society of America*, *111*(5), 2275–2302, 2021.

Avouac, J.-P., F. Ayoub, S. Leprince, O. Konca, and D. V. Helmberger, The 2005, Mw 7.6 Kashmir earthquake: Sub-pixel correlation of ASTER images and seismic waveforms analysis, *Earth and Planetary Science Letters*, *249*(3–4), 514–528, 2006.

Bamler, R., and M. Eineder, ScanSAR processing using standard high precision SAR algorithms, *IEEE Transactions on Geoscience and Remote Sensing*, *34*(1), 212–218, 1996.

Baran, I., M. Stewart, B. Kampes, Z. Perski, and P. Lilly, A modification to the Goldstein Radar interferogram filter, *IEEE Transactions on Geoscience and Remote Sensing*, *41*(9), 2114–2118, 2003.

Bechor, N. B., and H. A. Zebker, Measuring two-dimensional movements using a single InSAR pair, *Geophysical Research Letters*, *33*(16), 2006.

Bekaert, D., R. Walters, T. Wright, A. Hooper, and D. Parker, Statistical comparison of InSAR tropospheric correction techniques, *Remote Sensing of Environment*, *170*, 40–47, 2015.

Bendat, J. S., and A. G. Piersol, *Random Data: Analysis and Measurement Procedures*, John Wiley & Sons, New York, 2011.

Berardino, P., G. Fornaro, R. Lanari, and E. Sansosti, A new algorithm for surface deformation monitoring based on small baseline differential SAR interferograms, *IEEE Transactions on Geoscience and Remote Sensing*, *40*(11), 2375–2383, 2002.

Bertran-Ortiz, A., and H. A. Zebker, ScanSAR-to-Stripmap mode interferometry processing using ENVISAT/ASAR data, *IEEE Transactions on Geoscience and Remote Sensing*, *45*(11), 3468–3480, 2007.

Downloaded from https://www.cambridge.org/core. IP address: 189.217.92.64, on 11 Feb 2026 at 15:51:46, subject to the Cambridge Core terms of use, available at https://www.cambridge.org/core/terms. https://www.cambridge.org/core/product/1F8951EFC610A352837B95E4DAEFBAEB

Bevis, M., S. Businger, S. Chiswell, T. A. Herring, R. A. Anthes, C. Rocken, and R. H. Ware, GPS meteorology: Mapping zenith wet delays onto precipitable water, *Journal of Applied Meteorology (1988–2005)*, *33*(3), 379–386, 1994.

Biggs, J., and T. J. Wright, How satellite InSAR has grown from opportunistic science to routine monitoring over the last decade, *Nature Communications*, *11*(1), 1–4, 2020.

Bracewell, R., *The Fourier Transform and Its Applications*, 2nd ed., McGraw-Hill Book Company, New York, 1978.

Brcic, R., A. Parizzi, M. Eineder, R. Bamler, and F. Meyer, Ionospheric effects in SAR interferometry: An analysis and comparison of methods for their estimation, in *2011 IEEE International Geoscience and Remote Sensing Symposium*, pp. 1497–1500, IEEE, 2011.

Bürgmann, R., P. A. Rosen, and E. J. Fielding, Synthetic aperture radar interferometry to measure Earth's surface topography and its deformation, *Annual Review of Earth and Planetary Sciences*, *28*(1), 169–209, 2000.

Cerri, L., et al., Precision orbit determination standards for the Jason series of altimeter missions, *Marine Geodesy*, *33*(S1), 379–418, 2010.

Chelton, D. B., and F. J. Wentz, Global microwave satellite observations of sea surface temperature for numerical weather prediction and climate research, *Bulletin of the American Meteorological Society*, *86*(8), 1097–1116, 2005.

Chen, C. W., and H. A. Zebker, Network approaches to two-dimensional phase unwrapping: Intractability and two new algorithms, *Journal of the Optical Society of America A*, *17*(3), 401–414, 2000.

Chen, C. W., and H. A. Zebker, Two-dimensional phase unwrapping with use of statistical models for cost functions in nonlinear optimization, *Journal of the Optical Society of America A*, *18*(2), 338–351, 2001.

Chen, C. W., and H. A. Zebker, Phase unwrapping for large SAR interferograms: Statistical segmentation and generalized network models, *IEEE Transactions on Geoscience and Remote Sensing*, *40*(8), 1709–1719, 2002.

Chen, J., H. A. Zebker, and R. Knight, A persistent scatterer interpolation for retrieving accurate ground deformation over InSAR-decorrelated agricultural fields, *Geophysical Research Letters*, *42*(21), 9294–9301, 2015.

Chen, J., R. Knight, and H. A. Zebker, The temporal and spatial variability of the confined aquifer head and storage properties in the San Luis Valley, Colorado inferred from multiple InSAR missions, *Water Resources Research*, *53*(11), 9708–9720, 2017.

Colesanti, C., and J. Wasowski, Investigating landslides with space-borne Synthetic Aperture Radar (SAR) interferometry, *Engineering Geology*, *88*(3–4), 173–199, 2006.

Costantini, M., S. Falco, F. Malvarosa, and F. Minati, A new method for identification and analysis of persistent scatterers in series of SAR images, in *IGARSS 2008–2008 IEEE International Geoscience and Remote Sensing Symposium*, vol. 2, pp. II-449–II-452, 2008.

Costantini, M., S. Falco, F. Malvarosa, F. Minati, F. Trillo, and F. Vecchioli, Persistent scatterer pair interferometry: Approach and application to COSMO-SkyMed SAR data, *IEEE Journal of Selected Topics in Applied Earth Observations and Remote Sensing*, *7*(7), 2869–2879, 2014.

Curlander, J. C., and R. N. McDonough, *Synthetic Aperture Radar: Systems and Signal Processing*, John Wiley & Sons, New York, chapter 4, 1991.

Daout, S., H. Sudhaus, T. Kausch, A. Steinberg, and B. Dini, Interseismic and post-seismic shallow creep of the North Qaidam thrust faults detected with a multi-temporal InSAR analysis, *Journal of Geophysical Research: Solid Earth*, *124*(7), 7259–7279, 2019.

Downloaded from https://www.cambridge.org/core. IP address: 189.217.92.64, on 11 Feb 2026 at 15:51:46, subject to the Cambridge Core terms of use, available at https://www.cambridge.org/core/terms. https://www.cambridge.org/core/product/1F8951EFC610A352837B95E4DAEFBAEB

Daout, S., B. Dini, W. Haeberli, M. P. Doin, and B. Parsons, Ice loss in the Northeastern Tibetan Plateau permafrost as seen by 16 yr of ESA SAR missions, *Earth and Planetary Science Letters*, *545*, 116404, 2020a.

Daout, S., A. Steinberg, M. P. Isken, S. Heimann, and H. Sudhaus, Illuminating the spatio-temporal evolution of the 2008–2009 Qaidam earthquake sequence with the joint use of InSAR time series and teleseismic data, *Remote Sensing*, *12*(2850), 1–23, 2020b.

Doin, M.-P., C. Lasserre, G. Peltzer, O. Cavalié, and C. Doubre, Corrections of stratified tropospheric delays in SAR interferometry: Validation with global atmospheric models, *Journal of Applied Geophysics*, *69*(1), 35–50, 2009.

Donlon, C. J., M. Martin, J. Stark, J. Roberts-Jones, E. Fiedler, and W. Wimmer, The operational sea surface temperature and sea ice analysis (OSTIA) system, *Remote Sensing of Environment*, *116*, 140–158, 2012.

Drusch, M., et al., Sentinel-2: ESA's optical high-resolution mission for GMES operational services, *Remote Sensing of Environment*, *120*, 25–36, 2012.

Ebmeier, S. K., Application of independent component analysis to multitemporal InSAR data with volcanic case studies, *Journal of Geophysical Research: Solid Earth*, *121*(12), 8970–8986, 2016.

Elachi, C., *Spaceborne Radar Remote Sensing: Applications and Techniques*, IEEE Press, New York, 1988.

Elachi, C., and J. J. Van Zyl, *Introduction to the Physics and Techniques of Remote Sensing*, John Wiley & Sons, 2021.

Emardson, T., M. Simons, and F. Webb, Neutral atmospheric delay in interferometric synthetic aperture radar applications: Statistical description and mitigation, *Journal of Geophysical Research: Solid Earth*, *108*(B5), 2003.

Farr, T. G., et al., The shuttle radar topography mission, *Reviews of Geophysics*, *45*(2), 1–33, 2007.

Fattahi, H., *Geodetic Imaging of Tectonic Deformation with InSAR*, University of Miami, Miami, 2015.

Fattahi, H., M. Simons, and P. Agram, InSAR time-series estimation of the ionospheric phase delay: An extension of the split range-spectrum technique, *IEEE Transactions on Geoscience and Remote Sensing*, *55*(10), 5984–5996, 2017.

Fernandez, J., D. Escobar, H. Bock, and P. Femenias, Copernicus POD Operations – Orbital Accuracy of Sentinel-1A and Sentinel-2A, *International Symposium on Space Flight Dynamics*, *4*(2), 201–213, an optional note, 2015.

Ferretti, A., C. Prati, and F. Rocca, Nonlinear subsidence rate estimation using permanent scatterers in differential SAR interferometry, *IEEE Transactions on Geoscience and Remote Sensing*, *38*(5), 2202–2212, 2000.

Ferretti, A., C. Prati, and F. Rocca, Permanent scatterers in SAR interferometry, *IEEE Transactions on Geoscience and Remote Sensing*, *39*(1), 8–20, 2001.

Ferretti, A., A. Fumagalli, F. Novali, C. Prati, F. Rocca, and A. Rucci, A new algorithm for processing interferometric data-stacks: SqueeSAR, *IEEE Transactions on Geoscience and Remote Sensing*, *49*(9), 3460–3470, 2011.

Fialko, Y., M. Simons, and D. Agnew, The complete (3-D) surface displacement field in the epicentral area of the 1999 Mw7. 1 Hector Mine earthquake, California, from space geodetic observations, *Geophysical Research Letters*, *28*(16), 3063–3066, 2001.

Franceschetti, G., and R. Lanari, *Synthetic Aperture Radar Processing*, CRC press, Boca Raton, 2018.

Freeman, A., G. Krieger, P. Rosen, M. Younis, W. T. Johnson, S. Huber, R. Jordan, and A. Moreira, SweepSAR: Beam-forming on receive using a reflector-phased array feed combination for spaceborne SAR, in *2009 IEEE Radar Conference*, pp. 1–9, IEEE, 2009.

Downloaded from https://www.cambridge.org/core. IP address: 189.217.92.64, on 11 Feb 2026 at 15:51:46, subject to the Cambridge Core terms of use, available at https://www.cambridge.org/core/terms. https://www.cambridge.org/core/product/1F8951EFC610A352837B95E4DAEFBAEB

Fu, L.-L., and A. Cazenave, *Satellite Altimetry and Earth Sciences: A Handbook of Techniques and Applications*, Elsevier, 2000.

Fuhrmann, T., and M. C. Garthwaite, Resolving three-dimensional surface motion with InSAR: Constraints from multi-geometry data fusion, *Remote Sensing*, *11*(3), 241, 2019.

Gaddes, M. E., A. Hooper, M. Bagnardi, H. Inman, and F. Albino, Blind signal separation methods for InSAR: The potential to automatically detect and monitor signals of volcanic deformation, *Journal of Geophysical Research: Solid Earth*, *123*(11), 10,226–10,251, 2018.

Gaddes, M. E., A. Hooper, and M. Bagnardi, Using machine learning to automatically detect volcanic unrest in a time series of interferograms, *Journal of Geophysical Research: Solid Earth*, *124*(11), 12,304–12,322, 2019.

Galetzka, J., et al., Slip pulse and resonance of the Kathmandu basin during the 2015 Gorkha earthquake, Nepal, *Science*, *349*(6252), 1091–1095, 2015.

Galloway, D. L., and J. Hoffmann, The application of satellite differential SAR interferometry-derived ground displacements in hydrogeology, *Hydrogeology Journal*, *15*(1), 133–154, 2007.

Ghiglia, D. C., and M. D. Pritt, *Two-Dimensional Phase Unwrapping: Theory, Algorithms, and Software*, A Wiley Interscience Publication, New York, 1998.

Ghiglia, D. C., and L. A. Romero, Robust two-dimensional weighted and unweighted phase unwrapping that uses fast transforms and iterative methods, *Journal of the Optical Society of America A*, *11*(1), 107–117, 1994.

Goel, K., and N. Adam, A distributed scatterer interferometry approach for precision monitoring of known surface deformation phenomena, *IEEE Transactions on Geoscience and Remote Sensing*, *52*(9), 5454–5468, 2014.

Goldstein, R., and C. Werner, Radar ice motion interferometry, in *Proceedings 3rd ERS Sympposium*, vol. 2:11, pp. 969–972, Florence, Italy, 1997.

Goldstein, R. M., and C. L. Werner, Radar interferogram filtering for geophysical applications, *Geophysical Research Letters*, *25*(21), 4035–4038, 1998.

Goldstein, R. M., H. A. Zebker, and C. L. Werner, Satellite radar interferometry: Two-dimensional phase unwrapping, *Radio Science*, *23*(4), 713–720, 1988.

Goldstein, R. M., H. Engelhardt, B. Kamb, and R. M. Frolich, Satellite radar interferometry for monitoring ice sheet motion: Application to an Antarctic ice stream, *Science*, *262*(5139), 1525–1530, 1993.

Gomba, G., and F. De Zan, Bayesian data combination for the estimation of ionospheric effects in SAR interferograms, *IEEE Transactions on Geoscience and Remote Sensing*, *55*(11), 6582–6593, 2017.

Gomba, G., A. Parizzi, F. D Zan, M. Eineder, and R. Bamler, Toward operational compensation of ionospheric effects in SAR interferograms: The split-spectrum method, *IEEE Transactions on Geoscience and Remote Sensing*, *54*(3), 1446–1461, 2015.

Grandin, R., E. Klein, M. Métois, and C. Vigny, Three-dimensional displacement field of the 2015 Mw8. 3 Illapel earthquake (Chile) from across-and along-track Sentinel-1 TOPS interferometry, *Geophysical Research Letters*, *43*(6), 2552–2561, 2016.

Gray, A. L., K. E. Mattar, and G. Sofko, Influence of ionospheric electron density fluctuations on satellite radar interferometry, *Geophysical Research Letters*, *27*(10), 1451–1454, 2000.

Guarnieri, A. M., and S. Tebaldini, On the exploitation of target statistics for SAR interferometry applications, *IEEE Transactions on Geoscience and Remote Sensing*, *46*(11), 3436–3443, 2008.

Guns, K., X. Xu, Y. Bock, and D. Sandwell, GNSS-corrected InSAR displacement time-series spanning the 2019 Ridgecrest, CA earthquakes, *Geophysical Journal International*, *230*(2), 1358–1373, 2022.

Downloaded from https://www.cambridge.org/core. IP address: 189.217.92.64, on 11 Feb 2026 at 15:51:46, subject to the Cambridge Core terms of use, available at https://www.cambridge.org/core/terms. https://www.cambridge.org/core/product/1F8951EFC610A352837B95E4DAEFBAEB

Haines, A. J., and W. E. Holt, A procedure for obtaining the complete horizontal motions within zones of distributed deformation from the inversion of strain rate data, *Journal of Geophysical Research*, *98*(B7), doi:10.1029/93jb00892, 1993.

Haines, A. J., L. L. Dimitrova, L. M. Wallace, and C. A. Williams, *Introduction to the Vertical Derivatives of Horizontal Stress (VDoHS) Rates*, pp. 9–18, Springer International Publishing, Cham, 2015.

Hanssen, Ramon F. *Radar Interferometry: Data Interpretation and Error Analysis*. Vol. 2. Springer Science & Business Media, New York, 2001.

He, L., G. Feng, W. Xu, Y. Wang, Z. Xiong, H. Gao, and X. Liu, Coseismic kinematics of the 2023 Kahramanmaras, Turkey earthquake sequence from InSAR and optical data, *Geophysical Research Letters*, *50*(17), e2023GL104,693, 2023.

Hooper, A., and H. A. Zebker, Phase unwrapping in three dimensions with application to InSAR time series, *Journal of the Optical Society of America A*, *24*(9), 2737–2747, 2007.

Hooper, A., H. Zebker, P. Segall, and B. Kampes, A new method for measuring deformation on volcanoes and other natural terrains using InSAR persistent scatterers, *Geophysical Research Letters*, *31*(23), 2004.

Hu, X., R. Bürgmann, X. Xu, E. Fielding, and Z. Liu, Machine-learning characterization of tectonic, hydrological and anthropogenic sources of active ground deformation in California, *Journal of Geophysical Research: Solid Earth*, *126*(11), 1–21, 2021.

Huang, S., and H. A. Zebker, Persistent scatterer density by image resolution and terrain type, *IEEE Journal of Selected Topics in Applied Earth Observations and Remote Sensing*, *12*(7), 2069–2079, 2019.

Hussain, E., A. Hooper, T. J. Wright, R. J. Walters, and D. P. Bekaert, Interseismic strain accumulation across the central North Anatolian Fault from iteratively unwrapped InSAR measurements, *Journal of Geophysical Research: Solid Earth*, *121*(12), 9000–9019, 2016.

Itoh, K., Analysis of the phase unwrapping algorithm, *Applied Optics*, *21*(14), 2470–2470, 1982.

Jackson, J. D., *Classical Electrodynamics*, John Wiley & Sons, New York, 2012.

Jin, Z., and Y. Fialko, Finite slip models of the 2019 Ridgecrest earthquake sequence constrained by space geodetic data and aftershock locations, *Bulletin of the Seismological Society of America*, *110*(4), 1660–1679, 2020.

Joughin, I., R. Kwok, and M. Fahnestock, Estimation of ice-sheet motion using satellite radar interferometry: Method and error analysis with application to Humboldt Glacier, Greenland, *Journal of Glaciology*, *42*(142), 564–575, 1996a.

Joughin, I., D. Winebrenner, M. Fahnestock, R. Kwok, and W. Krabill, Measurement of ice-sheet topography using satellite-radar interferometry, *Journal of Glaciology*, *42*(140), 10–22, 1996b.

Joughin, I., B. E. Smith, and W. Abdalati, Glaciological advances made with interferometric synthetic aperture radar, *Journal of Glaciology*, *56*(200), 1026–1042, 2010.

Kaula, W. M., *Theory of satellite geodesy: Applications of satellites to geodesy*, p. 124, Blaisdell Publlishing Company, Waltham Massachusetts, 1966.

Khoshmanesh, M., M. Shirzaei, and R. M. Nadeau, Time-dependent model of aseismic slip on the central San Andreas Fault from InSAR time series and repeating earthquake, *Journal of Geophysical Research: Solid Earth*, *120*, 3076–6658–6679, 2015.

Lazeckỳ, M., A. Hooper, and P. Piromthong, InSAR-derived horizontal velocities in a global reference frame, *Geophysical Research Letters*, *50*(10), e2022GL101,173, 2023.

Lemrabet, L., M. P. Doin, C. Lasserre, and P. Durand, Referencing of continental-scale InSAR-derived velocity fields: Case study of the Eastern Tibetan plateau, *Journal of Geophysical Research: Solid Earth*, *128*(7), 1–28, 2023.

Downloaded from https://www.cambridge.org/core. IP address: 189.217.92.64, on 11 Feb 2026 at 15:51:46, subject to the Cambridge Core terms of use, available at https://www.cambridge.org/core/terms. https://www.cambridge.org/core/product/1F8951EFC610A352837B95E4DAEFBAEB

Li, X., S. Jónsson, and Y. Cao, Interseismic deformation from Sentinel-1 burst-overlap interferometry: Application to the southern Dead Sea fault, *Geophysical Research Letters*, *48*(16), e2021GL093,481, 2021.

Li, Y., R. Bürgmann, and T. Taira, Spatiotemporal variations of surface deformation, shallow creep rate, and slip partitioning between the San Andreas and Southern Calaveras Fault, *Journal of Geophysical Research: Solid Earth*, *128*(1), 1–23, 2023.

Li, Z., R. Zhao, J. Hu, L. Wen, G. Feng, Z. Zhang, and Q. Wang, InSAR analysis of surface deformation over permafrost to estimate active layer thickness based on one-dimensional heat transfer model of soils, *Scientific Reports*, *5*(October), 1–9, 2015.

Liang, C., and E. J. Fielding, Measuring azimuth deformation with L-band ALOS-2 ScanSAR interferometry, *IEEE Transactions on Geoscience and Remote Sensing*, *55*(5), 2725–2738, 2017.

Liang, C., P. Agram, M. Simons, and E. J. Fielding, Ionospheric correction of InSAR time series analysis of C-band Sentinel-1 TOPS data, *IEEE Transactions on Geoscience and Remote Sensing*, *57*(9), 6755–6773, 2019.

Lindsey, E. O., V. J. Sahakian, Y. Fialko, Y. Bock, S. Barbot, and T. K. Rockwell, Interseismic strain localization in the San Jacinto fault zone, *Pure and Applied Geophysics*, *171*(11), 2937–2954, 2014.

Lindsey, E. O., R. Natsuaki, X. Xu, M. Shimada, M. Hashimoto, D. Melgar, and D. T. Sandwell, Line-of-sight displacement from ALOS-2 interferometry: Mw 7.8 Gorkha Earthquake and Mw 7.3 aftershock, *Geophysical Research Letters*, *42*(16), 6655–6661, 2015.

Liu, F., J. R. Elliott, T. J. Craig, A. Hooper, and T. J. Wright, Improving the resolving power of InSAR for earthquakes using time series: A case study in Iran, *Geophysical Research Letters*, *48*(14), e2021GL093,043, 2021.

Liu, F., J. R. Elliott, S. K. Ebmeier, T. J. Craig, A. Hooper, C. Novoa Lizama, and F. Delgado, First onset of unrest captured at Socompa: A recent geodetic survey at central Andean volcanoes in Northern Chile, *Geophysical Research Letters*, *50*(10), e2022GL102,480, 2023.

Lv, X., B. Yazıcı, M. Zeghal, V. Bennett, and T. Abdoun, Joint-scatterer processing for time-series InSAR, *IEEE Transactions on Geoscience and Remote Sensing*, *52*(11), 7205–7221, 2014.

Lyons, S., and D. Sandwell, Fault creep along the southern San Andreas from interferometric synthetic aperture radar, permanent scatterers, and stacking, *Journal of Geophysical Research: Solid Earth*, *108*(B1), 2003.

Madsen, S., Estimating the Doppler centroid of SAR data., *IEEE Trans. Aerospace and Electronic Systems*, *AES-25*, 134–140, 1989.

Markus, T., et al., The Ice, Cloud, and land Elevation Satellite-2 (ICESat-2): Science requirements, concept, and implementation, *Remote Sensing of Environment*, *190*, 260–273, 2017.

Massonnet, D., and K. L. Feigl, Radar interferometry and its application to changes in the Earth's surface, *Reviews of Geophysics*, *36*(4), 441–500, 1998.

Massonnet, D., and T. Rabaute, Radar interferometry: Limits and potential, *IEEE Transactions on Geoscience and Remote Sensing*, *31*(2), 455–464, 1993.

Materna, K., J. Maurer, and L. Sandoe, Strain-2D (version 1.1.1), doi:10.5281/zenodo.5240908, 2021.

Maubant, L., E. Pathier, S. Daout, M. Radiguet, M.-P. P. Doin, E. Kazachkina, V. Kostoglodov, N. Cotte, and A. Walpersdorf, Independent component analysis and parametric approach for source separation in InSAR time series at regional scale: Application to the 2017–2018 slow slip event in Guerrero (Mexico), *Journal of Geophysical Research: Solid Earth*, *125*(3), 1–18, 2020.

Downloaded from https://www.cambridge.org/core. IP address: 189.217.92.64, on 11 Feb 2026 at 15:51:46, subject to the Cambridge Core terms of use, available at https://www.cambridge.org/core/terms. https://www.cambridge.org/core/product/1F8951EFC610A352837B95E4DAEFBAEB

Maurer, J., and K. Materna, Quantification of geodetic strain rate uncertainties and implications for seismic hazard estimates, *Geophysical Journal International*, pp. 4–7, 2023.

McCarthy, D. D., G. Petit, et al., *IERS conventions (2003)*, Bundesamt für Kartographie und Geodäsie Frankfurt am Main, Germany, 2004.

McClain, E. P., W. G. Pichel, and C. C. Walton, Comparative performance of AVHRR-based multichannel sea surface temperatures, *Journal of Geophysical Research: Oceans*, *90*(C6), 11,587–11,601, 1985.

Meta, A., J. Mittermayer, P. Prats, and U. Steinbrecher, TOPS imaging with TerraSAR-X: Mode design and performance analysis, *Geoscience and Remote Sensing, IEEE Transactions on*, *48*(2), 759–769, 2010.

Meyer, F., R. Bamler, N. Jakowski, and T. Fritz, The potential of low-frequency SAR systems for mapping ionospheric TEC distributions, *IEEE Geoscience and Remote Sensing Letters*, *3*(4), 560–564, 2006.

Milliner, C. W., J. F. Dolan, J. Hollingsworth, S. Leprince, F. Ayoub, and C. G. Sammis, Quantifying near-field and off-fault deformation patterns of the 1992 Mw 7.3 L anders earthquake, *Geochemistry, Geophysics, Geosystems*, *16*(5), 1577–1598, 2015.

Miranda, N., Definition of the TOP SSLC deramping function for products generated by the S-1 IPF, *Tech. rep.*, European Space Agency, cOPE-GSEG-EOPG-TN-14- 0025, 2015.

Mittermayer, J., et al., TOPS Sentinel-1 and TerraSAR-X processor comparison based on simulated data., in *Synthetic Aperture Radar (EUSAR), 2010 8th European Conference on.*, VDE, 2010.

Morishita, Y., M. Lazecky, T. J. Wright, J. R. Weiss, J. R. Elliott, and A. Hooper, LiCSBAS: An open-source insar time series analysis package integrated with the LiCSAR automated sentinel-1 InSAR processor, *Remote Sensing*, *12*(3), 5–8, 2020.

Neely, W. R., A. A. Borsa, and F. Silverii, Ginsar: A cGPS correction for enhanced insar time series, *IEEE Transactions on Geoscience and Remote Sensing*, *58*(1), 136–146, 2020.

Neely, W. R., A. A. Borsa, J. A. Burney, M. C. Levy, F. Silverii, and M. Sneed, Characterization of groundwater recharge and flow in california's San Joaquin Valley from InSAR-observed surface deformation, *Water Resources Research*, *57*(4), e2020WR028,451, 2021.

Ou, Q., S. Daout, J. R. Weiss, L. Shen, M. Lazecký, T. J. Wright, and B. E. Parsons, Large-scale interseismic strain mapping of the NE Tibetan plateau from Sentinel-1 interferometry, *Journal of Geophysical Research: Solid Earth*, *127*(6), 1–29, 2022.

Pagani, C., T. Bodin, M. Métois, and C. Lasserre, Bayesian estimation of surface strain rates from global navigation satellite system measurements: Application to the Southwestern United States, *Journal of Geophysical Research: Solid Earth*, *126*(6), 1–25, doi:10.1029/2021JB021905, 2021.

Pany, T., "Tropospheric GPS slant delays at very low elevations." Proc. Int., Workshop on GPS Meteorology, Tsukuba, Japan, 2003.

Prats-Iraola, P., R. Scheiber, L. Marotti, S. Wollstadt, and A. Reigber, TOPS interferometry with TerraSAR-X. Geoscience and remote sensing, *Geoscience and Remote Sensing, IEEE Transactions on*, *50*(8), 3179–3188, 2012.

Press, W., S. Teukolsky, W. Vetterling, and B. Flannery, *Numerical Recipes in C*, second edition ed., Cambridge University Press, New York City, 994 pp, 1992.

Press, W. H., S. A. Teukolsky, W. T. Vetterling, and B. P. Flannery, *Numerical Recipes 3rd Edition: The Art of Scientific Computing*, Cambridge University Press, Cambridge, 2007.

Downloaded from https://www.cambridge.org/core. IP address: 189.217.92.64, on 11 Feb 2026 at 15:51:46, subject to the Cambridge Core terms of use, available at https://www.cambridge.org/core/terms. https://www.cambridge.org/core/product/1F8951EFC610A352837B95E4DAEFBAEB

Qiao, X., and Y. Zhou, Geodetic imaging of shallow creep along the Xianshuihe fault and its frictional properties, *Earth and Planetary Science Letters*, *567*, 117,001, 2021.

Rees, W., *Physical Principles of Remote Sensing*, Cambridge University Press, Cambridge, 2001.

Reichle, R. H., R. D. Koster, P. Liu, S. P. Mahanama, E. G. Njoku, and M. Owe, Comparison and assimilation of global soil moisture retrievals from the Advanced Microwave Scanning Radiometer for the Earth Observing System (AMSR-E) and the Scanning Multichannel Microwave Radiometer (SMMR), *Journal of Geophysical Research: Atmospheres*, *112*(D9), 2007.

Rignot, E., S. Gogineni, W. Krabill, and S. Ekholm, North and northeast Greenland ice discharge from satellite radar interferometry, *Science*, *276*(5314), 934–937, 1997.

Rodriguez, E., and J. Martin, Theory and design of interferometric synthetic aperture radars, in *IEE Proceedings F (Radar and Signal Processing)*, vol. 139, pp. 147–159, IET, 1992.

Rosen, P., S. Hensley, H. Zebra, F. Webb, and E. Felding, Surface deformation and coherence measurements of Kilauea Volcano, Hawaii from SIR-C radar interferometry, *Journal of Geophysical Research*, *101*(E10), 23,109–23,125, 1996.

Rosen, P., S. Hensley, S. Shaffer, W. Edelstein, Y. Kim, R. Kumar, T. Misra, R. Bhan, and R. Sagi, The NASA-ISRO SAR (NISAR) mission dual-band radar instrument preliminary design, in *2017 IEEE International Geoscience and Remote Sensing Symposium (IGARSS)*, pp. 3832–3835, IEEE, 2017.

Rosen, P. A., S. Hensley, I. R. Joughin, F. K. Li, S. N. Madsen, E. Rodriguez, and R. M. Goldstein, Synthetic aperture radar interferometry, *Proceedings of the IEEE*, *88*(3), 333–382, 2000.

Rosen, P. A., E. Gurrola, G. F. Sacco, and H. Zebker, The InSAR scientific computing environment, in *EUSAR 2012; 9th European Conference on Synthetic Aperture Radar*, pp. 730–733, VDE, 2012.

Sack, M., M. Ito, and I. Cumming, Application of efficient linear fm matched filtering algorithms to synthetic aperture radar processing, in *IEE Proceedings F (Communications, Radar and Signal Processing)*, vol. 132, pp. 45–57, IET, 1985.

Sandwell, D. T., and E. J. Price, Phase gradient approach to stacking interferograms, *Journal of Geophysical Research: Solid Earth*, *103*(B12), 30,183–30,204, 1998.

Sandwell, D. T., and L. Sichoix, Topographic phase recovery from stacked ERS interferometry and a low-resolution digital elevation model, *Journal of Geophysical Research: Solid Earth*, *105*(B12), 28,211–28,222, 2000.

Sandwell, D. T., and P. Wessel, Interpolation of 2-D vector data using constraints from elasticity, *Geophysical Research Letters*, *43*(10), 10,703–10,709, 2016.

Sansosti, E., P. Bernardino, M. Manunta, F. Serafino, and G. Fornaro, Geometrical SAR image registration, *IEEE Transactions on Geoscience and Remote Sensing*, *44*(10), 2861, 2006.

Sarychikhina, O., E. Glowacka, R. Mellors, and F. Vidal, Land subsidence in the Cerro Prieto Geothermal Field, Baja California, Mexico, from 1994 to 2005: An integrated analysis of DInSAR, leveling and geological data, *Journal of Volcanology and Geothermal Research*, *204*(1), 76–90, 2011.

Satalino, G., F. Mattia, M. W. Davidson, T. Le Toan, G. Pasquariello, and M. Borgeaud, On current limits of soil moisture retrieval from ERS-SAR data, *IEEE Transactions on Geoscience and Remote Sensing*, *40*(11), 2438–2447, 2002.

Scheiber, R., and A. Moreira, Coregistration of interferometric SAR images using spectral diversity, *IEEE Transactions on Geoscience and Remote Sensing*, *38*(5), 2179–2191, 2000.

Downloaded from https://www.cambridge.org/core. IP address: 189.217.92.64, on 11 Feb 2026 at 15:51:46, subject to the Cambridge Core terms of use, available at https://www.cambridge.org/core/terms. https://www.cambridge.org/core/product/1F8951EFC610A352837B95E4DAEFBAEB

Schmidt, D. A., and R. Bürgmann, Time-dependent land uplift and subsidence in the Santa Clara valley, California, from a large interferometric synthetic aperture radar data set, *Journal of Geophysical Research: Solid Earth*, *108*(B9), 2003.

Segall, P., *Earthquake and Volcano Deformation*, Princeton University Press, Princeton, NJ, 2010.

Shanker, A. P., and H. A. Zebker, Sparse two-dimensional phase unwrapping using regular grid methods, *IEEE Geoscience and Remote Sensing Letters*, *6*(3), 519–522, 2009.

Shanker, P., and H. Zebker, Persistent scatterer selection using maximum likelihood estimation, *Geophysical Research Letters*, *34*(22), 2007.

Simons, M., and P. Rosen, Interferometric ynthetic aperture radar geodesy, *Geodesy*, *3*, 391–446, 2007.

Simons, M., and P. Rosen, 3.12 – Interferometric synthetic aperture radar geodesy, in *Treatise on Geophysics (Second Edition)*, edited by G. Schubert, second edition ed., pp. 339–385, Elsevier, Oxford, 2015.

Smith, W., and P. Wessel, Gridding with continuous curvature splines in tension, *Geophysics*, *55*(3), 293–305, 1990.

Sneed, M., and J. Brandt, Detection and measurement of land subsidence using GPS surveying and InSAR, Coachella Valley, California, 1996–2006, *Tech. Rep. 2007-5251*, USGS Scientific Investigations Report, New York City, 2007.

Sneed, M., J. Brandt, and M. Solt, Land subsidence, groundwater levels, and geology in the Coachella Valley, California, 1993–2010, *Tech. rep.*, US Geological Survey, 2014.

Stephenson, O. L., Y.-K. Liu, Z. Yunjun, M. Simons, P. Rosen, and X. Xu, The impact of plate motions on long-wavelength InSAR-derived velocity fields, *Geophysical Research Letters*, *49*(21), e2022GL099,835, 2022.

Strozzi, T., A. Luckman, T. Murray, U. Wegmuller, and C. L. Werner, Glacier motion estimation using SAR offset-tracking procedures, *IEEE Transactions on Geoscience and Remote Sensing*, *40*(11), 2384–2391, 2002.

Sundal, A. V., A. Shepherd, P. Nienow, E. Hanna, S. Palmer, and P. Huybrechts, Melt-induced speed-up of Greenland ice sheet offset by efficient subglacial drainage, *Nature*, *469*(7331), 521–524, 2011.

Swarztrauber, P., *Vectorizing the FFTs, in Parallel Computations (G. Rodrigue, ed.)*, pp. 51–83, Academic Press, Cambridge, MA, 1982.

Teunissen, P. J., and O. Montenbruck, *Springer Handbook of Global Navigation Satellite Systems*, vol. 10, Springer, 2017.

Tong, X., and D. Schmidt, Active movement of the Cascade landslide complex in Washington from a coherence-based InSAR time series method, *Remote Sensing of Environment*, *186*, 405–415, 2016.

Tong, X., D. Sandwell, and Y. Fialko, Coseismic slip model of the 2008 Wenchuan earthquake derived from joint inversion of interferometric synthetic aperture radar, GPS, and field data, *Journal of Geophysical Research*, *115*(B04314), 2010.

Tymofyeyeva, E., and Y. Fialko, Mitigation of atmospheric phase delays in InSAR data, with application to the eastern California shear zone, *Journal of Geophysical Research: Solid Earth*, *120*(8), 5952–5963, 2015.

Van Leijen, F. J., Persistent scatterer interferometry based on geodetic estimation theory, Ph.D. thesis, Delft University of Technology, 2014.

Van Puymbroeck, N., R. Michel, R. Binet, J.-P. Avouac, and J. Taboury, Measuring earthquakes from optical satellite images, *Applied Optics*, *39*(20), 3486–3494, 2000.

Wang, C., X. Mao, and Q. Wang, Landslide displacement monitoring by a fully polarimetric SAR offset tracking method, *Remote Sensing*, *8*(8), 624, 2016.

Downloaded from https://www.cambridge.org/core. IP address: 189.217.92.64, on 11 Feb 2026 at 15:51:46, subject to the Cambridge Core terms of use, available at https://www.cambridge.org/core/terms. https://www.cambridge.org/core/product/1F8951EFC610A352837B95E4DAEFBAEB

Wang, H., and T. J. Wright, Satellite geodetic imaging reveals internal deformation of western Tibet, *Geophysical Research Letters*, *39*(7), 1–5, 2012.

Wang, K., and J. Chen, Accurate persistent scatterer identification based on phase similarity of radar pixels, *IEEE Transactions on Geoscience and Remote Sensing*, pp. 1–1, 2022.

Wang, K., X. Xu, and Y. Fialko, Improving burst alignment in TOPS interferometry with bivariate enhanced spectral diversity, *IEEE Geoscience and Remote Sensing Letters*, *14*(12), 2423–2427, 2017.

Wang, M., and Z.-K. Shen, Present-day crustal deformation of continental China derived from GPS and its tectonic implications, *Journal of Geophysical Research: Solid Earth*, *125*(2), 3782–3803, 2020.

Wegnüller, U., C. Werner, T. Strozzi, A. Wiesmann, O. Frey, and M. Santoro, Sentinel-1 support in the GAMMA software, *Procedia Computer Science*, *100*, 1305–1312, 2016.

Wei, M., Location and source characteristics of the 2016 January 6 North Korean nuclear test constrained by InSAR, *Geophysical Journal International*, *209*(2), 762–769, 2017.

Werner, C., U. Wegmuller, T. Strozzi, and A. Wiesmann, Precision estimation of local offsets between pairs of SAR SLCs and detected SAR images, in *International Geoscience and Remote Sensing Symposium*, vol. 7, p. 4803, 2005.

Wessel, P., and W. Smith, New, improved version of Generic Mapping Tools released, *EOS Transactions of the American Geophysical Union*, *79*(47), 579, 1998.

Wessel, P., W. Smith, S. R, J. Luis, and F. Wobbe, Generic Mapping Tools: Improved version released, *EOS Transactions of the American Geophysical Union*, *94*, 409–410, 2013.

Wessel, P., J. Luis, L. Uieda, R. Scharroo, F. Wobbe, W. H. Smith, and D. Tian, The generic mapping tools version 6, *Geochemistry, Geophysics, Geosystems*, *20*(11), 5556–5564, 2019.

Wright, T. J., B. E. Parsons, and Z. Lu, Toward mapping surface deformation in three dimensions using InSAR, *Geophysical Research Letters*, *31*(1), 2004.

Xu, X., and D. T. Sandwell, Toward absolute phase change recovery with InSAR: Correcting for earth tides and phase unwrapping ambiguities, *IEEE Transactions on Geoscience and Remote Sensing*, *58*(1), 726–733, 2019.

Xu, X., D. T. Sandwell, E. Tymofyeyeva, A. Gonzalez-Ortega, and X. Tong, Tectonic and anthropogenic deformation at the Cerro Prieto geothermal step-over revealed by Sentinel-1A InSAR, *IEEE Transactions on Geoscience and Remote Sensing*, *55*(9), 5284–5292, 2017.

Xu, X., D. T. Sandwell, and B. Smith-Konter, Coseismic displacements and surface fractures from Sentinel-1 InSAR: 2019 Ridgecrest earthquakes, *Seismological Research Letters*, *91*(4), 1979–1985, 2020.

Xu, X., D. T. Sandwell, E. Klein, and Y. Bock, Integrated Sentinel-1 InSAR and GNSS time-series along the San Andreas Fault System, *Journal of Geophysical Research: Solid Earth*, *126*(11), 1–14, 2021.

Yague-Martinez, N., and P. Prats-Iraola, Accurate azimuth ground deformation estimation from Sentinel-1 time series, *IEEE Geoscience and Remote Sensing Letters*, *19*, 1–5, 2022.

Yu, C., Z. Li, N. T. Penna, and P. Crippa, Generic atmospheric correction model for interferometric synthetic aperture radar observations, *Journal of Geophysical Research: Solid Earth*, *123*(10), 9202–9222, 2018.

Zebker, H., and K. Chen, Accurate estimation of correlation in InSAR observations, *IEEE Geoscience and Remote Sensing Letters*, *2*(2), 124–127, 2005.

Zebker, H. A., User-friendly InSAR data products: Fast and simple timeseries processing, *IEEE Geoscience and Remote Sensing Letters*, *14*(11), 2122–2126, 2017.

Downloaded from https://www.cambridge.org/core. IP address: 189.217.92.64, on 11 Feb 2026 at 15:51:46, subject to the Cambridge Core terms of use, available at https://www.cambridge.org/core/terms. https://www.cambridge.org/core/product/1F8951EFC610A352837B95E4DAEFBAEB

Zebker, H. A., and J. J. Van Zyl, Imaging radar polarimetry: A review, *Proceedings of the IEEE*, *79*(11), 1583–1606, 1991.

Zebker, H. A., and J. Villasenor, Decorrelation in interferometric radar echoes, *IEEE Transactions on Geoscience and Remote Sensing*, *30*(5), 950–959, 1992.

Zebker, H. A., T. G. Farr, R. P. Salazar, and T. H. Dixon, Mapping the world's topography using radar interferometry: The TOPSAT mission, *Proceedings of the IEEE*, *82*(12), 1774–1786, 1994.

Zebker, M. S., J. Chen, and M. A. Hesse, Robust surface deformation and tropospheric noise characterization from common-reference interferogram subsets, *IEEE Transactions on Geoscience and Remote Sensing*, *61*, 1–14, 2023.

Zhang, J., Y. Bock, H. Johnson, P. Fang, S. Williams, J. Genrich, S. Wdowinski, and J. Behr, Southern California Permanent GPS Geodetic Array: Error analysis of daily position estimates and site velocities, *Journal of Geophysical Research*, *102*(B8), 18,005–18,035, 1997.

Zhang, P.-Z., Beware of slowly slipping faults, *Nature Geoscience*, *6*(5), 323–324, doi:10.1038/ngeo1811, 2013.

Zheng, Y., and H. A. Zebker, Phase correction of single-look complex radar images for user-friendly efficient interferogram formation, *IEEE Journal of Selected Topics in Applied Earth Observations and Remote Sensing*, *10*(6), 2694–2701, 2017.

Zheng, Y., H. Fattahi, P. Agram, M. Simons, and P. Rosen, On closure phase and systematic bias in multilooked SAR interferometry, *IEEE Transactions on Geoscience and Remote Sensing*, *60*, 1–11, 2022.

Zink, M., M. Bachmann, B. Brautigam, T. Fritz, I. Hajnsek, A. Moreira, B. Wessel, and G. Krieger, TanDEM-X: The new global DEM takes shape, *IEEE Geoscience and Remote Sensing Magazine*, *2*(2), 8–23, 2014.

Zitova, B., and J. Flusser, Image registration methods: A survey, *Image and Vision Computing*, *21*(11), 977–1000, 2003.

Downloaded from https://www.cambridge.org/core. IP address: 189.217.92.64, on 11 Feb 2026 at 15:51:46, subject to the Cambridge Core terms of use, available at https://www.cambridge.org/core/terms. https://www.cambridge.org/core/product/1F8951EFC610A352837B95E4DAEFBAEB

Index

angular resolution, 10
aperture
  1-D, 8
  2-D, 13
  synthetic, 15
apogee, 22
atmospheric modeling, 133
azimuth, 6
azimuth compression, 46, 48

back projection, 19, 36
bandwidth, 14
baseline, 38, 64, 78, 82
  critical, 62, 65, 76
  decorrelation, 73, 75
  parallel, 62, 63
  perpendicular, 61–63
burst, 107
  acquisition, 111
  overlap, 108, 112
burst overlap interferometry (BOI), 119, 152

carrier frequency, 42
centrifugal force, 23
chirp, 41
  bandwidth, 47
  frequency modulated, 58
  slope, 47
coherence, 75
  baseline, 75
  Doppler, 75
  image, 78
  radar noise, 75
  temporal, 75
  X, C, L, 76
coherent radiation, 9
convolution
  2D, 148
  theorem, 148
coordinates
  Earth-centered Earth-fixed (ECEF), 168
  East North Up (ENU), 168
coregistration, 115, 117
correlation, 74
cross correlation function, 148

deconvolve, 47
deformation
  east, 171
  ENU, 170
  LOS, 170
  north and up, 171
demodulate, 41
deramping, 115
dielectric constant, 137
digitize, 42
Doppler
  centroid, 36, 50, 51, 58
  frequency rate, 50, 51
  shift, 15
  zero, 36, 58, 72
dynamic form factor J_2, 24

Earth-fixed coordinate system, 26
effective speed, 49, 51
enhanced spectral diversity, 111, 117

fast time, 7
filter
  boxcar, 74
  Gaussian, 74
  Goldstein, 79
focused image, 52
Fourier transform, 2-D, 89

Downloaded from https://www.cambridge.org/core. IP address: 189.217.92.64, on 11 Feb 2026 at 15:51:46, subject to the Cambridge Core terms of use, available at https://www.cambridge.org/core/terms. https://www.cambridge.org/core/product/1F8951EFC610A352837B95E4DAEFBAEB

Fraunhofer diffraction
  1-D, 8
  2-D, 13
  integral, 10, 11
Fresnel distance, 12

geocode, 69
  SLC, 71
geometric image alignment, 38
global navigation satellite system (GNSS), 166
global positioning system (GPS), 166
GMTSAR, 2, 4, 71
  *.LED, 20
  *.PRM, 45
  *.raw, *.SLC, *.PRM, 42
  configure.txt, 38
  esarp, 42, 60, 105
  fitoffset, 60
  phasediff, 62
  resamp, 37, 60, 113
  SAT_baseline, 38, 63
  SAT_llt2rat, 36
  SAT_look, 171
  solid_tide, 144
  trans.dat, 36, 70
  xcorr, 60, 149
GNSS
  correcting InSAR LOS, 171
  vector deformation, 166
Green's theorem, 87
group velocity, 128, 138–140

Hermite polynomial
  interpolation, 19, 56
Hermitian symmetry, 42
heterodyne, 42
hyperbola, 49

image
  cross correlation, 147
  geometric alignment, 115
  master, 60
  reference, 60, 61, 68
  repeat, 60, 61, 68
  secondary, 60
  traditional image alignment, 113
imaging modes, 101
in phase, quadrature, 42
incidence angle, 63, 64, 72, 169
inclination of orbit plane, 24
InSAR, 1
interferogram, 60, 65, 69
  artifacts, 123
  filtering, 73
  fringes, 123
interseismic
  velocity, 172
interseismic velocity uncertainty, 172

ionosphere
  correction, 140
  F region, 136
  plasma, 137
  split spectrum, 128, 141, 142
ionospheric advance, 136

J_2 dynamic form factor, 24

Kepler
  elements, 21
    argument of perigee, 24
    eccentricity, 24
    inclination, 24
    longitude of node, 24
    semimajor axis, 24
    true anomaly, 24
  second law, 22

latitude
  geocentric, 28
  geographic, 28, 169
line of sight (LOS), 56, 76, 81, 84, 95, 111, 128, 133, 134, 147, 151, 154, 156, 159, 167, 169, 170, 172
look angle, 63, 64
looks, 76

master and secondary, 37
matched filter, 47, 50
multilook, 74, 76
multiple aperture interferometry (MAI), 150

near range, 49
NISAR, 119, 121

orbit
  dynamics, 19
  exact repeat, 33
  frequency, 23
  geostationary, 19, 30
  geosynchronous, 30
  near polar, 19
  period, 22, 23
  precession, 21, 24
  precise, 19, 34, 53
  Sun synchronous, 21, 31

parabolic approximation, 56
parametric modeling, 134
patch processing, 43
perigee, 22
persistent scatterer (PS), 161
phase
  aliasing, 86
  closure, 96
  Earth curvature, 61, 122
  gradient, 79, 87, 89
  gradient stacking, 90

Downloaded from https://www.cambridge.org/core. IP address: 189.217.92.64, on 11 Feb 2026 at 15:51:46, subject to the Cambridge Core terms of use, available at https://www.cambridge.org/core/terms. https://www.cambridge.org/core/product/1F8951EFC610A352837B95E4DAEFBAEB

ionosphere advance, 61, 122
layover, 86
noise, 61, 86, 122
orbit error, 61, 122
residue, 87, 92
shadow, 86
surface deformation, 61, 122
tides, 61, 122
topography, 61, 122
troposphere delay, 61, 122
unwrapping, 84
branch cut, 92
Fourier transform, 89
global, 89
Goldstein, 93
minimum cost flow, 93
nearest neighbor, 95
SNAPHU, 94
phase velocity, 125, 127, 136, 138, 139
Piñon, 48
pixel offset tracking (POT), 148, 149
plasma, 136
plasma frequency, 138
Poisson's equation, 89
polarization, 103
precession of orbit plane, 24
PRF, 16, 38, 42, 45, 46, 51, 52, 58, 76, 107, 108, 111, 119, 151, 152
constraints, 16, 101, 102
PRM
chirp_ext, 42
chirp_slope, 42
near_range, 42
pulse_dur, 42
radar_wavelength, 42
rng_samp_rate, 42
pulse duration, 47
pulse repetition frequency–PRF, 7

quadrature, in phase, 42

$\ddot{R}$ range acceleration, 53
radar
wavelength, 85
radar echo, 42
radar reflectors, 48
radius of Earth, 28
equatorial, 28
polar, 28
range, 6
acceleration, 50, 51, 53
compression, 43, 46
far, 16, 101
migration, 12, 44
near, 16, 101
rate, 36, 50
sampling rate, 47
vs. slow time, 56
range–Doppler algorithm, 41
raw signal data, 43
reference and repeat, 37
refractive index
dry troposphere, 126
ionosphere, 125
troposphere, 125
wet troposphere, 126
refractivity, 127
resolution
azimuth, 14, 104
ground range, 14
range, 65, 104
slant range, 14

SAR, 1, 8
processor, 41, 44
spotlight mode, 50
strip mode, 15, 41, 50
ScanSAR, 103, 105
ScanSAR interferometry, 108, 111
ScanSAR processing, 105
shift property, 41
sidelobes, 10
sidereal day, 21, 23
sinc function
1-D, 10
2-D, 13
single look complex (SLC), 41, 46, 60, 68
slow time, 7, 49
Small BAseline Subset (SBAS), 156
SNAPHU, 93, 94, 98
solar cycle, 137
spheroid, 28
spotlight mode SAR, 10
squint angle, 57
SRTM, 67
stacking, 133, 154
common scene, 155
state vector, 19
strain rate
dilitation, 174
second invariant, 174
shear, 174
strain rate tensor, 174
strip mods, 103
subswath, 107, 111
swath width constraints, 102
SweepSAR, 119, 121
synthetic aperture
length, 52

terrain observation by progressive scans (TOPS), 111
tide, 122
aliasing, 145
solid earth, 142, 144

Downloaded from https://www.cambridge.org/core. IP address: 189.217.92.64, on 11 Feb 2026 at 15:51:46, subject to the Cambridge Core terms of use, available at https://www.cambridge.org/core/terms. https://www.cambridge.org/core/product/1F8951EFC610A352837B95E4DAEFBAEB

time series
  GNSS, 177
  InSAR, 177
topography, 67, 68
total electron content (TEC), 123, 126, 128, 136, 140, 142
troposphere
  stratification, 130
  turbulence, 130
troposphere delay, 128
  mitigation, 133
  spatial characteristics, 131
  temporal characteristics, 131

velocity
  effective, 52, 57
  ground track, 52
  spacacraft, 52

water vapor, 127
WGS84
  ellipsoid, 63

zenith hydrostatic delay, 129
zenith wet delay, 129

Downloaded from https://www.cambridge.org/core. IP address: 189.217.92.64, on 11 Feb 2026 at 15:51:46, subject to the Cambridge Core terms of use, available at https://www.cambridge.org/core/terms. https://www.cambridge.org/core/product/1F8951EFC610A352837B95E4DAEFBAEB